Universität für Bodenkultur Wien

CONDUCTIVE NANOMEMBRANES FOR ELECTRICALLY DRIVEN REACTIONS AND SEPARATIONS

Department für Biotechnologie

Institut für angewandte Mikrobiologie

Vorstand: Reingard Grabherr, Univ.Prof. Dipl.-Ing. Dr.nat.techn.

Betreuer: Alois Jungbauer, Univ.Prof. Dipl. -Ing. Dr.nat.techn.

Dissertation

zur Erlangung des Doktorgrades

an der Universität für Bodenkultur Wien

Eingereicht von

Christian Schuster Dipl.-Ing. Bakk.techn.

Wien, August 2019

Acknowledgements

First and foremost, I want to express my sincere gratitude to Alois for his encouraging and purposeful, yet open-minded mentorship and supervision. It was a joy to learn so many things from you. I want to thank Rupert for his valuable input as well as his help and guidance throughout the whole journey. I am very grateful to Jasmin who, among so much else, provided me with stimulating and productive teamplay, made the work environment joyful and rough times bearable. I thank Agnes for thoroughly acquainting me with the research topic and the project, for the teamwork and the pleasant time we spent. Thank you, Stephan, for our fruitful scientific exchange and discussions as well as your help. A big thank you to the whole downstream processing working group for the cheerful working environment and the countless other pleasant aspects of being part of it.

Finally, I am very thankful for the help, support and loving environment my family and dear friends provide and the time I get to spend with them. Especially, I am sincerely grateful and proud of my girls Marie, Matilda and Johanna for going through this time together with me.

Abstract

Permeable membranes are omnipresent and often indispensable in separations science and technology enabling a wide variety of processes. Efforts to enhance their performance are constantly made, for instance by developing ever thinner membranes, to a point where they are molecularly thin. For the processing of fluids that bear content of biological origin, such ‘nanomembranes’ have been demonstrated to possess intriguing properties and the potential to contest industrial paradigms. They could enable new technologies such as (bio-) sensors, membrane reactors, Janus-type or switchable membranes and even actively pumping membranes. Progress to apply nanomembranes for bioseparations on industrial scale as well as progress to devise new functionally active nanomembranes has been stalling. Harnessing their beneficial properties requires macroscopically stable and robust membranes while being compatible with the compounds contained in the surrounding solution. Polymer based nanomembranes combining these two crucial characteristics were developed in this thesis to potentially initiate the widespread application of nanomembranes in biotechnological production chains. Two types of ultrathin polymer films (thickness less than 100 nm) were shown to be compatible with and applicable for the size-based separation of both, small organic molecules and proteins, respectively. The scalability of the fabrication procedures was demonstrated by showcasing the compatibility with the dip-coating technique. Furthermore, the functionalization of the nanomembrane surface with nanostructured and conductive metal coatings has been studied. By providing an appropriate characterization and a predictive basis for their formation, the presented research should facilitate the creation of new technologies relying on electrically functional nanocomposite membranes.

Kurzfassung

Permeable Membranen sind allgegenwärtig und oft unersetzbar für Wissenschaft und Technik der Stofftrennung wo sie die Grundlage für eine Reihe von Prozessen bilden. Als Teil von ständig betriebenen Anstrengungen zur Verbesserung ihrer Funktion werden immer dünnere Membranen, bis hin zu Dicken von molekularer Dimension, entwickelt. Für das Bearbeiten von Flüssigkeiten mit Bestandteilen biologischer Herkunft besitzen solche ‚Nanomembranen' bemerkenswerte Eigenschaften und das Potenzial vorherrschende industrielle Standards zu ersetzen. Es könnten auch neue Technologien wie beispielsweise (Bio-) Sensoren, Membranreaktoren, Janus- oder schaltbare Membranen oder gar aktiv fördernde Membranen durch Nanomembranen ermöglicht werden. Der Fortschritt in diese Richtungen, Nanomembranen für Bioseparation im industriellen Maßstab sowie neuartige aktiv arbeitende Membranen, verläuft jedoch schleppend. Um sich ihre Vorzüge zunutze machen zu können, müssen Nanomembranen auf makroskopischer Ebene stabil und robust, sowie kompatibel mit der Arbeitsumgebung sein. Polymerbasierte Nanomembranen, welche diese wesentlichen Eigenschafen vereinen, wurden im Rahmen dieser Dissertation entwickelt, um eine weitreichende Anwendung in biotechnologischen Produktionsprozessen voranzutreiben. Hierzu wurde die Eignung und Kompatibilität zweier verschiedener Arten von ultradünnen Polymerfilmen (Dicke unter 100 nm) zur Trennung von kleinen organischen Molekülen bzw. von Proteinen gezeigt. Des Weiteren wurde die Skalierbarkeit der Herstellungstechnik anhand ihrer Eignung für die Tauchbeschichtung veranschaulicht. Außerdem wurde die Funktionalisierung der Nanomembranoberfläche mit nanostrukturierten und leitfähigen Metallbeschichtungen untersucht. Durch eine entsprechende Charakterisierung und das Bereitstellen einer Basis für die Prognostizierung ihrer Formgestaltung sollte die Entwicklung von neuartigen, auf diesen Nanoverbundstoffen basierenden Technologien ermöglicht werden.

Table of Contents

1 Introduction

The performance of membranes used for separation purposes is always subject to a certain tradeoff between the mass transfer across the separation layer and its associated selectivity[1]. Membrane thickness is one of two characteristics that are of vital importance for the mass transport properties. It is intriguing that, given a negligible thickness of the separation layer, half-maximal diffusion rates are theoretically achievable at porosities well below one percent[2]. In general, the thickness can be regarded as negligible once it approaches the size of the compounds being separated. A threshold of a thickness below 100 nm is often invoked so that this class of membranes is commonly termed ultrathin membranes or nanomembranes. The associated benefits of a thickness reduction become very apparent when considering both, Darcy's law and Fick's first law where the respective flux is inversely proportional to the traveled distance. The second aspect of crucial importance is the pore (or porosity) size and its distribution[1] influencing both, transport efficiency and selectivity. Once the thickness of the membrane is adequately low it also becomes feasible to have pore sizes approach the size of the compounds the membrane is designed to separate. For such ultrathin membranes the separation event (i.e. traveling from one side to the other) for a single molecule of interest becomes increasingly fast and interactions with the pore walls scarce, to a point where the time needed for pore discovery equals or exceeds that needed to traverse it[3]. This is not the case for thicker membranes where membrane crossing time is always dominant and pore sizes are usually much larger than the separated species. Although it is intuitive that thicker membranes have longer traverse times, quite surprisingly, prior to equilibrium they also exhibit less accurate discrimination between permeation and retention. In conventional filtration membranes, the contribution of diffusion to the total orthogonal mass transport is negligible compared to convective transport. For ultrathin membranes, mass transport due to diffusion becomes increasingly relevant and may even exceed convective flow. Thus, besides the obvious potential to enhance separation efficiency this also suggests the possibility of significantly elevated filtrate concentrations[4]. In addition to their potential application as highly efficient membranes in existing processes, the supremely fast and accurate separation characteristics of nanomembranes could enable them to contest longstanding paradigms such as distillation[5,6] or chromatography[4].

In general, two types of membranes can be distinguished with respect to the free volume elements penetrating the membrane matrix and the consequential mode of separation[6]: (i) dense membranes with a certain porosity intrinsic to the membrane material and (ii) membranes with geometrically defined porous structures such as single perforations or interconnected networks of solvent filled pores. Compounds either diffuse through the membrane material itself at different speeds (dense) or pass through pores still dissolved in

solvent (porous). Depending on the size of the compound of interest either only the second type (e.g. large organic molecules, proteins, viruses or cells) or both types (e.g. for solvents, ions or small/intermediate organic molecules) are suited as a separation device. This classification and the respective use cases also apply to ultrathin membranes. Notwithstanding the intricacies of optimization and scale up [7,8], it should be noted that nanomembranes of the first type are more straightforward to devise in terms of the production process due to their lack of geometric features, such as perforations, that have to be introduced. In contrast, the creation of geometrically defined porous structures or perforations at the nanometer scale presents a challenge starting at the level of fabrication process development.

In recent years the advent of nanofabrication for microelectronics has led to methods which were harnessed to enable the development of such nanomembranes[9]. The ability to precisely control nanometer scale patterns was used to combine the two crucial characteristics, low thickness and adequate pore size distribution to push the boundaries of the permeability-selectivity tradeoff[10,11]. Although it is a technological and scientific achievement to develop such membranes in itself, due to significant scientific interest it has been demonstrated frequently. However, only a fraction of the demonstrated procedures has the potential to be applicable for the actual production of separation devices on reasonable scales[9]. Accordingly, the approaches to produce such advanced membranes have been comprehensively reviewed recently with special emphasis on methods that are reasonably practicable[10]. Notably, the majority of these membranes are derived from inorganic materials such as metal oxides and ceramics (e.g. Figure 1a). Owing to their strong internal bonds these materials possess high mechanical strength[12] and chemical resistance which, in conjunction with established processing techniques, makes them a very appealing choice for ultrathin separation membrane development. Despite the evident assets of inorganic materials some pivotal aspects must be considered especially in view of separation tasks involving large amounts of fluids and solutions that contain biologically derived compounds: (i) although the methods and techniques for the processing of ultrathin inorganic materials are suited for mass production[4], they are generally restricted to the scale which is common in the field they were devised for and hence, incompatible with large scale, (ii) a majority of the fabrication processes require either quite sophisticated, laborious or time intensive processing steps, and (iii) proteins and other macromolecules contained in biological fluids tend to adsorb to inorganic materials deteriorating separation performance.

Polymer-based membranes have the potential to circumvent these shortcomings. On the one hand, the wealth of techniques for the fabrication and processing of polymer membranes traditionally encompasses well scalable methods without complex processing steps allowing their widespread application in many global industries[1]. This possibility to increase the scale of polymer membrane fabrication is largely facilitated by their solution-based processing prior

to solidification. On the other hand, biological matter exhibits a comparatively low tendency to adsorb to polymer membrane surfaces. This is, in part, why polymer materials occupy an indispensable position for the processing of biological fluids. For membrane based processes, they are applied almost exclusively[13]. However, the cost for these advantages is the comparatively low strength of polymer-based materials when the thickness approaches molecular dimensions. Therefore, the formation of freestanding ultrathin films purely based on polymeric materials that are robust over large lateral dimensions (centimeters, for that matter) without external support has been quite challenging[14]. Pioneering work presented some thirteen years ago began to unlock such polymer based 'giant nanomembranes'. By using materials that could be covalently crosslinked with high interconnection density first hybrid[14,15] and then purely polymer based[16] nanomembranes were devised. Ever since these developments, their anticipated immediate application in demanding tasks in separations science[16–18] has been somewhat pending. Especially for nanomembranes enabling the separation of proteins of biopharmaceutically relevant size there seems to be a gap in the literature. This has been the case in spite of the tremendous progress that has been made in the fabrication and development of freestanding polymeric nanomembranes in recent years intended for other applications[19,20]. However, a few studies have demonstrated the formation of freestanding perforated nanomembranes based on a polymeric material. For instance by arranging nanoparticles in a layer of polymerizable organic membrane material assembled at the water-air interface, so that after crosslinking the particles could be dissolved and leave perforations behind[21]. In another, quite exceptional way, the formation of a porous layer of polymer was induced on a substrate by dewetting of the polymer and then selectively building up a membrane on top of this network-like structure in a layer-by-layer fashion[22]. Thereby, the resulting perforations were adjustable in size by successive narrowing of the pores with each deposited layer. In another study focused on phase separation phenomena in thin films, the authors effectively prepared ultrathin polymeric nanomembranes using the phase separation of two immiscible polymers during film formation with perforations[23] that would possibly be suitable for the filtration of viruses. Another, intriguing demonstration of a polymer nanomembrane with pores was accomplished by growing the membrane by atom-transfer radical polymerization from a patterned surface[24]. The grown membrane was shown to be pH sensitive with drastic structural changes inducing complete pore constriction. Although these studies provided nice concepts and detailed analysis of the resultant membranes, they lack (at least) a characterization of their capability to function as a separation membrane. Additionally, the scales at which these membranes can be freely suspended without support are often only in the low µm range which does not promise macroscopic stability and integrity. Other nanomembranes, based on the dewetting of poly(L-lactic acid) from an underlying substrate during temperature induced crystallization (Figure 1b) have been demonstrated to be

applicable for the size-based separation of small organic dyes and small proteins[25]. The nanomembranes were used in diffusion-based permeability tests while being suspended over 8 µm holes. In another approach, the structure formation induced by local phase separation of a block copolymer has been leveraged for the formation of ultrathin filtration membranes with defined pores[26]. The formed porous structures were of adequate size to afford high flux and efficient separation of small viruses (Figure 1d). In a similar fashion, nanomembranes were prepared and demonstrated to be stable when freely suspended over 20 µm openings (Figure 1c) for the separation of two organic molecules[27]. A completely different approach was pursued by the formation of freestanding membranes from silk nanofibrils[28]. The wet-laid membranes showed exceptional water permeances as well as pores suitable for the processing of proteins (Figure 1e) although only thick (~ 500 nm) membranes were shown to be freestanding.

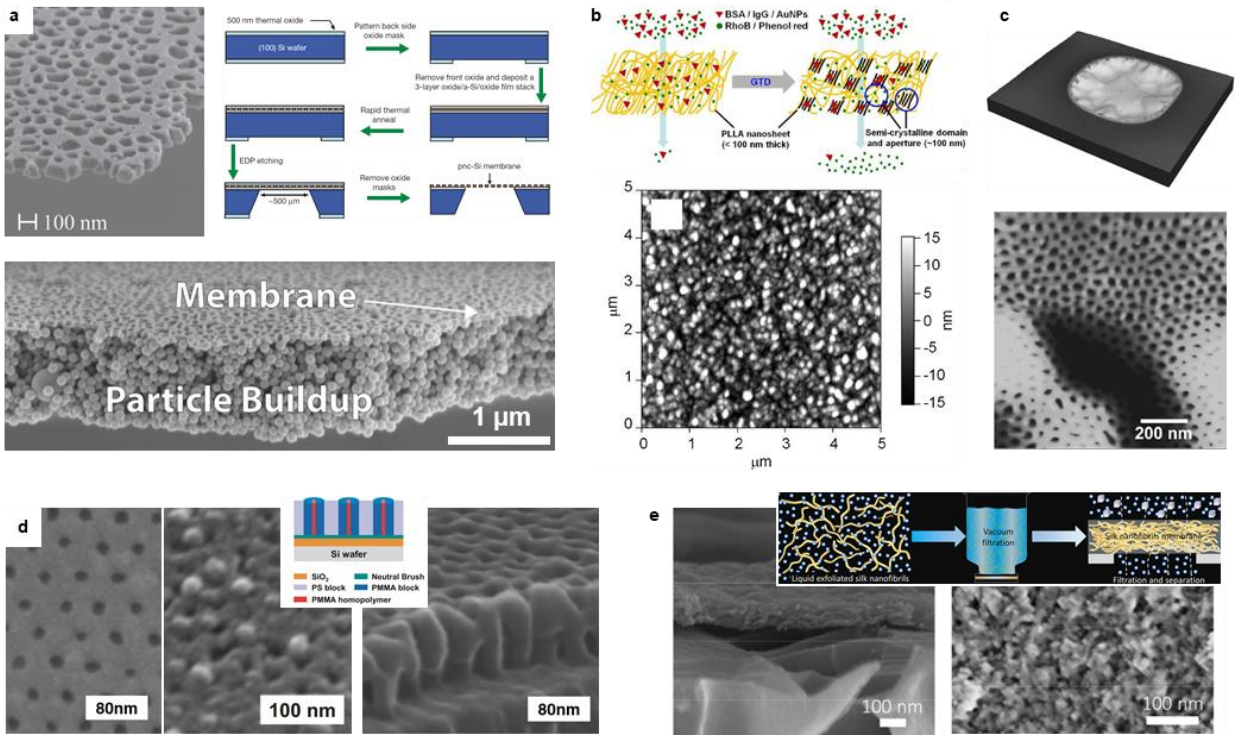

Figure 1. State-of-the-art freestanding perforated nanomembranes with demonstrated protein separation capabilities. a) Inorganic, silicon-based nanomembranes with mesopores (upper left and bottom) produced with microelectronics fabrication derived techniques (upper right). b) Poly(L-lactic acid) nanomembranes with perforations formed by temperature induced partial crystallization. c) Block-copolymer based membranes freely suspended over 20 µm openings during separation (upper). Uniform, close packed pores result from demixing of the polymer blocks and subsequent dissolution. d) Nanomembranes with highly ordered mesopores (left) suitable for high flux virus filtration (middle) prepared from a block-copolymer similar to (c) (inset) with cylindrical cross section (right). e) Biopolymer-based membranes produced from exfoliated silk nanofibrils by filtration (inset) with more irregular, tortuous porous structures. Reproduced and adapted with permission from References: a) 11,12,29 b) 25 c) 27 d) 26 e) 28. Copyright lies with the respective publisher.

Although some of the above approaches seem promising and could be further pursued, the resulting nanomembranes have (i) either not been shown to be stable on macroscopic scale or (ii) do not exhibit the necessary features to enable the precise separation of protein sized compounds and (iii) have either not demonstrated or suggested feasible ways and means to realize a larger scale production. Thus, for the processing of biotechnological production streams, there is a gap in the literature concerned with nanomembranes aiming to tackle or satisfy pressing problems and needs in this field in spite of their potential to do so.

In contrast to other branches of separation science (e.g. organic solvent nanofiltration, water desalination), the size range of compounds which are typically of interest when fluids that bear content of biological origin are processed commands the applicability of both dense as well as porous membranes. For instance, small organic compounds derived from biotechnological production streams aspire to serve as the foundation of a future bio-based economy as they constitute building blocks for sustainable engineering in bulk quantities[30,31]. Energy- and resource-efficient isolation to an adequate purity is a prerequisite in preserving their sustainable nature which could be afforded by cutting edge dense membrane materials with scalability to the required dimensions. A similar argument can be made for the separation of biomacromolecules of therapeutic relevance from process derived impurities and bioburden where extensive downstream processing prevails[32,33]. Processes based on ultrathin membranes with superior resolution and flux could induce a paradigm shift for membranes from mere concentration to actual purification purposes with high selectivity so as to challenge more expensive standards.

In addition to their potential as advanced separation devices working in traditional settings nanomembranes are compelling candidates for emerging applications. With their extraordinarily low thicknesses of less than 10 nm biological membranes were, in part, the inspiration to strive for an ultrathin synthetic analog. Achieving a dimensional similarity immediately suggests the incorporation of functionalities that are already present in nature. Starting from single nanopores in thick membranes such functionalization approaches were combined with nanofabricated ultrathin membranes to give small arrays (several μm^2) of very selective nanopores[34]. The progress in the last decade has led to the availability of synthetic nanomembranes that are finally approaching the dimensions of their natural paragon while being macroscopically stable[16,29]. Since macroscopic lateral dimensions are indispensable for separation tasks focusing on quantity these developments have been a prerequisite to develop purification devices applying the above concepts. Thereby, the functionalization of synthetic nanomembranes with biological assemblies that already impart natures membranes with superior permeability and selectivity would greatly expand the realm of possible applications. Intriguingly, it has indeed been demonstrated that nanomembranes can be equipped with biologically derived selectivity by incorporation of selective proteins (Figure 2) despite

rudimentary control of functionalization. One study[34] showed how proteins derived from the nucleopore complex could be immobilized on an inorganic nanomembrane whereby diffusion selectivity of was imparted to discriminate between an importin and bovine serum albumin (Figure 2a). Another work[35] demonstrated a change in permeability for small ions by immobilization of an outer membrane protein on polymeric perforated nanomembranes (Figure 2b). For such approaches the pore size is just as important as an adequately low membrane thickness for appropriate accommodation of the functional entities[34,35].

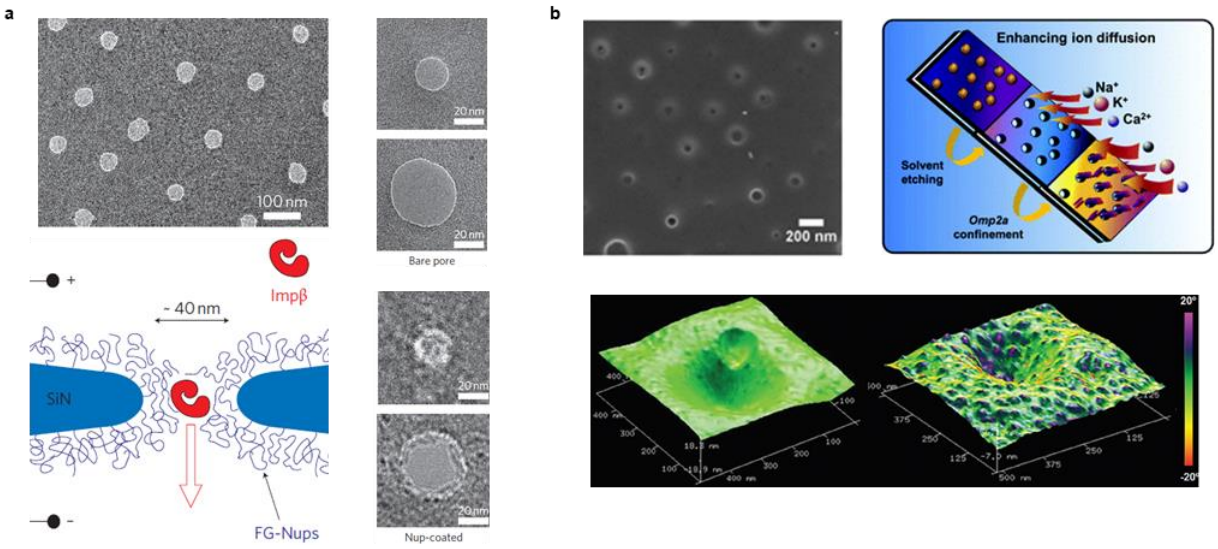

Figure 2. Functionalized biomimetic nanomembranes. a) Silicon nitride nanomembrane with perforations (upper panels) functionalized with nucleopore complex derived proteins (lower panels) imparting selectivity towards an importin (Impβ) with respect to bovine serum albumin. Reproduced and adapted with permission from Reference 34. Copyright (2011) Macmillan Publishers Limited. b) Polymeric perforated nanomembranes (upper left panel) functionalized with outer membrane protein aggregates (lower panel) to impart selectivity with respect to small ion diffusion (upper right panel). Reproduced and adapted with permission from Reference 35. Copyright (2016) The Royal Society of Chemistry.

One step ahead, the exploitation of systems that are not only highly selective but are also able to catalyze the selective accumulation of compounds against a concentration gradient (such as transport proteins) is also conceivable. Nanomembranes could be engineered to actively accumulate a cargo of choice while simultaneously separating it from process derived impurities. Nanomembrane reactors where the conversion of a selected compound is catalyzed at one side could be used to selectively convert and remove inhibiting effectors to enhance process performance *in situ*. Such actively functional nanocomposites have yet to be developed. This is not surprising in light of the fact that, regardless of the function, the driving force needed to accomplish catalytic activity would need to be replenished for such attempts of functionalization not to be futile. Thus, in order to impart synthetic nanomembranes with active functionality derived from nature in a feasible fashion they must be equipped with the ability to regenerate the required driving force. Catalytic activity is chiefly coupled either to the

hydrolysis of adenosine triphosphate, to the redox coupling with nicotinamide (and flavin) adenine dinucleotide or to the energy stored in pH (or chemical) gradients. A very suitable route to replenish the latter two energy sources can be the taken via electrochemical regeneration at metal surfaces. Redox cofactors can be rapidly and readily regenerated at solid metal electrodes[36,37]. A pH gradient can also be established or maintained by the electrochemical splitting of water at metal electrodes[38,39]. It would therefore be a leap in the right direction to furnish nanomembranes that are compatible with functional biological assemblies with a metal electrode to eventually afford electrically powered molecularly precise pumps or membrane reactors.

3 Important concepts

In this section several concepts are introduced in brevity that should assist to lucidly appreciate the following research content of the thesis. Emphasis is placed only on certain aspects that fit the appropriation in this thesis to omit unnecessarily extensive reading.

3.1 Polymer thin film formation

Since ultrathin membranes, regardless of their chemical composition, cannot be handled as freely as their thicker counterparts, adequate methods must be applied. This starts with the choice of the film formation process which lays out much of the subsequently necessary and possible steps. As established above, a great asset of polymeric thin films is the possibility of solution-based processing providing flexibility as well as scalability. A wealth of techniques is available to form or deposit polymer thin films each with a unique set of advantages and drawbacks[40,41]. One technique that has seen immense attention by research and industry, largely facilitated by the microelectronics- as well as the optoelectronics revolution[42,43], is spin-coating (Figure 3). It is a quite simple process to conduct where a flat solid substrate is rotated after it is covered with a coating solution of the target polymer. The substrate is usually held in place by a vacuum that clamps it to the rotating socket (Figure 3a).

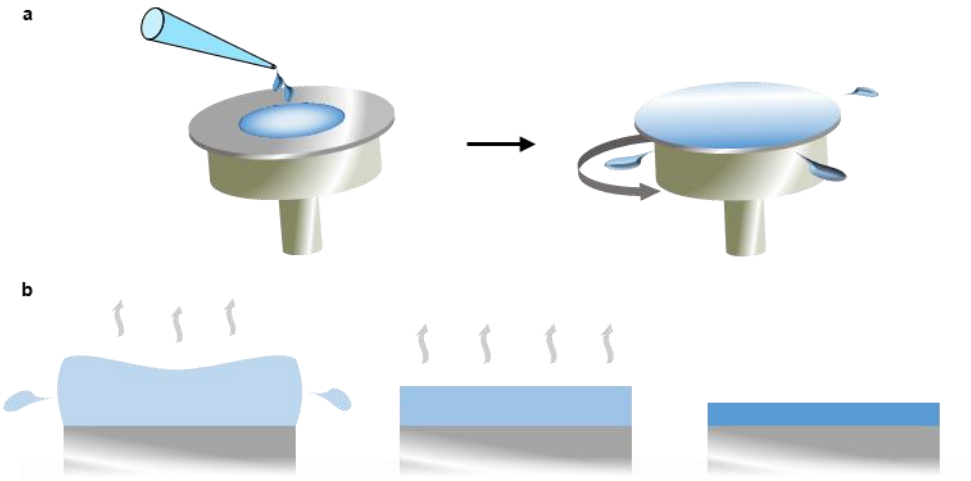

Figure 3. Schematic representation of the spin-coating process. a) 3D representation of the overall process from the application of the casting solution to spinning. b) Illustration of the film as it transitions from hydrodynamic (left) through evaporative thinning (middle) into a dry film (right).

Through the action of rotating the casting solution is spread out relatively evenly onto the revolving substrate. After spreading, the fluid continues to flow outward and off the substrate during a stage termed hydrodynamic thinning[43] (Figure 3b). It is important to realize that even in this early stage of the process, where drag forces and viscous flow are predominantly

responsible for film thinning, the evaporation of solvent into the ambient atmosphere is constantly contributing. At a certain point the film gets thin and concentrated enough for hydrodynamic effects to start becoming insignificant and the system transitions into the second stage of evaporative thinning[44]. Eventually the film enters a dry state through the above two stages after which the spin-coating process is completed. Notably, in the process of film formation the polymer solution undergoes a change from its initial composition to the (relatively) dry end state while continuously transitioning through all intermediate concentrations. The resulting film thickness can be altered by several factors[41] where the initial conditions of the casting solution and the spin-speed are the most instructive and straightforward ones. Higher spin-speeds will result in thinner liquid films at the crossover from hydrodynamic to evaporative thinning and thus to thinner dry films. Intuitively, higher polymer concentrations give thicker films due to the higher mass fraction in the liquid film and increased viscosity contributes to more resistance to hydrodynamic thinning. Importantly, it is possible to deposit another layer on top of the previously cast thin film provided that the second solvent does not dissolve the first layer. This can be conveniently leveraged to gently separate thin films from the casting substrate by first applying a so called ‘sacrificial layer’ which is dissolved after the polymer film of interest has been cast on top.

Dip-coating is a second technique that is very simple to conduct and allows the formation of high-quality thin films on substrates of virtually arbitrary forms and sizes, primarily however, on rigid substrates[41]. In conventional dip-coating (Figure 4) the substrate to be coated is immersed in a casting solution bath at a rate that ensures complete displacement of the ambient atmosphere from the surface. The substrate is then withdrawn from the coating bath so that a thin liquid film is left behind. The thickness of this initial liquid film is largely determined by the balance between four forces (the remaining two of six are often negligible)[45]. The upward forces of viscous drag mediated by the moving substrate and inertia of the arriving boundary layer are balanced by a net downward force of the meniscus and gravity (solid arrows in Figure 4b). The liquid flow traveling (or dragged) upward with the substrate splits in two, one that recirculates into and the other that follows the substrate out of the bath (dashed arrows in Figure 4b). The initial liquid film then enters the stage where thinning by evaporation dominates and the solution gradually dries into a solid layer. Again, the coated liquid film with a certain initial composition continuously transitions through all intermediate concentrations into a dry polymer film via hydrodynamic and later evaporative thinning. Counterintuitively, however, the resulting liquid film thickness after hydrodynamic thinning is proportional to the speed at which the substrate is withdrawn. This means that faster withdrawal rates lead to thicker films and vice versa.

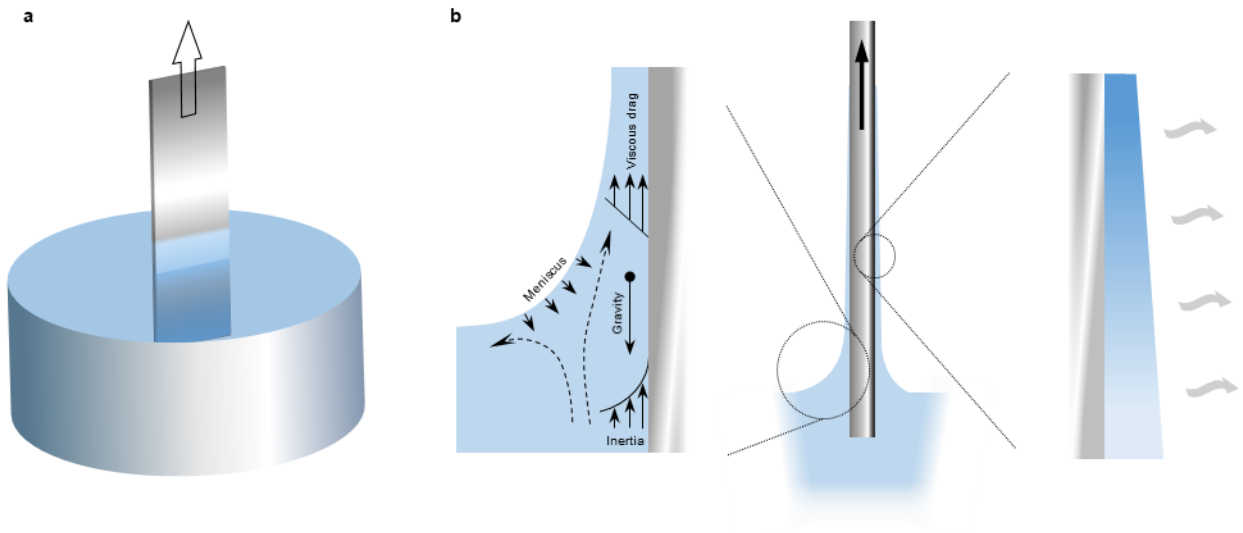

Figure 4. Schematic representation of the dip-coating process. a) 3D illustration of a flat substrate being vertically (arrow) withdrawn from the casting solution. b) Side view of the substrate where it exits the bath (middle) with detailed representations of the film formation at the meniscus (left) and evaporative thinning (right).

3.2 Structural features through phase separation

The phase separation of incompatible components is a widely used phenomenon in many industries. Particularly for the solution-based casting of polymer thin films it has facilitated their tremendous importance for functional materials[43,46]. While the casting of a solution where only a single polymer is dissolved in a single solvent leads to a uniformly structured layer, a vast variety of structures can be obtained by just adding a second, chemically dissonant component. During the casting of an appropriate polymer blend the associated transition from initial concentrations to the dry film forces the system through a continuous increase in concentration and thereby also into the mixing gap (blue arrow in Figure 5a). Thus, the system is unstable and will spontaneously separate into two phases where the respective components enrich[47]. In fact, there will be many domains of the minor phase dispersed within the other or some sort of co-continuous arrangement (Figure 5b middle). The system will tend towards thermodynamic equilibrium where, for instance, the interfacial area (more precisely interfacial free energy) of the newly formed phases is minimized as illustrated in the lower panel of Figure 5b. Here, the phases have separated completely. In thin films the influence of gravity is negligible and the system tends towards a coarsening of the phases to reduce interfacial area unless a stratification is favored to begin with[48]. Fortunately, however, the process of reaching thermodynamic equilibrium is a gradual one so that by complete evaporation of the solvent, in the dry film the intermediate phase morphology is pinned by kinetic constraints (e.g. diffusion limited) and preserved. Another vital aspect is that this phase separation process in thin films

happens under spatial conditions that are confined between the two interfaces of the film. The phase separated domains, even small ones, can thereby span from one interface to the opposite. The interfaces are facing either the air above or the substrate below the film during spin-coating and are therefore termed top and bottom interface, respectively. The chemical difference of the two components, the prerequisite for this phenomenon, can furthermore be exploited to selectively remove one phase while leaving the other untouched by dissolution in an appropriate solvent[48]. This technique can thus be leveraged for the preparation of functional nano- and micro-structured thin films[49]. The system gets more complex and the obtainable morphologies are more numerous if a third polymer component is added to the mixture. Such systems have been well studied and can further be modeled by numerical simulations[46] to (at least) give insight into the possibly obtainable morphologies and how to approach them.

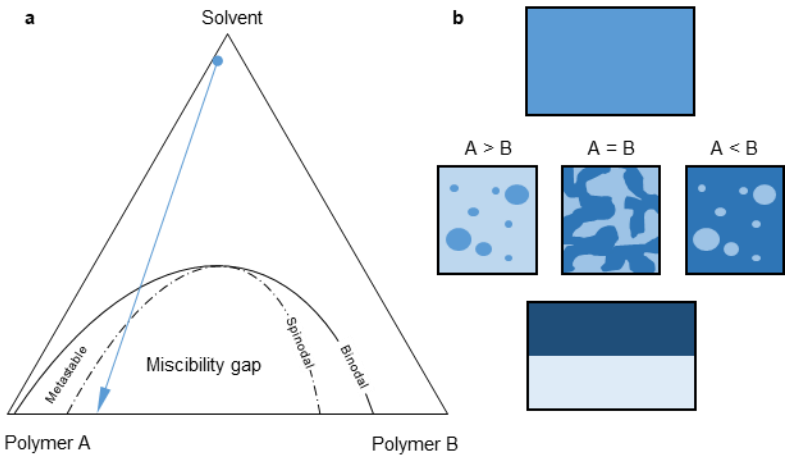

Figure 5. Phase transition diagram and schematic representation of phase separation. a) Phase diagram of a polymer blend in a common solvent. The transition in a thin film is indicated by the blue arrow for the case A > B. b) Illustration how a mixed system (upper) undergoes different phase separation routes depending on the (mole) ratio of the components (middle) to an end state in thermodynamic equilibrium (lower).

3.3 Metal coating by sputter deposition

For the deposition of thin uniform metal and ceramic films onto surfaces magnetron sputtering is a very popular method for substrates that are tolerant to vacuum conditions[50–52]. Its capability to generate high quality thin films at industrially relevant scale and rates along with its versatility with respect to thin film chemistry and substrate complexity make magnetron sputtering the method of choice for many applications[52]. Magnetron sputter deposition is usually conducted within a tightly sealed chamber filled with a low-pressure processing gas (Figure 6a). Key element for the principle of operation is a glow discharge plasma which is generated in this low-pressure atmosphere by a high voltage bias. Magnets are arranged behind the source material in a special way, called magnetron, so that the plasma is confined (to a certain degree[52]) in its vicinity. The high electrical potential gradient accelerates the plasma ions towards the cathodic material of choice where they knock out atoms. This process of bombardment with high energy ions is called sputtering of a target.

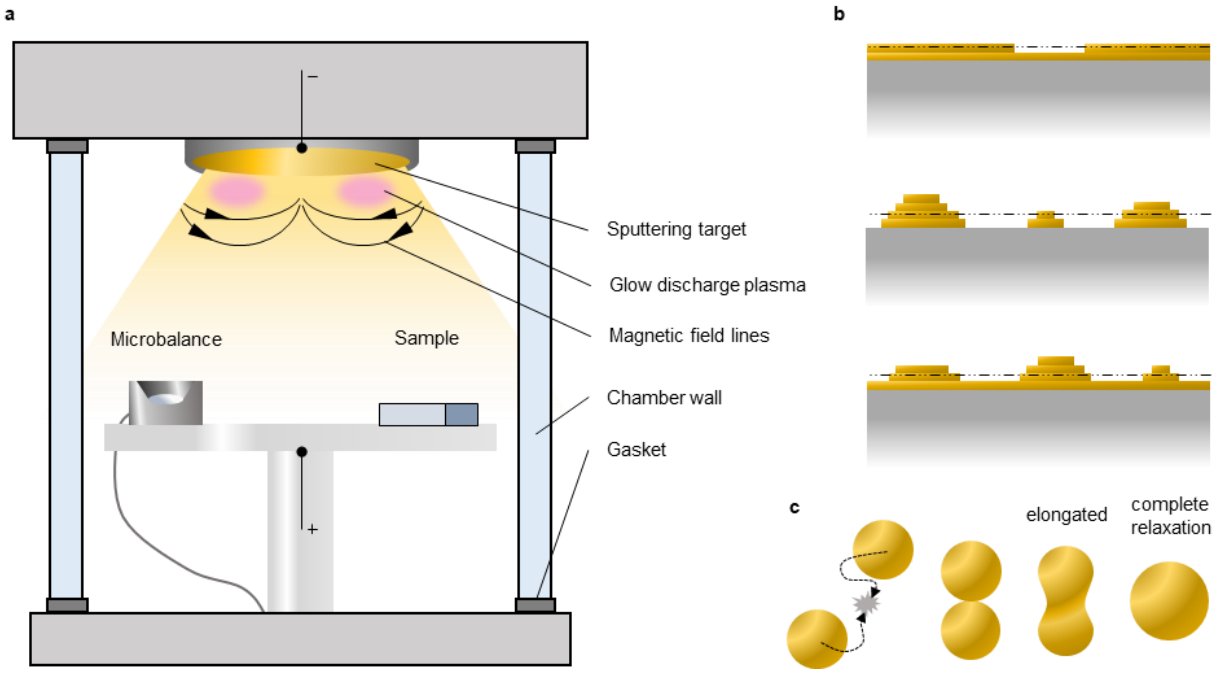

Figure 6. Schematic representation of the sputter coating setup, growth modes and cluster merging. a) Typical sputter coating setup with an electric field generating a plasma that is confined near the target material by the magnetic field of a magnetron. Ion bombardment knocks out atoms that travel to the sample and form a thin film. A microbalance is used to determine film thickness. b) Illustration of different growth modes. Layer-by-layer (upper), 3D island formation (middle), and 3D islands on initial uniform layer(s) (lower). The nominal film thickness is identical and indicated by a dash-dotted line. c) Top view sketch of two merging clusters from touching over elongated to completely relaxed and compact state with circular footprint.

The effectively sublimated atoms then travel away from the target in a random direction, potentially hitting other atoms, and eventually arrive at a random position somewhat opposite

of the origin. Thereby, atom for atom, a thin film of the source material is formed on surfaces in the surroundings of the sputtering target. The deposited material will display a certain tendency to form an interface with the coated surface depending on the specific interactions between the involved materials which leads to different modes of growth (Figure 6b). Interactions resulting in a strong tendency to form an interface lead to the growth of an initial uniform layer. If the coherent interaction of the deposited material is also strong, the film will proceed to grow layer by layer (Figure 6b upper sketch). In the opposite case (Figure 6b middle sketch), the deposited material has a low tendency to form an interface with the coated surface so that the interfacial area is reduced by the formation of clusters that are higher than the thickness of a homogenous film of equivalent mass (i.e. nominal film thickness). The intermediate case is where only one or several layers grow uniformly upon which a 3D island growth mode is initiated (Figure 6b lower sketch). The above phenomenological picture can, of course, be described by physical considerations. Thermodynamic arguments are frequently invoked to rationalize the occurrence and specific properties of the different growth modes[53]. These arguments are based on the concept of surface free energies and their balancing by the interfacial area formed between the three phases (surface, metal and gas). For this thesis, it turns out that only the second growth mode is relevant and needs further clarification.

The impinging atoms coming from the sputtered target will either reenter the gaseous phase or adsorb to the surface retaining some degree of mobility. Thus, adsorbed atoms diffuse on the surface eventually colliding and coordinating with other atoms to nucleate clusters. Depending on their size and the strength of interaction also the clusters are mobile to some extent[54] and migrate to merge with atoms as well as other clusters to grow in size quickly relaxing into their equilibrium shape (Figure 6c). As the interface and the associated strength of adhesion between the metal islands and the surface becomes sufficiently large, merging clusters do not relax into a compact equilibrium shape anymore. At least not until the next merging event takes place. Instead, at the touching points the cluster surface curvature is minimized (high curvature regions are energetically unfavorable) while the overall shape remains elongated whereby the clusters spread out to touch each other. Eventually, the metal structures form a conductive network at a point termed ‘percolation threshold’ while a considerable portion of the surface can remain uncovered[55]. These remaining gaps between the metal structures are then gradually filled during further deposition and the trenches relax in a similar fashion to reduce curvature until a continuous film with a certain surface roughness is obtained.

3.4 Thermosetting epoxy resin

Thermosetting polymers based on epoxy resins are among the stronger (and harder) spectrum of synthetic polymers[16,56]. A representative resin has therefore been introduced in a pioneering work for the preparation of robust nanomembranes with large lateral dimensions and aspect ratios higher than one million[16]. This thermosetting polymer and the technique to process it into nanomembranes has been used throughout the present thesis for the new developments and advances in polymer nanomembrane fabrication and further investigations. The final polymer is formed from two precursor components each being a polymer in their own right: poly[(*o*-cresyl glycidyl ether)-*co*-formaldehyde (PCGF) containing the epoxide functionalities and branched polyethyleneimine (PEI) bearing amine moieties (Figure 7a).

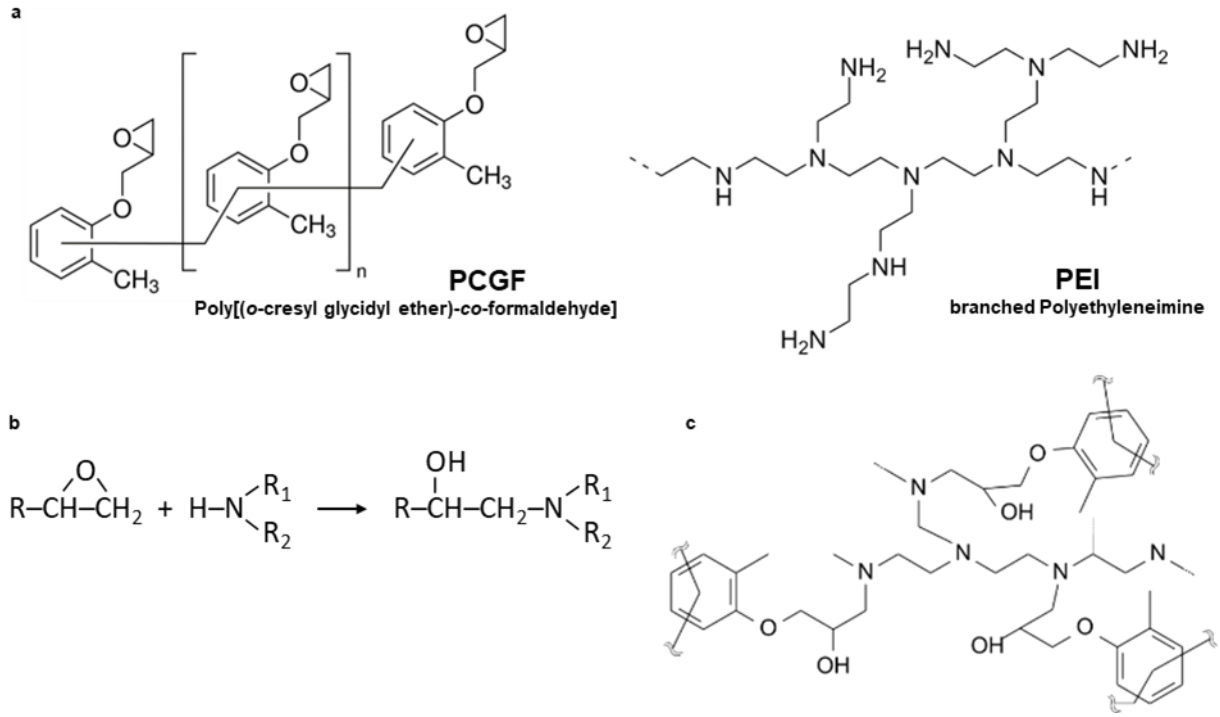

Figure 7. Thermosetting resin. Components, crosslinking reaction and resulting covalent network structure. a) Structures of the two components comprising the thermosetting polymer, the epoxy resin (left) and the polyamine (right) for curing. b) Condensation reaction of the functional groups resulting in a covalent bond, a higher order amine and a secondary alcohol. c) Schematic representation of the emergent covalently crosslinked network.

The functional groups of these two polymer components can undergo a condensation reaction to form a covalent bond[57] which, on a macroscopic scale, is called curing or setting (Figure 7b). This condensation reaction is quite slow or kinetically unfavorable at room temperature and can be accelerated by increasing temperature; hence the name thermosetting. By thoroughly mixing the two in an appropriate ratio and subsequent thermal treatment it is possible to turn the initial polymer blend into a covalently crosslinked network (Figure 7c). The

density of covalent linkages in this network will be a function of the ratio of the two components and have an impact on its mechanical properties. It is important to note that PEI is a branched polymer and that it contains not only primary but also secondary and tertiary amines where the former two can undergo condensation with epoxy functionalities. The two components individually are also soluble in many different organic solvents and have several common solvents. This enables the highly desirable solution-based processing as well as the possibility to use high molecular weight versions. Another aspect to bear in mind is that their different chemical nature bestows the two precursors with different interaction behavior with the respective solvent that they are processed in. In the relevant case of high molecular weight PEI, moderately sized PCGF and chloroform PEI is significantly less soluble than PCGF.

4 Objectives

The application of nanomembranes in diverse fields of research and even as industrial devices has been ongoing since roughly a decade. However, progress in the transfer of these incredibly valuable concepts to the realm of polymer-based ultrathin (bio-) separation membranes has been stalling and research concerned with this matter is scarce.

It was therefore the objective of this thesis to build on existing knowledge and techniques to establish a platform upon which polymer based nanomembranes could be advanced towards applicability in various fields. In particular, it should be investigated and shown how dense ultrathin polymer membranes could serve as selective separation devices to address the isolation of small organic compounds. Further, as a core element, a method for the introduction of geometrically defined porous structures should be devised in order to allow the applicability of the polymeric nanomembranes for the separation of biomacromolecules with particular emphasis on proteins. Finally, the functionalization of the polymer surface with a conductive metal coating should be demonstrated and investigated to pave the way for their use as devices with electronic functionality. Consequently, the following four points were the cornerstone objectives of this thesis where the last one represents a necessity to fulfill the former:

– Investigation of dense nanomembranes for the separation of small organic compounds within aqueous solutions
– Development of nanomembranes with geometrically defined perforations enabling the separation of proteins
– Demonstration of the possibility to functionalize the membrane surface with a conductive nanoscale metal coating and the investigation of structure-function relationships at the polymer-metal interface
– Establishment of suitable methods for the verification and characterization of functionality for both types of nanomembranes as well as the electronic and structural properties of the metal coatings

5 Summary of the work

The research undertaken in the scope of this thesis encompasses the development and investigation of polymer based ultrathin membranes with the capability to separate organic- and biomolecules in aqueous solutions as well as their functionalization with thin metal coatings. These efforts were made bearing in mind the intended fields and scales of operation and the associated necessity for adequately applicable fabrication concepts or techniques. In this respect, using polymeric materials is the fundamental commitment and the methodology to prepare such nanomembranes with macroscopic lateral dimensions was adopted from previous investigations[16]. The used polymer material, formed from a thermosetting resin comprising an epoxy (PCGF) and a polyamine component (PEI), was the key element of the developments and investigations presented in this thesis. The resin can be crosslinked to form a covalently bonded network structure at elevated temperatures and was demonstrated to retain its strength when prepared as an ultrathin freestanding membrane allowing large lateral dimensions. As a valuable deviation from the initially published procedure water soluble poly(sodium 4-styrenesulfonate) was used as a sacrificial layer rather than poly(4-hydroxystyrene). This results in a tremendous ease of handling as the nanomembrane can be released from the casting substrate to float on the surface of water and is confined to a stretched-out state at this interface instead of being submerged and freely floating.

In order to further enhance the robustness of the nanomembranes a systematic investigation on the mechanical properties was conducted (Publication I). The influence of the composition of the casting solution on the tensile strength and stiffness was studied by bulging tests (Figure 8). These bulging tests were performed with a customized setup (Figure 8a and b) where increasing hydrostatic pressure was exerted on the membranes. The pressure was related to the resulting deflection to deduce the relevant material parameters. Variations of the ratio between the two precursor components present in the casting solution were found to drastically change the mechanical properties of the resulting nanomembranes (Figure 8c). These changes were attributable to the resulting change in density of covalent crosslinking present in the membrane material. At stoichiometric unity of reactive moieties (those functional groups capable of undergoing crosslinking reactions) nanomembranes with the highest mechanical strength were obtainable indicating the highest crosslinking density. Beyond certain compositional combinations nanomembranes with sufficiently large lateral dimensions were not stable and fragmented into small pieces upon release which set the boundaries for the range of meaningful operation.

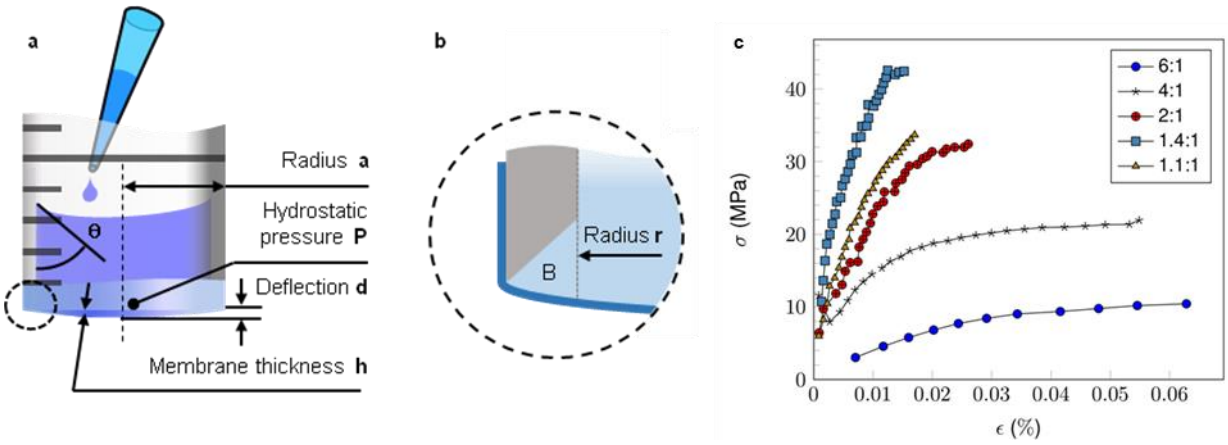

Figure 8. Bulging test setup and resulting stress-strain plots. a) Schematic representation of a bulging test conducted with the costomized setup. Parameters necessary to derive stress-strain relationships are indicated. b) Detailed sketch of the tube edge (grey) showing how the nanomembranes (blue) were positioned. B is the liquid (light blue) volume neglected in pressure calculations. c) Stress-strain plots derived from bulging tests of membranes which were produced from casting solutions of different precursor ratio as indicated in the graph legend.

A diffusion based photometric setup was further developed in order to investigate the transport properties of the individual nanomembranes (Figure 9a). As a prerequisite for these investigations the membranes had to be stable in a freely suspended state while spanning a circular opening of roughly 7 mm in diameter. In that setup the area of unsupported membrane separates the retentate from the permeate solution and only molecules able to traverse the membrane can enter the permeate compartment. The permeate solution is confined in a quartz cuvette and monitored by a UV-Vis spectrophotometer in order to identify changes in analyte concentration. For nanomembranes, due to their exceptionally low mass transfer resistance, it stands to reason that the integrity may be compromised without being readily detectable from the observed flux. It was therefore a necessity to continuously account for this possibility by adding a large rejection marker molecule to the retentate compartment and to preclude its absence in the permeate solution (blue particle rejected in the detail of Figure 9a). This rejection marker was selected to exhibit a UV-Vis spectrum suitable to be unequivocally distinguished from the analyte. Thereby, the observed mass transport from one side to the other could be attributed solely to the flux allowed by the membrane itself.

With the permeability test setup, the capability of the polymer material when prepared as a dense nanomembrane to act as a permselective barrier was initially demonstrated by the separation of two dyes in aqueous solution (Publication I, Figure 9b). The nanomembranes were prepared with the established spin-coating procedure with a thickness of 85 nm on a scale of roughly 20 cm² limited only by the casting substrate. The adjustable nature of the mechanical properties by virtue of the crosslinking density suggested that it was very interesting to investigate effects on the permselectivity as well. Such investigations were

conducted and complemented with the assessment of the compatibility with several other small organic molecules of potential industrial relevance (Figure 9c). Several differently composed membranes were tested for their permeability towards the various molecules. It could be demonstrated that the nanomembranes were indeed adjustable in terms of permeability as well as selectivity for all investigated organic molecules. Nanomembranes with the highest strength, and presumably the highest crosslinking density, displayed the lowest permeability and vice versa. However, the effects of thickness variations or lowering were not investigated which is, since the used material is not composed of long linear polymer chains, likely to enable increased[5,58] and maybe unexpected performance.

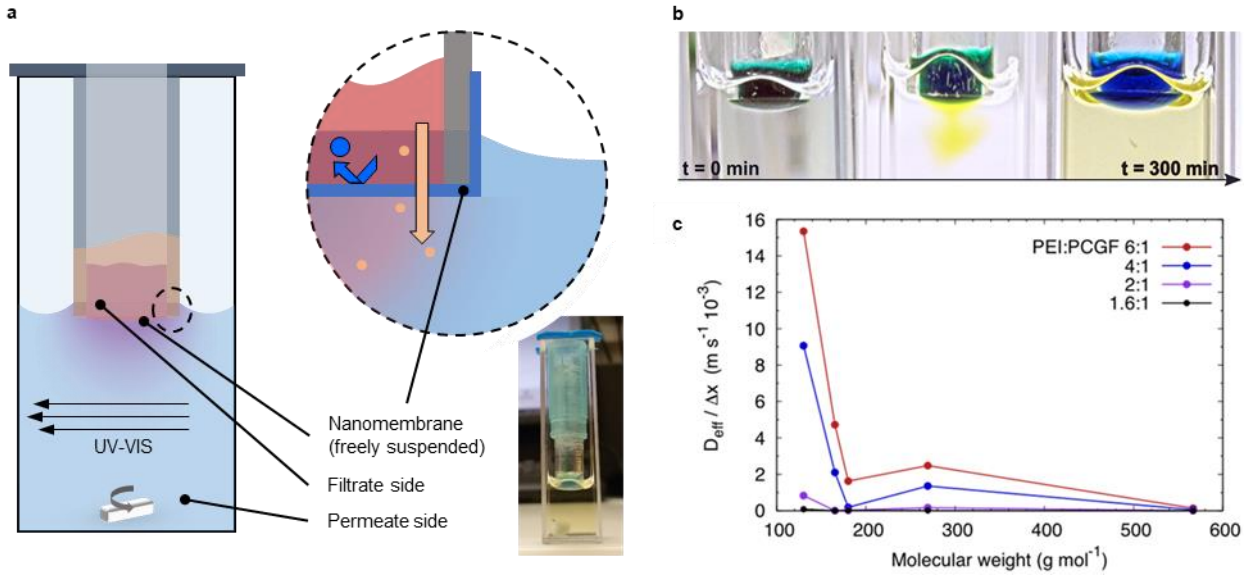

Figure 9. Photometric permeability test setup and permeability of dense nanomembranes a) Schematic representation and photograph of the diffusion test setup. The freely suspended nanomembrane separates the retentate compartment in the tube from the permeate compartment in the cuvette. b) Photographs of the diffusive separation of the two dyes Methyl Red (MW = 269.3 g mol^{-1}) and Patent Blue (MW = 566.6 g mol^{-1}) by a dense nanomembrane freely suspended and covering the 7 mm tube opening. c) Diffusive fluxes of different small organic molecules across differently composed dense nanomembranes versus their molecular mass.

In a next step, the procedure to produce these remarkably robust ultrathin films was modified to work towards nanomembranes with geometrically defined perforations allowing the permeation of larger particles such as proteins. To this end a bottom up approach was pursued in the form of the self-assembly of adequately sized pore templates induced by phase separation during thin film formation. This was demonstrated to be possible in two separate publications (Publications II and III) in two different ways. The first, conceptually more straightforward strategy involved the addition of a separate, incompatible polymer component (poly(D,L-lactide-*co*-glycolide), PLGA) to the casting solution. Thereby the necessary conditions for appropriate small-scale phase segregation should be established (Publication

II). The solubility of this third component in the casting solution would be exceeded at some point during evaporative thinning causing it to enrich in small phase separated domains that span from one film interface to the other (Figure 10a). After completion of film formation and covalent crosslinking of the membrane material to render it insoluble, perforations could be formed as the pore templates were selectively dissolvable by washing in the pure casting solvent (Figure 10b). By adjusting the parameters of thin film formation, the fabrication of 75 nm thick nanomembranes with perforations of roughly 26 nm diameter could be demonstrated (Figure 11, Publication II).

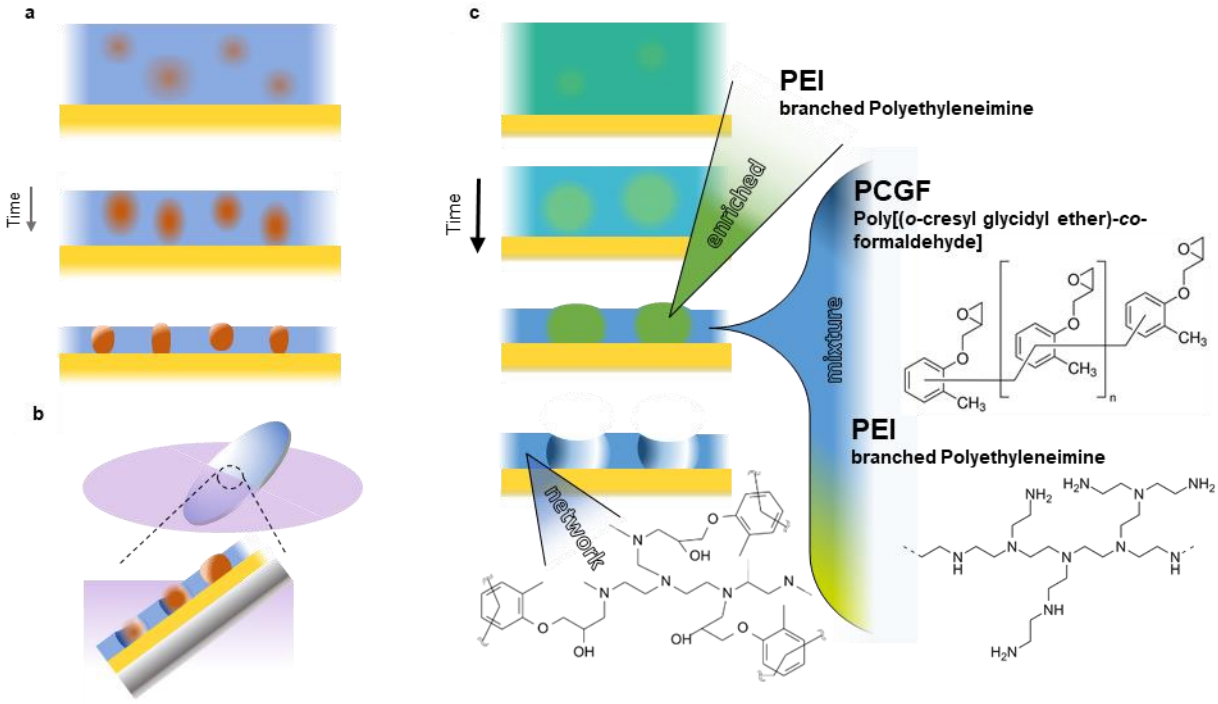

Figure 10. Schematic representation of the two pore formation strategies. a) Phase separation of the third polymer (PLGA) from the common solvent into small domains (brown) within the membrane matrix (blue). b) Sketch of the immersion of the crosslinked nanomembrane in chloroform. While still attached to the sacrificial layer and the casting substrate the PLGA domains are dissolved to leave perforations behind [adapted from Publication II]. c) Phase separation of the polyamine during casting into small PEI-rich domains. The depletion of PEI from the remaining thermoseting resin mixture is illustrated by a change in color. The formed PEI droplets can be removed after crosslinking of the mixture into a covalent network to generate perforations [Publication III]. The underlying sacrificial PSS layer is always represented in yellow.

The second strategy required a more profound acquaintance with the polymer material and the fabrication procedure for its conception. Using only the thermosetting resin with its two components, the possibility to adjust the casting procedure for dense nanomembranes to allow for an intrinsic phase separation was demonstrated. In essence, the polyamine component alone simultaneously serves as a curing agent for the covalent membrane matrix as well as a self-assembling pore template (Figure 10c). This was accomplished by three adjustments. First, by choosing the ratio of the two precursor polymer components to be significantly shifted

towards the amine content to facilitate its phase separation. Secondly, by lowering the spin-coating rotation speed to have a thicker liquid film at the transition to evaporative thinning. This would then provide a sufficiently long period in which phase separation can develop before the dry state is reached. And finally, by using more dilute casting solutions the thickness of the resulting nanomembrane was maintained appropriately low. Again, after crosslinking of the membrane matrix the nanoscale polyamine domains could be removed by dissolution in solvent to leave perforations behind (Figure 10c). Consequently, the method to obtain dense nanomembranes was altered so that perforations with a diameter of roughly 40 nm could be obtained within the 75 nm thick films (Figure 11, Publication III). The development of this method should serve the reduction of complexity and facilitate a reproducible nanomembrane fabrication especially in view of a potential production on larger scale. Nanomembranes obtained with this method shall be referred to as two-component nanomembranes in the following text. Nanomembranes with perforations obtained by adding a third polymer to the casting solution, as described above, will be referred to as three-component nanomembranes.

Both types of perforated nanomembranes were characterized in detail by high resolution microscopy techniques (Figure 11) whereby the formation of perforations could be visually demonstrated. The average size of the pores was estimated from scanning electron microscopy (SEM) images while a nanometer-scale thickness of the membranes could be shown and estimated by both, SEM and atomic force microscopy (AFM). The morphology of the three-component nanomembranes was reminiscent of one particular thin film structure[a] presented in a study on ternary polymer blends[59]. In that thin film, features were observable which seemed suitably sized for protein separations if they were perforations in a membrane. The conditions to obtain that thin film structure had actually served as a guideline for the phase separation approach. Thus, a core achievement was the replication of such small features using the thermoset resin. The presence of perforations was revealed to leave the nanomembranes largely unaffected in terms of mechanical strength by bulging tests. They were further shown to be tolerant to 1M NaOH and highly stable in organic solvents.

In contrast to the three-component nanomembranes, where the resulting morphology was anticipated, it was found that the two component nanomembranes displayed an unexpected and quite exceptional structure. While their top surface was quite smooth, they consistently exhibited a rugged bottom surface of meandering undulations with perforations being mostly located at the apexes. In conjunction with their wettability and other macroscopic observations, it was possible to contrive and propose a phase separation mechanism that provides an

[a]As presented in Figure 5 of Reference 59.

explanation for the observed morphologies. In brief, it was hypothesized that a compositional gradient establishing within the thin film from top to bottom during casting was responsible. By accumulation of the hydrophilic amine component at the bottom interface its phase separation is initiated there which then propagates through the film towards the top interface. The film is captured during this propagation as it enters the dry state and the morphology is pinned by covalent crosslinking. X-ray photoelectron spectroscopy investigations of the two membrane surfaces indeed revealed a compositional difference in accordance with the proposed compositional gradient. The mechanical strength was also higher than expected for nanomembranes cast from solutions of that composition. This further demonstrated that the amine content was depleted from the membrane matrix to shift its composition towards a more robust precursor ratio.

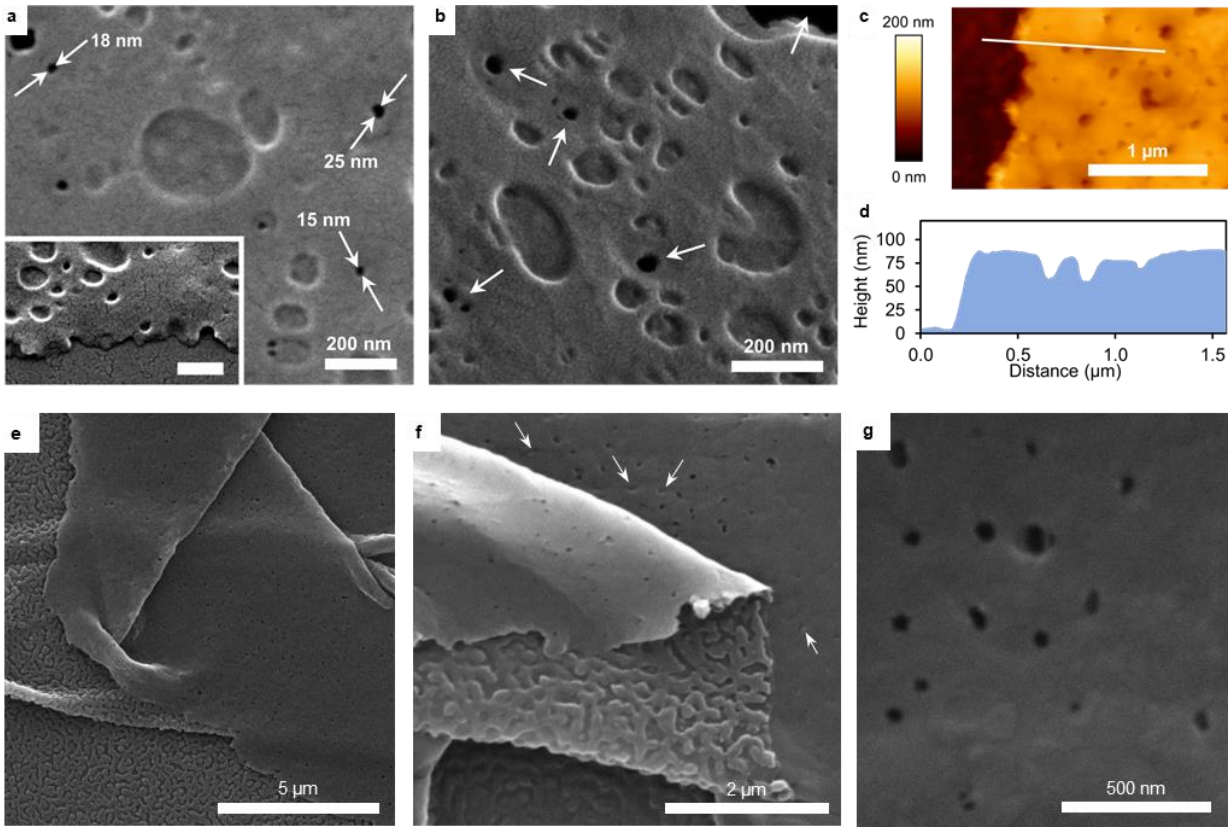

Figure 11. High resolution images of the two types of perforated nanomembranes. a) and b) SEM images of the top surface of three-component nanomembranes with perforations indicated by arrows. The side view of a ripped edge (inset) demonstrates that the membrane is truly perforated. c) and d) AFM scan of a ripped membrane edge demonstrating the nanometer scale thickness by the height profile extracted along the white line. e) and f) SEM images of folded two-component nanomembranes revealing their exceptionally structured bottom surface. g) SEM image of a collection of perforations appearing as dark circular features with an average diameter of 42 nm. [Upper row a) – d): Publication II ; Lower row e) – f): Publication III].

Estimations of the surface free energy of the top as well as the bottom surface were done for the three-component nanomembranes by the static contact angle method. The

nanomembrane material could thereby be shown to be mildly hydrophilic and possess a moderately low surface free energy, properties that are typically linked to low protein adsorption. It was concluded that nanomembranes composed of the thermosetting epoxy resin, due to their polymeric nature, should indeed be nicely compatible with solutions bearing content of biological origin such as proteins. This compatibility was evaluated in systematic investigations of their permeability for various proteins with the photometric permeability test setup. These proteins were selected with increasing hydrodynamic sizes ranging from roughly 3.5 nm to 17 nm in diameter to effectively represent a size ladder.

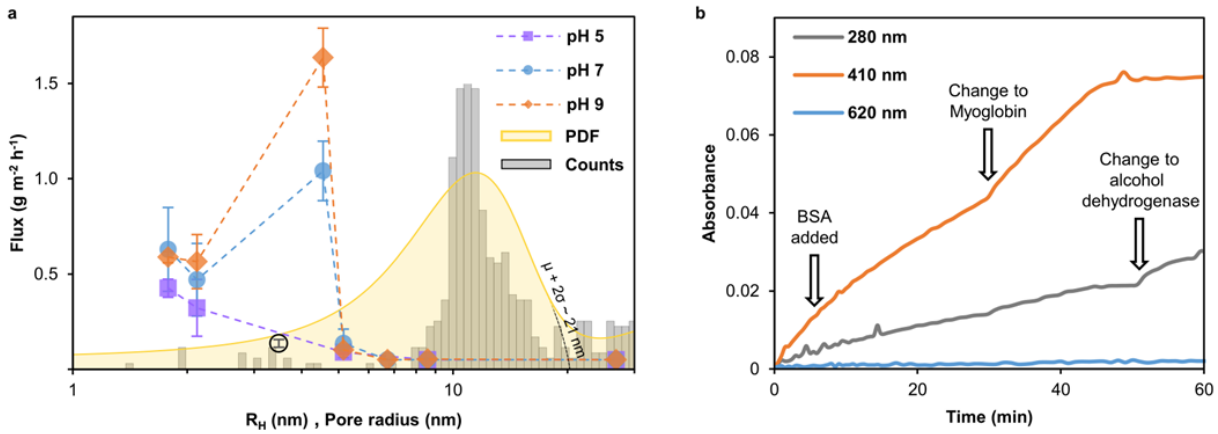

Figure 12. Separation performance of perforated nanomembranes. a) Diffusion rates of different proteins across the membrane versus the respective hydrodynamic size for different pH values. The size distribution of perforations as deduced from SEM images (as histogram in grey and the derived probability density function in yellow) is additionally provided. 95% of detected perforations are smaller than the statistical parameter $\mu + 2\sigma$ roughly equal to 21 nm. b) Permeability test of cytochrome c. The addition of BSA after 6 minutes does not change the permeation rate of cytochrome *c*. Myoglobin and alcohol dehydrogenase are subsequently tested also exhibiting permeation rates expected for unimpaired diffusion.

As expected, the diffusion rates were highly dependent on the size of the respective protein. For the three-component nanomembranes a sharp decline in permeability was observable for proteins larger than 9 nm and complete rejection of proteins larger than 10 nm (Figure 12a). The permeation retention behavior was demonstrated to be sensible to the pH value of the protein solutions. In addition to changes in protein net charge this behavior was attributed to the surface charge of the membrane due to the presence of potentially charged amine groups. Furthermore, in a simple experiment the adsorption of bovine serum albumin, a notoriously ‘sticky’ protein, to the membrane material was precluded to demonstrate that the membranes were indeed very suitable for the processing of proteins (Figure 12b). The addition of a highly concentrated bovine serum albumin solution to the retentate compartment was shown to have no effect on the permeation rate observed for a smaller protein in the permeability test setup. For the two-component nanomembranes a size-based permeability cut-off could be determined in a similar fashion with complete rejection of proteins larger than 13.5 nm in

diameter. The permeation rates could also be shown to vary significantly with pH by evaluating diffusion rates at pH values of 5, 7 and 9.

Membrane processes in industrial settings are typically operated at scales that are incompatible with spin-coating. Thus, a significant step towards the potential application of the polymer based perforated nanomembranes was taken by demonstrating their fabrication by the well scalable dip-coating technique (Publication III, Figure 13a – c and e). To this end, the reduced complexity of the two-component method (as compared to the three-component approach) proved to be beneficial as it could be directly migrated.

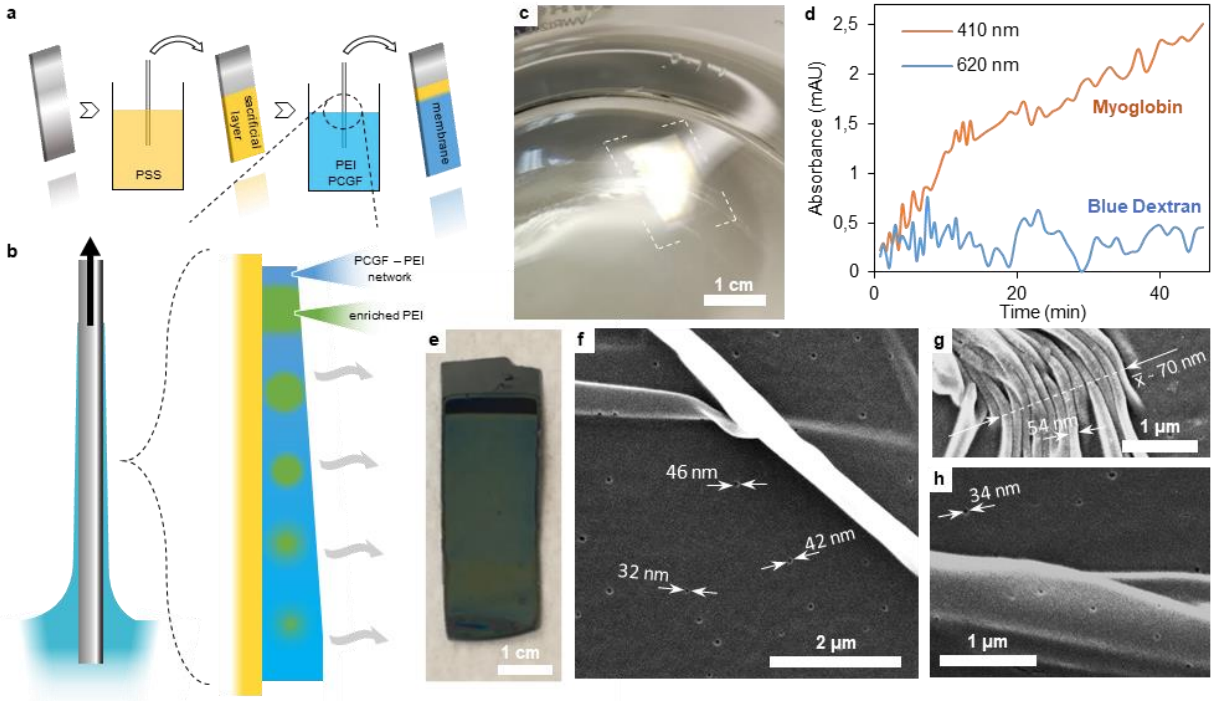

Figure 13. Dip-coating approach to fabricate perforated nanomembranes and their characteristics. a) Representation of the steps necessary for thin film formation. b) Phase separation of excess PEI from the casting mixure during evaporative thinning. c) Appearance of a piece of nanomembrane floating on water. d) Permeability plot of myoglobin and blue dextran. The absorbance change at the indicated wavelength is representative of diffusion of the respective compound across the membrane. e) Photograph of a finished perforated nanomembrane still attached to the casting substrate. f – h) SEM images of the resulting nanomembranes showing perforations of roughly 40 nm and a thickness between 55 and 70 nm. [Publication III].

In fact, only two different casting solution compositions were adopted from the two-component spin-coating process and used to successfully screen for appropriate fabrication conditions. First, the dip-coating speed, the rate at which the substrate is withdrawn, was varied. Subsequent investigations of the resultant ultrathin films by SEM allowed a thickness estimation as well as the identification of features indicative of appropriate phase separation phenomena. Then, at optimal coating speed, the dilution of the casting solution was varied.

Thereby, the necessary balance between domain size governed by the time available for phase separation during evaporative thinning and the final film thickness could be established. The formation of domains rich in amine component that span across the entire film thickness was achieved (Figure 13b) and perforations could be introduced by selective dissolution after nanomembrane crosslinking. The resulting nanomembranes showed a thickness in the range of 54 to 70 nm and perforations with an average diameter of roughly 40 nm (Figure 13f – h). The size selective separation of a small protein from a larger particle could be demonstrated with the permeability test setup (Figure 13d). This proved the successful and straightforward transition of the whole procedure to produce freely suspended perforated polymer nanomembranes suitable for protein separations to the dip-coating technique.

In order to facilitate the development of nanomembranes actively performing reactions to convert or transport target compounds in a renewable fashion, electronic properties will be essential. To this end, the readily available and well scalable path of coating with ultrathin metal films was taken by using direct current magnetron sputtering. Also for potential applications in the field of voltage charging, Janus-type membranes, sensors and activators as well as optoelectronic uses, polymer-metal nanocomposites are highly interesting. Gaining insight into their structural evolution in conjunction with the electronic properties will be beneficial also for the above sectors and not exclusively to devise (re)active membranes. Correlating these insights with certain material parameters could additionally yield an understanding of some factors governing the structure-function relationship of the growing metal films unlocking predictive capabilities. This was accomplished by a systematic study of the thin film formation on the polymer nanomembrane surface using the four representative metals Copper, Gold, Nickel and Silver (Publication IV).

For this study a setup was developed that allowed the simultaneous investigation of the electronic properties and the thickness of ultrathin metal films growing on polymer based nanomembranes *in situ* (Figure 14a). The polymer surface could be contacted during functionalization with the respective metal in the processing chamber to directly and continuously determine the sheet resistance of the metal coatings. Their nominal thickness was monitored with a microbalance located at an equivalent position. The growth of thin films of the four different metals on the polymeric nanomembrane surface was investigated with this setup. The transition from insulating to electrically conductive was shown to be consistently characterized by a sharp decline in resistance (Figure 14b) at a certain critical nominal coating thickness distinct for the respective metal. It could be inferred from these experiments that the growth of the metal films was progressing through an initial 3D island formation stage into a conductive but porous metal network (Figure 14b) before a continuous film is formed.

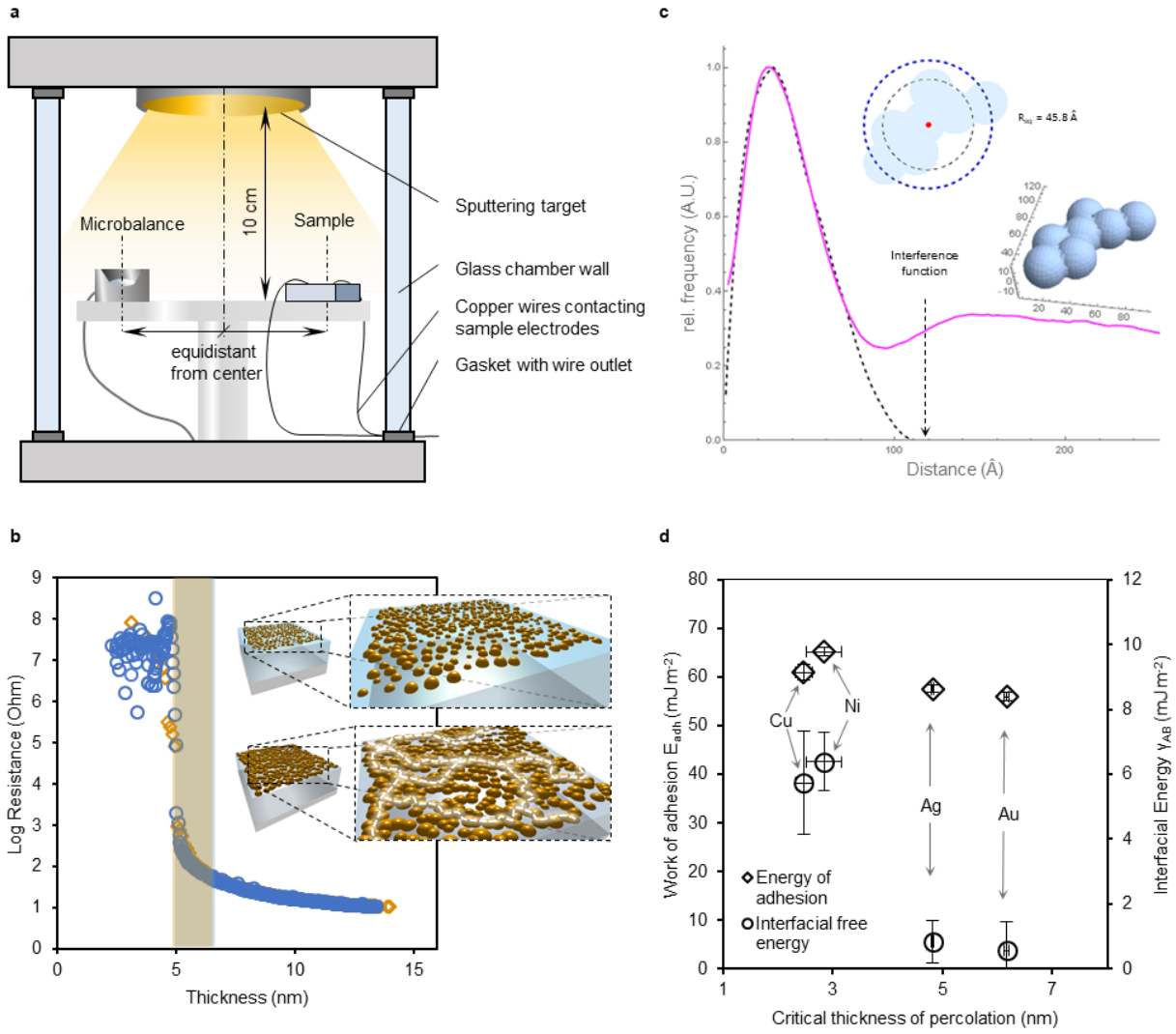

Figure 14. Sputter coating setup, resulting metal-insulator transition data, cluster structure and estimated interfacial parameters. a) Schematic setup of sputter coating chamber with wires to contact the sample surface for in situ resistance measurements leading out of the chamber through a costomized gasket. b) Two replicates of resistance versus nominal thickness data obtained for one metal in the metal-insulator transition region. Schematic representation of the inferred 3D island growth mode forming a conductive network. c) Representative cluster geometry estimation obtained from x-ray scattering data. The dashed line indicats the data obtained from the model cluster shown in the insets. d) Energy parameters estimated for the polymer-metal interfaces versus the observed critical thicknes of percolation. A slight trend is observable for the Energy of adhesion. [Adapted from Publication IV].

By performing grazing incidence small angle x-ray scattering experiments a characterization of the structural aspects of this transition was possible. The data were found to strongly corroborate the inferred growth mode as they hinted towards somewhat ordered separated clusters that grow in size with increasing coating thickness. Furthermore, the scattering data were treated with a novel approach to estimate the involved morphologies at the polymer-metal interface in detail (Figure 14c). It was found that the metal clusters were progressing from compact to more elongated and spread out shape. Finally, the surface free energies of the

involved materials, the polymer surface and the sputter-coated metals, were estimated from static contact angle measurements. Ultimately, this allowed the estimation of the energy balance present at the polymer-metal interface in the form the work of adhesion. This parameter was found to correlate, albeit weakly, with the observed metal-insulator transition behavior (Figure 14d) and fruitfully complemented the detailed structural investigations. Similarly, a commonly used parameter acting as a measure for reactivity, the most negative standard heat of metal oxide formation for the respective metal, was found to correlate with the film formation behavior. Using the above two parameters, the conducted research should indeed enable more confident predictions for the structural and functional evolution of metallized polymer nanomembranes or polymer surfaces in general.

In summary, it was demonstrated how polymer based nanomembranes acting with two different modes of operation can be formed from a common base material. When prepared as a uniform thin film, the polymer material was shown to be permeable for small organic compounds with tunable properties and a size-based permeation cut-off at roughly 2 nm. Two methods were developed to impart the ultrathin polymer films with geometrically defined perforations to afford the permeation of larger molecules such as proteins. A detailed structural characterization with high resolution microscopy was performed and confirmed the nanometer-sized thickness and the formation of perforations. The nanomembranes could be further shown to possess outstanding mechanical robustness even when deliberately prepared with defects, with perforations. Sharp, size-based permeation cut-offs were observed allowing the separation of proteins with pH-dependent selectivity. One method to produce such nanomembranes was further developed to be migrated from the spin-coating to the dip-coating technique in order to afford production on industrially relevant scales. Finally, the functionalization of the nanomembrane surface with ultrathin metal coatings was investigated in a systematic study. Insights into some factors governing the morphology and geometry of the structures present at the polymer-metal interface were generated to allow for more confident predictions of structure and function.

6 Conclusions

As a concluding remark for the summary of the presented research, for the thesis, it can be confidently stated that the formulated objectives have been accomplished. It was indeed essential to establish several customized techniques and setups to afford detailed investigations. These tools could be used in order to accomplish the necessary, in-depth characterization of the various types of nanomembranes. The investigations allow the conclusion that the use of the polymer material in the form of dense nanomembranes for the separation of small organic compounds in aqueous environment is feasible. It is furthermore possible to prepare these nanomembranes with geometrically defined perforations not only suitable in size for the separation but also the incorporation of proteins. The straightforward functionalization of the nanomembrane surface with nanostructured and/or conductive metal coatings lays the basis for future developments and design of functional composite nanomembranes intended for, but not limited to, electrically driven reactions and separations.

Judging from the state of the art and the literature concerned with the production and application of polymeric perforated nanomembranes, especially for biotechnological uses, it may be concluded that this field is remarkably understudied. This is especially striking in view of some achievements that were shown to be possible with their inorganic analogs despite the evident restriction to relatively small scale. Thus, rather than attempts to deliver immediately applicable materials the presented developments can be viewed as proofs of concept and suggestions to eventually leverage the superior properties nanomembranes can offer. In this regard, the choice of the polymer material for the research on polymeric nanomembranes proved to be very appropriate. The use of the crosslinked polymer networks presents an advantage over linear polymers as permeability is expected to increase at such low thicknesses which is apparently not the case for linear polymers[5,60]. The significantly enhanced nanomembrane strength by using appropriate fabrication conditions might allow the formation of substantially thinner but still robust membranes. It will be very interesting how the permeation properties of the network will change upon further lowering of the thickness. In contrast, the demonstrated routes to obtain perforated nanomembranes bear the potential for significant optimization towards porosity rather than thickness. Such optimizations will be necessary to fully harness the benefits of their nanoscale thickness and pore size. Here, the bottom-up fashion of the approach to introduce perforations will be vital for the fabrication on the intended scales and should be adhered to. Importantly, the ability to optimize the nanomembranes and possible support structures independently enabled by their macroscopic robustness in freestanding state is pivotal in facilitating the design of composite separation membranes superior to asymmetric single step materials[8]. Furthermore, the evident

robustness of the presented nanomembranes in freely suspended state even on macroscopic scale could facilitate their application in lab- and organ-on-a-chip devices. For the interaction with living biological matter in such systems, their comparatively soft character with respect to inorganic and crystalline materials could also be of considerable interest to better mimic natural biological environment. The demonstrated functionalization of the surface with a nanostructured metal coating is straightforward and could be readily exploited to generate conductive but porous membranes or nanoparticle-decorated membranes. Thus, their utilization in the assembly of catalytically active nanocomposite membranes is within reach. Furthermore, such functionalized nanomembranes could additionally enable a variety of possible applications. Permselective (bio-)sensor membranes based on surface plasmon resonance or surface enhanced Raman scattering, capacitive humidity sensors or Janus-type separation membranes based on electrowetting or voltage-charging could be realized.

7 References

1. Park HB, Kamcev J, Robeson LM, Elimelech M, Freeman BD. Maximizing the right stuff: The trade-off between membrane permeability and selectivity. *Science*. 2017;356(6343). doi:10.1126/science.aab0530

2. Berg HC. *Random Walks in Biology*. Princeton University Press; 1993.

3. Snyder JL, Clark Jr. A, Fang DZ, et al. An experimental and theoretical analysis of molecular separations by diffusion through ultrathin nanoporous membranes. *Journal of Membrane Science*. 2011;369(1–2):119-129. doi:10.1016/j.memsci.2010.11.056

4. Gaborski TR, Snyder JL, Striemer CC, et al. High-Performance Separation of Nanoparticles with Ultrathin Porous Nanocrystalline Silicon Membranes. *ACS Nano*. 2010;4(11):6973-6981. doi:10.1021/nn102064c

5. Jimenez-Solomon MF, Song Q, Jelfs KE, Munoz-Ibanez M, Livingston AG. Polymer nanofilms with enhanced microporosity by interfacial polymerization. *Nat Mater*. 2016;15(7):760-767. doi:10.1038/nmat4638

6. Gin DL, Noble RD. Designing the Next Generation of Chemical Separation Membranes. *Science*. 2011;332(6030):674-676. doi:10.1126/science.1203771

7. Shannon MA, Bohn PW, Elimelech M, Georgiadis JG, Mariñas BJ, Mayes AM. Science and technology for water purification in the coming decades. *Nature*. 2008;452(7185):301-310. doi:10.1038/nature06599

8. Marchetti P, Jimenez Solomon MF, Szekely G, Livingston AG. Molecular Separation with Organic Solvent Nanofiltration: A Critical Review. *Chem Rev*. 2014;114(21):10735-10806. doi:10.1021/cr500006j

9. Jakšić Z, Matovic J. Functionalization of Artificial Freestanding Composite Nanomembranes. *Materials*. 2010;3(1):165-200. doi:10.3390/ma3010165

10. Mireles M, Gaborski TR. Fabrication techniques enabling ultrathin nanostructured membranes for separations. *ELECTROPHORESIS*. 2017;38(19):2374-2388. doi:10.1002/elps.201700114

11. Winans JD, Smith KJP, Gaborski TR, Roussie JA, McGrath JL. Membrane capacity and fouling mechanisms for ultrathin nanomembranes in dead-end filtration. *Journal of Membrane Science*. 2016;499:282-289. doi:10.1016/j.memsci.2015.10.053

12. Gillmer SR, Fang DZ, Wayson SE, et al. Predicting the failure of ultrathin porous membranes in bulge tests. *Thin Solid Films*. 2017;631:152-160. doi:10.1016/j.tsf.2017.04.004

13. van Reis R, Zydney A. Bioprocess membrane technology. *Journal of Membrane Science*. 2007;297(1):16-50. doi:10.1016/j.memsci.2007.02.045

14. Vendamme R, Onoue S-Y, Nakao A, Kunitake T. Robust free-standing nanomembranes of organic/inorganic interpenetrating networks. *Nat Mater*. 2006;5(6):494-501. doi:10.1038/nmat1655

15. Jiang C, Markutsya S, Pikus Y, Tsukruk VV. Freely suspended nanocomposite membranes as highly sensitive sensors. *Nature Materials*. 2004;3(10):721. doi:10.1038/nmat1212

16. Watanabe H, Kunitake T. A Large, Freestanding, 20 nm Thick Nanomembrane Based on an Epoxy Resin. *Adv Mater*. 2007;19(7):909-912. doi:10.1002/adma.200601630

17. Kunitake T. Perspectives: Synthetic Bilayer Membrane and Giant Nanomembrane. *Langmuir*. 2016;32(47):12265-12268. doi:10.1021/acs.langmuir.6b02030

18. Watanabe H, Muto E, Ohzono T, Nakao A, Kunitake T. Giant nanomembrane of covalently-hybridized epoxy resin and silica. *J Mater Chem*. 2009;19(16):2425-2431. doi:10.1039/B819213H

19. Pérez-Madrigal M, Armelin E, Puiggalí J, Alemán C. Insulating and semiconducting polymeric free-standing nanomembranes with biomedical applications. *Journal of Materials Chemistry B*. 2015;3(29):5904-5932. doi:10.1039/C5TB00624D

20. Fujie T. Development of free-standing polymer nanosheets for advanced medical and health-care applications. *Polymer Journal*. 2016;48(7):773-780. doi:10.1038/pj.2016.38

21. Xu H, Goedel WA. Polymer−Silica Hybrid Monolayers as Precursors for Ultrathin Free-Standing Porous Membranes. *Langmuir*. 2002;18(6):2363-2367. doi:10.1021/la011026m

22. Zimnitsky D, Shevchenko VV, Tsukruk VV. Perforated, Freely Suspended Layer-by-Layer Nanoscale Membranes. *Langmuir*. 2008;24(12):5996-6006. doi:10.1021/la7038575

23. Zhang H, Takeoka S. Morphological Evolution within Spin-Cast Ultrathin Polymer Blend Films Clarified by a Freestanding Method. *Macromolecules*. 2012;45(10):4315-4321. doi:10.1021/ma3005394

24. Kang C, Ramakrishna SN, Nelson A, et al. Ultrathin, freestanding, stimuli-responsive, porous membranes from polymer hydrogel-brushes. *Nanoscale*. 2015;7(30):13017-13025. doi:10.1039/C5NR03147H

25. Fujie T, Kawamoto Y, Haniuda H, et al. Selective Molecular Permeability Induced by Glass Transition Dynamics of Semicrystalline Polymer Ultrathin Films. *Macromolecules*. 2013;46(2):395-402. doi:10.1021/ma302081e

26. Yang SY, Ryu I, Kim HY, Kim JK, Jang SK, Russell TP. Nanoporous Membranes with Ultrahigh Selectivity and Flux for the Filtration of Viruses. *Adv Mater*. 2006;18(6):709-712. doi:10.1002/adma.200501500

27. Nuxoll EE, Hillmyer MA, Wang R, Leighton C, Siegel RA. Composite Block Polymer−Microfabricated Silicon Nanoporous Membrane. *ACS Appl Mater Interfaces*. 2009;1(4):888-893. doi:10.1021/am900013v

28. Ling S, Jin K, Kaplan DL, Buehler MJ. Ultrathin Free-Standing Bombyx mori Silk Nanofibril Membranes. *Nano Letters*. 2016;16(6):3795-3800. doi:10.1021/acs.nanolett.6b01195

29. Striemer CC, Gaborski TR, McGrath JL, Fauchet PM. Charge- and size-based separation of macromolecules using ultrathin silicon membranes. *Nature*. 2007;445(7129):749-753. doi:10.1038/nature05532

30. Erickson B, Nelson, Winters P. Perspective on opportunities in industrial biotechnology in renewable chemicals. *Biotechnology Journal*. 2012;7(2):176-185. doi:10.1002/biot.201100069

31. Harmsen PFH, Hackmann MM, Bos HL. Green building blocks for bio-based plastics. *Biofuels, Bioproducts and Biorefining*. 2014;8(3):306-324. doi:10.1002/bbb.1468

32. Gronemeyer P, Ditz R, Strube J. Trends in Upstream and Downstream Process Development for Antibody Manufacturing. *Bioengineering*. 2014;1(4):188-212. doi:10.3390/bioengineering1040188

33. Marichal-Gallardo PA, Álvarez MM. State-of-the-art in downstream processing of monoclonal antibodies: Process trends in design and validation. *Biotechnology Progress*. 2012;28(4):899-916. doi:10.1002/btpr.1567

34. Kowalczyk SW, Kapinos L, Blosser TR, et al. Single-molecule transport across an individual biomimetic nuclear pore complex. *Nat Nano*. 2011;6(7):433-438. doi:10.1038/nnano.2011.88

35. Puiggalí-Jou A, Pérez-Madrigal MM, Valle LJ del, et al. Confinement of a β-barrel protein in nanoperforated free-standing nanomembranes for ion transport. *Nanoscale*. August 2016. doi:10.1039/C6NR04948F

36. Ali I, Khan T, Omanovic S. Direct electrochemical regeneration of the cofactor NADH on bare Ti, Ni, Co and Cd electrodes: The influence of electrode potential and electrode material. *Journal of Molecular Catalysis A: Chemical*. 2014;387:86-91. doi:10.1016/j.molcata.2014.02.029

37. Damian A, Maloo K, Omanovic S. Direct Electrochemical Regeneration of NADH on Au, Cu and Pt-Au Electrodes. *Chemical and biochemical engineering quarterly*. 2007;21(1):21-32.

38. Diaz-Morales O, Calle-Vallejo F, Munck C de, M. Koper MT. Electrochemical water splitting by gold: evidence for an oxide decomposition mechanism. *Chemical Science*. 2013;4(6):2334-2343. doi:10.1039/C3SC50301A

39. Suen N-T, Hung S-F, Quan Q, Zhang N, Xu Y-J, Chen HM. Electrocatalysis for the oxygen evolution reaction: recent development and future perspectives. *Chem Soc Rev*. 2017;46(2):337-365. doi:10.1039/C6CS00328A

40. Aegerter MA, Mennig M. *Sol-Gel Technologies for Glass Producers and Users*. Boston: Kluwer Academic Publishers; 2004. https://link.springer.com/openurl?genre=book&isbn=978-1-4020-7938-2. Accessed July 24, 2019.

41. Schweizer PM, Kistler SF, eds. *Liquid Film Coating: Scientific Principles and Their Technological Implications*. Springer Netherlands; 1997. https://www.springer.com/gp/book/9789401062466. Accessed July 24, 2019.

42. Bornside DE, Macosko CW, Scriven LE. MODELING OF SPIN COATING. *Journal of Imaging Technology*. 1987;13(4):122-130.

43. Toolan DTW, Howse JR. Development of in situ studies of spin coated polymer films. *J Mater Chem C*. 2013;1(4):603-616. doi:10.1039/C2TC00026A

44. Meyerhofer D. Characteristics of resist films produced by spinning. *Journal of Applied Physics*. 1978;49(7):3993-3997. doi:10.1063/1.325357

45. Scriven LE. Physics and Applications of DIP Coating and Spin Coating. *MRS Online Proceedings Library Archive*. 1988;121. doi:10.1557/PROC-121-717

46. Nauman EB, He DQ. Morphology predictions for ternary polymer blends undergoing spinodal decomposition. *Polymer*. 1994;35(11):2243-2255. doi:10.1016/0032-3861(94)90757-9

47. van de Witte P, Dijkstra PJ, van den Berg JWA, Feijen J. Phase separation processes in polymer solutions in relation to membrane formation. *Journal of Membrane Science*. 1996;117(1–2):1-31. doi:10.1016/0376-7388(96)00088-9

48. Walheim S, Böltau M, Mlynek J, Krausch G, Steiner U. Structure Formation via Polymer Demixing in Spin-Cast Films. *Macromolecules*. 1997;30(17):4995-5003. doi:10.1021/ma9619288

49. Walheim S, Schäffer E, Mlynek J, Steiner U. Nanophase-Separated Polymer Films as High-Performance Antireflection Coatings. *Science*. 1999;283(5401):520-522. doi:10.1126/science.283.5401.520

50. Bräuer G. 4.03 - Magnetron Sputtering. In: Hashmi S, Batalha GF, Van Tyne CJ, Yilbas B, eds. *Comprehensive Materials Processing*. Oxford: Elsevier; 2014:57-73. doi:10.1016/B978-0-08-096532-1.00403-9

51. Hora J, Hall C, Evans D, Charrault E. Inorganic Thin Film Deposition and Application on Organic Polymer Substrates. *Advanced Engineering Materials*. 20(5):1700868. doi:10.1002/adem.201700868

52. Kelly PJ, Arnell RD. Magnetron sputtering: a review of recent developments and applications. *Vacuum*. 2000;56(3):159-172. doi:10.1016/S0042-207X(99)00189-X

53. Campbell CT. Ultrathin metal films and particles on oxide surfaces: structural, electronic and chemisorptive properties. *Surface Science Reports*. 1997;27(1):1-111. doi:10.1016/S0167-5729(96)00011-8

54. Lazzari R, Renaud G, Revenant C, Jupille J, Borensztein Y. Adhesion of growing nanoparticles at a glance: Surface differential reflectivity spectroscopy and grazing incidence small angle x-ray scattering. *Phys Rev B*. 2009;79(12):125428. doi:10.1103/PhysRevB.79.125428

55. Yu X, Duxbury PM, Jeffers G, Dubson MA. Coalescence and percolation in thin metal films. *Phys Rev B*. 1991;44(23):13163-13166. doi:10.1103/PhysRevB.44.13163

56. Ashby MF. *Materials Selection in Mechanical Design*. 5 edition. Cambridge, MA: Butterworth-Heinemann; 2016.

57. *Chemistry and Technology of Epoxy Resins*. 1993 edition. Dordrecht: Springer; 2012.

58. Karan S, Jiang Z, Livingston AG. Sub–10 nm polyamide nanofilms with ultrafast solvent transport for molecular separation. *Science*. 2015;348(6241):1347-1351. doi:10.1126/science.aaa5058

59. Walheim S, Ramstein M, Steiner U. Morphologies in Ternary Polymer Blends after Spin-Coating. *Langmuir*. 1999;15(14):4828-4836. doi:10.1021/la981467e

60. Gorgojo P, Karan S, Wong HC, Jimenez-Solomon MF, Cabral JT, Livingston AG. Ultrathin Polymer Films with Intrinsic Microporosity: Anomalous Solvent Permeation and High Flux Membranes. *Advanced Functional Materials*. 2014;24(30):4729-4737. doi:10.1002/adfm.201400400

8 Publications

I Rodler A, Schuster C, Berger E, Tscheließnig R, Jungbauer A. Freestanding ultrathin films for separation of small molecules in an aqueous environment. Journal of Biotechnology. 2018;288:48-54. doi:10.1016/j.jbiotec.2018.10.002

II Schuster C, Rodler A, Tscheliessnig R, Jungbauer A. Freely suspended perforated polymer nanomembranes for protein separations. Scientific Reports. 2018;8(1):4410. doi:10.1038/s41598-018-22200-4

III Schuster C, Matzinger J, Jungbauer A. Micro-Phase Separation within Epoxy Resin Yields Ultrathin Mesoporous Membranes with Increased Scalability by Conversion from Spin- to Dip-Coating Process. Macromolecular Materials and Engineering. 2019;0(0):1900321. doi:10.1002/mame.201900321

IV Schuster C, Rennhofer H, Jungbauer A and Tscheliessnig R. Metal-insulator transition, associated growth morphology and relations to surface free energy and reactivity of ultrathin sputtered metals on reticulated polymer thin films. (2019) SUBMITTED to Journal of Colloid and Interface Science.

Publication I

Journal of Biotechnology 288 (2018) 48–54

Contents lists available at ScienceDirect

Journal of Biotechnology

journal homepage: www.elsevier.com/locate/jbiotec

Freestanding ultrathin films for separation of small molecules in an aqueous environment

Agnes Rodler[a], Christian Schuster[a], Eva Berger[a], Rupert Tscheließnig[a], Alois Jungbauer[a,b,*]

[a] Austrian Centre of Industrial Biotechnology, Muthgasse 11, 1190, Vienna, Austria
[b] University of Natural Resources and Life Sciences Vienna, Muthgasse 18, 1190, Vienna, Austria

ARTICLE INFO

Keywords:
Ultrathin films
Small molecule separation
Biopharmaceuticals
Functional polymers
Intrinsic porosity

ABSTRACT

Alternative separation methods operating in an aqueous environment are of increasing importance for further progress of molecular separation in life sciences and other industrial sectors working towards a biobased economy. By spincoating, membranes with thicknesses under 100 nm and 20 cm^2 surface area were prepared from an epoxy based resin. For the first time such ultrathin epoxy films were used for the selective separation of small molecules and metabolites within an aqueous environment. Initially, selectivity is demonstrated by the separation of two dyes of similar size (0.7 and 1.4 nm diameter). By variation of the precursor concentrations, both mechanical stability and selectivity for molecular transport are shown to be tunable. The observed transport properties of the different membranes correlated with their biaxial moduli and ultimate tensile strengths which were in the range of 0.3–3.5 GPa and 10–44 MPa, respectively. These observations agreed with the conclusion drawn from FTIR analysis that variations in the covalent crosslinking density determine the emergent properties. Finally, permeation rates for small molecules of industrial relevance were assessed to confirm a size based diffusion cutoff for compounds with hydrodynamic diameters below 2 nm.

1. Introduction

The separation of small molecules within aqueous environments and production streams using cutting edge membranes as an orthogonal method to other unit operations offers tremendous potential for lowering economic and ecological footprints (van Reis and Zydney, 2007). Applications range from water desalination over protein and virus separation (Grein et al., 2014) to biohybrid organs (Groth and Liu, 2008) and biomedical applications. The performance of membrane separations is tightly bound to the thickness of the membrane and especially membranes below 100 nm in thickness (nanomembranes) have been shown to exhibit highly desirable mass transfer properties. Thereby, nanomembranes present the prospect of considerable economic benefits for countless industrially relevant separation tasks. Widespread implementation of such highly efficient membranes is one of the future goals for biotechnological processes in view of a potential biobased economy as well as for water purification (Geise et al., 2010), purification of fragrants and flavors and in oil refinery (Hoek et al., 2018; Jimenez-Solomon et al., 2016).

Since two decades nanomembranes have received increasing interest from industry originally starting with their widely established application in coating- or microelectronics industries (Matovic and Jakšić, 2009; Cavallo and Lagally, 2010). A paradigm shift from empirical to materials sciences led to the integration of nanotechnology in numerous applications also in biotechnology (Stroeve and Ileri, 2011; Tong et al., 2004; Striemer et al., 2007; Agrawal et al., 2010; Montagne et al., 2012). The variety of materials and fabrication techniques is diverse ranging from carbon-based nanomembranes for gas separation over room-temperature ionic liquid films, inorganic silicon nitride membrane arrays to crosslinked polymeric nanofilms for organic solvent filtration (Jimenez-Solomon et al., 2016; Striemer et al., 2007; Ai et al., 2014; Gin and Noble, 2011).

The benefits of thinner membranes are their enhanced selectivity and mass transfer properties where pore finding diffusivity dominates transmembrane diffusivity as a rate-limiting factor (Snyder et al., 2011). Thereby, a reduction of processing time and required steps is a great asset ultrathin membranes could provide. Nanomembranes have been demonstrated to feature surface areas in the square-centimeter range with aspect ratios greater than 10^6 making them promising candidates for industrial scale research (Watanabe et al., 2009).

Abbreviations: AFM, atomic force microscopy; GPa, Gigapascal; MPa, Megapascal; PCGF, poly[(*o*-cresyl glycidylether)-*co*-formaldehyde]; PEI, branched Polyethylenimine; PSS, poly(sodium 4-styrenesulfonate); SEM, scanning electron microscopy

* Corresponding author at: University of Natural Resources and Life Sciences Vienna, Muthgasse 18, 1190, Vienna, Austria.
E-mail address: alois.jungbauer@boku.ac.at (A. Jungbauer).

https://doi.org/10.1016/j.jbiotec.2018.10.002
Received 8 May 2018; Received in revised form 19 September 2018; Accepted 10 October 2018
Available online 11 October 2018

Remarkably, beneficial bulk properties such as mechanical stability and chemical resistance can be preserved (Markutsya et al., 2005; Vendamme et al., 2006; Kang et al., 2013; Watanabe et al., 2007a) while the absence of a bulk phase may induce the emergence of new or altered properties such as increased flexibility at similar strength (Watanabe et al., 2013).

Especially for a biobased economy, novel separation materials and methods for small molecules such as organic acids and metabolites will play a crucial role for further development and implementation of new industrial processes. A lot of conventional methods for separation of organic acids and metabolites consume high amounts of energy (Yang et al., 2013). Given for the example of organic acids, they are currently manufactured by crystallization after removal of biomass. This requires the addition of high amounts of sulfuric acid for protonation and subsequent crystallization and results in a high ecological as well as economical footprint being in far distance from the principles of sustainable engineering (Anastas and Zimmermann, 2003). Alternative methods such as reactive extraction require vast amounts of organic solvent and thus also do not meet the goals of a biobased economy. This asks for membrane processes and materials with adequate selectivity for this group of small molecules to overcome these shortcomings.

In this study we describe how epoxy nanomembranes (Watanabe et al., 2007a) can be used as an easy-to-fabricate separation material with outstanding mechanical stability that allows permeation of small organic molecules in aqueous environment. We show that these membranes have a tunable intrinsic permeability and provide first demonstrations of small molecule separation. An intrinsic microporosity of the polymer network is inferred to enable permeation of solutes across the ultrathin polymer membranes. Additionally, it is shown how different compositions of epoxy and amine can be employed to yield nanomembranes with tailored sieving properties. By adjustment of the precursor ratio the separation performance and the mechanical properties can be controlled which is attributed to variations in the crosslinking density of the polymer network. The fact that the fabrication of these nanomembranes is highly reproducible and can be completed in less than ten minutes makes them promising candidates for application in industry. No complex reaction techniques nor special infrastructure are needed and a minimum amount of chemicals is required. These nanomembranes are compatible with an aqueous environment, which is in full accordance with the production of compounds in bioreactors. Therefore, these nanomembranes have great potential for in-situ removal of metabolites or inhibitors since, for biotechnological applications, such biocompatible membranes are excellently suited (Agrawal et al., 2010).

2. Experimental

2.1. Fabrication of ultrathin films

A uniform thin film from 5% (w/w) aqueous poly(sodium 4-styrenesulfonate) (PSS, M_w 70.000 g mol^{-1}) solution was spincoated (Spin Coater P6700; Specialty Coating Systems Inc., Indianapolis, Indiana, USA) on a Plasma cleaned silicon wafer as a sacrificial layer.150 µL of membrane casting solution with the components of the epoxy-precursor solution, branched polyethylenimine (PEI, M_w 25.000 g mol^{-1}) (Sigma, 408727) and poly[(*o*-cresyl glycidylether)-*co*-formaldehyde] (PCGF, M_w 870 g mol^{-1})(Sigma, 405515) were used for thin epoxy film casting. The precursors were dissolved separately in chloroform at a concentration of 10 mg mL^{-1} (PEI) and 20 mg mL^{-1} (PCGF). To ensure a proper dissolution of both constituents, the solutions were stirred in sealed glass containers at room temperature for at least 30 min at 300 rpm. Mixing of both solutions at the respective PEI to PCGF ratios (stochiometric ratios of reactive amine hydrogens to epoxy groups) of 1:1; 1.2:1; 1.4:1; 1.6:1; 2:1; 3.5:1; 4:1 or 6:1 was done in glass vials for 2 min and then used as the casting solution. After spincoating for 60 s at 8000 rpm, the membranes were baked on a hot plate for 5 min at 120 °C to initiate the crosslinking. The membrane was then released from the silicon wafer by dissolution of the sacrificial layer by delamination in water.

2.2. Bulging tests

Stress-strain curves were recorded using the camera and software of the contact angle device (Krüss DSA 30S, Advance software, Krüss, Hamburg, Germany). The membrane was attached to a plastic tube of 5 mm diameter by lifting it from the water surface. The tube was aligned vertically and filled with water in 100 µL steps. A detailed description of the bulging test can be found in Schuster et al., 2018.

For the effect of temperature on bulging, the membranes were investigated on a plastic tube with 9 mm inner diameter on the water surface, as sketched in Fig. S2a.

2.3. Separation

After delaminating the precut ultrathin film in water to dissolve the PSS sacrificial layer, a 1.5 cm^2 piece was lifted out by glass tubes of 7 and 9 mm inner diameter. The membrane was fixed on the glass holder solely by its adhesion properties. Approximately 2340 µL of 0.1 M KCl (Merck, Darmstadt, Germany) were placed into a 3500 µL/10 mm quartz-cuvette (Hellma Analytics, Germany) and the membrane covered glass holder was inserted so that the freely suspended part of the membrane was fully immersed. 50 µL of a mixture of two synthetic dyes in 0.1 M KCl (Patent Blue V sodium salt, Sigma 21605 and Methyl Red sodium salt, Sigma 114502) where the final concentration of each dye was adjusted to 500 µM, was pipetted onto the membrane on the retentate side. For Acetylsalicylic acid (Sigma A5376), a 0.1 M citric acid/sodium phosphate buffer pH 3.3 was used, for L-Phenylalanine (Sigma P5482) 0.1 M KCl pH 5.5. Itaconic acid (Sigma I29204) transport was investigated in 0.1 M phosphoric acid/sodium phosphate buffer pH 3.1). Blue Dextran (M_w 2.000 kDa, Sigma D4772) was added to the feed solutions as leakage control. During the measurements in the cuvette, the permeate chamber was constantly stirred by a magnetic stirrer (Fisher Scientific, Waltham, MA, US) at 150 rpm. The measurement was conducted in a Varian Cary60 UV-VIS spectrophotometer (Agilent, CA, US) at the absorption maxima of the small molecules at the respective pH which had been previously determined by wavelength scans, and automatically sampled within the Cary WinUV Kinetics application (version 5.0.0.999).

2.4. High resolution microscopy imaging

Scanning electron microscopy (SEM) micrographs were captured with a FEI Inspect S50 (FEI, Eindhoven, NL) using the software xTm (Version: 4.1.1). Atomic force microscopy (AFM) images and cross-section scans were acquired with a JPK NanoWizard II (JPK Instruments, Carpinteria, CA, US) in dry contact mode with silicon nitride tips (NP-S10, Bruker, Billerica, MA, US) and evaluated with the software JPKSPM. For high resolution microscopy the epoxy thin films were picked up from the water surface with silicon wafer pieces. Samples were coated with a thin (~10 nm) gold layer for SEM imaging.

2.5. FTIR spectroscopy

Samples for FT IR were prepared on double-sided polished silicon wafers by directly coating the membrane polymer to avoid background noise caused by the PSS sacrificial layer. FTIR measurements were done with a Perkin Elmer Spectrum One (Perkin Elmer, Waltham, MA, US) using the software Spectrum One. Spectra were collected between 400–4000 cm^{-1} at a resolution of 8 cm-1.

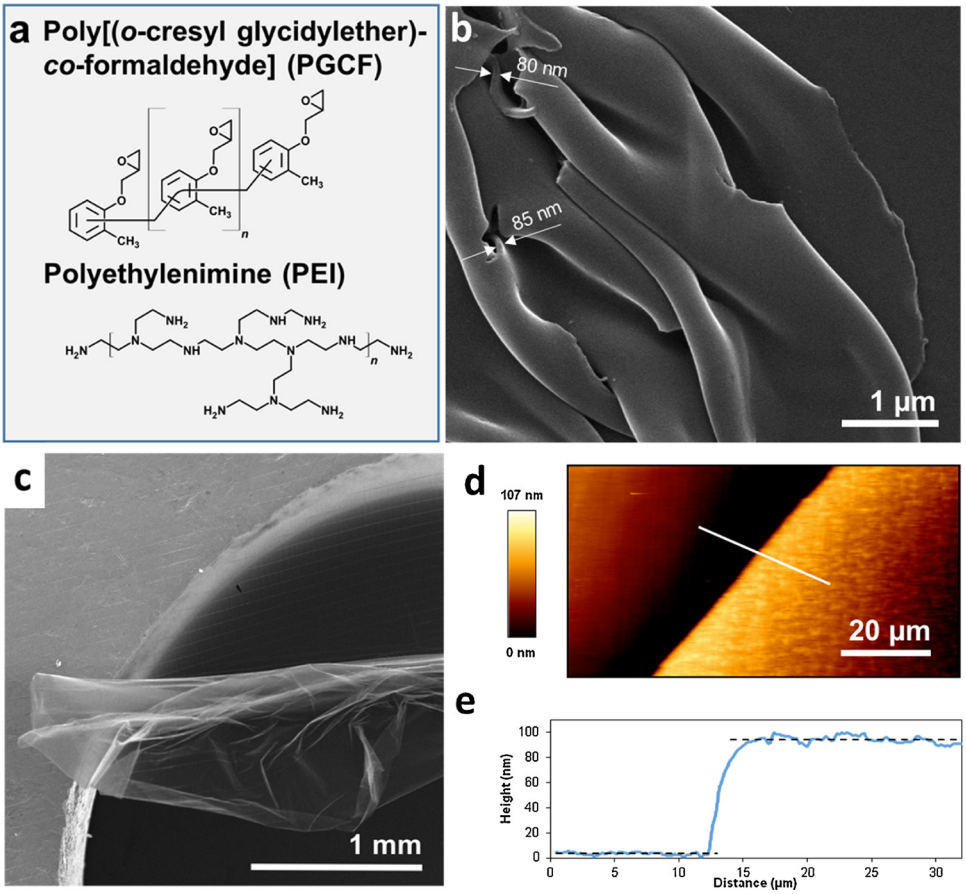

Fig. 1. Chemical structure, morphology and thickness of an epoxy ultrathin film. a) Structural formulas of the precursor polymers PCGF and PEI. b) SEM image of an interfolded ultrathin film showing regions with a thickness below 90 nm. c) SEM image of an ultrathin film composed from a PEI:PCGF ratio of 4:1 after pickup on a metal rim, showing periodic lamellar morphology. d) AFM height image of the edge of an ultrathin film sitting on a silicon wafer. The white line indicates where the height profile was extracted. e) Cross-sectional AFM scan of the ultrathin film with a thickness of 90 nm. The dashed lines indicate the average level of the silicon wafer (left) and the membrane top surface (right), respectively.

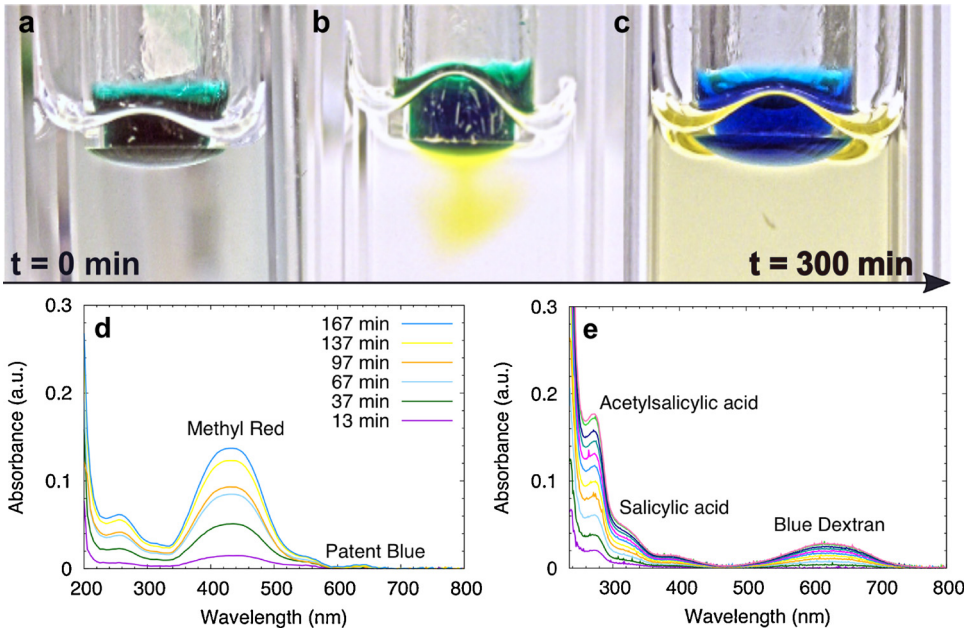

Fig. 2. *In situ determination of small molecule separation.* a–c) Cuvette filtration module for spectrophotometric in situ determination of the permeation of a 1:1 mixture of Methyl Red and Patent Blue V through an epoxy ultrathin film (PEI:PCGF 2:1). a) Both molecules had an initial concentration of 500 µmol L^{-1} in 0.1 M KCl. The retentate was filled with 50 µL solution, the permeate space contained 2340 µL 0.1 M KCl. The green solution represents a mixture of the two compounds, the permeating Methyl Red is visible as yellow liquid. b) Capture of the initial permeation stage illustrating the Methyl Red diffusion front. d) Selected absorbance spectra of the permeate as function of time captured for a membrane of PEI:PCGF ratio 4:1. e) Time course of leakage detection with Blue Dextran, shown for the permeation of Acetylsalicylic acid through a membrane composed from PEI:PCGF 4:1. Increasing peak maxima correspond to increasing time (For interpretation of the references to colour in this figure legend, the reader is referred to the web version of this article).

3. Results and discussion

The polymeric membranes studied in this work were fabricated with a conventional spin coating approach where a solution of precursors is cast onto a thin sacrificial polymer layer. After spincoating, covalent crosslinking of the two building blocks yields an ultrathin film that is insoluble in water and various organic solvents. The glycidylether epoxy resin, poly[(*o*-cresyl glycidylether)-*co*-formaldehyde] (PGCF), and the polyamine, branched polyethylenimine (PEI), undergo covalent crosslinking to form a polymer network (Fig. 1a). The epoxy group, which is under high cyclic stress reacts by nucleophilic addition of an amino group resulting in a quaternary amine that is subsequently transformed into a hydroxyl group by addition of a hydrogen. Every reacted epoxy group creates a hydroxyl group which is responsible for the excellent adhesion properties of epoxy resins (Pascault et al., 2010). We could take advantage of this property for our analysis methods

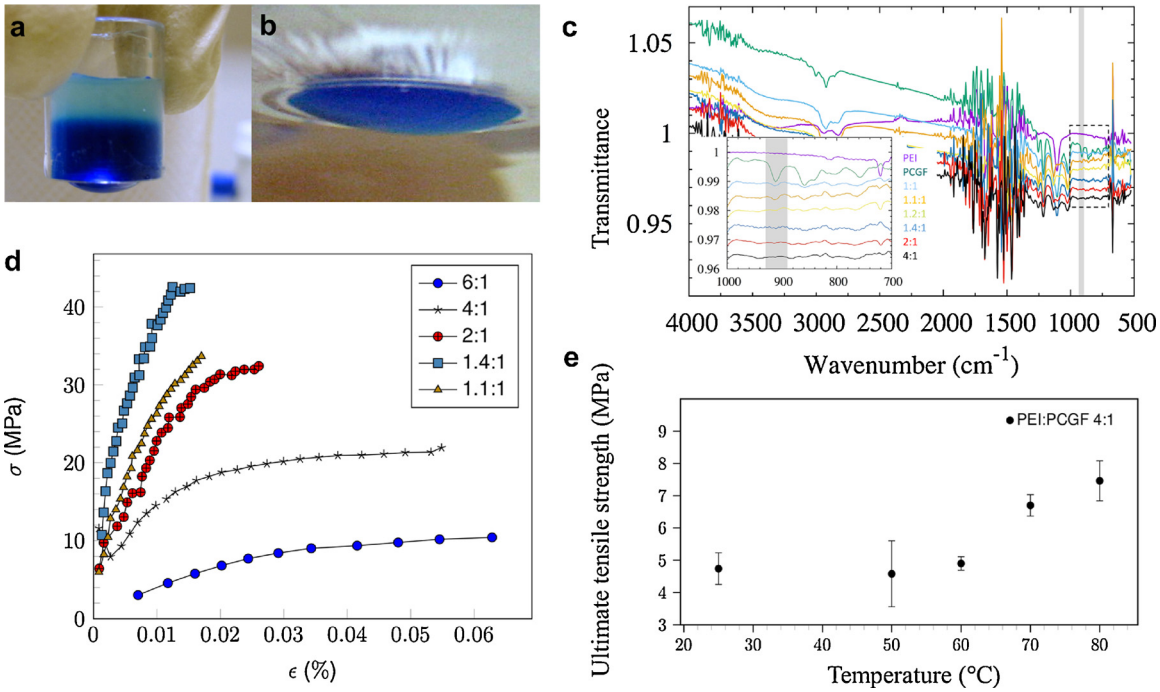

Fig. 3. *Mechanical stability of epoxy ultrathin films.* a) Unsupported membrane loaded with solution in air. The inner diameter of the tube is 9 mm. b) Zoom into the bottom view of the membrane when burdened with Patent Blue V solution. c) Normalised FTIR spectra of ultrathin films with decreasing PCGF content. For better visibility, the spectra were shifted relative to the *y*-axis. The region with the stretching vibration of the epoxy group (915 cm^{-1}) is highlighted in grey. The inset is a detailed graph of the fingerprint region. d) Stress-strain curves of dense epoxy ultrathin films composed from different ratios of amine to epoxy (PEI:PCGF). The respective end points of the curves correspond to the rupture points (ultimate tensile strength). The corresponding setup for these bulging tests is depicted in Figure S1 a. e) Dependence of the ultimate tensile strength on the annealing temperature for a membrane composed of the ratio PEI:PCGF 4:1 (For interpretation of the references to colour in this figure legend, the reader is referred to the web version of this article).

where attachment of the membrane on glass or plastics was achieved without additive or clamping. For the two-component system investigated, the equivalent weight of one repeating unit PCGF was 174 g ($g\ eq^{-1}$), having one functional epoxy group. One repeating unit of PEI has a molecular weight of 473 g mol^{-1}, comprising 11 reactive amine hydrogens, thus the amine hydrogen equivalent weight is 43 g. After spincoating and subsequent crosslinking at 120 °C, separation from the substrate was achieved by dissolution of the sacrificial layer in water whereby ultrathin polymeric membranes were obtained in a free-standing state floating on the surface.

Fig. 1b – e shows the morphology of epoxy resin based ultrathin films of 85 nm average thickness in supported, unsupported, warped and stretched state imaged with SEM and AFM. Fig. 1d shows an AFM image of the edge of a membrane sitting on a flat silicon wafer. A corresponding cross-sectional AFM scan in Fig. 1e confirms the thickness of roughly 90 nm deduced from Fig. 1b. The membranes are robust on a macroscopic scale and can be attached to various substrates for analytics as demonstrated in Figs. 2 and 3. Note that the total area of defect-free ultrathin films was only restricted by the size of the used substrate and that scale-up is not only conceivable for spincoating but also by translation to other coating techniques.

It is one of the prospects for polymer based ultrathin films to design a size-specific porosity in order to obtain a permselective membrane (Kunitake, 2016). The nature of epoxy resins, which are known to possess a certain porosity towards water (Soles and Yee, 2000; Apicella et al., 1984) and the potential ability to adjust the network composition suggested that permeable membranes could be fabricated from this material. To this end, we investigated the separation ability of the ultrathin epoxy films and used two small synthetic dyes: Methyl Red and Patent Blue V, differing in molecular weight by 300 Da. The mixture is visible as a green colored transparent feed solution in Fig. 2a and the permeation of one of the dyes (Methyl Red) could be readily observed by the unaided eye (Fig. 2b). Small molecule transport enabled by the intrinsic porosity of the membrane material was evidenced and studied in situ with a spectrophotometer in detail. For this purpose, a cuvette with an inset glass tube served as a small filtration module. Fig. 2 shows the straightforward experimental setup enabling real-time determination of concentration profiles at the permeate side in a stirred cuvette with 1 cm path length. The membranes were used completely unsupported allowing large diffusion areas and excluding the possibility for solute adsorption and mass transfer resistance by any support material. Images in Fig. 2a and b show the initial and early state of separation without stirring. Fig. 2c shows the system after equilibrium had been reached. Note that it is clearly visible how the ultrathin film separated the mixture into its respective components. The larger molecule Patent Blue V was retained in the upper reservoir while Methyl Red could migrate through the ultrathin film, indicated by the yellow color of the permeate solution and the now blue-colored retentate. In Fig. 2d, wavelength scans of the permeate solution show the corresponding UV–vis-spectra over time, corroborating the macroscopic observation. The absorbance at the peak maximum of Methyl Red increases with time whereas there is very little absorbance that indicates diffusion of the larger molecule Patent Blue V. This experiment clearly demonstrates that ultrathin epoxy resin membranes can be used as a separation membrane in an aqueous environment. The respective hydrodynamic diameters for Methyl Red and Patent Blue V are 0.7 nm and 1.4 nm. As such, the cutoff between permeation and retention is situated in the microporous (< 2 nm) regime. By adding a large molecule to the feed solution (Blue Dextran 2000) corresponding to a hydrodynamic radius of roughly 26 nm (Armstrong et al., 2004), immediate leakage detection could be ensured. This is shown exemplarily for Acetylsalicylic acid in Fig. 2e where membrane failure is indicated by the increase of the Blue Dextran peak at 620 nm with time. Note that the retentate solution is not agitated during the experiments whereas the permeate chamber is constantly stirred by a magnetic bar.

It has been established in previous studies (Watanabe et al., 2009,

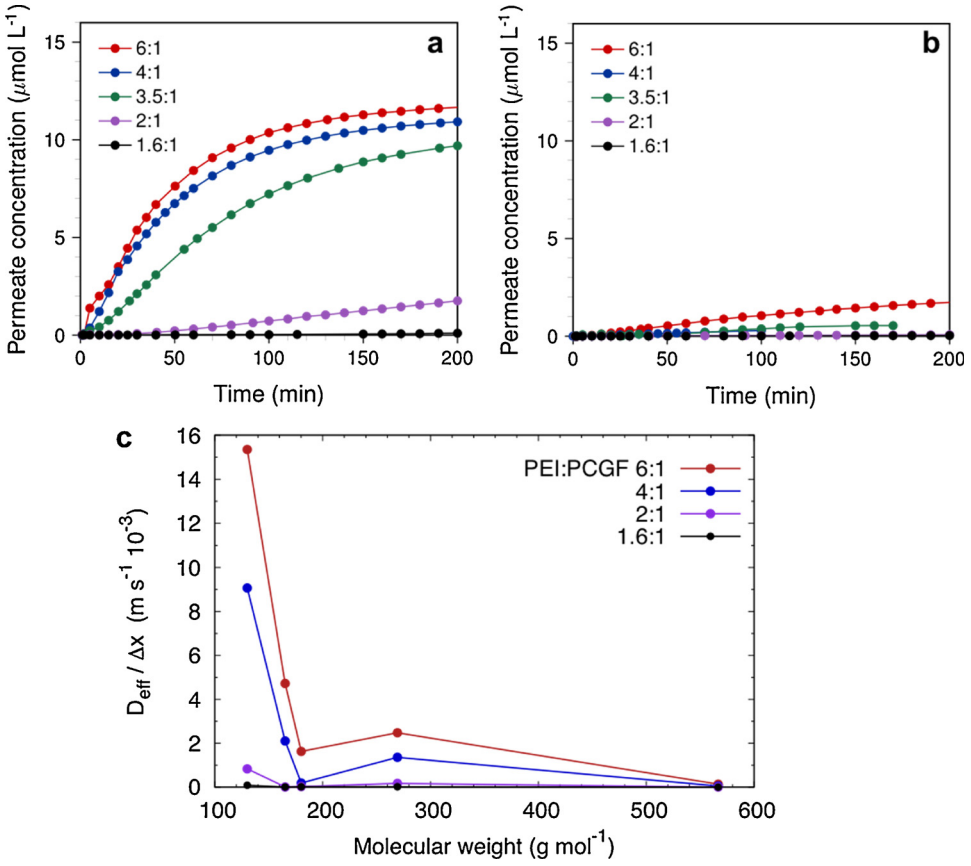

Fig. 4. Separation performance of ultrathin epoxy films. a) Permeation profile of Methyl Red through epoxy ultrathin films based on different stoichiometric PEI:PCGF ratios. b) Permeation profile of Patent Blue V. Initial concentrations of Methyl Red and Patent Blue were 500 µmol L^{-1}. c) Molecular weight cutoff for ultrathin films of four different ratios of epoxy to amine content. The effective diffusion coefficient D_{eff} of the solutes Itaconic acid (M_w 130.1 g mol^{-1}), L-Phenylalanine (M_w 165.19 g mol^{-1}), Acetylsalicylic acid (M_w 180.16 g mol^{-1}), Methyl Red (M_w 269.30 g mol^{-1}) and Patent Blue V (M_w 566.60 g mol^{-1}) was determined at the initial slope of the gradient at their absorption maxima by UV–vis spectroscopy. (For interpretation of the references to colour in this figure legend, the reader is referred to the web version of this article).

2007a) that the crosslinking density of polymeric ultrathin films drastically influences their mechanical properties and toughness. Therefore, the change of mechanical properties in dependence of chemical composition would determine to which extent these membranes could be used in freestanding or freely suspended state. In accordance to the intended use we used bulging tests in an aqueous environment to characterize mechanical properties. Bulging tests correlate the deflection of the ultrathin membrane in dependence of the external pressure until rupture. The results from bulging tests should always be discussed in terms of the used geometry since for films of nanometer thickness often dimensions in the sub mm range are used.

In terms of nanotechnology we applied a large scale approach by employing a bulging diameter close to 1 cm. This is one order of magnitude larger than usual bulging test dimensions (Markutsya et al., 2005; Watanabe et al., 2007a) and allows us to gauge the scalability of the technique. The optical images in Fig. 3a and b give a qualitative impression of the strength and toughness of the membranes as well as the dimensions in which the bulging tests were carried out in aqueous conditions. As indicated previously, the unsupported ultrathin film was attached to the liquid reservoir tube solely by means of the adhesion properties of the epoxy resin, avoiding additional mounting steps and the associated possibility of damage.

We have fabricated membranes of various different precursor compositions and tested their stress-strain behavior in order to investigate how the mechanical properties are influenced. These relationships are shown in Fig. 3d, where vastly different mechanical properties of ultrathin films with different composition can be observed. Ultrathin films with compositions close to stoichiometric unity of epoxy functionalities and reactive amine hydrogens exhibit the highest ultimate tensile strengths and elastic moduli. This indicates that the crosslinking density is highest when the reactive groups are present in nearly equal amounts and a decreasing crosslinking density might be a cause for the lower toughness of membranes with higher amine content. Interestingly, when the number of functional epoxy groups was closest to stoichiometric saturation of amine groups (PEI:PCGF 1.1:1) the stability and stiffness was slightly lower than that of PEI:PCGF 1.4:1. This might be assigned to steric hindrance effects within the polymer network preventing complete reaction of all functional groups leading to an overall loss of crosslinking density. For slightly higher amine contents, corresponding to PEI:PCGF ratios of 1.4:1 and 2:1, the Hooke's law region is covered at elongations below 1%. The most robust membranes were produced from a PEI:PCGF ratio of 1.4:1 where the rupture point lied at 1.5% elongation, corresponding to a stress of approximately 42 MPa. For the ratio of 4:1, the ultimate tensile strength was 22.4 MPa which is in very good agreement with an ultimate tensile strength of 22 MPa reported for a 24 nm thick membrane with the same chemical composition (Watanabe et al., 2007b). These results also demonstrate that the larger bulging diameter had little effect on the deduced material parameters. Note that residual stress, since it is quite susceptible to operator variations and therefore subject to large fluctuations, was neglected as a material related parameter (See Figures S2 and S3).

Fig. 3e shows how the choice of annealing temperature influences the mechanical stability of the resulting membrane, given for the ratio PEI:PCGF 4:1. The onset of increased mechanical stability due to elevated temperature is located around 60 °C. Such low temperature curing could be beneficial when biological or temperature-sensitive materials are used as functional additives within the membrane matrix (Pérez-Madrigal et al., 2015).

In order to corroborate the results of the mechanical characterization and the conclusions drawn, FTIR spectra of the respective membranes were recorded (Fig. 3c). The characteristic epoxy stretching vibration at 915 cm^{-1} (best visible for thin films consisting of pure PCGF) disappears upon opening of the ring for the crosslinking reaction with PEI. Therefore, with increasing content of PEI this absorbance peak gradually vanishes and is completely absent for PEI:PCGF ratios of 1.4:1

and higher. For these ratios, complete saturation of the epoxy groups with amine hydrogens can be assumed while at amine to epoxy ratios of 1:1 to 1.2:1 the epoxy stretching vibration peak is still visible. This is indicative of unreacted epoxy groups and correlates with the lower mechanical stability. Likewise, membranes with higher PEI content exhibit lower stability which we contribute to unreacted amine residues. Both observations align well with the notion of crosslinking density being a critical factor that can be controlled by adjusting the precursor ratio.

These results suggested that the intrinsic porosity of the polymer network might also be an adjustable parameter that can be targeted by the alteration of precursor composition. To investigate this, adequate experiments were performed and Fig. 4 shows how the amine content affects transport rates. Fig. 4a and b show the concentration profiles of Methyl Red and Patent Blue V over time for membranes of different composition. The molecular flux clearly increases with increasing amount of PEI, suggesting the presence of larger voids or channels within the polymer matrix. The underlying phenomenon might be based on the extent of participation of every PEI molecule in the network. Only partial saturation of the amines by epoxy groups would lead to a loose network where individual sidechains of PEI are left to move freely. At the lowest PEI content of 1.6:1 the permeation of Methyl Red converges to zero, indicating a pore size in a range that would be more suitable for solvent nanofiltration (Marchetti et al., 2014). Note that, for the denser membranes we can only see the initial phase of diffusion, while for the less dense ones we are also able to see the system reach equilibrium because of the faster diffusion. This is the reason for the difference of the permeation behavior and why a plateau for some membranes is observable. In order to overcome the reduced permeation rate by increasing concertation in the permeate, one can design a membrane module, where the permeate is constantly washed away by a carrier solvent analogously to pervaporation, where the permeate is removed by a carrier gas or vacuum.

The permeation of Patent Blue V was significantly slower than that of Methyl Red for all investigated membranes and was only marginally present for PEI:PCGF ratios of 4:1 and below (Fig. 4b). Additionally, we found that at a PEI:PCGF ratio of 8:1 (data not shown) the permeation rates were comparable to those of 6:1 albeit having significantly lower mechanical stability manifesting in considerable difficulties at membrane pick up.

It should be noted that efforts were made to determine the pore size by nitrogen adsorption. However, the data could not be fitted by the Brunauer-Emmett-Teller (BET) equation due to very low nitrogen adsorption.

The feasibility of the membranes for the separation of different molecules as well as the cutoff between permeation and retention are important features for diverse applicability. In this context, it was of great interest how other molecules would interact with the membranes and how the permeation is influenced by the size of the compound. To this end, we chose three small molecules of industrial relevance and decreasing molecular weight, L-Phenylalanine, Acetylsalicylic acid and Itaconic acid (Steiger et al., 2013; Klement and Büchs, 2013) and determined transport rates across the different membranes. Owing to the photometric nature of the setup and the difference in extinction coefficient, different concentrations for permeation measurements of these molecules were chosen to enable detection of the analytes with sufficient accuracy. However, the observed diffusion rates were normalized with respect to the initial concentration gradient of the diffusing species.

Table 1 summarizes the separation performance of the epoxy ultrathin films in terms of the effective diffusion coefficient over the distance Δx, captured at the initial slope of the gradient. The smallest molecule, Itaconic acid, showed a diffusivity four- to five-fold larger than Acetylsalicylic acid and Methyl Red. The lower diffusivity of Acetylsalicylic acid compared to Methyl Red could on the one hand be caused by partial hydrolysis into Salicylic acid resulting in a lowered gradient. On the other hand, the effective charge of the solute, which was positive for Acetylsalicylic acid and negative for Methyl Red and L-Phenylalanine, might be responsible. Indeed is seems that electric charge has an influence on the permeation rate since the membrane itself could be charged by protonation of amine groups, but the size of the molecule is dominating. In general, however, we were able to observe the same trend of increasing molecular transport rates with increasing amine content for all molecular probes, illustrated in detail in Figures S4-S6. Fig. 4c depicts this behavior, showing that at an amine to epoxy ratio of 1.4:1 (respectively 1.6:1 for Methyl Red and Patent Blue V), corresponding to the highest mechanical stability (see Fig. 3), no noteworthy transport for solutes with a molecular weight larger than 180 g mol^{-1} is observable. The lower crosslinking density inferred from mechanical stability data and FTIR spectra of membranes with a composition of 2:1 or larger also correlates well with increased transport rates.

The uniformity of the network of the membrane will have a certain effect on the cut off and permeation rate. It the pore size distribution changes to a more broad distribution we would expect enhanced permeation rates at the cost of separation resolution.

4. Conclusion

We demonstrated that ultrathin epoxy based membranes show permeability for small molecules in aqueous environment. The origin of this permeability was attributed to a porosity that is intrinsic to the emergent polymer network. In order to facilitate applicability of the membranes we have performed experiments to optimize the precursor concentrations towards increased mechanical strength. We have attributed the change in mechanical properties to the notion of covalent crosslinking density which was corroborated by FTIR investigations. We then hypothesized, that the tunability of the crosslinking density would represent a tool to adjust the sieving behavior and confirmed this by testing the permeability of differently composed membranes. Furthermore, the compatibility of the membranes with different small organic molecules of industrial relevance was investigated. It was shown that the general trend of decreasing permeability at higher crosslinking density could be observed for all analytes tested. Additionally, it was shown that the diffusion rate across the membrane is generally faster for smaller molecules manifesting in a size selective permeability cutoff. This size based cutoff in combination with the ability to adequately adjust the permeability and the macroscopic stability makes this material interesting for transition to industrial separation tasks.

Author contributions:

A. J. designed and supervised the research project. R.T. supervised the research project and guided the design of experiments. A. R. developed membrane fabrication and characterization methods, conducted laboratory experiments and drafted the manuscript. C. S. performed bulging experiments and membrane fabrication. E. B. performed laboratory experiments and membrane fabrication.

All authors read the manuscript and agree to submission to Journal of Biotechnology.

Additional Information:

Competing interests

The authors declare no competing interests.

Acknowledgements

This work has been supported by the Federal Ministry for Digital and Economic Affairs (bmwd), the Federal Ministry for Transport, Innovation and Technology (bmvit), the Styrian Business Promotion Agency SFG, the Standortagentur Tirol, Government of Lower Austria and ZIT - Technology Agency of the City of Vienna through the COMET-Funding Program managed by the Austrian Research Promotion Agency FFG. The funding agencies had no influence on the conduct of this

Table 1
Properties and effective diffusion coefficients D_{eff} of several small molecules used for sieving experiments.

Molecule	Patent Blue V	Methyl Red	Acetylsalicylic acid	L-Phenylalanine	Itaconic acid
M_w (Da)	566.60	269.30	180.16	165.19	130.10
pKa	2.7	5.1	3.5	2.2	3.9
pH	5.5	5.5	3.3	5.5	3.1
λ_{max} (nm)	635	434	274	256	210
$D_{eff}/\Delta x_{PEI:PCGF\ 6:1}$ ($m\ s^{-1}\ 10^{-3}$)	0.1376	2.481	1.628	4.724	15.35
$D_{eff}/\Delta x_{PEI:PCGF\ 4:1}$ ($m\ s^{-1}\ 10^{-3}$)	0.05182	1.360	0.1869	2.105	9.067
$D_{eff}/\Delta x_{PEI:PCGF\ 2:1}$ ($m\ s^{-1}\ 10^{-3}$)	0.005544	0.1730	0.02470	0.01019	0.8325
$D_{eff}/\Delta x_{PEI:PCGF\ 1.6:1}$[a] ($m\ s^{-1}\ 10^{-3}$)	0.001705	0.01759	0.01850	0.005099	0.08614

[a] For Acetylsalicylic acid, L-Phenylalanine and Itaconic acid, the ratio of amine to epoxy was changed from 1.6:1 to 1.4:1 based on mechanical stability data.

research. We want to thank Hirohmi Watanabe for his help to establish the method in our laboratory. We want to thank Gerhard Sekot for assistance with SEM and AFM and Jasmin Matzinger for help with membrane fabrication.

Appendix A. Supplementary data

Supplementary material related to this article can be found, in the online version, at doi:https://doi.org/10.1016/j.jbiotec.2018.10.002.

References

Agrawal, A.A., Nehilla, B.J., Reisig, K.V., Gaborski, T.R., Fang, D.Z., Striemer, C.C., Fauchet, P.M., McGrath, J.L., 2010. Porous nanocrystalline silicon membranes as highly permeable and molecularly thin substrates for cell culture. Biomaterials 31, 5408–5417.
Ai, M., Shishatskiy, S., Wind, J., Zhang, X., Nottbohm, C.T., Mellech, N., Winter, A., Vieker, H., Qiu, J., Dietz, K.-J., Gölzhäuser, A., Beyer, A., 2014. Carbon nanomembranes (CNMs) supported by polymer: mechanics and gas permeation. Adv. Mater. 26, 3421–3426.
Anastas, P.T., Zimmermann, J.B., 2003. Design through the twelve principles of green engineering. Environ. Sci. Tech. 37, 94A–101A.
Apicella, A., Tessieri, R., de Cataldis, C., 1984. Sorption modes of water in glassy epoxies. J. Membr. Sci. 18, 211–225.
Armstrong, J.K., Wenby, R.B., Meiselman, H.J., Fisher, T.C., 2004. The hydrodynamic radii of macromolecules and their effect on red blood cell aggregation. Biophys. J. 87, 4259–4270.
Cavallo, F., Lagally, M.G., 2010. Semiconductors turn soft: inorganic nanomembranes. Soft Matter 6, 439–455.
Geise, G.M., Lee, H.-S., Miller, D.J., Freeman, B.D., McGrath, J.E., Paul, D.R., 2010. Water purification by membranes: the role of polymer science. J. Polym. Sci. Part B Polym. Phys. 48, 1685–1718.
Gin, D.L., Noble, R.D., 2011. Designing the next generation of chemical separation membranes. Science 332, 674.
Grein, T.A., Michalsky, R., Czermak, P., 2014. In: Pörtner, R. (Ed.), Animal Cell Biotechnology: Methods and Protocols. Humana Press, Totowa, NJ, pp. 459–491.
Groth, T., Liu, Z.-M., 2008. Membranes for the Life Sciences. Wiley-VCH, Weinheim.
Hoek, E.M.V., Pendergast, M.T.M., Ghosh, A.K., 2014. In: Street, A., Sustich, R., Duncan, J., Savage, N. (Eds.), Nanotechnology Applications for Clean Water (Second Edition). William Andrew Publishing, Oxford.
Jimenez-Solomon, M.F., Song, Q., Jelfs, K.E., Munoz-Ibanez, M., Livingston, A.G., 2016. Polymer nanofilms with enhanced microporosity by interfacial polymerization. Nat. Mater. 15, 760–767.
Kang, E., Ryoo, J., Jeong, G.S., Choi, Y.Y., Jeong, S.M., Ju, J., Chung, S., Takayama, S., Lee, S.-H., 2013. Large-scale, ultrapliable, and free-standing nanomembranes. Adv. Mater. 25, 2167–2173.
Klement, T., Büchs, J., 2013. Itaconic acid – a biotechnological process in change. Biorefineries 135, 422–431.
Kunitake, T., 2016. Perspectives: synthetic bilayer membrane and giant nanomembrane. Langmuir 32, 12265–12268.
Marchetti, P., Jimenez Solomon, M.F., Szekely, G., Livingston, A.G., 2014. Molecular separation with organic solvent nanofiltration: a critical review. Chem. Rev. 114, 10735–10806.
Markutsya, S., Jiang, C., Pikus, Y., Tsukruk, V.V., 2005. Freely suspended layer-by-layer nanomembranes: testing micromechanical properties. Adv. Funct. Mater. 15, 771–780.
Matovic, J., Jakšić, Z., 2009. In: Takahata, K. (Ed.), Micro Electronic and Mechanical Systems. InTech, Rijeka, pp. 61–84.
Montagne, F., Blondiaux, N., Bojko, A., Pugin, R., 2012. Molecular transport through nanoporous silicon nitride membranes produced from self-assembling block copolymers. Nanoscale 4, 5880–5886.
Pascault, J.-P., Williams, R.J.J., 2010. Epoxy Polymers. Wiley-VCH Verlag GmbH & Co. KGaA.
Pérez-Madrigal, M.M., del Valle, L.J., Armelin, E., Michaux, C., Roussel, G., Perpète, E.A., Alemán, C., 2015. Polypyrrole-supported membrane proteins for bio-inspired ion channels. ACS Appl. Mater. Interfaces 7, 1632–1643.
Schuster, C., Rodler, A., Tscheliessnig, R., Jungbauer, A., 2018. Freely suspended perforated polymer nanomembranes for protein separations. Sci. Rep. 8, 4410.
Snyder, J.L., Clark, A., Fang, D.Z., Gaborski, T.R., Striemer, C.C., Fauchet, P.M., McGrath, J.L., 2011. An experimental and theoretical analysis of molecular separations by diffusion through ultrathin nanoporous membranes. J. Membr. Sci. 369, 119–129.
Soles, C.L., Yee, A.F., 2000. A discussion of the molecular mechanisms of moisture transport in epoxy resins. J. Polym. Sci. Part B Polym. Phys. 38, 792–802.
Steiger, M.G., Blumhoff, M.L., Mattanovich, D., Sauer, M., 2013. Biochemistry of microbial itaconic acid production. Front. Microbio. 4, 1–5.
Striemer, C.C., Gaborski, T.R., McGrath, J.L., Fauchet, P.M., 2007. Charge- and size-based separation of macromolecules using ultrathin silicon membranes. Nature 445, 749–753.
Stroeve, P., Ileri, N., 2011. Biotechnical and other applications of nanoporous membranes. Trends Biotechnol. 29, 259–266.
Tong, H.D., Jansen, H.V., Gadgil, V.J., Bostan, C.G., Berenschot, E., van Rijn, C.J.M., Elwenspoek, M., 2004. Silicon nitride nanosieve membrane. Nano Lett. 4, 283–287.
van Reis, R., Zydney, A., 2007. Bioprocess membrane technology. J. Membr. Sci. 297, 16–50.
Vendamme, R., Onoue, S.-Y., Nakao, A., Kunitake, T., 2006. Robust free-standing nanomembranes of organic/inorganic interpenetrating networks. Nat. Mater. 5, 494–501.
Watanabe, H., Kunitake, T., Large, A., 2007a. Freestanding, 20 nm Thick nanomembrane based on an epoxy resin. Adv. Mater. 19, 909–912.
Watanabe, H., Ohzono, T., Kunitake, T., 2007b. Fabrication of large, robust nanomembranes from diverse, cross-linked polymeric materials. Macromolecules 40, 1369–1371.
Watanabe, H., Muto, E., Ohzono, T., Nakao, A., Kunitake, T., 2009. Giant nanomembrane of covalently-hybridized epoxy resin and silica. J. Mater. Chem. 19, 2425–2431.
Watanabe, H., Fujimoto, A., Takahara, A., 2013. Concealing surface topography by attachment of nanometer-thick film. Langmuir 29, 2906–2911.
Yang, S.-T., Yu, M., Chang, W.-L., Tang, I.-C., 2013. In: Yang, S.-T., El-Enhansy, H.A., Thongchul, N. (Eds.), Bioprocessing Technologies in Biorefinery for Sustainable Production of Fuels, Chemicals, and Polymers. John Wiley & Sons, Inc, pp. 351–374.

Publication I

Supplementary Information

Freestanding ultrathin films for separation of small molecules in an aqueous environment

Supporting information

Agnes Rodler,[a] Christian Schuster,[a] Eva Berger,[a] Rupert Tscheließnig[a] and Alois Jungbauer[a,b,*]

[a]Austrian Centre of Industrial Biotechnology, Muthgasse 11, 1190 Vienna, Austria

[b]University of Natural Resources and Life Sciences Vienna, Muthgasse 18, 1190 Vienna, Austria

[*]**Corresponding author**
Alois Jungbauer
University of Natural Resources and Life Sciences Vienna
Muthgasse 18
1190 Vienna, Austria
E-mail: alois.jungbauer@boku.ac.at

Additional data and schemes:

Membrane thickness:

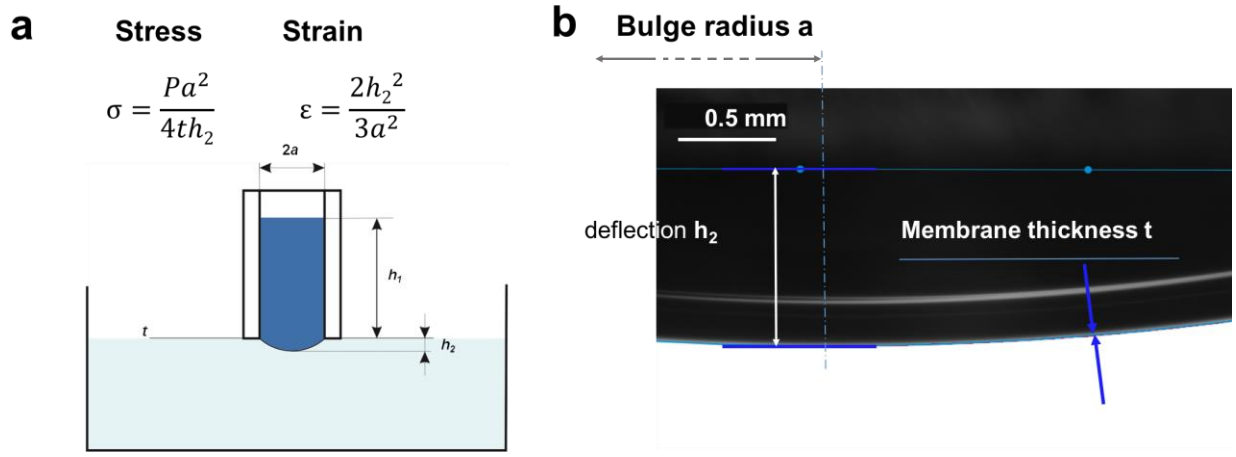

Figure S1: *General scheme of a bulging test to obtain the stress parameter* σ *and the elongation* ε. a) The ultrathin film with the thickness *t* is covering the opening of the tube with radius a. The membrane is loaded with liquid of height h_1, resulting in a hydrostatic pressure *P*. Burdening the membrane with this pressure results in the deflection h_2. b) Image of a bulged membrane section as obtained during bulging tests freely suspended in air. The increment of the deflection h_2 relative to the baseline upon increasing pressure exposure was captured by optical imaging and evaluated using the equations shown in *a*.

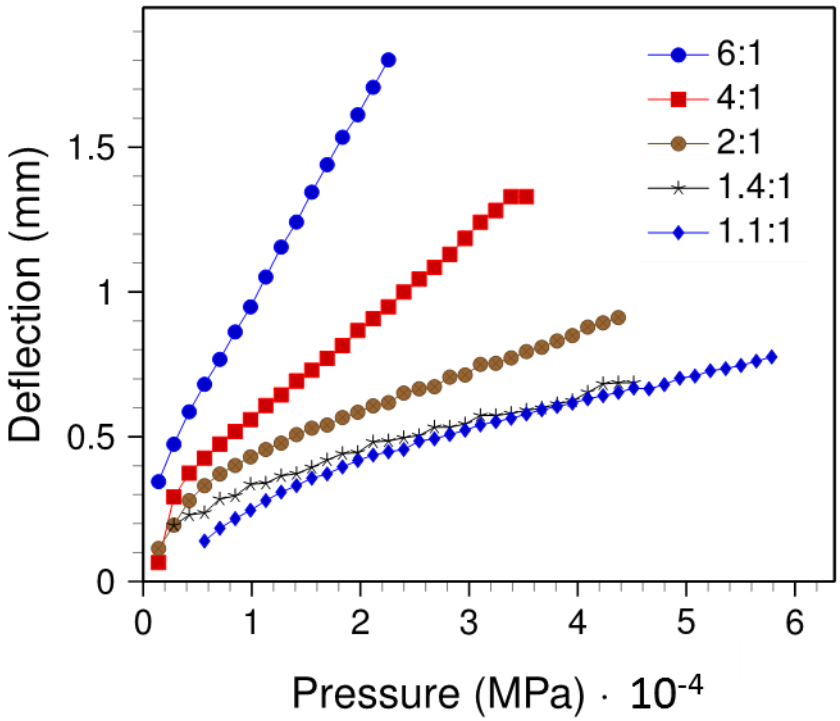

Figure S2: Pressure-deflection curves for 90 nm thick ultrathin films fabricated from different ratios of amine to epoxy precursor obtained by bulging experiments.

In Figure S3, the extent of deflection as a function of the applied pressure is shown. The higher the PEI content, the higher is the deformation of the membranes, where dense network ratios of PEI:PCGF 1.1:1 and 1.4:1 show only minor variation. For all ratios, the behavior is non-linear and satisfies the cubic version of the bulging equation.[1] The plots in Figure S4 show the deflection-normalized pressure against the square of the deflection. By extrapolating the linear trendlines to the *y*-axis (when the bulging equation is written in linear form), the intercept is obtained which is proportional to the residual stress.

The ultimate tensile strength and biaxial modulus were calculated according to Small and Nix, 1992[2].

Table S1: Parameters characterizing the membrane stability. Ultimate tensile strength, biaxial modulus (*Y*-modulus) and residual stress for epoxy ultrathin films based on different intrinsic porosities

Precursor ratio PEI:PCGF	Ultimate tensile strength (MPa)	*Biaxial*-modulus (GPa)
6:1	10.86±1.86	0.32±0.01
4:1	22.44±0.11	1.04±0.05
2:1	29.60±2.13	1.94±0.89
1.4:1	43.79±2.64	3.55±0.15
1.1:1	38.18±3.54	2.92±0.42

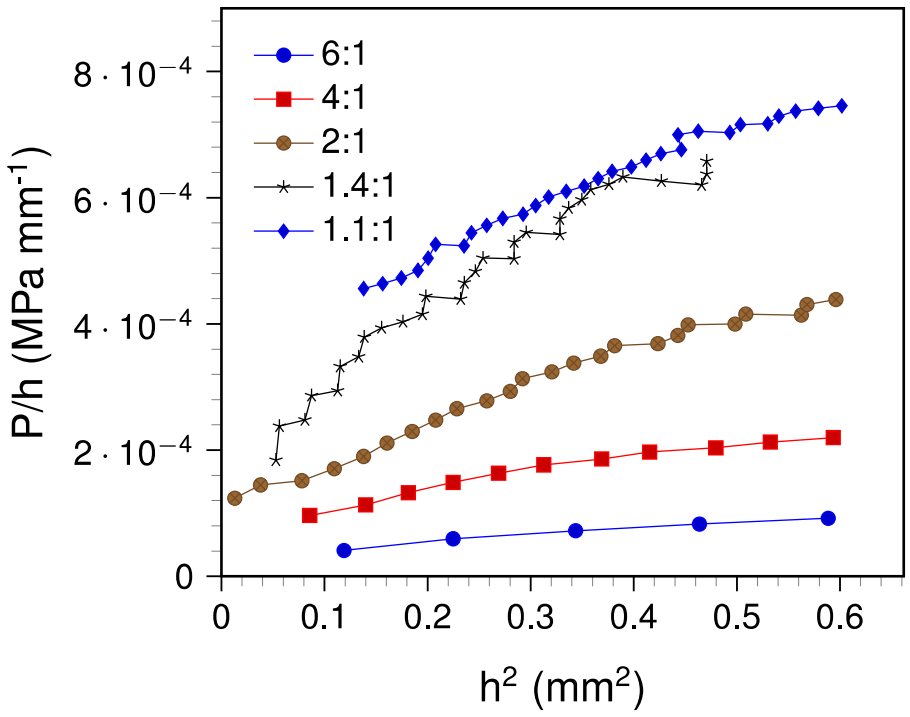

Figure S3: Normalized pressure versus the square of the deflection for the same membranes to estimate the residual stress from the *y*-axis intercept.

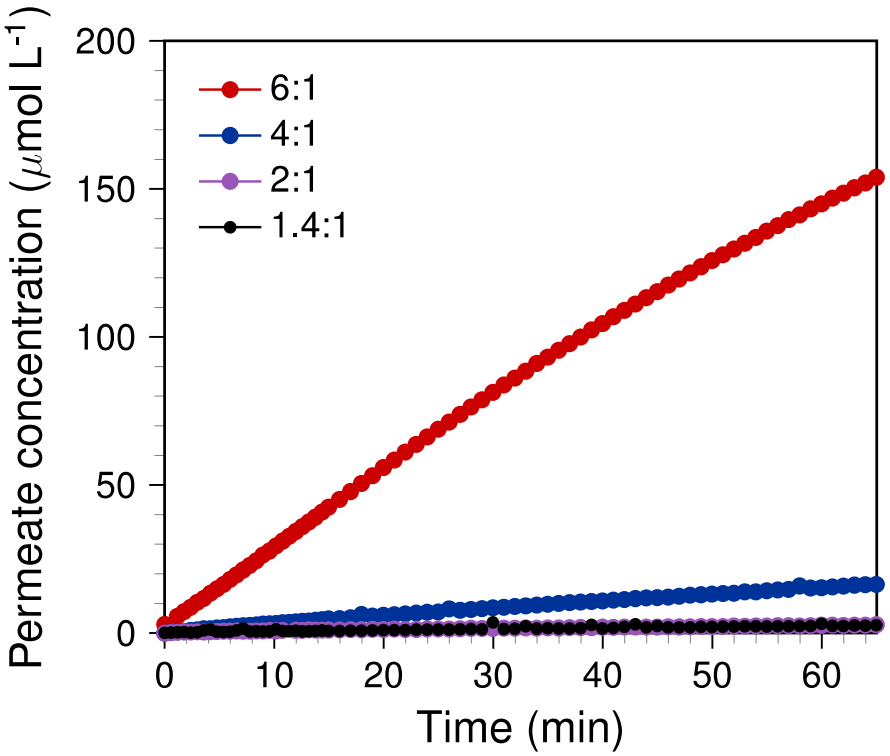

Figure S4: Permeation profiles of Acetylsalicylic acid in Citric acid/phosphate buffer at pH 3.3 through epoxy ultrathin films based on different ratios of amine to epoxy measured in a spectrophotometer at λ=274 nm. "6:1" denotes the highest amine content related to the amount of epoxy, "1.4:1" the lowest. For better visibility, the plot for the data "1.4:1" was inserted with a smaller size of the marks.

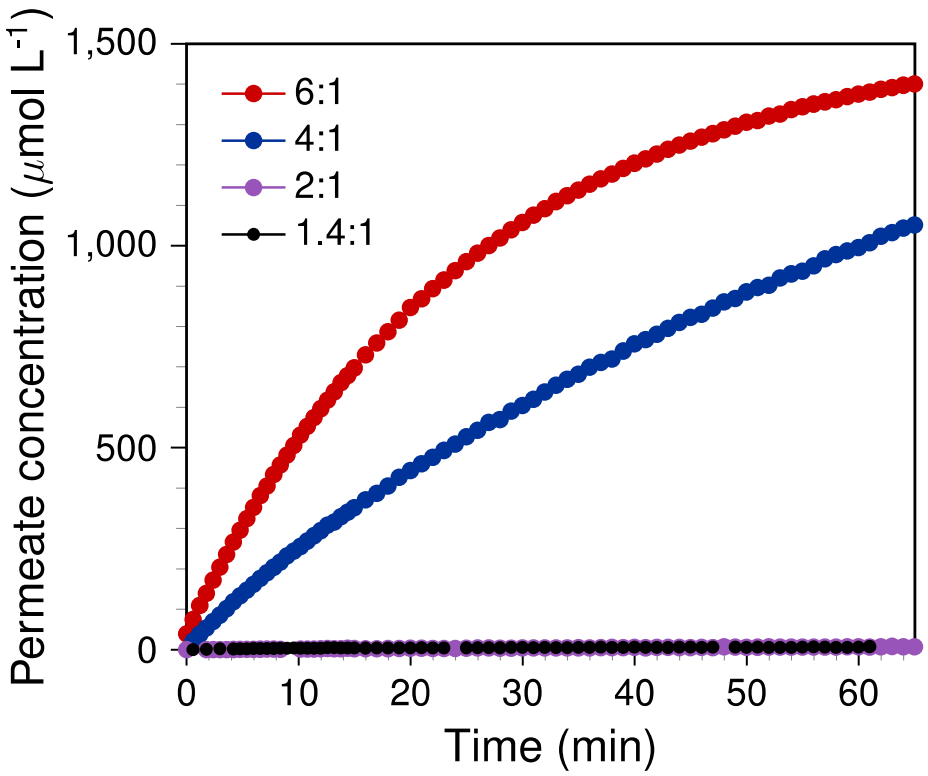

Figure S5: Permeation profiles of L-Phenylalanine through epoxy ultrathin films based on different ratios of amine to epoxy in KCl buffer at pH 5.5 measured in a spectrophotometer at λ=256 nm. "6:1" denotes the highest amine content related to the amount of epoxy, "1.4:1" the lowest. For better visibility, the plot for the data "1.4:1" was inserted with a smaller size of the marks.

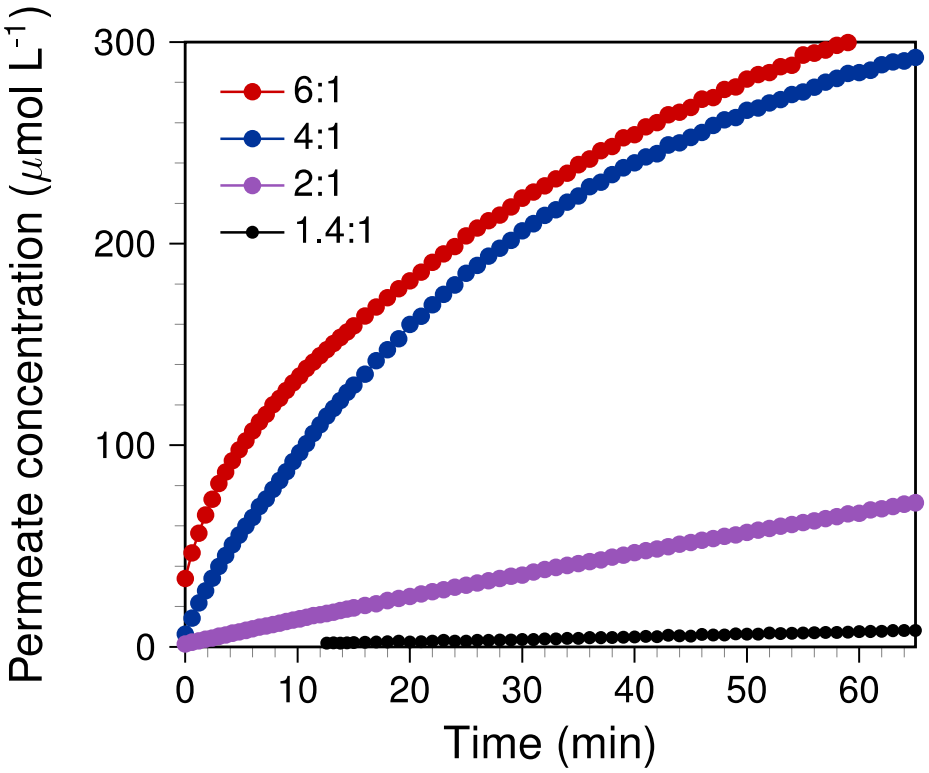

Figure S6: Permeation profiles of Itaconic acid through epoxy ultrathin films based on different ratios of amine to epoxy in phosphoric acid/sodium phosphate buffer at pH 3.1 measured in a spectrophotometer at λ=210 nm. "6:1" denotes the highest amine content related to the amount of epoxy, "1.4:1" the lowest. For better visibility, the plot for the data "1.4:1" was inserted with a smaller size of the marks.

Supplemental References

(1) Poilane, C., Delobelle, P., Lexcellent, C., Hayashi, S., Tobushi, H. Analysis of the mechanical behavior of shape memory polymer membranes by nanoindentation, bulging and point membrane deflection tests. *Thin Solid Films,* **2000**, *379,* 156-165.

(2) Small, M.K. & Nix, W. Analysis of the accuracy of the bulge test in determining the mechanical properties of thin films. *Journal of Materials Research*, **1992,** *7,* 1553–1563.

Publication II

SCIENTIFIC REPORTS

OPEN

Freely suspended perforated polymer nanomembranes for protein separations

Received: 2 October 2017
Accepted: 19 February 2018
Published online: 13 March 2018

Christian Schuster[1], Agnes Rodler[1], Rupert Tscheliessnig[1] & Alois Jungbauer[1,2]

Selective removal of nanometer-sized compounds such as proteins from fluids is an often challenging task in many scientific and industrial areas. Addressing such tasks with highly efficient and selective membranes is desirable since commonly used chromatographic approaches are expensive and difficult to scale up. Nanomembranes, molecularly thin separation layers, have been predicted and shown to possess outstanding properties but in spite ultra-fast diffusion times and high-resolution separation, to date they generally lack either of two crucial characteristics: compatibility with biological fluids and low-cost production. Here we report the fast and easy fabrication of highly crosslinked polymer membranes based on a thermoset resin (poly[(*o*-cresyl glycidyl ether)-*co*-formaldehyde (PCGF) cured with branched polyethyleneimine (PEI)) with nanoscale perforations of 25 nm diameter. During spin casting, microphase separation of a polylactide-*co*-glycolide induces the formation of nanometer sized domains that serve as templates for perforations which penetrate the 80 nm thick membranes. Ultrathin perforated nanomembranes can be freely suspended on the cm scale, exhibit high mechanical strength, low surface energies and a sharp permeability cutoff at a hydrodynamic diameter of 10 nm suitable for protein separations.

Permeable membranes with nanoscale thickness, defined pore geometries and sizes, namely perforated nanomembranes, are the ideal separation materials of tomorrow's industry as they combine high mass transfer with sharp cut-off consequently enabling fast and high-resolution separations. Currently, membranes applied in biotechnology are predominantly used for concentration by ultrafiltration or buffer exchange by ultra-diafiltration[1,2]. They are rarely used for protein separations where chromatographic processes occupy a seemingly indispensable position. Hindrance theory as well as experimental evidence suggest that the performance of separation membranes improves with decreasing thickness. This is especially the case when the thickness of the separation layer approaches its nominal pore size and the size of the molecules being separated[3]. Hence, porous nanomembranes represent an alternative or complementary material for protein purification by high resolution or group separations with the potential to induce a paradigm shift in separations technology. Since peptide purification for pharmaceutical formulation has become the major cost driver such highly efficient nanomembrane based separations bear enormous economic potential. However, this has not yet been widely adopted by the industry[1,4]. In pharmaceutical biotechnology and biomanufacturing the use of disposables and single use separation materials is a current trend[5,6] where a high degree of quality but still reasonable costs are a prerequisite. For nanomaterials the costs associated with the fabrication process clearly dominate material costs and scalable, economically feasible fabrication is sought with considerable effort[4].

Perforated nanomembranes have been produced by numerous groups and many are derived from inorganic silicon based materials[4,7–9] with very regular structures. Various different approaches have been developed in the past decade to impart such nanoscale patterns to different materials. For instance, self-assembly of nanoparticles as templates[10,11] and self-organizing polymers[12–14] have been used to generate nanoscale patterns acting as processing masks to eventually generate perforations in thin sheets of material. While the geometries are excellently suited for separation of proteins and other biomolecules, these inorganic materials have the drawback of poor compatibility with biological fluids and the contained proteins. A high surface free energy of such materials leads to proteins intercalating and thus adsorbing at the water-solid interface to reduce the overall energy of the system[7,15,16]. Similarly, hydrophobicity of some materials poses a threat to actual applicability due to biomolecule

[1]Austrian Centre of Industrial Biotechnology, Vienna, Austria. [2]University of Natural Resources and Life Sciences, Vienna, Austria. Correspondence and requests for materials should be addressed to A.J. (email: alois.jungbauer@boku.ac.at)

adsorption and fouling[16]. Self-organization of block copolymers has not only been used to generate masks but also presents a powerful route to generate polymeric membranes with porous structures[17–19]. The length and chemical difference of the polymer subunits can be utilized to govern the resulting structure of the material and its features[20]. Highly size selective and permeable membranes supported by a robust porous substrate were demonstrated for efficient virus filtration with such a method[21]. In another approach, nanoparticle assisted templating has been employed to prepare perforated, pH-stimuli responsive hydrogel-brush nanomembranes which close their pores at low pH values[22]. Despite their high potential, these materials are typically restricted to small lab scale and entail tedious polymer synthesis or lengthy processing steps, hurdles which have to be overcome for industrial production.

Other, polymer-based nanomembranes have been introduced where an epoxy resin (poly[(*o*-cresyl glycidyl ether)-*co*-formaldehyde], PCGF) is cured with branched polyethyleneimine (PEI) to form a continuous non-porous (from here on referred to as dense) and highly crosslinked nanothick (<100 nm thickness) polymer film[23]. The authors showed that, by employing a simple spin coating process, such covalently crosslinked polymeric nanomembranes can be fabricated with aspect ratios of more than 10^6 for which they coined the term 'large'[23] or 'giant'[24] nanomembranes. Apart from their intended use for sensor and insulator materials these polymer films may be well compatible with biological fluids and proteins since similar polymers are used for fabrication of chromatography beads and monoliths for protein separation. In fact, PEI is known for improving shelf stability of proteins and protective effects in unfavorable environments[25]. Despite their outstanding combination of mechanical and chemical properties encompassing high tensile strength, chemical resistance, adhesive properties and dimensional stability[23], thin films derived from thermoset resins have yet to be exploited for the preparation of porous or perforated separation nanomembranes[26]. Such nanomembranes would possess sufficient mechanical and chemical robustness while providing superior biocompatibility and the benefits associated with polymer processing such as fast and low cost processes and scalability.

Phase separation occurring in ternary mixtures due to rapid compositional quenching during spin coating has been studied and used to obtain functional nanostructured thin films in a bottom up fashion[27,28]. An intriguing aspect is that moderate variations of mixture composition or Flory-Huggins interaction parameters make a wide variety of resulting morphologies accessible. They range from meander- and network like structures to well dispersed circular domains with sizes of several µm down to tens of nm. In consequence, it was shown that phase separation is a possibility to introduce voids into thin polymeric films if one component can be removed selectively. Recently, porous freestanding nanomembranes have been cast from a binary mixture of poly(lactic acid) and poly(vinyl alcohol) with a thickness down to ~60 nm and average pore diameters between 65 and 800 nm[29]. The authors showed that the viability of epithelial cells during adherent growth on these perforated nanomembranes was enhanced compared to non-perforated membranes. This effect was attributed to the dimensional similarity of the perforations and the filopodia filaments of the cells. In a follow up study the fabrication procedure has been tuned to yield perforated nanomembranes with an average pore size of 51 nm[30]. These perforations were then used as immobilization sites for ~27 nm large trimers of bacterial outer membrane protein. Thereby the authors prepared ultrathin freestanding separation membranes with passive diffusion selectivity for certain metal ions. Although these membranes, with pore sizes down to ~51 nm, represent an interesting separation material and could potentially also be used for viral clearance purposes or cell removal the pores seem to be too large for the separation of regular proteins with satisfying resolution. Nevertheless, such a polymer based approach is well suited for economic production and scaling to large separation areas given a sufficiently robust material.

In this work, we demonstrate the bottom-up manufacture of nanothick freestanding polymer separation membranes with low cost equipment which is devoid of any complex processing steps. We use a covalently crosslinking thermoset resin in combination with lateral structure formation by phase separation induced during spin coating of a ternary polymer blend. The resulting thin film can be transformed into a self-supporting, perforated polymeric nanomembrane preserving the specific mechanical and chemical properties observed for equivalent dense nanomembranes. The system is well suited to fabricate nanomembranes with perforations of defined geometry for the separation of proteins and the use with biological fluids. Their hydrophilic nature and low surface free energy promotes biocompatibility such that these nanomembranes will be an excellent choice for the development and implementation of single use membrane devices for biotechnological applications.

Membrane Fabrication and Material Related Characteristics

Ultrathin polymer films were produced by spin coating a ternary polymer mixture of PCGF, PEI and poly(D,L-lactide-*co*-glycolide) (PLGA) dissolved in chloroform onto a water-soluble polystyrene sulfonate sacrificial layer (Fig. 1a-1,a-2). Phase separation occurring during casting, governed by the different solubilities of the polymers in the common solvent, leads to small circular domains of PLGA that are dispersed in a continuous epoxy matrix (PCGF/PEI) (Fig. 1b). Covalent crosslinking of the functional residues within the continuous matrix, initiated at elevated temperature (Fig. 1a-3), results in high mechanical and chemical stability and pins this non-equilibrium morphology. Consequently, the epoxy matrix is rendered insoluble such that the PLGA domains can subsequently be dissolved selectively with the casting solvent to form regular perforations (Fig. 1a-4). Immersion into water dissolves the sacrificial layer to separate the perforated nanomembrane from the wafer. By appropriate immersion, water can penetrate and dissolve the sacrificial layer before the nanomembrane is submerged which leads to floating of the nanomembrane on the surface (Fig. 1a-5). In this state the nanomembranes maintain a stretched and completely flat shape rendering pick up procedures onto supports and tubes very easy (Fig. 2c). In contrast, when submerged, nanomembranes are freely floating and show a crumpled morphology. Note that the adhesive properties of the membrane material mediate tight attachment to a variety of materials for characterization so that clamping or gluing steps can be avoided (Fig. 2c). The entire fabrication process is typically completed within 20–30 minutes.

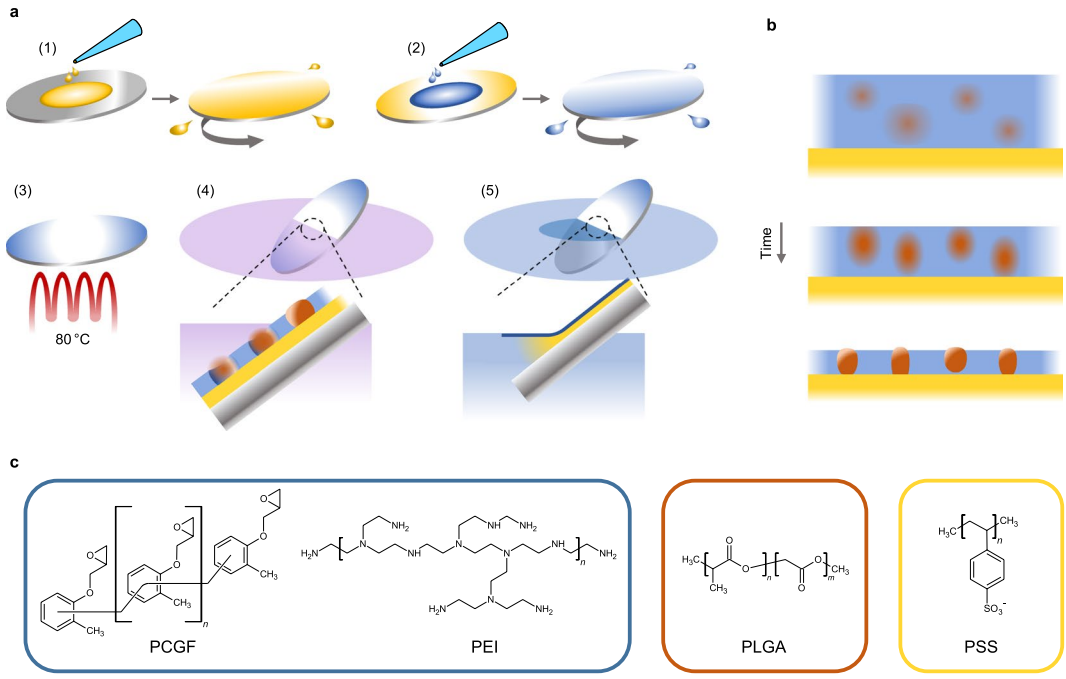

Figure 1. Fabrication of perforated nanomembranes. (**a**) Illustration of the fabrication procedure: (1) Sacrificial layer casting onto polished silicon wafer. (2) Coating of the nanomembrane casting solution containing PEI, PCGF and PLGA dissolved in chloroform onto sacrificial layer. (3) Baking step to crosslink thermoset resin component. (4) Selective dissolution of PLGA by immersion into chloroform to create perforations in the continuous nanomembrane matrix. (5) Immersion into water releasing the nanomembrane from the wafer onto the water surface. (**b**) Schematic of phase separation events occurring during spin coating illustrated at several points in time. (**c**) Chemical structures of the polymers used for nanomembrane fabrication: Thermoset resin constituents poly[(*o*-cresyl glycidyl ether)-*co*-formaldehyde] (PCGF) and branched polyethyleneimine (PEI) comprise the nanomembrane matrix, poly(D,L-lactide-*co*-glycolide) (PLGA) acts as phase separating porogen and polystyrene sulfonate (PSS) is used as a water soluble sacrificial layer.

It is conceivable from previous studies[27,28] that careful and adequate adjustment of polymer blend concentrations and spin coating parameters can lead to morphologies that are of proper scale for protein separations. Accordingly, the presented nanomembrane fabrication procedure was adjusted to yield regular voids of appropriate size. Specifically, the amount of each of the three polymers in the casting solution was varied in small steps while the total polymer concentration, and thereby the resulting thickness, was kept constant. While the membrane precursor ratio (initially at unity) was very slightly adjusted towards PCGF resulting in an increased stability, the ratio of thermoset resin to porogen was increased to 15:1 from the initially used 10:1. Thereby, the resulting dimensions of approximately 25 nm diameter (see Supplementary Figure 9 for pore radius distributions) of the porogen phases that penetrate the entire thickness (perforations) as shown in electron microscopy images (Fig. 2a,b,d and e) were obtained. These domains of phase separated PLGA have been dissolved to form regular perforations. The membranes shown in Fig. 2e,d were freely suspended during imaging to enhance the contrast between membrane material and voids to highlight the perforations. The inset in Fig. 2d shows a side view of the ripped edge of a membrane illustrating the low thickness and membrane spanning pores. A thickness of 68 nm was estimated from the membrane folds in Fig. 2a. Surface depressions of around 150 nm diameter and 20 nm depth originate from discontinuous domains of larger length scale which phase separate in parallel but do not penetrate the entire thickness of the nanomembrane matrix (Fig. 2f,g). This is in agreement with observations of Walheim and co-workers and the anticipated morphologies could be reproduced in the present study with different polymers. The crack like structures observed in SEM, best visible in Fig. 2b,d, are features not intrinsic to the nanomembrane surface but result from the poor wetting of the surface with sputter coated gold (Supplementary Figure 1)[31]. Line profiles extracted from atomic force microscopy (AFM) data confirm the nanoscale thickness (~75 nm) of the perforated polymer films. The dimensions and geometry of the cantilever tip obstructs adequate profiling since the small pore diameter does not allow sufficient penetration (Fig. 2g). The good correlation between UV absorbance of the nanomembranes with their chemical composition and thickness enables rapid determination of membrane thickness in a spectrophotometer (Supplementary Figure 2). Thereby, sufficiently robust perforated nanomembranes were determined to be typically 70 nm thick which is in good agreement with estimations from SEM and AFM.

Mechanical and Chemical Properties

It was of great interest to verify whether addition of a third polymer and the introduction of perforations has considerable impact on the outstanding mechanical properties of the thermoset resin. Mechanical properties were

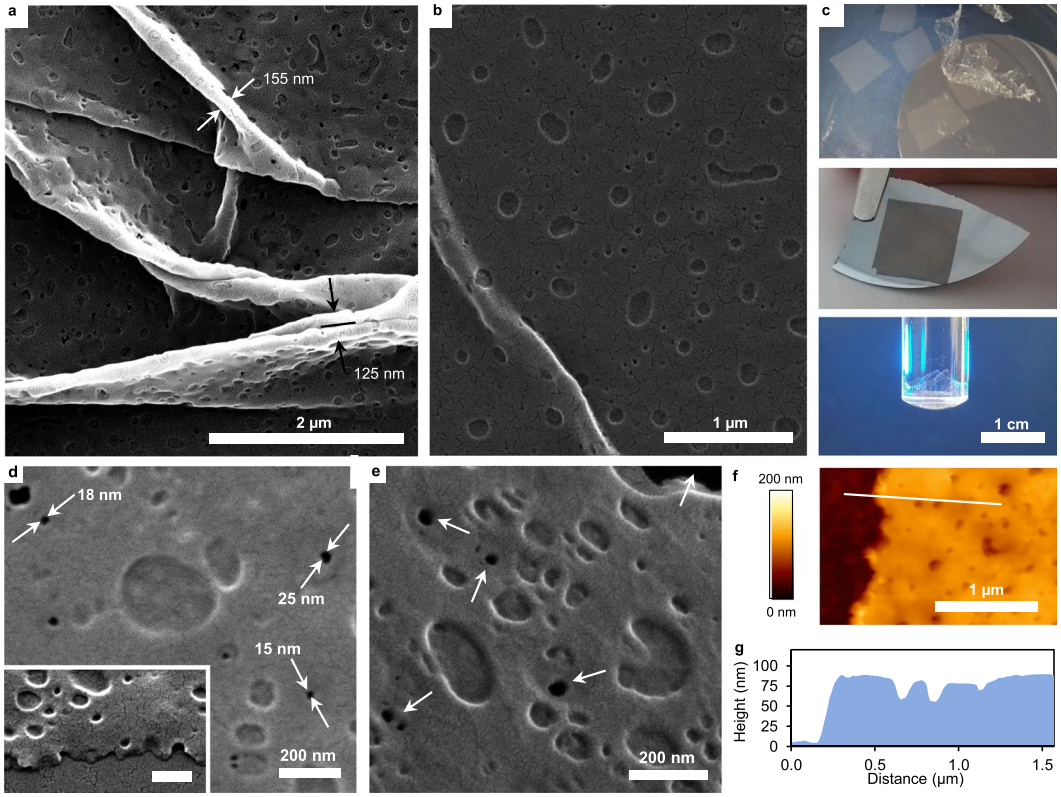

Figure 2. Structural characteristics of perforated nanomembranes. (**a**) SEM image of a warped perforated nanomembrane illustrating the surface topology of pores and depressions. Arrows indicate positions for membrane thickness approximation where it is folded without a gap in between. (**b**) SEM image of a membrane stretched out on a silicon wafer with a small ridge. The difference in length scale of the phase separated domains is clearly visible. (**c**) Photographs of membrane pieces floating on the surface of water (rectangular shapes) and a submerged piece (crumpled shape) (upper image), a membrane picked up on top of a silicon wafer held with tweezers (middle image) and a freely suspended membrane burdened with ~3 g of 2-propanol (lower image). (**d**) Higher magnification SEM image of a freely suspended membrane showing high contrast between membrane material and voids. The inset shows the edge of a membrane as viewed from the side. Scale bar: 200 nm (**e**) Higher magnification SEM micrograph showing a freely suspended perforated nanomembrane in tilted view. The background in the upper right corner visible in black and perforations appearing similarly dark are indicated by the arrows. (**f**) AFM image of the edge of a membrane on top of a silicon wafer. g, Height profile extracted from f corresponding to the white line.

determined by bulging tests with a specialized but simple setup. The nanomembranes were freely suspended over the opening of a tube (Fig. 3a) and burdened by pipetting increasing amounts of liquid onto the surface within the tube until membrane rupture. The resulting deflection of the nanomembranes was monitored by taking optical images and can be used to calculate stress and strain (Supplementary Section 1 and Fig. 3). The biaxial modulus, ultimate tensile strength and residual stress were derived (Table 1) from the stress (σ) – strain (ε) relationships obtained with different liquids (Fig. 3b,c). In contrast to air pressure the use of liquids allows the determination of mechanical stability in aqueous environment (under operating conditions), in hydrated or swollen state caused by other solvents. Perforated nanomembranes show similar mechanical stability as their non-perforated counterparts described and measured by Watanabe and Kunitake (Young's modulus: 350 MPa equivalent to 500 MPa biaxial modulus[32], ultimate tensile strength: 22 MPa). Table 1 lists the biaxial moduli (Y) determined for dense and perforated nanomembranes with our setup in wet state. They were in the same range with 506 MPa for dense and 700 MPa for perforated nanomembranes, respectively. Membrane rupture points, representing the ultimate tensile strength, were also similar with 14.8 and 17.9 MPa, respectively.

We have preferred bulging to the frequently used Strain-Induced Elastic Buckling Instability for Mechanical Measurement (SIEBIMM) since it is simpler to conduct and additional parameters (ultimate tensile strength and residual stress) can be derived. Nevertheless, residual stress is highly dependent on slight variations in the process of membrane pick up and should be neglected as a material related parameter. Studies on porous or perforated freestanding thin films rarely focus on mechanical strength although it is a potentially crucial parameter and Young's modulus alone is not sufficient to adequately describe the mechanical robustness of a material. High mechanical strength of ultrathin separation layers will allow the use of supporting materials with larger pores ultimately decreasing overall mass transfer resistance. The presented bulging experiments reveal that the membranes exhibit high mechanical stability in spite of possessing only a moderate biaxial modulus compared to other polymeric perforated membranes[33].

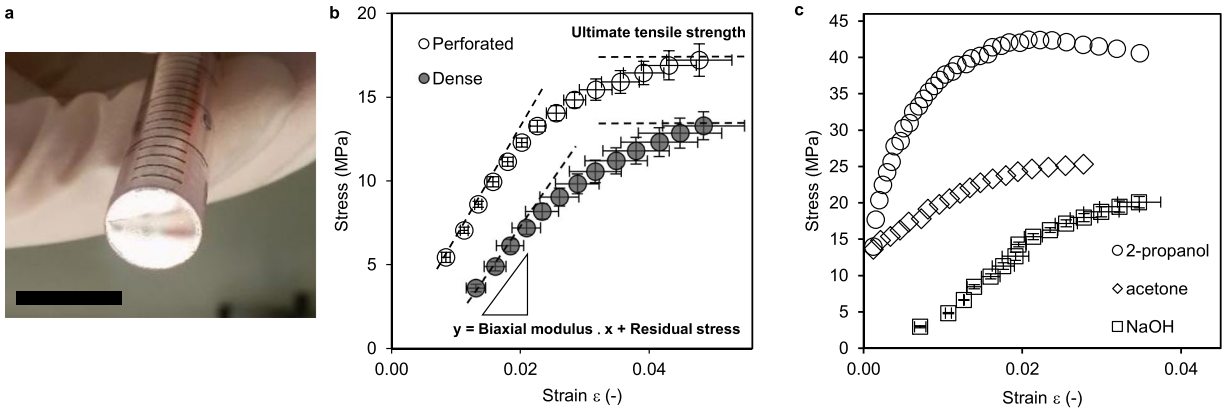

Figure 3. Mechanical properties with different solvents. (**a**) Photograph of a perforated nanomembrane suspended over the opening of a 9.4 mm diameter plastic tube used for bulging experiments. The nanomembrane is only visible due to reflection. Scale bar: 1 cm. (**b**) Stress - strain correlations of perforated and dense nanomembranes of identical matrix composition determined in aqueous environment. Material parameters extracted from the correlation are indicated. Dashed lines are a guide to the eye. (**c**) Stress - strain plots of perforated nanomembranes determined with the indicated organic solvent. Water was used for the nanomembranes incubated with 1 M NaOH beforehand.

	Y	UTS	σ_0
	(Mpa)		
Perforated	700 ± 121	17.9 ± 1.7	0.5 ± 0.9
Dense	506 ± 74	14.8 ± 2.0	−2.4 ± 0.5
1 M NaOH	938 ± 166	20.8 ± 0.7	−3.8 ± 1.2
2-propanol	3242 ± 645	35.2 ± 7.2	8.7 ± 4.6
Acetone	959 ± 99	21.5 ± 5.1	13.7 ± 8.3

Table 1. Mechanical parameters determined from bulging tests.

The nanomembranes are stable under harsh chemical conditions such as incubation with 1 M sodium hydroxide (pH = 14) for 30 minutes and in various organic solvents such as acetone and 2-propanol (Fig. 3c and Table 1). Their resistance towards sodium hydroxide is ideal for biotechnological applications, where materials are frequently cleaned and sanitized at high pH. The stability in organic solvents will allow a careful washing of the membranes to minimize amounts of leachables and extractables. Distinct changes in bulging behavior for acetone and 2-propanol manifested in high residual stress and considerable slack, respectively. Interestingly the membranes exhibited significantly higher strength and stiffness when bulged with 2-propanol. This might indicate that the nanomembrane matrix is not as easily penetrated by 2-propanol than by water or acetone since elastic properties scale negatively with swelling[34].

Surface free energies (SFE) of both perforated as well as dense nanomembranes were estimated by contact angle (θ) measurements with several liquids of different polarity and surface tension according to Zisman[35] and van Oss[36], respectively (Supplementary Section 2). SFE values obtained by the method of Zisman were very similar for both dense and perforated nanomembranes (both ~26.5 mJ m^{-2}) which is two orders of magnitude lower than that of silicon[37] and in the area of polymer SFE promoting low protein adsorption[16]. Interestingly, the surface that forms an interface with air during casting (top surface) is less hydrophilic than the surface facing the sacrificial layer (lower surface). The wettability (cos (θ)) of the lower surface (0.97) with water is optimal for low adsorption[38] but the overall wetting behavior led to inconclusive results in the framework of Zisman (Supplementary Figure 7). The top surface wettability (0.2) is in the moderate hydrophilic range where many membrane and chromatography materials reside (Supplementary Table 1). When evaluated according to van Oss the top surface showed low values for the polar components with a more pronounced positive component (Positive: 2.3 mJ m^{-2} and Negative: 1.8 mJ m^{-2}) and a disperse component corresponding well to the Zisman value (32.0 mJ m^{-2}). The lower surface showed increased polar components with a similarly pronounced positive component (Positive: 22.6 mJ m^{-2} and Negative: 12.9 mJ m^{-2}) alongside a very similar disperse component (32.4 mJ m^{-2}). It has been shown that surfaces with high polar components tend to adsorb proteins more tightly and moderate values of SFE of both components are advantageous and have been linked to low protein adhesion[16]. Moreover, the asymmetric wetting behavior is an intriguing feature which may open up venues for functionalization, ordered and directed immobilization of functional enzymes.

Separation Performance

We have characterized the transport of proteins through the perforated nanomembranes by diffusion with a spectrophotometric setup. Separation performance has rarely been determined for freestanding nanomembranes

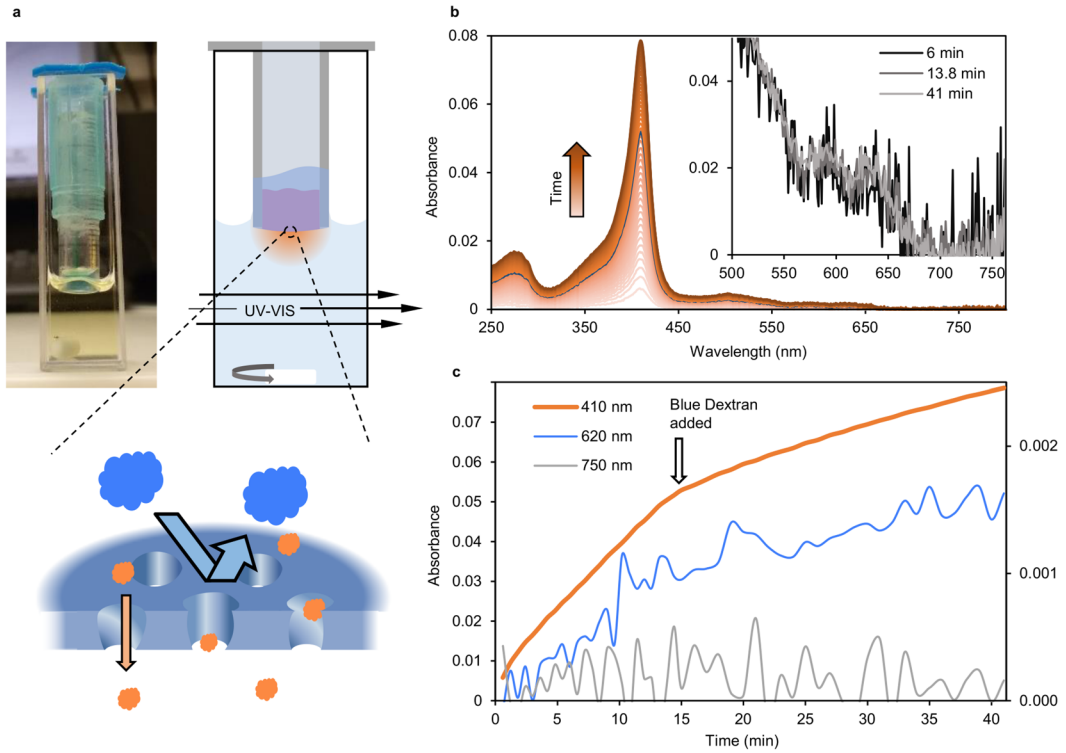

Figure 4. Diffusion based permeability assay. (**a**) Photograph and schematic representation of the assembly that is used in a spectrophotometer to follow size selective protein transport across perforated nanomembranes in real-time. The nanomembrane is freely suspended over the opening of the plastic tube (7 mm diameter) to separate the retentate solution (inside the tube) and the stirred permeate solution (inside the 10 mm pathlength cuvette). (**b**) UV-Vis absorbance spectra of the permeate solution over time (from light to dark orange). The highlighted spectrum was recorded directly before addition of Blue Dextran solution to the retentate side. The inset shows absorbance spectra normalized to unity at 410 nm to illustrate the absence of Blue Dextran based on their invariant shape. (**c**) Absorbance of the permeate solution at selected representative wavelengths: 410 nm for myoglobin, 620 nm for Blue Dextran and 750 nm for TiO_2 nanoparticles. 620 nm and 750 nm values are scaled according to the secondary y-axis.

and generally on µm scale whereas we demonstrate this at 1000-fold larger scale (~40 mm^2). The respective nanomembrane is freely suspended over the circular opening of a plastic tube and the inside of the tube (the retentate chamber) is partially filled with the test solution. The end of the tube that is sealed by the nanomembrane is inserted into a quartz cuvette filled with buffer which acts as the permeate chamber that is constantly stirred by a magnetic bar and directly monitored for UV-Vis absorbance (Fig. 4a). The specific absorbance of the analytes is used to independently monitor their concentration on the permeate side in real time (Absorbance spectra see Supplementary Figure 4). It can be confirmed that the membrane is defect-free by proving the rejection of large probes such as Blue Dextran (2000 kDa, 50 nm diameter) or TiO_2 nanoparticles (100 nm diameter). Figure 4b,c summarizes a single separation experiment for illustration purposes where a solution initially containing myoglobin and TiO_2 nanoparticles has been loaded into the retentate chamber. Figure 4b shows the UV-VIS absorbance of the permeate solution over time. The absence of changes in absorbance at wavelengths over 750 nm in the permeate chamber indicates that the 100 nm nanoparticles have been fully retained. After 15 min a solution of Blue Dextran, which has a broad absorbance peak at 625 nm, has been thoroughly admixed to the retentate with a pipette. A minimal increase in permeate absorbance at 625 nm over time (Fig. 4c) can be attributed to myoglobin rather than Blue Dextran. The correlation of the rates of change in absorbance at 410 nm and 625 nm is present before as well as after Blue Dextran addition. Moreover, the spectra shown in the inset of Fig. 4b were normalized to unity at the peak maximum of myoglobin (410 nm) to clearly visualize that the shapes of the spectra did not change upon addition of Blue Dextran, i.e. no emerging absorbance peak around 625 nm is observable. Therefore a contribution of Blue Dextran to the spectral absorbance can be precluded corroborating that the membrane was intact. Note the distinct decrease in myoglobin diffusion rate upon addition of the Blue Dextran solution as a consequence of dilution (Fig. 4c). With such experiments, it can be clearly demonstrated that proteins pass through the perforated nanomembranes while larger species are fully retained. With non-perforated membranes there was no observable change in spectral absorbance at any wavelength (Supplementary Figure 5). It is also worth noting that the freely suspended nanomembranes are robust enough to withstand the perturbations caused by retentate mixing with a pipette, the changing of retentate as well as transfer to a different permeate chamber cuvette.

Analyte	Size		Charge				Transport rate		
	MW	R_H[a]	IEP[b]	charge at pH			($g\ m^{-2}\ h^{-1}$)		
	(kDa)	(nm)	(pH)	5	7	9	pH 5	pH 7	pH 9
Cytochrome c	12.5	1.78	10.04	+	+	+/0	0.38	0.58	0.54
Myoglobin	16.7	2.12	6.85/7.33	+	+/0	—	0.27	0.42	0.51
Bovine serum albumin	66	5.15	4.9	0	—	—	0.04	0.09	0.05
Alcohol dehydrogenase	150	4.55	5.4–5.8	+/0	—	—	n.d.	0.99	1.59
Apoferritin	443	6.73	4	—	—	—	n.d.	0	0
Thyroglobulin	670	8.58	4.5–5.0	0/—	—	—	0	0	0
Blue Dextran	2000	26.89	7	+	0	—	0	0	0

Table 2. Characteristics of the proteins used to characterize permeability cut-off and observed transport rates. n.d.: $1\ g\ L^{-1}$ protein solutions were not used for diffusion experiments due to aggregation. [a,b] Values for the hydrodynamic radii (R_H) and the isoelectric points (IEP) were taken from the literature as listed in Supplementary Table 2.

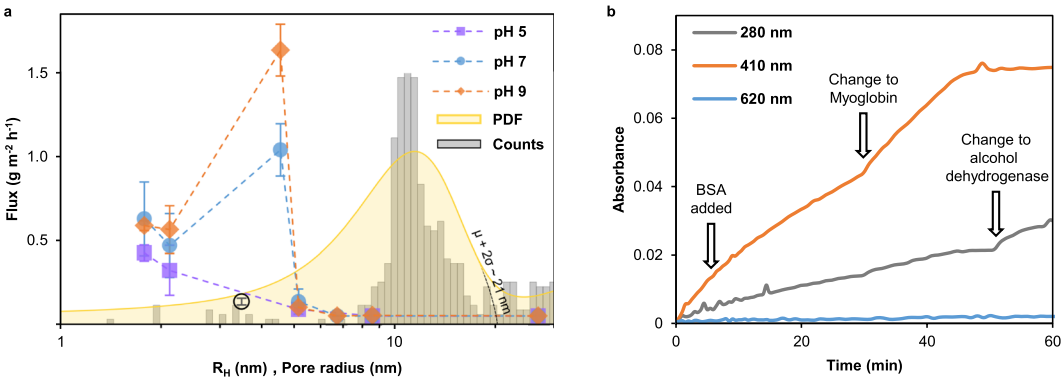

Figure 5. Separation performance for differently sized proteins and pore size distribution. (**a**) Transport rates of differently sized proteins across perforated nanomembranes plotted versus their hydrodynamic radius. The black circle represents bovine serum albumin at a smaller reported R_H value[45]. Grey bars represent the pore radius probability of occurrence while the corresponding probability density function is indicated in yellow as calculated from SEM images. The dashed line intersects the abscissa at ~21 nm and is indicative of $\mu + 2\sigma$. b, Absorbance of permeate chamber at selected wavelengths during a diffusion experiment with cytochrome c where highly concentrated BSA has been added after 6 minutes. After 30 and 50 minutes the retentate solution was changed to myoglobin and alcohol dehydrogenase, respectively.

Permeability of Various Model Compounds

From the time-dependent increase of permeate absorbance the diffusion or transport rate across the membrane was derived. Since the concentration gradient changes over time and the retentate side is far from being ideally mixed, the initial slope was considered to derive representative values for the transport rate. We have determined the transport rates for different model proteins of increasing molecular weight and hydrodynamic size (Table 2).

In each diffusion experiment the structural integrity of the respective nanomembrane was confirmed by full rejection of the large probe molecule Blue Dextran and each membrane was tested with several (at least two) different protein solutions to put the observed rates into context. We determined protein diffusion rates at pH values 5, 7 and 9 and examined the influence on separation behavior. Diffusion rates are average values of at least 3 different membranes and summarized in Table 2 and plotted versus the respective hydrodynamic radius in Fig. 5a. Additionally, a histogram of the pore radius distribution (grey bars) as estimated from SEM images (Supplementary Figures 8 and 9) is provided in Fig. 5a. The probability density function of the pore radius is overlaid in yellow which has its peak maximum at roughly 12 nm and 95% are smaller than 21 nm. As expected for nanomembranes with defined pore geometry a sharp transport rate cut-off is observable which is located between alcohol dehydrogenase and apoferritin. Diffusion of apoferritin, thyroglobulin and Blue Dextran was not observed in any experiment where an intact nanomembrane was confirmed. However, we observed changes of permeate spectra over time presumably caused by impurities which were present in apoferritin solutions despite dialysis with commercial devices (Supplementary Figure 6). Diffusion rates determined for alcohol dehydrogenase were significantly higher than those of myoglobin and cytochrome *c* at pH 7 and 9. A more negatively charged surface might be the reason for this behavior which adds an additional mode of selectivity[17]. The surface free energy calculations point towards positively charged surfaces of the nanomembranes which is in agreement with the general trend of lower transport rates as the proteins get more positively charged with decreasing pH. Interestingly, we observed very low diffusion rates for bovine serum albumin although its nominal molecular mass is less than half as that of alcohol dehydrogenase and despite an overall negative charge[39]. To preclude that

this observation was due to BSA adsorption to the pore walls it is adequate to refer to the experiment illustrated in Fig. 5b. After initial exclusive diffusion of cytochrome c (~0.57 g m^{-2} h^{-1}) for 6 minutes a small amount of highly concentrated (50 g L^{-1}) BSA solution was added to a final concentration of 5 g L^{-1} to the retentate whereby cytochrome c concentration is only marginally changed. It is apparent that the diffusion rate of cytochrome c was not significantly altered by the addition of BSA solution. Later the retentate solution was changed altogether twice, first after 30 minutes to 1 g L^{-1} myoglobin (~0.45 g m^{-2} h^{-1}) and then after 50 minutes to 1 g L^{-1} alcohol dehydrogenase (~1.1 g m^{-2} h^{-1}) showing that these diffusion rates were also largely unaffected. Therefore we conclude this might be attributed to the proposed non-globular conformation of BSA with dimensions of 14 nm × 4 nm × 4 nm[40]. Many different sizes have been reported for different conformations of bovine serum albumin most of which are larger than that of alcohol dehydrogenase[39,41,42]. Moreover, the observed transport rates nicely reflect a general trend of larger diameters at pH values distant from neutral pH highlighting the high-resolution size selectivity. Complete rejection of proteins larger than 13 nm in hydrodynamic diameter shows that the perforations are of appropriate scale to be used in protein separations. By carefully adjusting parameters such as polymer concentrations, porogen molecular weight and spin coating rotation speed the scale of the resulting nanofeatures and thereby the separation behavior will be readily tunable.

Conclusions

We have developed a procedure to fabricate ultrathin hydrophilic mesoporous polymer based membranes with characteristics suitable for protein separations. Our focus was on defined pore geometry of adequate size and biocompatibility as opposed to membranes with tortuous paths and inorganic or hydrophobic membranes. The demonstrated nanomembranes can be freely suspended over tens of mm^2 during characterization, highlighting their outstanding mechanical properties. They preserve their robustness in organic solvents and show resistance to high pH values which is ideal for implementation in biotechnological applications. Furthermore, the hydrophilic nature and low surface free energy with moderate polar components are optimal for low protein adsorption. The observed sharp cut-off between permeation and retention of proteins is in the desired range where industrially important biomolecules reside emphasizing the possibility for group separations. Transfer to any kind of desired support material is enabled by their freestanding nature. The membranes' asymmetric wetting behavior might open venues for directed immobilization and functionalization with biomolecules making them interesting for research. The development and demonstration of this fast and simple fabrication procedure is intended to reinforce and advance the economic feasibility of nanomembranes and thereby shrink the gap towards industrial applicability. We suggest that future development concerning such polymer-based nanomembranes should be dedicated to further improve mechanical stability and porosity of adjustable size distribution.

Methods

Materials. All chemicals, proteins and solvents were purchased from Sigma-Aldrich unless otherwise mentioned. HQ-H_2O (0.055 µS cm^{-1}) was used throughout the whole study. The chemicals Poly(sodium 4-styrenesulfonate) (PSS, Mw = 70 000), Poly[(*o*-cresyl glycidyl ether)-*co*-formaldehyde] (PCGF, Mn = 870), branched Polyethylenimine (PEI, Mn = 10 000) and Poly(D,L-lactide-*co*-glycolide) (PLGA, lactide:glycolide 75:25, Mw 76 000–115 000) were used as received. The polymers PCGF and PEI were dissolved in chloroform ($CHCl_3$) to a concentration of 15 mg mL^{-1} and PLGA to a concentration of 2 mg mL^{-1}. Chloroform solutions were filtered with 0.22 µm PTFE syringe filters. These solutions can be stored for months in glass vials with PTFE lined screw caps.

Test liquids for contact angle measurements diiodomethane (Sigma-Aldrich, 158429), ethylene glycol (Merck, 109621), formamide (Roth, P040.1), glycerol (Fisher Scientific, BP229-1) and toluene (Sigma-Aldrich, 648566) were used as received.

Protein formulations, except apoferritin, were used as received to prepare solutions with a 1 g L^{-1} protein concentration. Blue Dextran solutions were prepared to a concentration of 10 g L^{-1}. Protein and Blue Dextran solutions were buffered with a solution of desired pH prepared according to Britton and Robinson[43] with buffering species concentrations of 0.04 M and additional 0.1 M NaCl. Apoferritin was dialyzed (received as a 20 g L^{-1} solution) with a 2000-fold excess buffer volume with pH = 7.0 in a dialysis cassette (Slide-A-Lyzer™ 10 K MWCO, Thermo Fisher) for 24 hours from which 1 g L^{-1} apoferritin solutions were prepared with desired pH.

Titanium dioxide nanoparticles (TiO_2-NP) were obtained from CINKARNA (Celje) and a 2 g L^{-1} suspension was prepared with buffer of pH = 9 as described above. To counteract aggregation and settling, TiO_2-NP were treated in an ultrasonication bath for 30 minutes prior to use.

Nanomembrane fabrication. Silicon wafers with one polished side and 50.8 mm (2 inch) diameter (SiMat) were immersed in concentrated (96%) sulfuric acid for at least 15 minutes for cleaning and then thoroughly rinsed with distilled water prior to spin coating. All spin coating steps were done with a WS650Mz-23NPP Spincoater (Laurell). Sacrificial layers were formed by spin coating 300 µL of a 5% w/v solution of PSS in HQ-H_2O onto a cleaned silicon wafer at 3000 rpm for one minute. For the preparation of perforated nanomembranes 110 µL of PCGF and 90 µL of PEI solution (15 mg mL^{-1} each) were mixed at room temperature for 5 minutes before 100 µL of PLGA (2 mg mL^{-1}) solution was added. This membrane casting solution was vigorously shaken for one minute before 150 µL were spin coated on top of a freshly prepared sacrificial layer at 5000 rpm for one minute. The thermosetting resin was then cured by placing the silicon wafer onto an 80 °C hot plate for 20 minutes. Dense nanomembranes were produced with the same procedure but instead using 100 µL of both PCGF and PEI, without addition of PLGA and without the following 1 minute of vigorous stirring.

Selective solvent etching (SSE). The wafer bearing the cured nanomembrane on top of the sacrificial layer was allowed to cool to room temperature. The PLGA pore templates were subsequently dissolved by

immersing the silicon wafer in chloroform for one minute. The wafer was then allowed to dry in air before the, as of now perforated, nanomembrane was rinsed twice with $CHCl_3$.

Nanomembrane release. The nanomembrane could then be released on the surface of distilled water by gradually immersing the silicon wafer at an angle of approximately 30° thereby dissolving the sandwiched sacrificial layer. The floating membrane could then be picked up onto any desired substrate or device for further investigations.

Bulging. For bulging tests the individual floating nanomembrane pieces were picked up with a plastic tube of 9.7 mm diameter so that one opening of the tube is completely sealed. The nanomembranes adhered tightly to the tube walls without the need for any further fixation or clamping and were brought into air for drying. The tube was then vertically aligned with the sealed end facing downwards whereby the nanomembranes could then be gradually pressurized with increasing amounts of test liquid contained by the tube. The resulting deflection of the nanomembranes was captured by a digital camera (791×588 pixels, resolution: 265 pixels mm^{-1}) in steps of 100 µL and correlated to the hydrostatic pressures. Stress and strain calculation was done as described in the Supplementary section 1. To test the resistance to alkaline environment nanomembranes were floated on 1 M NaOH solution for 30 minutes before they were neutralized on the surface of water for 30 minutes. Following regeneration they were picked up for bulging with water as a pressurizing liquid. When bulged with organic solvents, nanomembranes were not dissolved but stable and only ruptured by means of increasing pressure after several minutes.

Diffusion. Nanomembranes were picked up on a 7 mm diameter plastic tube to seal one opening completely (Fig. 4a). Unless otherwise stated, 50 µL of filtrate solution (prepared from 45 µL of protein solution plus 5 µL of Blue Dextran solution) were then pipetted into the tube and on top of the nanomembrane. The sealed end of the tube was then immersed into 980 µL of permeate solution (Buffer without protein or Blue Dextran) contained in a 1 cm path length cuvette. The permeate solution volume of 980 µL was chosen so that the membrane edges were not immersed to ensure that the permeating species have to cross the membrane in order to enter the permeate side. UV-VIS spectra (230–800 nm) of the permeate solution were recorded at least every minute with a Cary 60 UV-Vis Spectrophotometer. The filtrate side was repeatedly mixed with a pipette and the permeate side was permanently stirred with a magnetic stirrer.

Contact angle measurements. Contact angles (θ) of the test liquids diiodomethane, ethyleneglycol, formamide, glycerol, water and toluene with the respective surface were determined in air. Optical images were taken with a DSA30 contact angle goniometer (Krüss) and the average value of both measureable θ in each photograph was used for further calculations. Contact angles were allowed to reach a constant value for 5 to 30 seconds after drop deposition and θ were obtained from at least 3 individual droplets of 0.5–1 µL. Surface free energy calculations were done as described in Supplementary section 2 and Supplementary Figure 7.

High resolution imaging. For high resolution imaging the nanomembranes were picked onto small pieces of highly polished silicon wafers (see above and Fig. 2c) or on copper grids for imaging in freely suspended state. Samples for scanning electron microscopy (SEM) were sputter coated with a thin conductive layer of gold and contacted with the SEM-stubs with conductive silver paste. SEM images were obtained with a QuantaTM 250 field-emission environmental scanning electron microscope with a Schottky field emission gun (FEI Europe B.V.) operated at 20 kV in a high vacuum of 1×10^{-6} mbar. Atomic force microscopy (AFM) images were obtained with a Nanowizard II atomic force microscope (JPK Instruments) using SiN cantilevers DNP-S10 (Bruker) with a nominal spring constant of 0.12 N m^{-1} having pyramidal tips with a nominal radius of 10 nm. Scans were done in contact mode in air. The probed areas were typically scanned with a 512-line resolution and a scan frequency of 2 Hz.

Pore size distribution. SEM images were processed with Mathematica 11.0 (Wolfram Research)[44]. A combination of several filters was applied to the respective SEM image in the following order: Blur, Erosion, RidgeFilter, MorphologicalComponents. Components too large to be of interest (background or artifacts) were deselected. The contours of the remaining components were adjusted to fit those in the image as judged by eye. This was done by detection of the component-edges (EdgeDetect) which were then thickened by a Dilation filter depleting the encompassed area to fit the pore area. The resulting image was inverted to give the encompassed areas (and the non-porous area which was deselected). For the obtained components, the "EquivalentDiskRadius" was calculated giving the pore radii. A series of images from several intermediate processing steps of a selected SEM image is shown in Supplementary Figure 8.

Data availability. The datasets generated during and/or analyzed during the current study are available from the corresponding author on reasonable request.

References

1. Saraswat, M. *et al*. Preparative Purification of Recombinant Proteins: Current Status and Future Trends. *BioMed Res. Int.* **2013**, e312709 (2013).
2. Saxena, A., Tripathi, B. P., Kumar, M. & Shahi, V. K. Membrane-based techniques for the separation and purification of proteins: An overview. *Adv. Colloid Interface Sci.* **145**, 1–22 (2009).
3. Snyder, J. L. *et al*. An experimental and theoretical analysis of molecular separations by diffusion through ultrathin nanoporous membranes. *J. Membr. Sci.* **369**, 119–129 (2011).
4. Mireles, M. & Gaborski, T. R. Fabrication techniques enabling ultrathin nanostructured membranes for separations. *ELECTROPHORESIS* n/a-n/a https://doi.org/10.1002/elps.201700114.

5. Gottschalk, U. Disposables in Downstream Processing. in *Disposable Bioreactors* 171–183 (Springer, Berlin, Heidelberg, 2009). https://doi.org/10.1007/10_2008_22.
6. Chico, K. Z. J. M. P.-C. E. The Impact of Disposables on Project Economics in a New Antibody Plant: A Case Study. Available at: http://www.biopharminternational.com/impact-disposables-project-economics-new-antibody-plant-case-study. (Accessed: 4th September 2017).
7. Striemer, C. C., Gaborski, T. R., McGrath, J. L. & Fauchet, P. M. Charge- and size-based separation of macromolecules using ultrathin silicon membranes. *Nature* **445**, 749–753 (2007).
8. Tong, H. D. *et al*. Silicon Nitride Nanosieve Membrane. *Nano Lett.* **4**, 283–287 (2004).
9. Lin, X., Yang, Q., Ding, L. & Su, B. Ultrathin Silica Membranes with Highly Ordered and Perpendicular Nanochannels for Precise and Fast Molecular Separation. *ACS Nano* **9**, 11266–11277 (2015).
10. Klein, M. J. K. *et al*. SiN membranes with submicrometer hole arrays patterned by wafer-scale nanosphere lithography. *J. Vac. Sci. Technol. B Nanotechnol. Microelectron. Mater. Process. Meas. Phenom.* **29**, 021012 (2011).
11. Lipson, A. L., Comstock, D. J. & Hersam, M. C. Nanoporous Templates and Membranes Formed by Nanosphere Lithography and Aluminum Anodization. *Small* **5**, 2807–2811 (2009).
12. Montagne, F., Blondiaux, N., Bojko, A. & Pugin, R. Molecular transport through nanoporous silicon nitride membranes produced from self-assembling block copolymers. *Nanoscale* **4**, 5880–5886 (2012).
13. Nuxoll, E. E., Hillmyer, M. A., Wang, R., Leighton, C. & Siegel, R. A. Composite Block Polymer−Microfabricated Silicon Nanoporous Membrane. *ACS Appl. Mater. Interfaces* **1**, 888–893 (2009).
14. Park, H. J., Kang, M.-G. & Guo, L. J. Large Area High Density Sub-20 nm SiO2 Nanostructures Fabricated by Block Copolymer Template for Nanoimprint Lithography. *ACS Nano* **3**, 2601–2608 (2009).
15. Wahlgren, M. & Arnebrant, T. Protein adsorption to solid surfaces. *Trends Biotechnol.* **9**, 201–208 (1991).
16. Frank, B. P. & Belfort, G. Atomic Force Microscopy for Low-Adhesion Surfaces: Thermodynamic Criteria, Critical Surface Tension, and Intermolecular Forces. *Langmuir* **17**, 1905–1912 (2001).
17. Qiu, X. *et al*. Selective Separation of Similarly Sized Proteins with Tunable Nanoporous Block Copolymer Membranes. *ACS Nano* **7**, 768–776 (2013).
18. Yang, S. Y. *et al*. Virus Filtration Membranes Prepared from Nanoporous Block Copolymers with Good Dimensional Stability under High Pressures and Excellent Solvent Resistance. *Adv. Funct. Mater.* **18**, 1371–1377 (2008).
19. Vriezekolk, E. J., Kudernac, T., de Vos, W. M. & Nijmeijer, K. Composite ultrafiltration membranes with tunable properties based on a self-assembling block copolymer/homopolymer system. *J. Polym. Sci. Part B Polym. Phys.* **53**, 1546–1558 (2015).
20. Yu, H. *et al*. Self-Assembled Asymmetric Block Copolymer Membranes: Bridging the Gap from Ultra- to Nanofiltration. *Angew. Chem. Int. Ed.* **54**, 13937–13941 (2015).
21. Yang, S. Y. *et al*. Nanoporous Membranes with Ultrahigh Selectivity and Flux for the Filtration of Viruses. *Adv. Mater.* **18**, 709–712 (2006).
22. Kang, C. *et al*. Ultrathin, freestanding, stimuli-responsive, porous membranes from polymer hydrogel-brushes. *Nanoscale* **7**, 13017–13025 (2015).
23. Watanabe, H. & Kunitake, T. A Large, Freestanding, 20 nm Thick Nanomembrane Based on an Epoxy Resin. *Adv. Mater.* **19**, 909–912 (2007).
24. Watanabe, H., Muto, E., Ohzono, T., Nakao, A. & Kunitake, T. Giant nanomembrane of covalently-hybridized epoxy resin and silica. *J. Mater. Chem.* **19**, 2425–2431 (2009).
25. Andersson, M. M. & Hatti-Kaul, R. Protein stabilising effect of polyethyleneimine. *J. Biotechnol.* **72**, 21–31 (1999).
26. Kunitake, T. Perspectives: Synthetic Bilayer Membrane and Giant Nanomembrane. *Langmuir* **32**, 12265–12268 (2016).
27. Nauman, E. B. & He, D. Q. Morphology predictions for ternary polymer blends undergoing spinodal decomposition. *Polymer* **35**, 2243–2255 (1994).
28. Walheim, S., Ramstein, M. & Steiner, U. Morphologies in Ternary Polymer Blends after Spin-Coating. *Langmuir* **15**, 4828–4836 (1999).
29. Puiggalí-Jou, A., Medina, J., del Valle, L. J. & Alemán, C. Nanoperforations in poly(lactic acid) free-standing nanomembranes to promote interactions with cell filopodia. *Eur. Polym. J.* **75**, 552–564 (2016).
30. Puiggalí-Jou, A. *et al*. Confinement of a β-barrel protein in nanoperforated free-standing nanomembranes for ion transport. *Nanoscale* https://doi.org/10.1039/C6NR04948F (2016).
31. Ruffino, F., Torrisi, V., Marletta, G. & Grimaldi, M. G. Growth morphology of nanoscale sputter-deposited Au films on amorphous soft polymeric substrates. *Appl. Phys. A* **103**, 939 (2011).
32. Small, M. K. & Nix, W. D. Analysis of the accuracy of the bulge test in determining the mechanical properties of thin films. *J. Mater. Res.* **7**, 1553–1563 (1992).
33. Zimnitsky, D., Shevchenko, V. V. & Tsukruk, V. V. Perforated, Freely Suspended Layer-by-Layer Nanoscale Membranes. *Langmuir* **24**, 5996–6006 (2008).
34. Candau, S., Bastide, J. & Delsanti, M. Structural, elastic, and dynamic properties of swollen polymer networks. in *PolymerNetworks* 27–71 (Springer, Berlin, Heidelberg, 1982). https://doi.org/10.1007/3-540-11471-8_2.
35. ZISMAN, W. A. Relation of the Equilibrium Contact Angle to Liquid and Solid Constitution. in *Contact Angle, Wettability, and Adhesion* **43**, 1–51 (AMERICAN CHEMICAL SOCIETY, 1964).
36. Good, R. J. & Oss, C. J. van. The Modern Theory of Contact Angles and the Hydrogen Bond Components of Surface Energies. in *Modern Approaches to Wettability*1–27 (Springer, Boston, MA, 1992). https://doi.org/10.1007/978-1-4899-1176-6_1.
37. Hara, S., Izumi, S., Kumagai, T. & Sakai, S. Surface energy, stress and structure of well-relaxed amorphous silicon: A combination approach of ab initio and classical molecular dynamics. *Surf. Sci.* **585**, 17–24 (2005).
38. Sethuraman, A., Han, M., Kane, R. S. & Belfort, G. Effect of Surface Wettability on the Adhesion of Proteins. *Langmuir* **20**, 7779–7788 (2004).
39. Böhme, U. & Scheler, U. Effective charge of bovine serum albumin determined by electrophoresis NMR. *Chem. Phys. Lett.* **435**, 342–345 (2007).
40. Wright, A. K. & Thompson, M. R. Hydrodynamic structure of bovine serum albumin determined by transient electric birefringence. *Biophys. J.* **15**, 137–141 (1975).
41. Babcock, J. J. & Brancaleon, L. Bovine serum albumin oligomers in the E- and B-forms at low protein concentration and ionic strength. *Int. J. Biol. Macromol.* **53**, 42–53 (2013).
42. Ferrer, M. L., Duchowicz, R., Carrasco, B., de la Torre, J. G. & Acuña, A. U. The conformation of serum albumin in solution: a combined phosphorescence depolarization-hydrodynamic modeling study. *Biophys. J.* **80**, 2422–2430 (2001).
43. Britton, H. T. S. & Robinson, R. A. CXCVIII.—Universal buffer solutions and the dissociation constant of veronal. *J. Chem. Soc. Resumed* **0**, 1456–1462 (1931).
44. Wolfram Research, Inc., Mathematica, Version 11.1, Champaign, IL (2017).
45. Axelsson, I. Characterization of proteins and other macromolecules by agarose gel chromatography. *J. Chromatogr. A* **152**, 21–32 (1978).

Author Contributions

A.J. conceived the idea, designed and supervised the research project. R.T. supervised the research project and guided the design of experiments. C.S. developed and conducted membrane fabrication as well as laboratory experiments and drafted the manuscript. A.R. developed membrane fabrication and conducted laboratory experiments.

Additional Information

Supplementary information accompanies this paper at https://doi.org/10.1038/s41598-018-22200-4.

Competing Interests: The authors declare no competing interests.

Publisher's note: Springer Nature remains neutral with regard to jurisdictional claims in published maps and institutional affiliations.

Publication II

Supplementary Information

Freely suspended perforated polymer nanomembranes for protein separations

Christian Schuster[1], Agnes Rodler[1], Rupert Tscheliessnig[1], Alois Jungbauer[1,2]*

[1]Austrian Centre of Industrial Biotechnology, Vienna, Austria,

[2]University of Natural Resources and Life Sciences, Vienna, Austria

*e-mail: alois.jungbauer@boku.ac.at

1. Bulging tests - calculation of mechanical properties

Mechanical properties were derived from plots of stress versus strain which were estimated as described later in the text. The biaxial moduli were calculated from the slope of the initial linear range of the stress-strain relationships (linear regression from at least 4 datapoints) and corrected according to Small and Nix[1] in the following manner:

$$Y = \frac{Y_{calc}}{1-0.24\nu-0.00027(1-\nu)\sigma_0} \qquad \textit{(Equation 1)}$$

where ν is Poisson's ratio (0.3 was assumed in all instances) and σ_0 is the residual stress which is given by the σ-intercept of the used linear regression. Furthermore, the relationship of biaxial- (Y) and elastic modulus (E) is given by:

$$Y = \frac{E}{1-\nu} \qquad \textit{Equation 2}$$

Stress (σ) induced by the hydrostatic pressure and the resulting deflection of the nanomembrane was calculated according to:

$$\sigma = \frac{Pa^2}{4hd} \qquad \textit{Equation 3}$$

with notation as indicated in Figure S 3-a. The hydrostatic pressure was calculated taking the inner cross-section of the tube as pressurized area which is burdened by the weight of the accumulating solvent with correction for the capillary pressure according to:

$$P = \frac{\rho g V}{A} - \Delta p_C \qquad \textit{Equation 4}$$

where ρ is the density of the liquid, g is the gravitational constant (9.81 m s^{-2}), V is the volume of the liquid and A is the inner cross-sectional area of the tube. The capillary pressure Δp_C was estimated according to:

$$\Delta p_C = \frac{2\gamma \cos\theta}{r} \qquad \textit{Equation 5}$$

where γ is the surface tension of the liquid, θ is the contact angle of the meniscus with the tube surface as indicated in Figure S 3-a and r is the inner radius of the tube.

Strain (ε) was estimated according to:

$$\varepsilon = \frac{2d^2}{3a^2}$$ *Equation 6*

with notation as indicated in Figure S 3-a.

It is necessary to point out that the outer tube radius (a) was used as the geometry parameter for the pressurized spherical cap model whereas the inner tube radius (r) was used to derive the hydrostatic pressure. The membrane is indeed bulged over the outer diameter of the tube and the major part of the liquid column has radius r. However, the deviation of the liquid column from cylindrical form, as indicated in Figure S 3-b, leads to a slight overestimation of hydrostatic pressure as the liquid height will be lowered. The liquid volume contained by B (Figure S 3-b) is roughly 4 µL and the resulting underestimation of hydrostatic pressure was neglected.

2. Surface free energy by contact angles

The contact angle (θ) values determined for perforated nanomembranes (top and lower surface) and for dense nanomembranes with 6 different liquids were evaluated according to Zisman[2] and according to van Oss[3].

According to Zisman the surface free energy can be estimated by calculating the critical surface tension of an imaginary liquid that would ideally wet (contact angle of 0 °) the surface in question. Hence, when plotting the liquids surface tensions vs their cos (θ), extrapolation of this correlation to cos (θ) = 1 gives the surface free energy.

Van Oss splits the interfacial tensions into three components: disperse interactions (σ_D) and polar interactions of positive (σ_+) and negative nature (σ_-). Following the equation with L for liquid and S for surface:

$$\sigma_L\,(cos\,\theta + 1) = 2(\sqrt{\sigma_D^L\,\sigma_D^S} + \sqrt{\sigma_-^L\,\sigma_+^S} + \sqrt{\sigma_+^L\,\sigma_-^S}) \qquad \textit{Equation 7}$$

we solved the resulting matrix system with 6 liquids for each of the three probed surfaces. The equation:

$$a_i = M_{ij} b_j \qquad \textit{Equation 8}$$

was rearranged:

$$a_i M_{ij}^{-1} = b_j \qquad \textit{Equation 9}$$

to solve for b_j where M_{ij}^{-1} is the Moore-Penrose pseudoinverse of the rectangular matrix M_{ij}. Here a_i comprises $\sigma_L\,(\cos\theta + 1)$ of the liquid i, the matrix components of M_{ij} hold the surface tension components j of the liquid i and b_j holds the surface energies j of the sampled surface.

3. SEM micrograph image processing for pore size distributions

The semi-automated detection of circular features was performed with a Mathematica routine (see Figure S 8) for various different SEM micrographs and detected pores were evaluated for their size (see Figure S 9). For each individual image the parameters for the applied filters had to be adjusted in accordance with resolution, contrast, brightness and magnification. The outlines of the detected features were superimposed onto the original images (as in Figure S 8-f) to aid parameter adjustment by sound operator judgement. It is worth noting that the algorithms tend to neglect doubtful features since putative 'pores' weak in contrast are both, less likely to be detected and more probable to be no true perforations. On the contrary, putative pores rich in contrast (i.e. darker features) are more probable to be membrane spanning and are selected preferentially.

It is furthermore dependent on the resolution and magnification of the SEM micrographs whether features can be adequately detected, measured and classified on a nanometer scale. The images processed in this study to evaluate pore size distributions exhibited a physical pixel size of less than 2.5 nanometers. Thus, pixels that are falsely allocated to or neglected from the pore area account for less than ten percent error of the calculated radius for radii larger than 2.9 nm. This error is lower than one percent for radii larger than 10 nm.

4. Additional SEM images

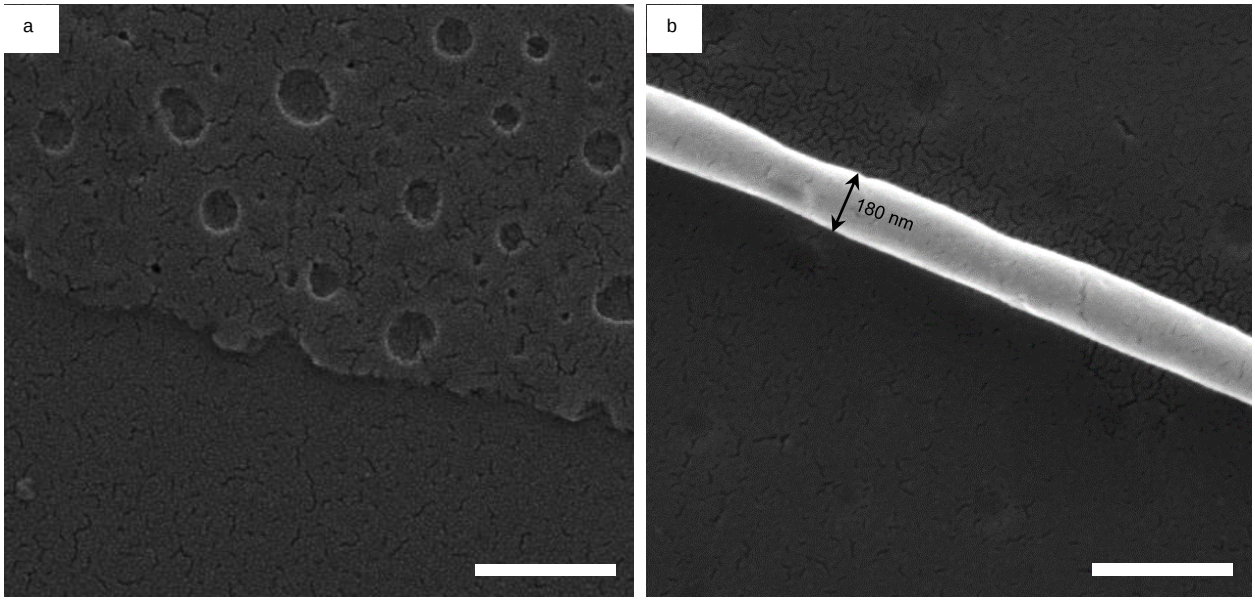

Supplementary Figure 1: Scanning electron microscopy images of nanomembranes on top of a silicon wafer.

a, A perforated nanomembrane on top of a highly polished silicon wafer. The presence of the small crack like structures on the wafer surface demonstrates that these are imperfections in the sputter-deposited gold coating. b, Image of a nanomembrane without perforations. The nanomembrane was cast from a solution with increased porogen (PLGA) concentration resulting in different phase separation phenomena. Note that the surface depressions of approximately 100 nm are still present but less pronounced. Scale bars are 500 nm.

5. Thickness estimation by UV Absorbance

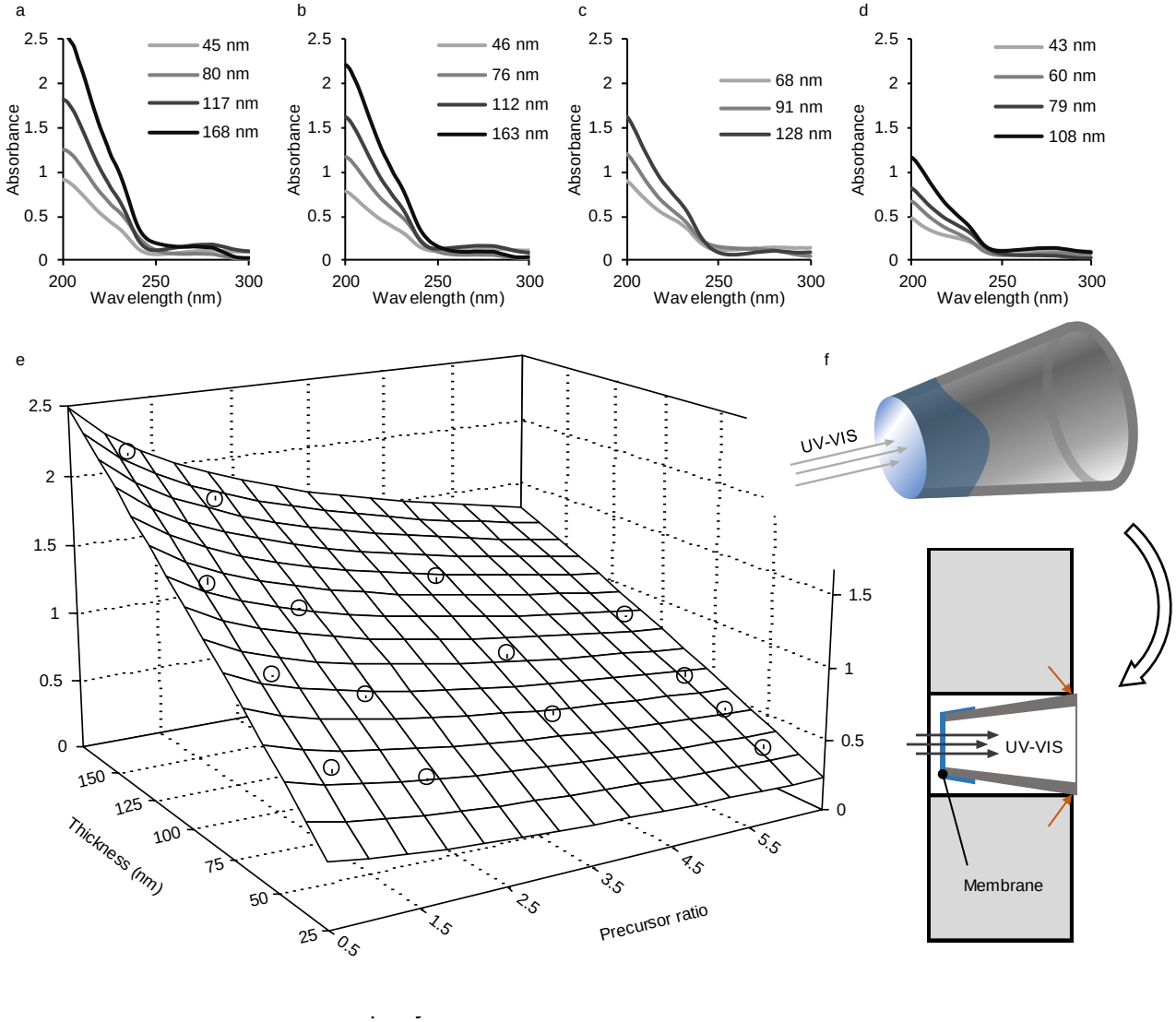

Rank 1 Eqn 151232656 lnz=a+bx^(0.5)+clny
r^2=0.9956939 DF Adj r^2=0.9945195 FitStdErr=0.035728237 Fstat=1387.3711
a=-3.4583322 b=-0.34964596
c=0.89403211

Supplementary Figure 2: Correlation of nanomembrane chemical composition, thickness and UV absorbance.

a – d, Absorbance spectra of nanomembranes with different precursor ratios (i.e. reactive group ratios in the form of amine:epoxy) of 1.1:1 (a), 2.0:1 (b), 4.1:1 (c) and 6.1:1 (d) and different thicknesses determined with atomic force microscopy height profiles. e, 3D-Plot of absorbance at 210 nm in dependence of thickness and chemical composition of the respective nanomembrane. The best surface fit was obtained by fitting the data to the equation ln(Absorbance)=a + b * Ratio$^{0.5}$+ c * ln (Thickness). Fitting was done with TableCurve3D v3. f, Schematic of the setup used to measure

the UV-VIS absorbance spectra in a spectrophotometer. The nanomembrane is freely suspended over the opening of a conical plastic tube, orange arrows indicate contact points of the tube with the specialized mounting cuvette.

6. Bulging test setup

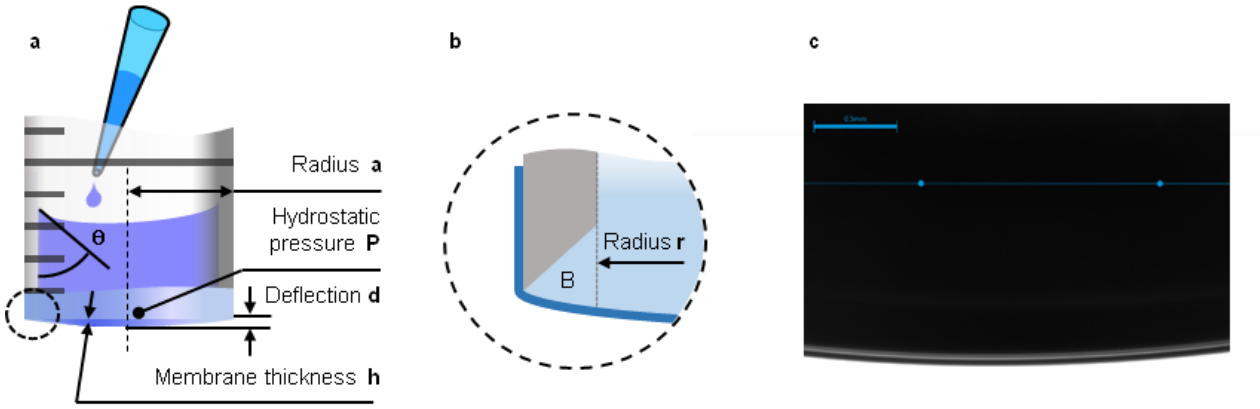

Supplementary Figure 3: Schematic setup and geometry of bulging tests.

a, b, Schematic representation of the bulging test setup (a) with indicated parameters necessary to derive stress – strain relationship (a and b) and a more detailed representation of the bulging tube geometry (b). c, Typical optical image captured during a bulging test. The blue line indicates the edge of the tube for determination of the deflection. Scale bar: 0.5 mm.

7. UV-VIS Absorbance spectra of used analytes

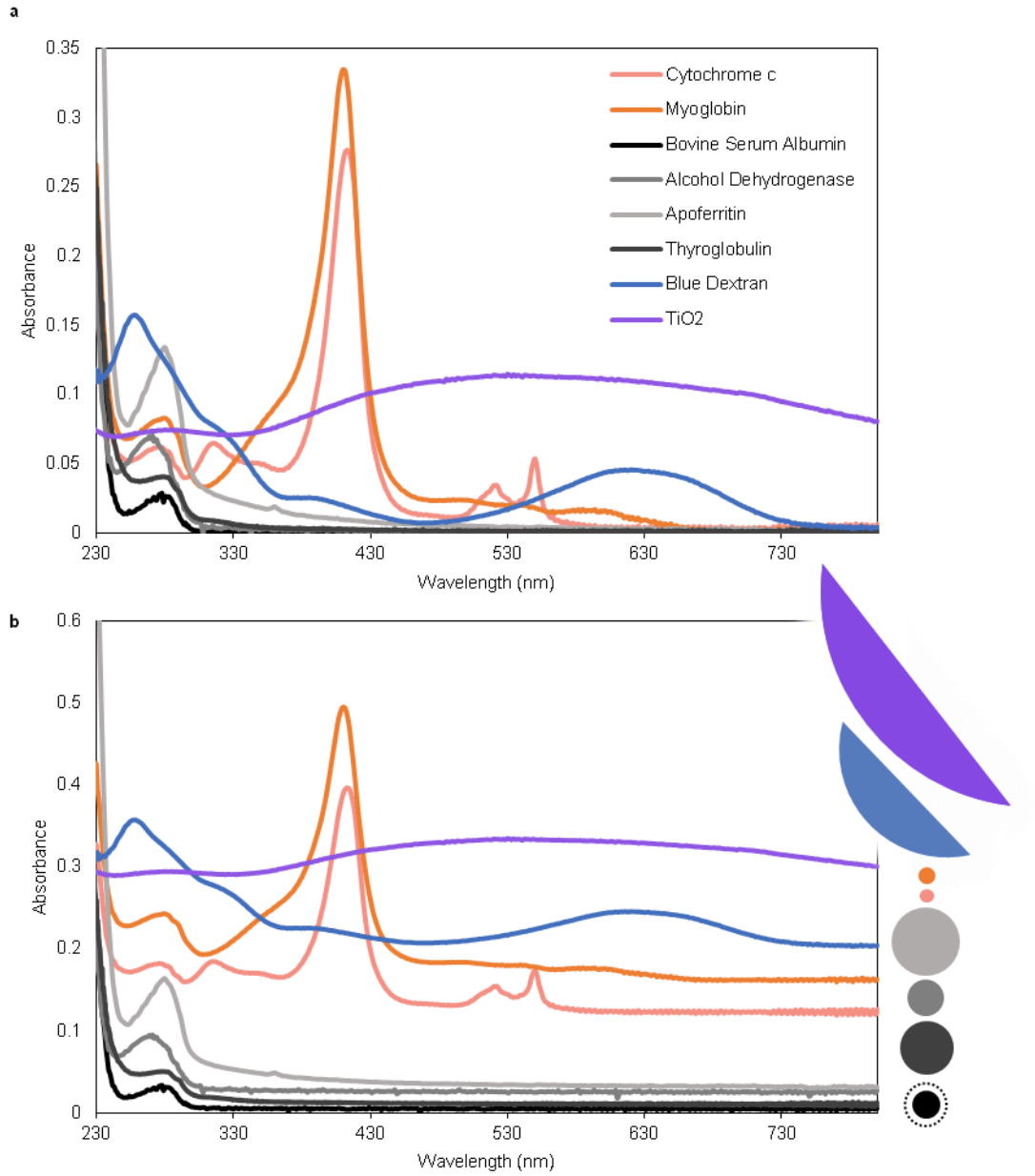

Supplementary Figure 4 UV-VIS absorbance spectra of proteins used in diffusion experiments.

a, Absorbance spectra in the UV-VIS range of model proteins used in this work to investigate separation performance. The displayed spectra were recorded at 0.46 mg mL^{-1}; concentrations that would be present after total equilibrium between retentate and permeate solution has been reached. b, For clarity, absorbance spectra were shifted along the y-axis and the respective hydrodynamic sizes are indicated by correspondingly colored circles (right). A larger size of bovine serum albumin reported in the literature[4] is represented by the dotted circle.

8. Non – perforated nanomembrane diffusion experiment with myoglobin.

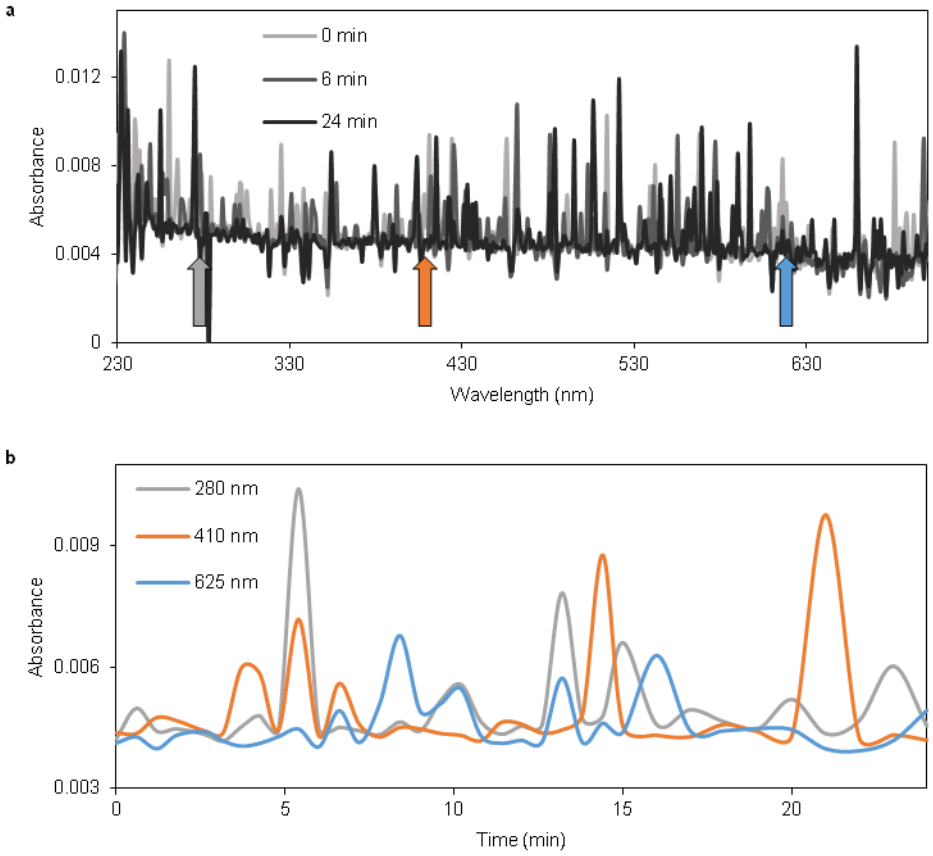

Supplementary Figure 5 Permeability assay with a dense nanomembrane.

a, UV-Vis absorbance spectra of the permeate solution at different points in time. Spectra are changing from gray to black with increasing time. Arrows indicate selected wavelengths plotted versus time in graph b. b, Absorbance of the permeate solution over time at selected wavelengths 280 nm, 410 nm (characteristic absorbance peak maximum of myoglobin) and 625 nm (characteristic absorbance peak maximum of Blue Dextran).

9. Apoferritin diffusion experiment

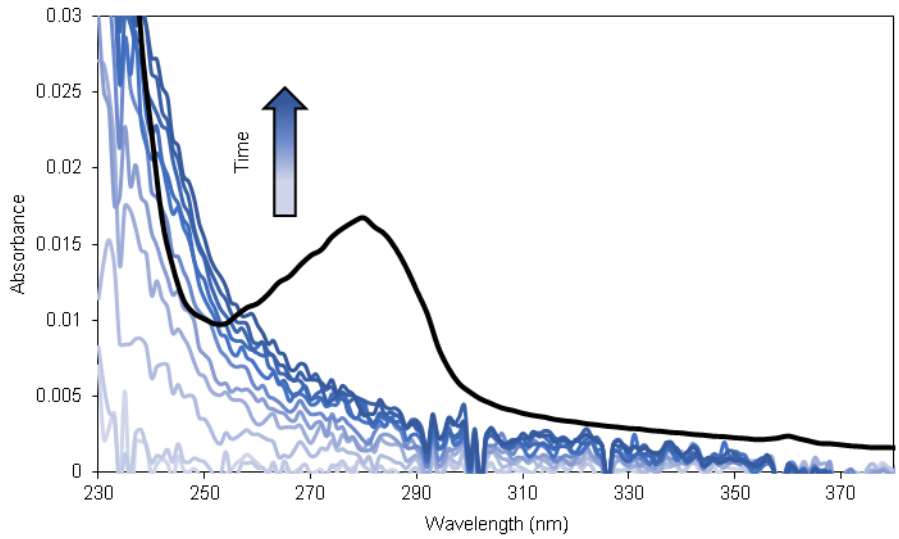

Supplementary Figure 6: Diffusion experiment with apoferritin solution.

UV absorbance spectra of the permeate side over time from light to dark blue with a 1 mg mL^{-1} apoferritin solution. The protein solution was dialyzed with a commercial dialysis membrane before use. The black spectrum represents the absorbance of the protein solution used on the retentate side.

10. Zisman plot

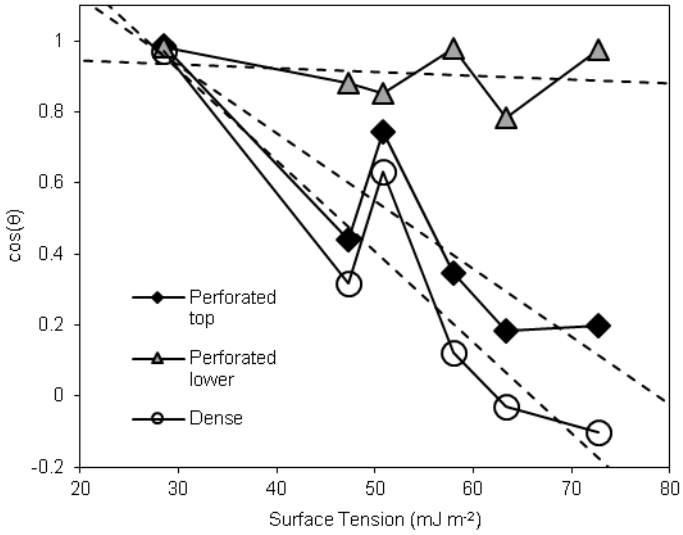

Supplementary Figure 7: Zisman plot of the tested liquids and surfaces.

The contact angle of all tested liquids with the respective surface (cos (θ)) versus the surface tension of the liquid. Extrapolation of the linear regressions to cos (θ) = 1 estimates the surface free energies of the tested surfaces. Results are summarized in Supplementary table 1.

11. Feature detection and pore size distribution from SEM images

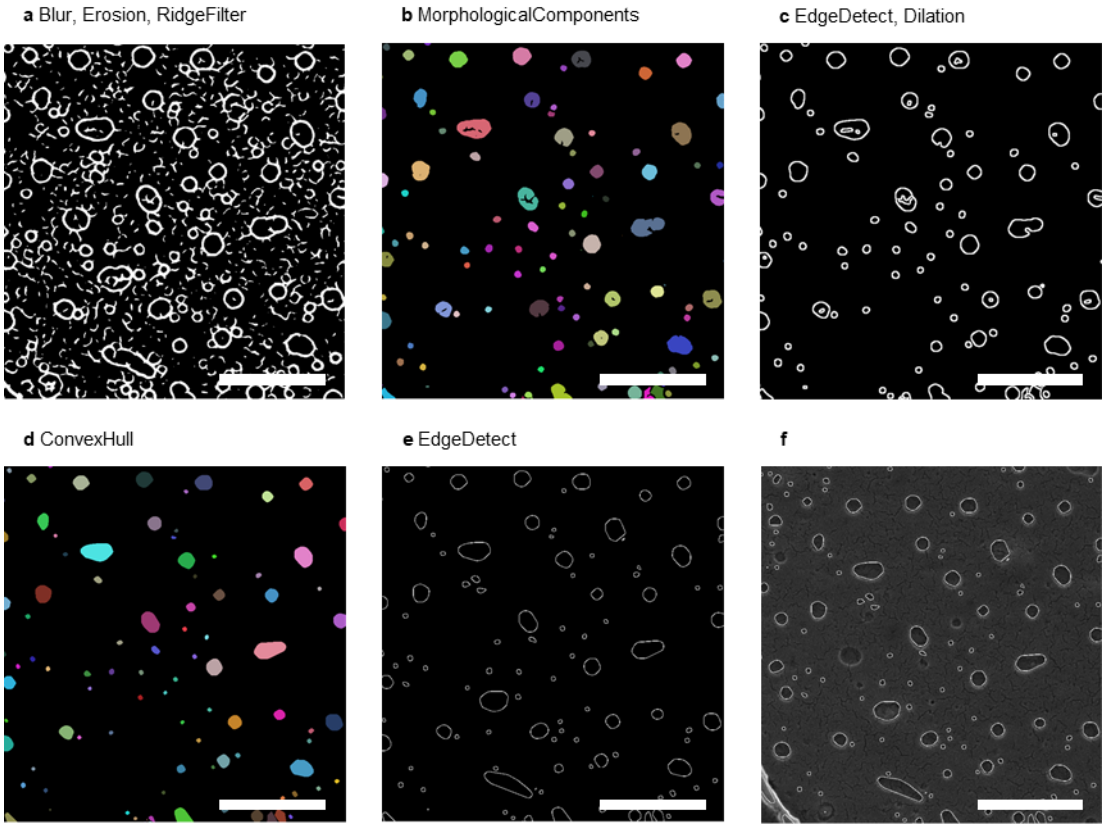

Supplementary Figure 8: Visualized intermediate steps from the processing of an SEM image.

a-d, The filters sequentially applied to the SEM image were visualized for a representative subsection. The detected and amplified edges of the circular features (a) served as boundaries to group the image into the morphological components (b) from which the large ones (e.g. the background) were neglected. The edges of the components were broadened until the encompassed area matched the pore area (c) and these areas were selected as convex features (d) from which the radii of disks with equivalent area were calculated. e, The edges of the detected components (as shown in d) provide better visibility of the result and were superimposed onto the original image in (f). Note that the depicted white lines are part of and contribute to the areas used for calculation. Scale Bars are 1 µm.

12. Pore size distributions obtained from SEM images

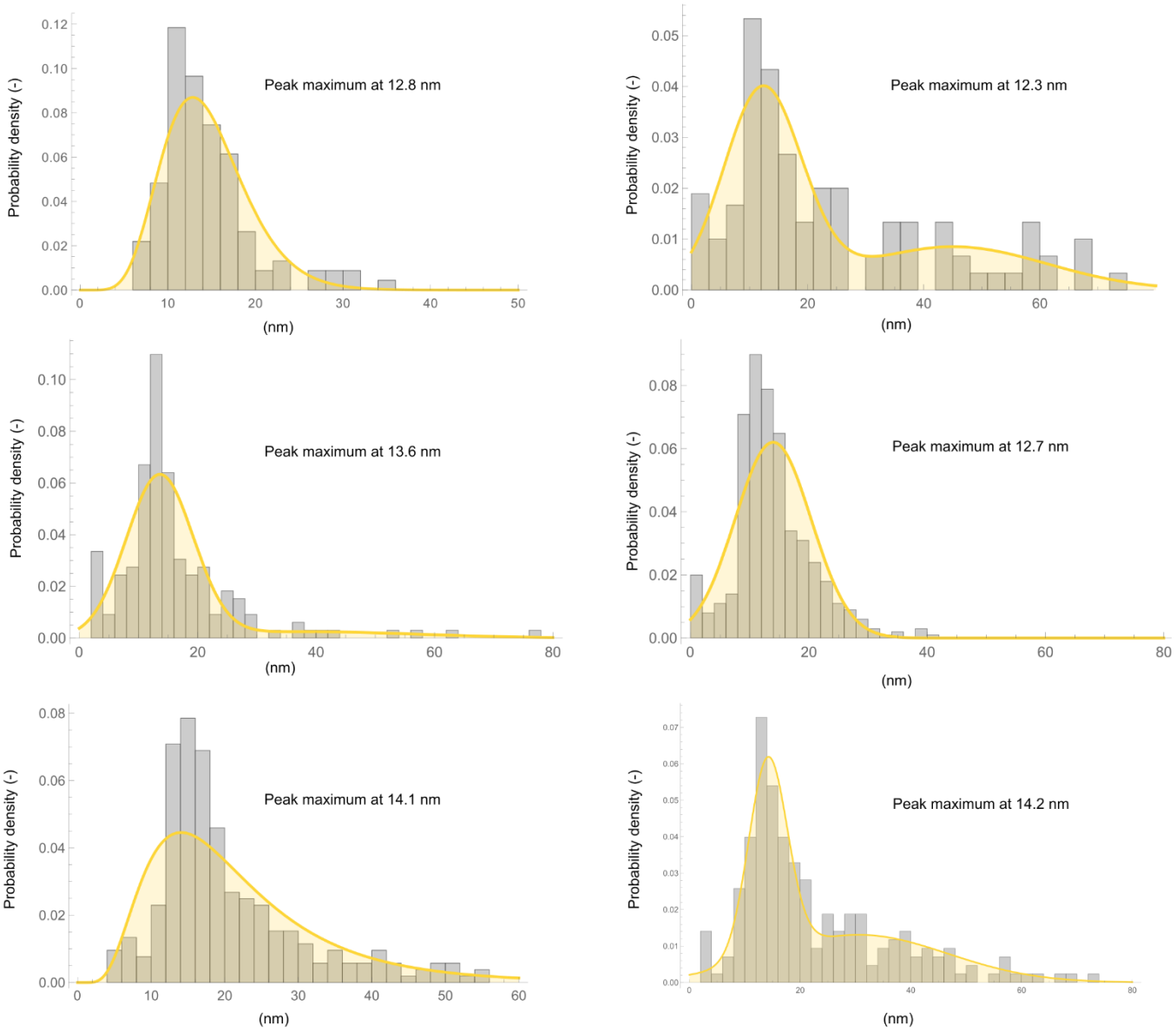

Supplementary Figure 9 Pore size distributions from various membranes.

An average value of the peak maximum of 13.1 ± 0.9 nm was determined from 7 different membranes which exhibited the desired permeability characteristics.

Where adequate, a second normal distribution was fit to the data representing the detected population of circular depressions that are considerably larger in size and would distort the probability density function of the pores.

Supplementary Table 1: Surface free energies of the probed surfaces, wettability of several conventional materials[a] used in protein separations and surface tensions of the test liquids[b].

	Critical / Total	Dispersive	Positive	Negative	$Cos(\theta_{Water})$
		$(mJ\ m^{-2})$			(-)
Dense	26.7	29.6	0.0	0.7	-0.10
Perforated top	26.3	32.0	2.3	1.8	0.20
Perforated lower	-35.5	32.4	22.6	12.9	0.97
Cellulose acetate					0.59
Poly(methyl methacrylate)					0.34
Poly(ethylene terephthalate)					0.16
Polystyrene					-0.02
Toluene	28.5	28.5	0	0.7	
Ethylene glycol	48	29	3.0	30.1	
Diiodomethane	50.8	50.8	0	0	
Formamide	58	39	2.3	39.6	
Glycerol	63.4	37	3.9	57.4	
Water	72.8	26.4	25.5	25.5	

[a] Values were taken from[5]

[b] Values were taken from[6]

Supplementary Table 2: Hydrodynamic radii (R_H) and isoelectric points (IEP) of compounds used in diffusion experiments with references.

Compound	R_H (nm)	Ref.	IEP (pH)	Ref.
Cytochrome c	1.78	7	10.04	8
Myoglobin	2.12	7	6.85 / 7.33	9
Bovine serum albumin	5.15 (4.5)	4(10)	4.9	11
Alcohol dehydrogenase	4.55	12	5.4-5.8	13,*
Apoferritin	6.73	14	4	15
Thyroglobulin	8.58	14	4.5-5.0	16
Blue Dextran	26.89	17	7	18

* Data from product information provided by Sigma-Aldrich.

13. Supplementary References

1. Small, M. K. & Nix, W. d. Analysis of the accuracy of the bulge test in determining the mechanical properties of thin films. *J. Mater. Res.* **7,** 1553–1563 (1992).
2. ZISMAN, W. A. Relation of the Equilibrium Contact Angle to Liquid and Solid Constitution. in *Contact Angle, Wettability, and Adhesion* **43,** 1–51 (AMERICAN CHEMICAL SOCIETY, 1964).
3. Good, R. J. & Oss, C. J. van. The Modern Theory of Contact Angles and the Hydrogen Bond Components of Surface Energies. in *Modern Approaches to Wettability* 1–27 (Springer, Boston, MA, 1992). doi:10.1007/978-1-4899-1176-6_1
4. Babcock, J. J. & Brancaleon, L. Bovine serum albumin oligomers in the E- and B-forms at low protein concentration and ionic strength. *Int. J. Biol. Macromol.* **53,** 42–53 (2013).
5. Van Oss, C. J., Good, R. J. & Chaudhury, M. K. Additive and nonadditive surface tension components and the interpretation of contact angles. *Langmuir* **4,** 884–891 (1988).
6. Oss, C. J. van. *Interfacial Forces in Aqueous Media*. (CRC Press, 1994).
7. Wilkins, D. K. *et al.* Hydrodynamic Radii of Native and Denatured Proteins Measured by Pulse Field Gradient NMR Techniques. *Biochemistry (Mosc.)* **38,** 16424–16431 (1999).
8. Barlow, G. H. & Margoliash, E. Electrophoretic Behavior of Mammalian-type Cytochromes c. *J. Biol. Chem.* **241,** 1473–1477 (1966).
9. Radola, B. J. Isoelectric focusing in layers of granulated gels. *Biochim. Biophys. Acta BBA - Protein Struct.* **295,** 412–428 (1973).
10. Böhme, U. & Scheler, U. Effective charge of bovine serum albumin determined by electrophoresis NMR. *Chem. Phys. Lett.* **435,** 342–345 (2007).
11. Conway-Jacobs, A. & Lewin, L. M. Isoelectric focusing in acrylamide gels: Use of amphoteric dyes as internal markers for determination of isoelectric points. *Anal. Biochem.* **43,** 394–400 (1971).

12. Potschka, M. Universal calibration of gel permeation chromatography and determination of molecular shape in solution. *Anal. Biochem.* **162,** 47–64 (1987).

13. Kidman, G., Park, H. & Northrop, D. B. Pressure stability of proteins at their isoelectric points. *Protein Pept. Lett.* **11,** 543–546 (2004).

14. Axelsson, I. Characterization of proteins and other macromolecules by agarose gel chromatography. *J. Chromatogr. A* **152,** 21–32 (1978).

15. Petsev, D. N. & Vekilov, P. G. Evidence for Non-DLVO Hydration Interactions in Solutions of the Protein Apoferritin. *Phys. Rev. Lett.* **84,** 1339–1342 (2000).

16. Heidelberger, M. & Pedersen, K. O. THE MOLECULAR WEIGHT AND ISOELECTRIC POINT OF THYROGLOBULIN. *J. Gen. Physiol.* **19,** 95–108 (1935).

17. Armstrong, J. K., Wenby, R. B., Meiselman, H. J. & Fisher, T. C. The Hydrodynamic Radii of Macromolecules and Their Effect on Red Blood Cell Aggregation. *Biophys. J.* **87,** 4259–4270 (2004).

18. Friscia, S., Turchi, S. L. & Hepfer, C. E. The influence of pH on electrophoretic mobility, a laboratory investigation. *Biochem. Educ.* **20,** 41–42 (1992).

Publication III

Macromolecular Materials and Engineering
www.mme-journal.de

Micro-Phase Separation within Epoxy Resin Yields Ultrathin Mesoporous Membranes with Increased Scalability by Conversion from Spin- to Dip-Coating Process

*Christian Schuster, Jasmin Matzinger, and Alois Jungbauer**

Ultrathin mesoporous membranes offer highly desirable characteristics for separation tasks regarding selectivity and mass transport of proteins. They have potential applications as separation devices in microfluidics, diagnostics, sensing, and high-precision separations for pharmaceutical formulation. Especially for large-scale and mass production, sophisticated production processes represent a barrier for wider application. A method is developed to produce nanomembranes with a thickness of 75 nm and 40 nm pores with an epoxy resin. The novolac resin is cured with branched polyethylenimine to form a covalently crosslinked polymer membrane with perforations spanning the entire thickness. Pore formation relies on micro-phase separation of the curing agent during casting and the selective dissolution of the emergent nanodomains which thereby serve as pore templates. The resulting membranes are hydrophilic and therefore suitable for applications with biological fluids. Mechanical testing of the flexible but robust thin films reveals an ultimate tensile strength of 15 MPa and a biaxial modulus of 0.8 GPa. Proteins with a diameter of less than 12 nm can diffuse through the pores and permeation rates are pH dependent. The entire fabrication process is transferred to a dip-coating approach, which is more suitable for a potential large-scale production.

1. Introduction

The efficiency of separation tasks addressed by membranes has increased tremendously by the introduction and advent of ultrathin separation layers in large industries such as water desalination[1] and organic solvent nanofiltration.[2] In addition to previous advances, further progress of ultrathin films may enable new technologies in various different fields such as sensors and actuators, bioseparations, microfluidics, and energy-related fields.[3] Especially in bioseparations, ultrathin films occupy a unique position as highly permeable and selective membranes which could revolutionize the industry but have yet to deliver on this potential at industrial scale. High permeation rates and enhanced selectivity have been demonstrated numerous times, often orders of magnitude higher than that of conventional separation membranes ideally leading to significantly enhanced performance.[4,5] Such nanomembranes have been developed with different features that grant permeability such as slits,[6] tortuous channels,[7] or conical pores[8] although cylindrical pores are most common.[4] Nevertheless, in contrast to macroscopic scale, introducing pores of desired size and geometry on nanometer scale is not trivial. Therefore, manufacturing procedures are often complex and sophisticated and do not satisfy the requirements or are not well suited for a production exceeding lab-scale. The most feasible strategies and the resulting materials were recently reviewed[9] where inorganic materials prevail. The control of size and distribution of pores is typically accompanied with a compromise with respect to production speed or scale. This is true for techniques based on both, organic and inorganic materials. However, polymer-based approaches can be favorable due to the availability of feasible routes for mass- and large-scale production with widely established and reliable techniques. In terms of polymeric membranes with thicknesses equivalent to several molecular layers, frequent approaches utilize block copolymers, etching, lithography, and self-assembly of particles or combinations of those.[9] Walheim et al. laid a basis for another bottom-up technique in the regime of self-assembly where phase segregation in binary and ternary mixtures during spin-coating was used to obtain functional nanostructured thin films.[10,11] During thin film formation, the solvent evaporates and the system undergoes a continuous transition from its initial concentration to dry state. If the polymer components are sufficiently incompatible in terms of solubility, this can lead to the formation of a 2D microemulsion from which one (or more) components can be removed selectively.[10,12] Based on these principles and on his group's contributions to ultrathin film research, Kunitake envisioned functional separation membranes fabricated by microphase separation from mixed homopolymers.[13] Accordingly, we have recently shown how nanomembranes with a cutoff suitable for the separation of proteins can be manufactured using phase separation during spin-casting.[14] The fabrication procedure

C. Schuster, J. Matzinger, Prof. A. Jungbauer
Austrian Centre of Industrial Biotechnology
1190 Vienna, Austria
E-mail: alois.jungbauer@boku.ac.at
Prof. A. Jungbauer
Department of Biotechnology
University of Natural Resources and Life Sciences
1190 Vienna, Austria
The ORCID identification number(s) for the author(s) of this article can be found under https://doi.org/10.1002/mame.201900321.

DOI: 10.1002/mame.201900321

relies on a ternary polymer blend in an organic solvent where one of the components forms a microemulsion within a continuous phase of the other two. This process and most of the other approaches to fabricate ultrathin separation membranes rely on spin-coating for thin film formation.[9] Although spin-coating is a very versatile and popular method for casting of ultrathin polymer films, such films are limited in lateral size by the nature of the technique and are therefore only partially scalable. To generate a thin film, the coating substrate is revolved at high speeds so that disk diameters of tens of centimeters are the upper limit. Furthermore, inconsistent thickness throughout the coated thin film[15] causes variations of the resulting features[16] which are important for membrane performance and therefore complicates the transition to different scales. This can lead to heterogeneous pore size distributions and reduce performance or even to the absence of pores and loss of function.

Although the performance of ultrathin membranes in the freestanding state is often outstanding with respect to mass transfer and selectivity, it is crucial that these benefits can be maintained during translation into practical separation devices. A supporting structure is usually needed to grant additional mechanical robustness to the ultrathin films at scales larger than the μm^2 range. Typically, supports are porous layers of tortuous structure often orders of magnitude thicker than the separation layer although microfabricated highly ordered supports have also been demonstrated.[17] Clearly, the mass transfer resistance imparted by such support layers can be kept minimal by increasing its porosity. This, however, requires the separation layer to be stable with as little support as possible making mechanical strength a key parameter to ultimately decrease mass transfer resistance of the whole separation device. Thus, in the development of new separation materials, not only low mass transfer resistance but also increased mechanical and chemical robustness should be strived for.[3,4,18]

In this article, ultrathin separation membranes are presented which are fabricated utilizing microphase separation during casting. The possibility that the excellent chemical and mechanical bulk properties of cured epoxy resins can be retained at the nanometer scale has been demonstrated before,[19] also for separation membranes using phase separation.[14] We hypothesized that, given the right parameters, the different solubility properties of the epoxy component and the curing agent could suffice to induce phase separation phenomena during casting which are appropriate to generate perforated ultrathin films. Using a novolac type epoxy resin and a branched polyethylenimine coating, parameters have been adjusted adequately to demonstrate the fabrication of ultrathin membranes with pores. The facile production process yields membranes that are mildly hydrophilic which is ideal for the processing of biological fluids. An interesting permeation-retention behavior with pronounced pH dependency is observed and attributed to electrostatic repulsion reducing the effective cross-section of the pores. Furthermore, an attempt to overcome some of the hurdles for the translation to a large-scale industrial reality is made by migrating the procedure directly to the dip-coating technique which is well suited for larger scale. The ultrathin films produced with dip-coating display similar pore sizes, morphological and separation characteristics. This proof of principle shall emphasize the feasibility and potential of the developed method for a transition of large area ultrathin separation membranes to industrial production.

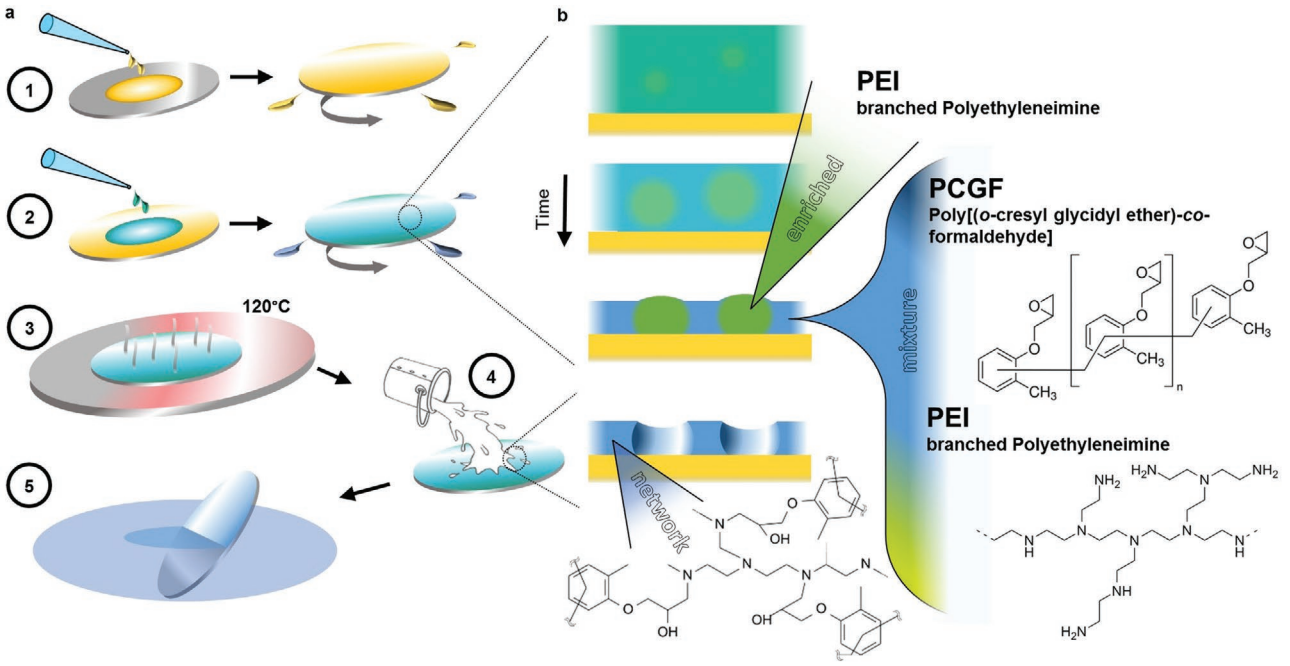

Figure 1. Schematic representation of membrane casting using a spin-coater and a silicon wafer as the casting substrate. a) Membrane fabrication procedure with 1) casting of the sacrificial layer, 2) casting of epoxy resin membrane material, 3) curing at 120 °C on a hotplate, 4) dissolution of pore templates, and 5) final membrane release onto the water surface. b) Representation of the microphase separation during the coating process and the final membrane with dissolved pore templates with indicated composition of the domains.

2. Results and Discussion

2.1. Membrane Spin-Casting

In the developed spin-coating procedure (**Figure 1**a), the ultrathin membranes are prepared from a mixture of epoxy resin (Poly[(*o*-cresyl glycidyl ether)-*co*-formaldehyde, PCGF) and curing agent (branched polyethylenimine, PEI) dissolved in the common solvent chloroform. The thin film is cast onto a previously prepared layer of poly(sodium 4-styrenesulfonate) (PSS) that can be dissolved to separate the membrane from the solid casting substrate after fabrication is finished. During the spin-coating process, the polymer mixture is spread over the sacrificial PSS layer while drag and viscous forces are primarily contributing to thinning. At a certain point, these effects get dominated by evaporative thinning as the solvent escapes into the surrounding air whereby the concentration of polymers in the film changes continuously until eventually only a dry polymer film is left (Figure 1b). These changes in concentration force one of the components to enrich in small domains as soon as its solubility is exceeded. The domains continue to accrete material while the film gradually dries until the mobility of the polymer molecules in the mixture is insufficient and the conformation effectively freezes. Conveniently, due to the nature of the thermoset resin, either component is soluble in chloroform on its own but once the resin is cured, covalent bonding renders the resulting polymer network insoluble in most organic solvents. This covalent crosslinking is initiated at elevated temperature[19,20] whereas the domains containing mostly one component are left soluble. Under appropriate conditions, these domains can span the entire thickness of the resulting film and circular perforations are formed by dissolution in an adequate solvent. Once the perforated thin film is formed, it can be further processed by surface functionalization, to add supporting structures or it can be separated from the casting substrate for microscopic analysis (**Figure 2**) and further testing (**Figures 3** and **4**).

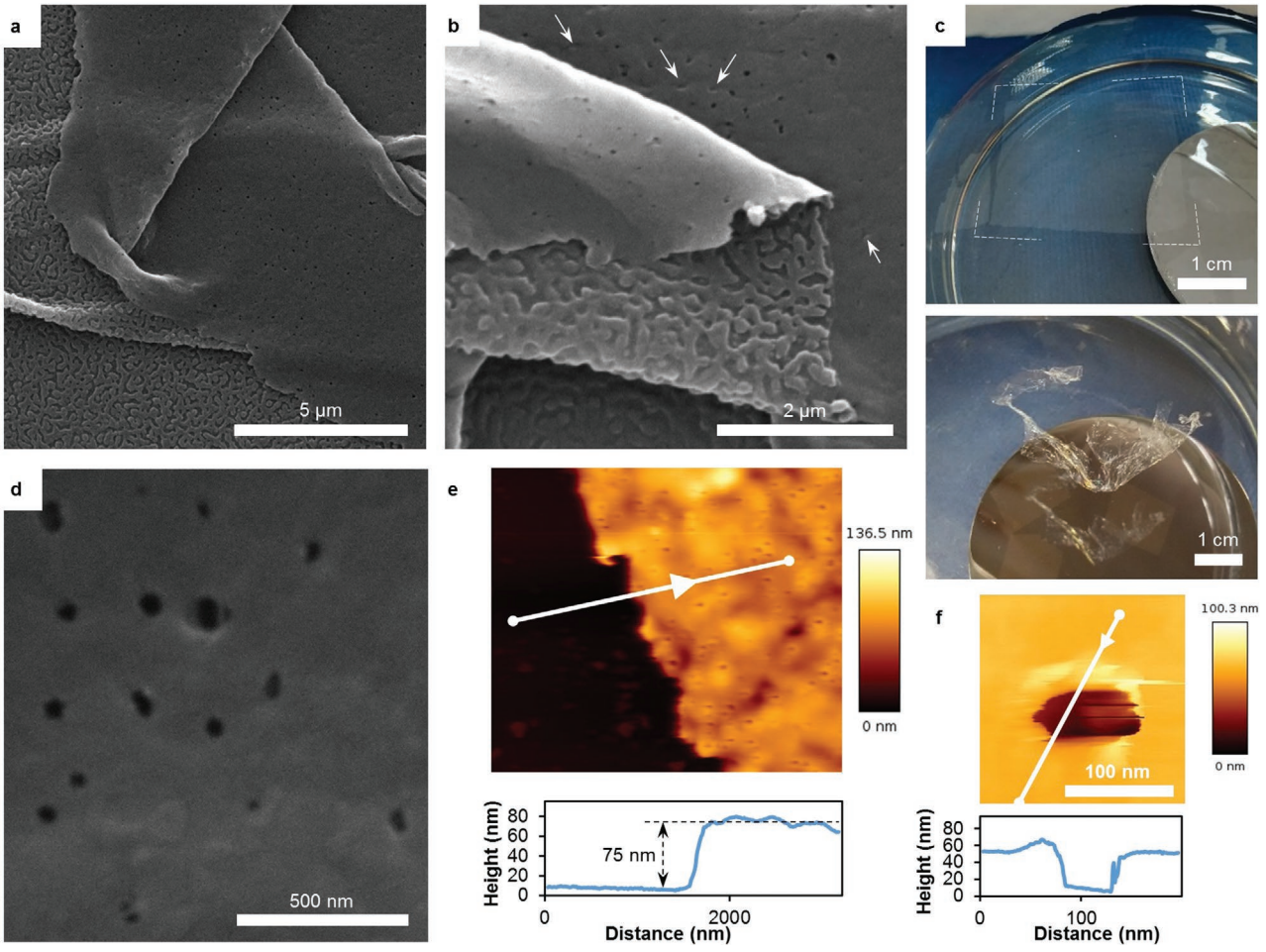

Figure 2. Morphological and structural appearance of ultrathin membranes. a) Low magnification SEM image of a membrane supported on flat silicon. The membrane is folded and reveals that the two surfaces appear distinctly different. Pores are only slightly visible as dark spots dispersed in the grey matrix. b) Higher magnification SEM image of a folded edge emphasizing the difference of surface topology and the low thickness of the membrane. Arrows indicate non-perforating pores. d) A more detailed resolution of some representative pores with an average diameter of 42 nm. c) Macroscopic appearance of ultrathin membranes when floating on top of water in a stretched out fashion (upper) and when submerged in water (lower). e) AFM image at the edge of a membrane supported on flat silicon at low resolution where pores appear as small brown spots. The height profile was obtained along the white line. f) Higher magnification AFM image of a single pore and the corresponding height profile along the indicated track.

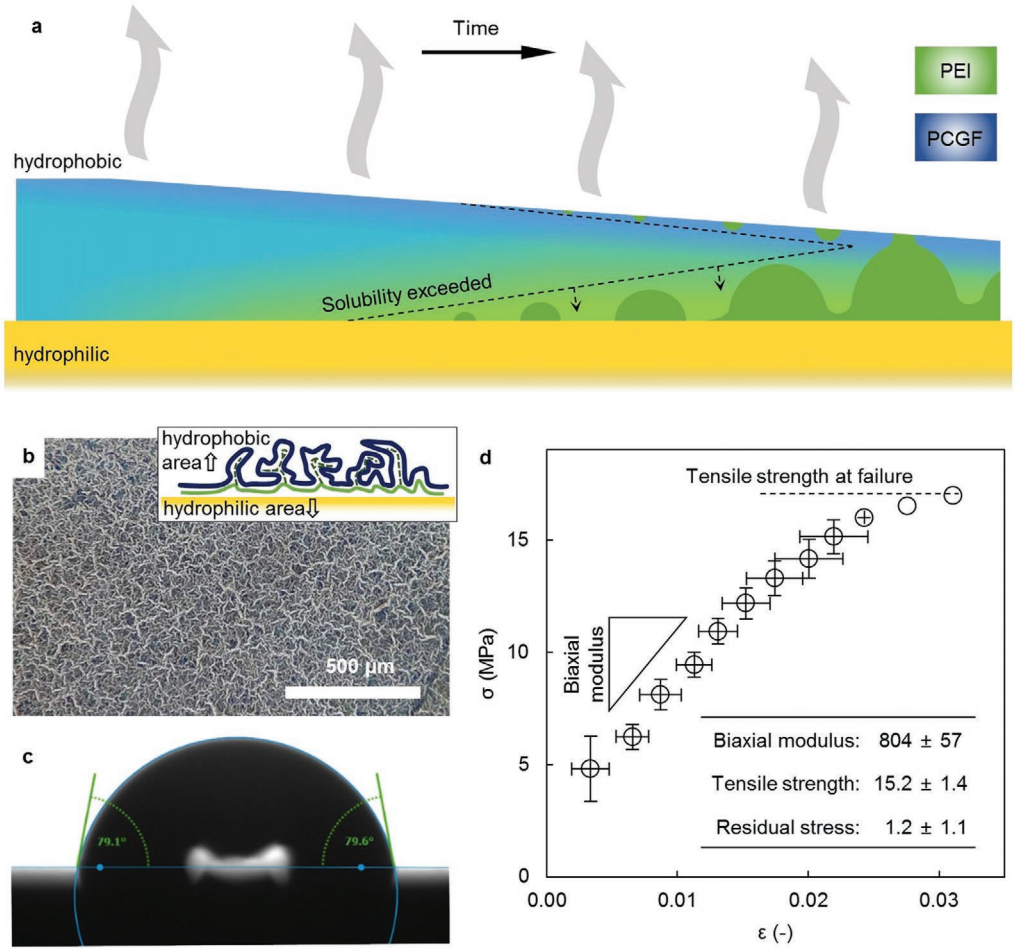

Figure 3. Suggested phase separation mechanism, membrane crumpling, mechanical properties, and contact angle. a) Illustration of the formation of a vertical concentration gradient leading to preferential phase separation of PEI at the bottom interface. The PEI-rich domains grow over time as the solubility boundary is shifting upward and the domains perforate the top surface. b) Microscopic image of a crumpled membrane on top of the sacrificial layer in a region appearing turbid and opaque on the wafer after incubation with chloroform. The inset illustrates how the surface area exposed to chloroform is increased for the more hydrophobic side and minimized for the more hydrophilic side by crumpling. Dashed lines indicate hydrophilic surface excluded from the solvent. c) Side view of a water droplet on the top surface of a membrane with estimated contact angles of roughly 79°. d) Stress–strain plot and corresponding estimated material parameters as determined by bulging with increasing hydrostatic pressure.

2.2. Membrane Morphology and Physical Properties

The ultrathin membranes can be delaminated in such a way (Step 5 in Figure 1a) that they conveniently float on the surface of water as visible for a membrane piece of roughly 3 × 3 cm in Figure 2c. They are self-standing on the water surface as well as under water where they adopt a slightly crumpled morphology. The membranes do not collapse or stick to themselves under water and when floating on the surface they do not show any irregularities. This suggests that both surfaces are hydrophilic. A membrane piece which was picked up onto a bare silicon wafer was investigated by atomic force microscopy (AFM) to estimate an average thickness of 75 nm (Figure 2e) at the ripped edge of the film. Scanning electron microscopy (SEM) investigations (Figure 2a,b) confirm a thickness in the range of tens of nanometers and that pores have been formed. The perforations are clearly visible at higher magnification (Figure 2d) and an average diameter of ≈42 nm was estimated from SEM images. From AFM analysis of pores that are large enough for the tip to penetrate, it is conceivable that they span through the entire membrane thickness (Figure 2f). This is further evidenced by a multitude of diffusion tests discussed below. Strikingly and unlike the top surface (the side facing the surrounding air during casting) which is quite smooth, the bottom surface shows a corrugated meander type structure.

This side of the membrane is in contact with the sacrificial layer during casting which is hydrophilic in contrast to air. It seems that the difference of interfacial properties, which the film is subjected to during casting, is responsible for the formation of these morphologies as schematically outlined in Figure 3a. We suggest that during coating, the hydrophobic moieties would preferentially migrate to the air-interface while more hydrophilic components accumulate at the bottom interface creating a concentration gradient of the two polymer species. This gradient would cause the solubility limit to be first exceeded at the bottom side initiating phase separation which

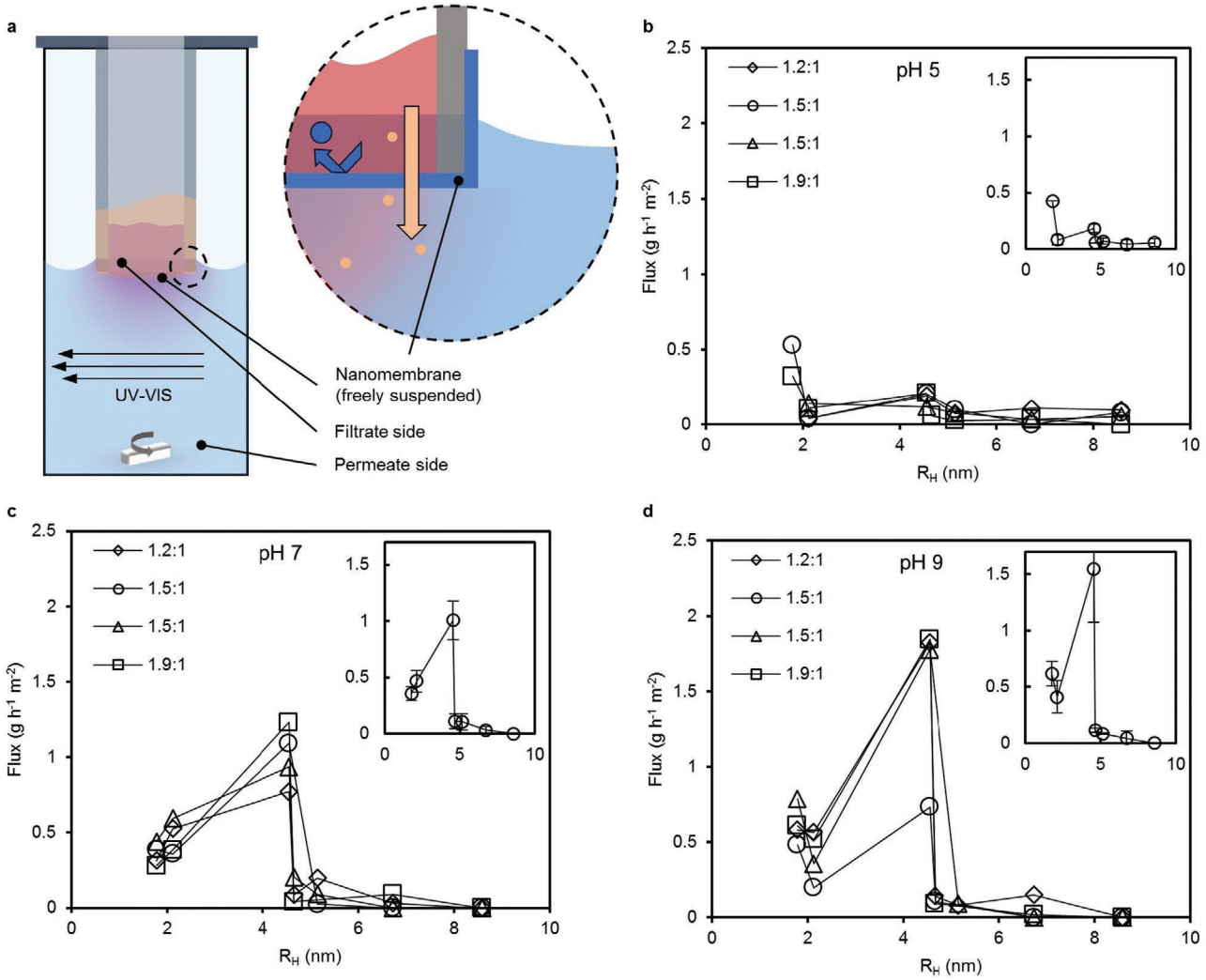

Figure 4. Diffusion experiments and mass transport of model proteins at different pH values. a) Schematic illustration of the photometric "diffusion cell" where the membrane-sealed tube containing filtrate solution is immersed in the permeate solution contained in a 1 × 1 cm quartz cuvette. A detail of the freely suspended membrane separating the two liquid reservoirs and the size exclusive permeation of different compounds is illustrated on the right side. b–d) Diffusive flux of model proteins with increasing hydrodynamic size across different membranes at various pH values. Insets are average values of all membranes. Membranes were produced with different precursor ratios as described in Section 4.

would then propagate to the other side as the film dries. At a later stage, phase separation also starts at the top surface so that top and bottom domains merge to perforate the entire film. This manifests in a difference in the length scale of the separated soluble domains with increasing size toward the bottom surface and explains the observed morphologies. Additionally, unmerged top surface domains would justify why some pores do not seem to be perforations but only depressions (indicated with arrows in Figure 2b) in the top surface. Further microscopic investigations of differently produced membranes revealed an influence of the coating parameters on the observed morphologies that falls in line with the proposed mechanism as discussed in Figure S1, Supporting Information. Finally, X-ray photoelectron spectroscopy (XPS) experiments were conducted on both sides of the membrane to investigate their elemental composition and potentially identify compositional differences (Figure S2 and Table S1, Supporting Information). Indeed, an apparent accumulation of nitrogen on the bottom side (8.2 at.%) with respect to the top side (1.8 at.%) was observed. Since PCGF is devoid of nitrogen, this strongly suggests that PEI accumulates at the bottom side during casting and corroborates the presence of a compositional gradient as a consequence of the proposed phase separation mechanism. Regardless of the underlying mechanism, these janus-type membrane properties with the distinctly different undulating bottom surface might be of considerable interest for applications in adherent cell culture,[21,22] cellular- and tissue barrier and coculture models[23] given the thickness of under 100 nm.

Furthermore, it was observed that some membranes seemed turbid and opaque on the silicon wafer after they had been treated with chloroform for pore template dissolution. Microscopic investigation revealed that this was accompanied and

probably caused by a morphology change where the membranes adopted a highly crumpled state (Figure 3b). This implies that the membrane was no longer firmly attached to the sacrificial layer and could slither on the surface to form such wrinkles. A PEI enriched layer adjacent to the sacrificial layer which is dissolved during chloroform treatment would justify this observation and is also consistent with the above hypothesis outlined in Figure 3a. The driving force could be the tendency to minimize the area of hydrophilic bottom surface that is exposed to chloroform as indicated in the inset of Figure 3b. This phenomenon should be studied more thoroughly since controlled crumpling could be utilized to significantly increase the active separation surface area and permeability of membranes. Such an advantageous effect has been demonstrated in the past for ultrathin solvent nanofiltration membranes.[24]

The assumption that the membranes are hydrophilic, based on membrane behavior within and on water, was corroborated by water contact angle measurements (Figure 3c). Both surfaces are slightly hydrophilic and in the range of polymeric materials that are routinely used for separations within biological fluids[25] and microfluidics.[26] Thus, the membrane material will be well suited for such purposes. An average of 79.4 ± 0.3 degrees for the top side and significantly lower 39.7 ± 2.2 degrees for the bottom side were observed, again coinciding with the notion of hydrophilic components accumulating at the bottom interface. However, since the smooth top surface is hydrophilic, a chemically identical rough bottom surface would be expected to display a reduced contact angle.[27] Thus, for the bottom side, an effective surface area four times that of the top side could account for the observed contact angles. Although such a large difference does not seem to be the case, it is worth noting that, at least to some extent, the hydrophilicity of the bottom surface is overestimated due to its roughness.

Bulging tests were conducted to estimate the mechanical strength and stiffness of the ultrathin films in freely suspended state. The bulging test procedure has been described in detail previously and experiments were carried out accordingly.[14] Briefly, for a bulging test, the membrane is unsupportedly spanning a hole of roughly 1 cm diameter and increasing hydrostatic pressure is exerted on the ultrathin film while the corresponding deflection is monitored to infer the resulting stress and strain.[28] From the relation of stress versus strain, the material parameters' ultimate tensile strength and biaxial modulus were estimated to be 15.2 ± 1.4 MPa and 804 ± 57 MPa, respectively (Figure 3). The low stiffness of the membranes despite covalent crosslinking is still in the MPa range and provides reasons for the high flexibility visible in Figure 2a,b without conceivable rupture or crack formation. This flexibility might be an asset which allows better contact between the membrane and a support structure and, in combination with its mechanical strength, lead to higher durability of separation devices.

2.3. Membrane Separation

The suitability of the membranes to separate proteins from larger particles was assessed with seven different model proteins with increasing molecular mass. The transport across the membranes has been tested in a diffusion cell as schematically depicted in Figure 4a. In this cell, the unsupported membrane separates the filtrate and the permeate side while the accumulation of protein on the permeate side is quantified by UV–vis spectroscopy (Figure S3, Supporting Information). The diffusive flux of the respective protein across the membrane was evidenced by an increase in absorbance over time or precluded by a stagnant spectrum (Figures S3 and S4, Supporting Information, respectively). Note that the mere observation of membranes which are completely tight for the diffusion of the smallest proteins (Figure S4, Supporting Information) confirms that diffusion of proteins can only be attributed to the presence of membrane spanning pores when membrane failure can be simultaneously precluded. The integrity of the membrane was validated in each experiment by evidencing the rejection of Blue Dextran (Figure S4, Supporting Information). The diffusion of the model proteins across several different membrane types was investigated in order to identify optimal conditions of fabrication and pore formation. The diffusion across the individual membranes was studied at three different pH values (Figure 4b–d) and a cutoff was localized around 6 nm hydrodynamic radius for all membranes for pH 7 and 9 (Figure 4c,d). Thus, if the ratio between pore size and molecular size is lower than 3.5 (42 nm vs 12 nm), we observed that the molecules are not able to traverse which is unexpectedly high. At pH 5, the diffusion of smaller proteins across the membrane was observed to be slower than at pH 7 and 9 (Figure 4b and Figure S5, Supporting Information). The chemical composition of the membrane material might be responsible for this interesting pH responsive behavior. Polyamines have been shown to act as proton conductors[29] and a swelling of the membrane material at acidic pH induced by the disruption of hydrogen bonds via incorporation of H^+ might cause the pores to shrink. Furthermore, positive charges accumulating at the membrane surface as free amino-groups get protonated, might increase electrostatic repulsion. The combination of these two effects could reduce the effective pore size significantly and explain such a difference in permeability. The charge of the proteins is also affected by the pH and alters their permeation behavior which is clearly visible for alcohol dehydrogenase. The mass transport rate is relatively high compared to the other proteins for pH 7 and 9. Once the pH falls below the isoelectric point (roughly pH = 5.6) the transport rate is greatly diminished since the protein will be overall positively charged and repelled by the membrane. A similar trend is present for the diffusion rates of myoglobin. On the other hand, cytochrome c has an isoelectric point of pH = 10 and an equivalent effect is not observable since the net charge would be positive at all tested pH values. A detailed tabulation of permeation rates at different pH, molecular diameter, and isoelectric point of the proteins is provided in Tables S2–S4, Supporting Information.

A clear trend of best conditions for membrane casting and pore formation is not conceivable from the conducted diffusion experiments with the differently produced membranes. It seems that variations within a certain range only change the amount of hydrophilic component accumulating at the bottom interface and do not alter the resulting morphology of the top surface. This dampening capability might impair the ability to adjust the resulting features such as the pore size to a certain degree. However, it shows that the protocol is robust enough

to tolerate small changes in polymer concentration without the loss of functionally significant morphologies. The size of the phase-separated features should be adjustable by the choice of PEI molecular size.[30] The diffusivity of the polymer molecules in the casting solution influences the size to which the phase separated domains can grow before the film has dried.

2.4. Dip-Coating

Spin-coating is a versatile technique to easily and quickly produce ultrathin layers and therefore widely adopted in several industries. Although it is well suited for the fabrication of membranes up to a size limit of some tens of centimeters in diameter and it is restricting scale up to larger lateral dimensions. Thus, it was very interesting whether the developed system could be migrated to a dip-coating setup which is typically more suited for large-scale or continuous casting. To this end, the whole procedure was directly applied to an approach which is using dip-coating as the thin film application technique (**Figure 5**a). As with the spin-coating process, a film of PSS was coated onto a rectangular silicon wafer piece and was used as the sacrificial layer for membrane casting. The substrate was then immersed in a bath of membrane casting solution and withdrawn at a constant speed. A thin liquid film is left on the substrate and the solvent evaporates at room temperature until a film of dry polymer remains (Figure 5b). The thickness of the initial liquid film is proportional to the speed at which the substrate is withdrawn and thereby directly influences the drying time and the thickness of the final membrane (Figure S6, Supporting Information). In the course of the drying process, phase separation phenomena which are similar to those occurring during spin-coating take place leading to isolated islands of soluble components (Figure 5b). After curing of the polymer network, these soluble islands could then be removed with chloroform to form a perforated thin film. By adjusting the coating parameters, withdraw speed, and final polymer concentrations, a procedure was established where robust perforated ultrathin films could be produced. Since the concept of fabrication remained unchanged, the ultrathin membranes could be released from the casting substrate as indicated in Figure 1a and the membranes were stable enough to be freestanding on the cm^2 scale (Figure 5b). The macroscopic appearance was strongly resembling the spin-coated membranes (Figure 5b) although it was generally more difficult to view them with the naked eye indicating a lower thickness. A thickness between 54 nm and 70 nm estimated from the high-resolution images (Figure 5g), corroborates the macroscopic observation. Pore sizes were

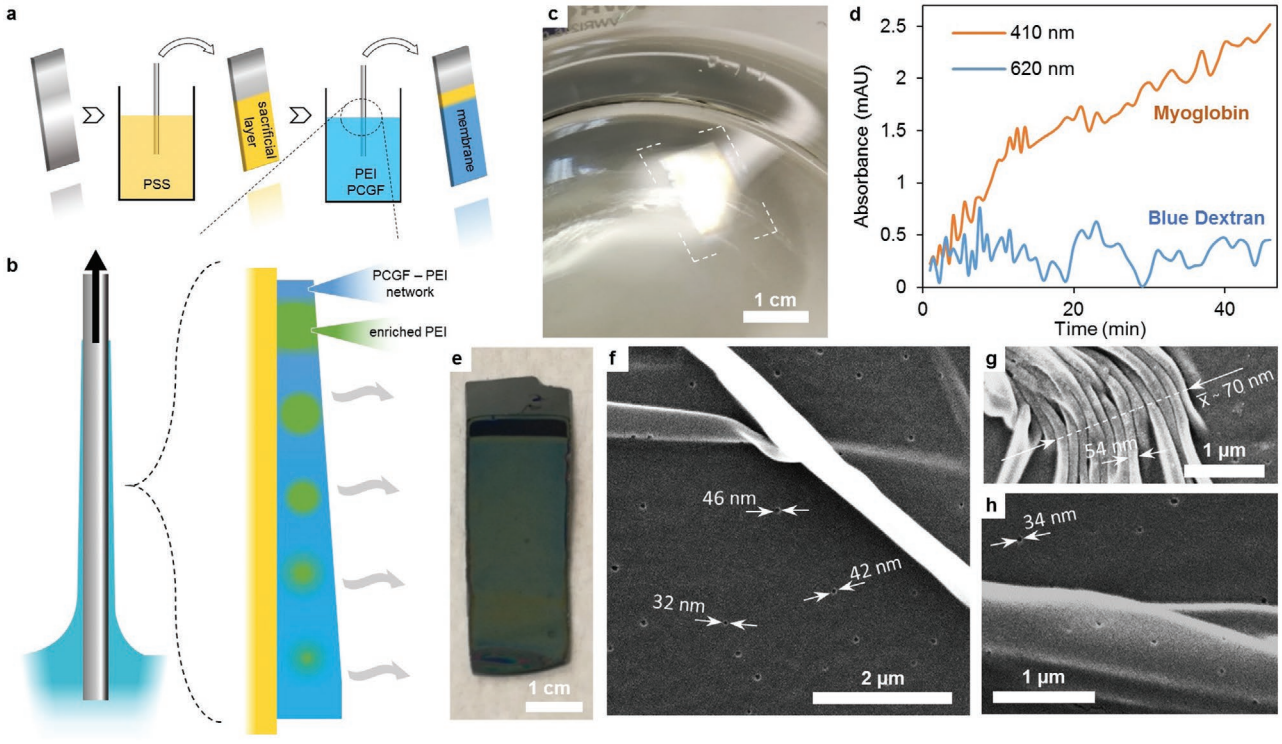

Figure 5. Summary of the dip-coating technique and characteristics of the corresponding membranes. a) Steps necessary for membrane casting on silicon wafer pieces starting with casting of the sacrificial layer, intermediate drying, coating of membrane polymer film, and final drying. The following steps are identical to those of spin-coated membranes. b) Schematic representation of the thin film formation and the associated phase separation into PEI-rich islands dispersed within a PCGF enriched membrane matrix. c) Picture of a freestanding membrane piece floating on the water surface with an area of roughly 2 cm^2. d) Absorbance of the permeate side at the indicated wavelengths during a diffusion experiment with myoglobin and Blue Dextran. e) Picture of a piece of silicon wafer dip-coated with a membrane on top of a sacrificial PSS layer. f–h) SEM images of membranes supported on flat silicon. Pores are visible as dark spots with an average diameter of roughly 39 nm and several diameters are indicated. A minimal thickness of 54 nm is estimated from one lamella in (g) while the maximum average thickness is 70 nm as estimated from 12 lamellae.

comparable to the ones found with the spin-coating process (Figure 5f–h) as determined from high-resolution microscopy where an average pore diameter of 39 nm was estimated. Interestingly, the membrane surface was markedly less uneven indicating a smoother bottom surface and also fewer pores were observable. Note that this accords with the hypothesized phase separation mechanism in combination with the lower observed thickness. Thinner films dry faster and the phase separated PEI-rich domains have less time to grow leading to a less rugged interface and fewer perforations. This would also rationalize the, albeit remarkably similar, but slightly smaller, observed pore size. To confirm that the membranes were truly perforated and the process had been successfully translated, the transport of myoglobin across dip-coated membranes was confirmed by diffusion tests (Figure 5d) in the photometric cell (Figure 4a). Since myoglobin has an absorbance peak of 410 nm, its exclusive permeation and the simultaneous rejection of Blue Dextran with an absorbance peak at 620 nm can be directly evidenced from the spectrum of the permeate solution (Figure S3, Supporting Information). While the absorbance of the permeate solution at 410 nm constantly rises with time, the absorbance at 620 nm does not deviate from the blank level (Figure 5d). Membranes where the pores did not penetrate the thin film were neither permeable for myoglobin nor for Blue Dextran (Figure S4, Supporting Information). These experiments confirm both, that the membranes with permeability toward myoglobin were intact without convective flow past the membrane and that pores of adequate dimensions to selectively separate the two species based on their size were perforating the ultrathin membrane. It should be noted that the employed small-scale and unsophisticated dip-coating setup only sufficed to produce several cm^2 of freestanding membrane. However, it should be possible to move the demonstrated concept to an industrial coating device with limited effort where such a technique could pave the way for nanomembranes to eventually change the industry.

3. Conclusion

A thermosetting epoxy resin and the immiscibility of its components can be used for the formation of nanometer scale perforations in membranes with a thickness of roughly 75 nm. The formed pores are roughly 40 nm in diameter and allow a selective separation of proteins based on their hydrodynamic size. However, the permeation behavior which could be expected from the estimated pore size distribution was not observable. Instead, it seems that the polymer network expands in aqueous environment and induces a certain degree of constriction. The charged nature of the membranes confers a certain selectivity which can be changed by pH, making them, in this respect, tunable and stimuli responsive. The difference in surface morphology makes these membranes potentially interesting for various fields of research and development. The accumulated PEI content at the bottom side hints toward the presence of amine groups and an associated possibility for covalent functionalization which would add another intriguing characteristic. It is conceivable that adjustment of pore size and number enabled by appropriate changes of the molecular weight of the precursors will allow for optimized and fine-tuned separation performance. Migrating the established spin-coating manufacturing process to a dip-coating approach may pave the way for such nanomembranes to enable high-performance bioseparations on a large industrial scale.

4. Experimental Section

Materials: HQ-H2O with a conductivity of 0.055 μS cm^{-1} was used for the preparation of all aqueous solutions. Bulk chemicals for buffer preparation, chloroform, polymers, and proteins were obtained from Sigma-Aldrich. The polymers were used as received without further purification. Poly[(o-cresyl glycidyl ether)-co-formaldehyde] (PCGF, Mn = 870) and branched polyethylenimine (PEI, Mn = 10 000) were dissolved in chloroform to final concentrations of (PCGF) = 20 mg mL^{-1} and (PEI) = 10 mg mL^{-1}. Chloroform was handled and added in appropriate amounts with a glass syringe as judged by weight on a balance assuming a density of 1.48 g mL^{-1}. The polymers were allowed to dissolve at room temperature for at least 30 min before they were filtered over PTFE syringe filters with a nominal pore size of 0.22 μm and stored in glass vials with PTFE screw caps. Chloroform used for the dilution of polymer solutions was also filtered over PTFE syringe filters with a nominal pore size of 0.22 μm. Poly(sodium 4-styrenesulfonate) (PSS, Mw = 70 000) was dissolved to a concentration of 50 mg mL^{-1} in water, filtered over PVDF filters with a nominal pore size of 0.45 μm, and stored in sterile Bio-One tubes from Greiner.

All protein solutions were prepared in Britton-Robinson buffer[31] adjusted to the respective pH. The proteins: cytochrome c, myoglobin, bovine serum albumin, and thyroglobulin were used as received. To remove impurities that would interfere with subsequent spectrophotometric tests, the formulations of apoferritin, alcohol dehydrogenase, and aldolase were purified before use. Apoferritin was purified by dialysis (Slide-A-Lyzer 10K MWCO, Thermo Fisher) overnight against a 1000-fold excess volume of target buffer. Alcohol dehydrogenase was purified by three 1:10 buffer changes in centrifugal filtration tubes (Amicon Ultra 15 50 kDa, Millipore). Aldolase was purified by 1:10 three buffer changes in centrifugal filtration tubes after (Amicon Ultra 0.5 100 kDa, Millipore). All proteins were dissolved in the respective buffer to a concentration of 1 g L^{-1}. Blue Dextran was dissolved to a concentration of 10 g L^{-1}.

Membrane Spin-Coating: Spin-coating was done with a WS650Mz-23NPP Spincoater (Laurell). Silicon wafers with 50.8 mm diameter served as solid casting substrates. They were cleaned with laboratory wipes, thoroughly rinsed with water to remove residual organic material and dried in a stream of nitrogen before they were immersed for at least 30 min in a 3:1 mixture of sulfuric acid and hydrogen peroxide (piranha solution) tempered at 60 °C. Note that care must be taken when preparing and handling this solution as it reacts violently with organic matter. After this treatment, silicon wafers were thoroughly rinsed with water. Thin films of PSS serving as sacrificial layers were formed by coating 300 μL of aqueous PSS solution at 3000 rpm. Ultrathin membranes were prepared by coating a mixture of PCGF and PEI solution (in chloroform) onto a previously and freshly produced sacrificial PSS layer at 5000 rpm. Casting solutions were prepared by mixing the precursor solutions at volumetric ratios leading to PEI:PCGF weight ratios of either 1.2:1 (67.5 μL PCGF and 165 μL PEI), 1.5:1 (60 μL PCGF and 180 μL PEI), or 1.9:1 (52.5 μL PCGF and 195 μL PEI). These mixtures were further diluted with 80 μL of pure chloroform and then used for spin-coating.

Membrane Dip-Coating: Dip-coating was done with pieces of silicon wafers which were clipped to be roughly rectangular and cleaned as described in the spin-coating section above. Dip-coated thin films were obtained by immersing the wafer pieces into the respective casting solution and vertically withdrawing at a constant pace. The customized dip-coating setup allowed adjustment of withdraw speeds between 10

and 400 mm min^{-1}. Sacrificial PSS layers were formed with the aqueous PSS solution and a coating speed of 15 mm min^{-1}. Membrane casting solutions were prepared with a PEI:PCGF weight ratio of 1.5:1 (volume ratio of 3:1) and diluted with chloroform by a factor of 1.25. Dip-coating was done by immersing wafers bearing a sacrificial layer at a speed of 100 mm min^{-1} to allow for proper wetting and withdrawing at 400 mm min^{-1}.

Curing, Selective Dissolution, and Membrane Release: After the ultrathin epoxy films had been cast using the respective method, covalent crosslinking of the resin was induced by heating the wafer to 120 °C for at least 5 min. The membranes were then allowed to cool to room temperature and rinsed two times with chloroform to selectively dissolve non-crosslinked domains of PEI for pore formation. After this production process, perforated nanomembranes could be detached from the casting substrate by dissolving the sacrificial layer in HQ-H2O. To ease membrane pick-up, the PSS layer was allowed to dissolve while the wafer was slowly immersed in a tilted way at roughly 30° so that the membranes are forced to stay atop the water surface. The membranes were cut to the desired shape with a scalpel while still on the wafer and prior to release.

Microscopy: Scanning electron microscopy images were obtained with a FEI QuantaTM 250 field-emission environmental scanning electron microscope with a Schottky field emission gun (FEI Europe B.V.) operated at 15 kV in a low-pressure atmosphere of $<1 \times 10^{-6}$ mbar. For imaging, membrane samples were picked up from the water surface onto small pieces of silicon wafer and left to dry before they were sputter-coated with a thin gold layer to avoid charge accumulation. Membrane samples for atomic force microscopy investigations were picked up onto silicon wafer pieces and dried in air before use. Imaging was done with a Nanowizard II atomic force microscope (JPK Instruments). SiN cantilevers DNP-S10 (Bruker) with a spring constant of 0.12 N m^{-1} and a nominal tip radius of 10 nm were used in contact mode in air. Images were obtained with a 512-line resolution and a line scan frequency of 2 Hz. Optical microscopy images were obtained with a stereomicroscope.

X-Ray Photoelectron Spectroscopy: Measurements were carried out on a Thermo Fisher Microlab 310/350-spectrometer equipped with a twin anode Al/Mg-Kα X-ray source (XR3) and a hemispherical analyzer. Samples were mounted onto the sample holders using double-sided carbon tape. A pass energy of 100 eV and an energy resolution of 1 eV were used (excitation energy: 1486.6 eV, beam power: 100 W, base pressure: 5×10^{-9} mbar, pressure during measurements: 9×10^{-9} mbar). All measurements were carried out over an analysis area of roughly 6×6 mm² with the sample in normal emission angle with respect to the analyzer. Data analysis was done using the CASA XPS and Thermo Fisher Avantage software packages employing Shirley/Tougaard backgrounds[32,33] and Scofield sensitivity factors.[34] Charge correction was applied to the spectra so the C 1s signal of adventitious carbon was shifted to 285 eV. The measurement accuracy is around 10–20% of the estimated values. Assignment of different components was primarily done according to refs. [35,36].

Contact Angle Measurements: Membrane pieces were carefully picked up onto silicon wafer pieces from the surface of water without any wrinkles and were allowed to dry in air. A DSA30 contact angle goniometer (Krüss) was used to obtain optical images of the contact angle formed between the membrane surface and 3 µL HQ-H2O droplets in air. Both observable contact angles of each image were evaluated from three independent droplets on the membrane.

Bulging Tests: The method we used to conduct bulging tests and the respective evaluation is described in detail in another article.[14] The membranes were picked up to be freely suspended over the circular opening of a 9.7 mm diameter tube. They were gradually pressurized until membrane rupture and the corresponding deflection was monitored and captured by a digital camera with image dimensions of 791×588 pixels and a resolution of 265 pixels mm^{-1}. Thin film stress and strain could be derived from the relation of pressure and corresponding deflection. From this relation, the ultimate tensile strength, residual stress, and biaxial modulus could be inferred.[28]

Diffusion Tests: The diffusion of proteins across the membranes was investigated in real time in a spectrophotometer. A plastic tube of 4.7 mm diameter was used to pick up membrane pieces so that one tube opening would be sealed by the ultrathin film. Forty-five microliters of the respective protein solution mixed with 5 µL of Blue Dextran solution were transferred into the tube by pipetting directly onto the surface of the freely suspended membrane. 960 µL of permeate solution were contained in a quartz cuvette with 10 mm pathlength. The tube was then inserted into the cuvette with the membrane and retentate solution side facing down so that the membrane would be immersed in permeate solution. In order to accommodate for the tube holding the membrane and the retentate compartment, the cuvette had to have a cross-section of 10×10 mm. UV–vis absorbance spectra of the permeate solution were then recorded every 30 s. The increase of absorbance at characteristic wavelengths per time interval and the respective molar extinction coefficient could be used to derive diffusive flux of protein across the membrane. In order for the edges of the membrane pieces not to be immersed and thereby preclude convective transport past the membrane, the fill level of the cuvette with permeate solution had to be adjusted accordingly.

Supporting Information

Supporting Information is available from the Wiley Online Library or from the author.

Acknowledgements

This work has been supported by the Federal Ministry for Digital and Economic Affairs (bmwd), the Federal Ministry for Transport, Innovation and Technology (bmvit), the Styrian Business Promotion Agency SFG, the Standortagentur Tirol, Government of Lower Austria and ZIT – Technology Agency of the City of Vienna through the COMET-Funding Program managed by the Austrian Research Promotion Agency FFG. The funding agencies had no influence on the conduct of this research. The authors want to thank the Analytical Instrumentation Center of the Technical University of Vienna for their support in conducting XPS experiments.

Conflict of Interest

The authors declare no conflict of interest.

Keywords

2D-materials, dip-coating, nanomembranes, phase separations, protein separations

Received: May 24, 2019
Revised: July 3, 2019
Published online:

[1] R. Semiat, J. Sapoznik, D. Hasson, *Desalin. Water Treat.* **2010**, *15*, 228.
[2] P. Marchetti, M. F. Jimenez Solomon, G. Szekely, A. G. Livingston, *Chem. Rev.* **2014**, *114*, 10735.
[3] Y. Zhao, Y. Xie, Z. Liu, X. Wang, Y. Chai, F. Yan, *Small* **2014**, *10*, 4521.
[4] X. Q. Cheng, Z. X. Wang, X. Jiang, T. Li, C. H. Lau, Z. Guo, J. Ma, L. Shao, *Prog. Mater. Sci.* **2018**, *92*, 258.

[5] J. L. Snyder, A. ClarkJr., D. Z. Fang, T. R. Gaborski, C. C. Striemer, P. M. Fauchet, J. L. McGrath, *J. Membr. Sci.* **2011**, *369*, 119.
[6] B. J. Feinberg, J. C. Hsiao, J. Park, A. L. Zydney, W. H. Fissell, S. Roy, *J. Membr. Sci.* **2017**, *536*, 44.
[7] S. Ling, K. Jin, D. L. Kaplan, M. J. Buehler, *Nano Lett.* **2016**, *16*, 3795.
[8] I. Vlassiouk, P. Y. Apel, S. N. Dmitriev, K. Healy, Z. S. Siwy, *Proc. Natl. Acad. Sci. USA* **2009**, *106*, 21039.
[9] M. Mireles, T. R. Gaborski, *Electrophoresis* **2017**, *38*, 2374.
[10] S. Walheim, M. Böltau, J. Mlynek, G. Krausch, U. Steiner, *Macromolecules* **1997**, *30*, 4995.
[11] S. Walheim, M. Ramstein, U. Steiner, *Langmuir* **1999**, *15*, 4828.
[12] E. B. Nauman, D. Q. He, *Polymer* **1994**, *35*, 2243.
[13] T. Kunitake, *Langmuir* **2016**, *32*, 12265.
[14] C. Schuster, A. Rodler, R. Tscheliessnig, A. Jungbauer, *Sci. Rep.* **2018**, *8*, 4410.
[15] D. P. Birnie, D. E. Haas, C. M. Hernandez, *Opt. Lasers Eng.* **2010**, *48*, 533.
[16] P. Mokarian-Tabari, M. Geoghegan, J. R. Howse, S. Y. Heriot, R. L. Thompson, R. A. L. Jones, *Eur. Phys. J. E* **2010**, *33*, 283.
[17] J. J. Miller, R. N. Carter, K. B. McNabb, J.-P. S. DesOrmeaux, C. C. Striemer, J. D. Winans, T. R. Gaborski, *J. Micromech. Microeng.* **2015**, *25*, 015011.
[18] H. B. Park, J. Kamcev, L. M. Robeson, M. Elimelech, B. D. Freeman, *Science* **2017**, *356*, eaab0530.
[19] H. Watanabe, T. Kunitake, *Adv. Mater.* **2007**, *19*, 909.
[20] A. Rodler, C. Schuster, E. Berger, R. Tscheließnig, A. Jungbauer, *J. Biotechnol.* **2018**, *288*, 48.
[21] A. Puiggalí-Jou, J. Medina, L. J. del Valle, C. Alemán, *Eur. Polym. J.* **2016**, *75*, 552.
[22] H. H. Chung, S. M. Casillo, S. J. Perry, T. R. Gaborski, *ACS Biomater. Sci. Eng.* **2018**, *4*, 222.
[23] R. N. Carter, S. M. Casillo, A. R. Mazzocchi, J.-P. S. DesOrmeaux, J. A. Roussie, T. R. Gaborski, *Biofabrication* **2017**, *9*, 015019.
[24] S. Karan, Z. Jiang, A. G. Livingston, *Science* **2015**, *348*, 1347.
[25] C. J. Van Oss, R. J. Good, M. K. Chaudhury, *Langmuir* **1988**, *4*, 884.
[26] S. Hu, X. Ren, M. Bachman, C. E. Sims, G. P. Li, N. Allbritton, *Anal. Chem.* **2002**, *74*, 4117.
[27] R. N. Wenzel, *Ind. Eng. Chem.* **1936**, *28*, 988.
[28] M. K. Small, W. D. Nix, *J. Mater. Res.* **1992**, *7*, 1553.
[29] Z. Yang, D. H. Coutinho, D.-J. Yang, K. J. Balkus, J. P. Ferraris, *J. Membr. Sci.* **2008**, *313*, 91.
[30] S. Walheim, E. Schäffer, J. Mlynek, U. Steiner, *Science* **1999**, *283*, 520.
[31] H. T. S. Britton, R. A. Robinson, *J. Chem. Soc.* **1931**, 1456.
[32] D. A. Shirley, *Phys. Rev. B* **1972**, *5*, 4709.
[33] S. Tougaard, *Surf. Interface Anal.* **1997**, *25*, 137.
[34] J. H. Scofield, *J. Electron Spectrosc. Relat. Phenom.* **1976**, *8*, 129.
[35] A. V. Naumkin, A. Kraut-Vass, S. W. Gaarenstroom, C. Powell, *NIST X-Ray Photoelectron Spectroscopy Database, Version 4.1,* **2012**, 10.18434/t4t88k.
[36] G. Beamson, D. Briggs, *J. Chem. Educ.* **1993**, *70*, A25.

Publication III

Supplementary Information

Supporting Information

for *Macromol. Mater. Eng.,* DOI: 10.1002/mame.201900321

Micro-Phase Separation within Epoxy Resin Yields Ultrathin Mesoporous Membranes with Increased Scalability by Conversion from Spin- to Dip-Coating Process

Christian Schuster, Jasmin Matzinger, and Alois Jungbauer*

WILEY-VCH

Supporting Information

Micro-phase separation within epoxy resin yields ultrathin mesoporous membranes with increased scalability by conversion from spin- to dip-coating process

*Christian Schuster, Jasmin Matzinger, Alois Jungbauer**

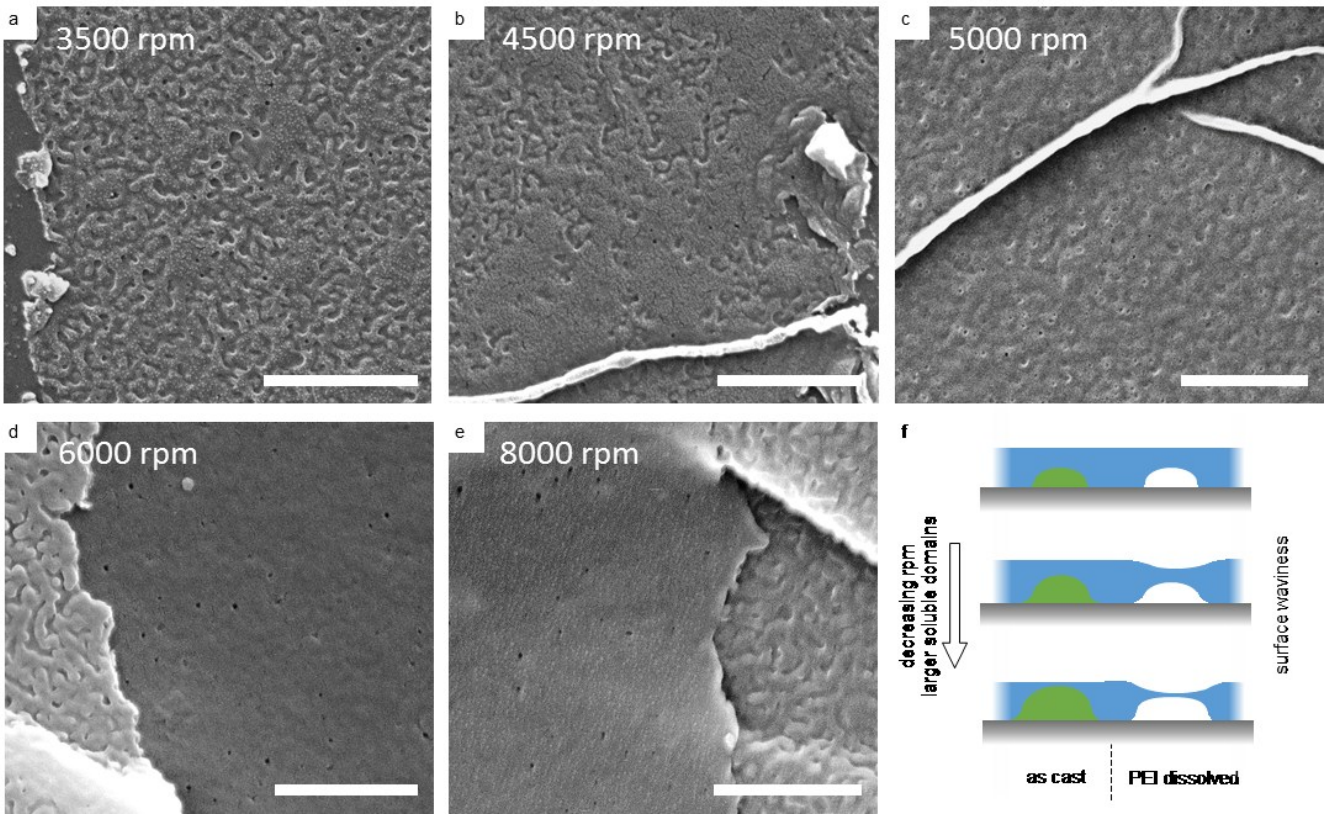

Figure S1:
Dependence of membrane morphology on spin-coating speed. SEM images in the upper row only show the top surface of the respective membrane while in the lower row also the bottom side is visible. Scale bars are 2 µm.

The thickness of spin-coated polymer films generally scales reciprocally with the spare root of the spin-speed[1]. In contrast to this, we observed that the films were more fragile and difficult to handle when cast at lower spin-speeds. Microscopic investigations (Figure S1) revealed that the morphology of the thin films is influenced by the coating speed. The structure of the bottom surface is increasingly imposed onto the top surface at lower coating speed. This implies that the domains of PEI, which leave these structures behind once dissolved, are larger and the remaining membrane matrix above these domains is thinner as illustrated in Figure S1 f. Thinner layers are less rigid and adjust to the underlying structures so that they become visible on the top side. Moreover, a lower thickness of the membrane between the thicker parts provides an explanation for the overall higher fragility of these films.

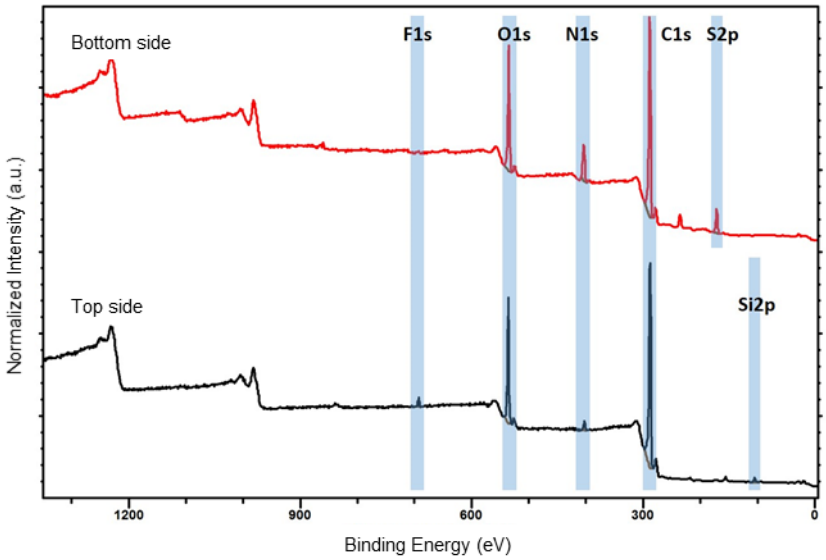

Figure S2: X-ray photoelectron spectroscopy (XPS) survey spectra obtained for both sides of a membrane produced by spin-coating. The areas of quantification are shaded in blue and the associated elemental orbital is indicated. The nitrogen-1s peak is markedly larger in the bottom side spectrum compared to the top side. The sulfur-2p peak is entirely absent in the top side spectrum. Refer to Table S1 for values obtained from a detailed evaluation.

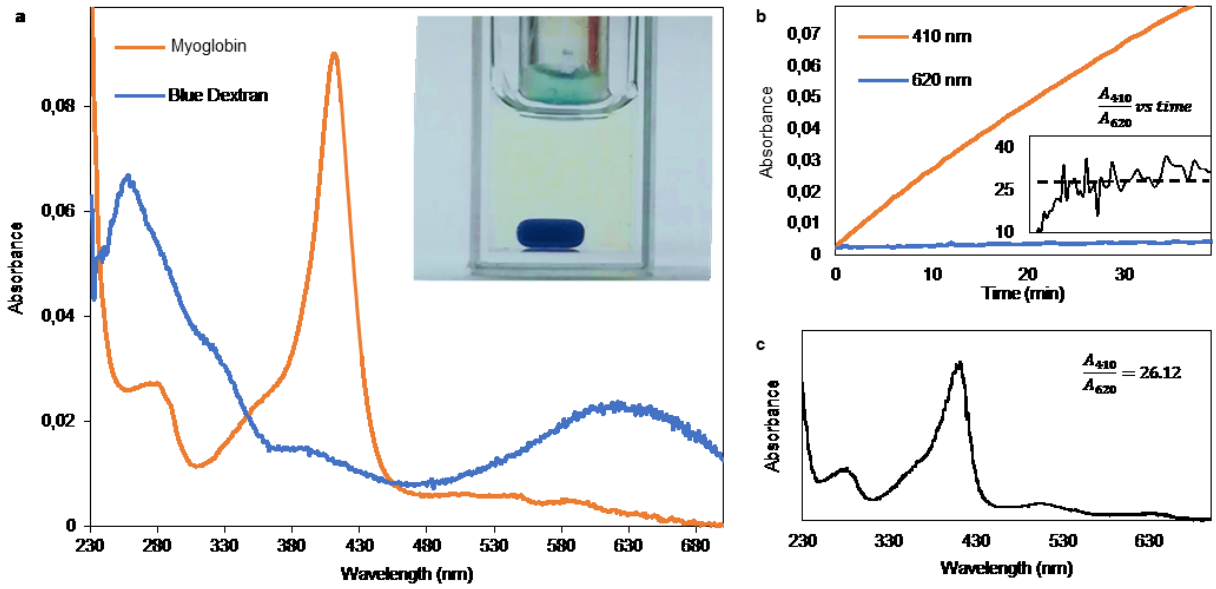

Figure S3: Diffusion test setup and exemplary data. (a) Absorbance spectra of the permeate side after 40 minutes and a Blue Dextran solution, respectively. The inset shows a picture of the diffusion cell with the two compartments separated by the ultrathin membrane. (b) Absorbance of the permeate side at indicated wavelengths over time. The inset is the evolution of the ratio between absorbance at 410 and 620 nm over time. The dashed line indicates this ratio for the pure protein. (c) Absorbance spectrum of the myoglobin solution without Blue Dextran with the ratio of absorbance at 410 vs 620 nm of the pure protein.

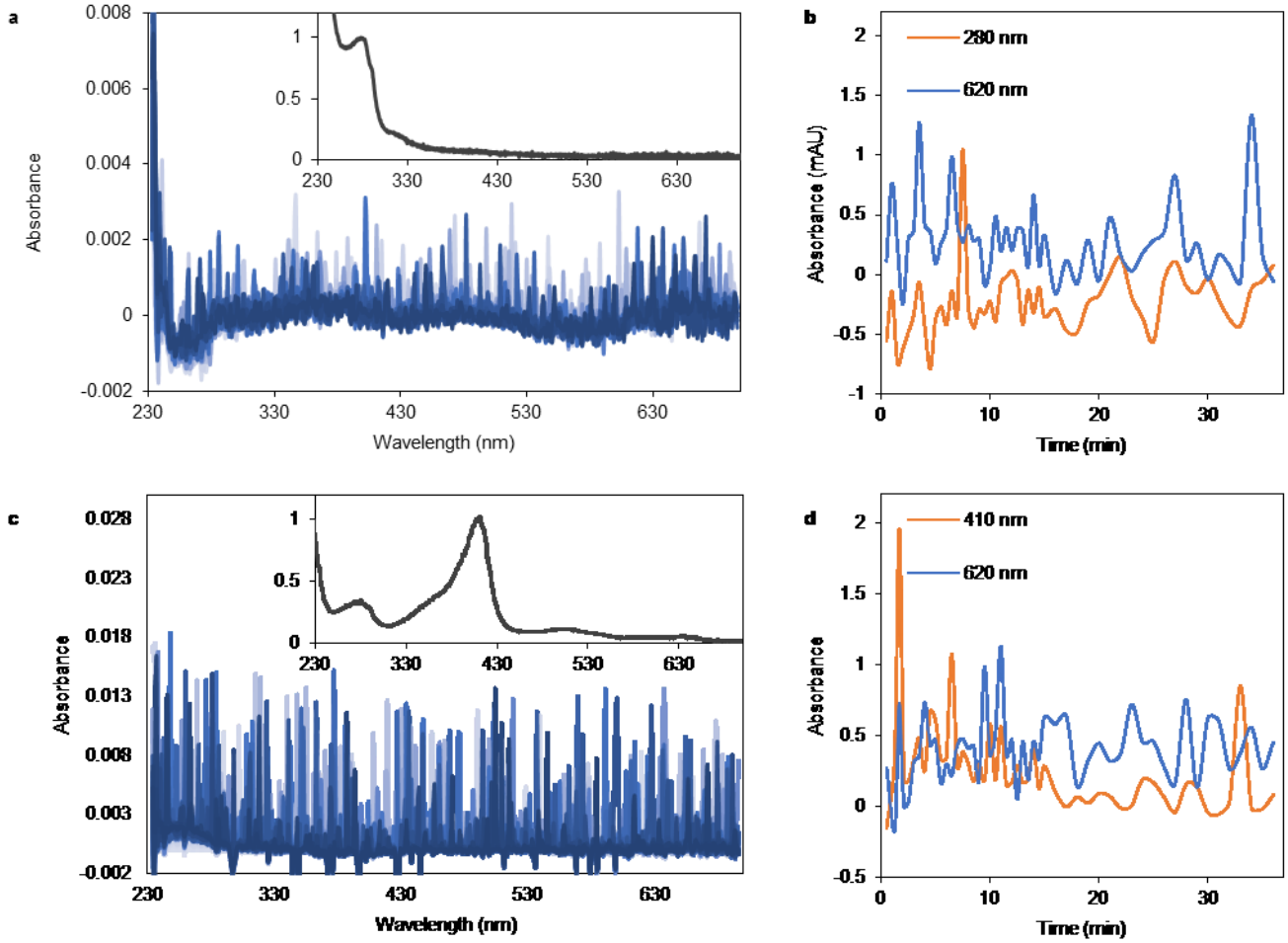

Figure S4: Diffusion tests of a non-perforated membranes. (a) and (b) Diffusion test of a of a non-perforated spin-coated membrane with thyroglobulin. (c) and (d) Diffusion test of a non-perforated dip-coated membrane with myoglobin. (a) and (c) Evolution of absorbance spectra of the permeate side with time (light blue at the start to dark blue at the end). The insets show the absorbance spectrum of thyroglobulin (a) and of myoglobin (c) for reference. (b) and (d) Absorbance at characteristic wavelengths vs time showing largely unchanged values.

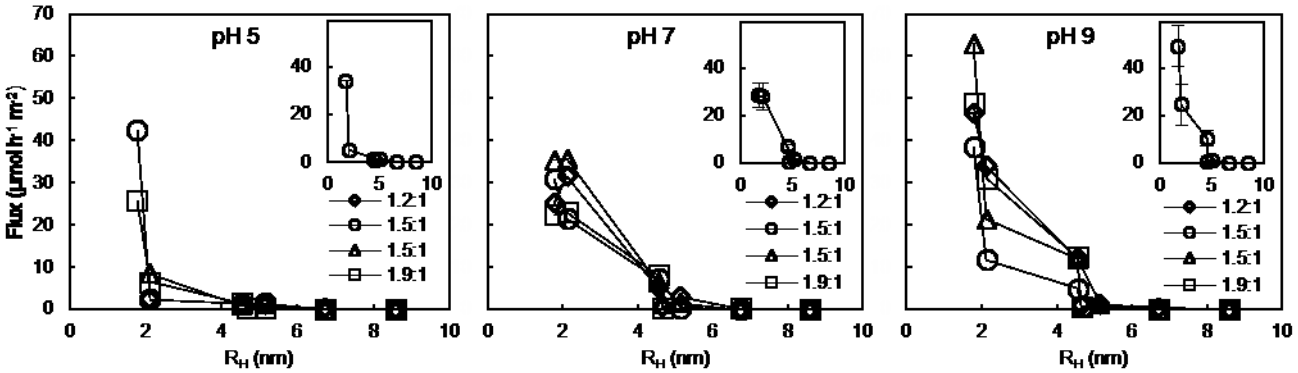

Figure S5: Diffusion of proteins across membranes at various pH values plotted as molar flux versus hydrodynamic radius. For the readers reference, complementary to Figure 4.

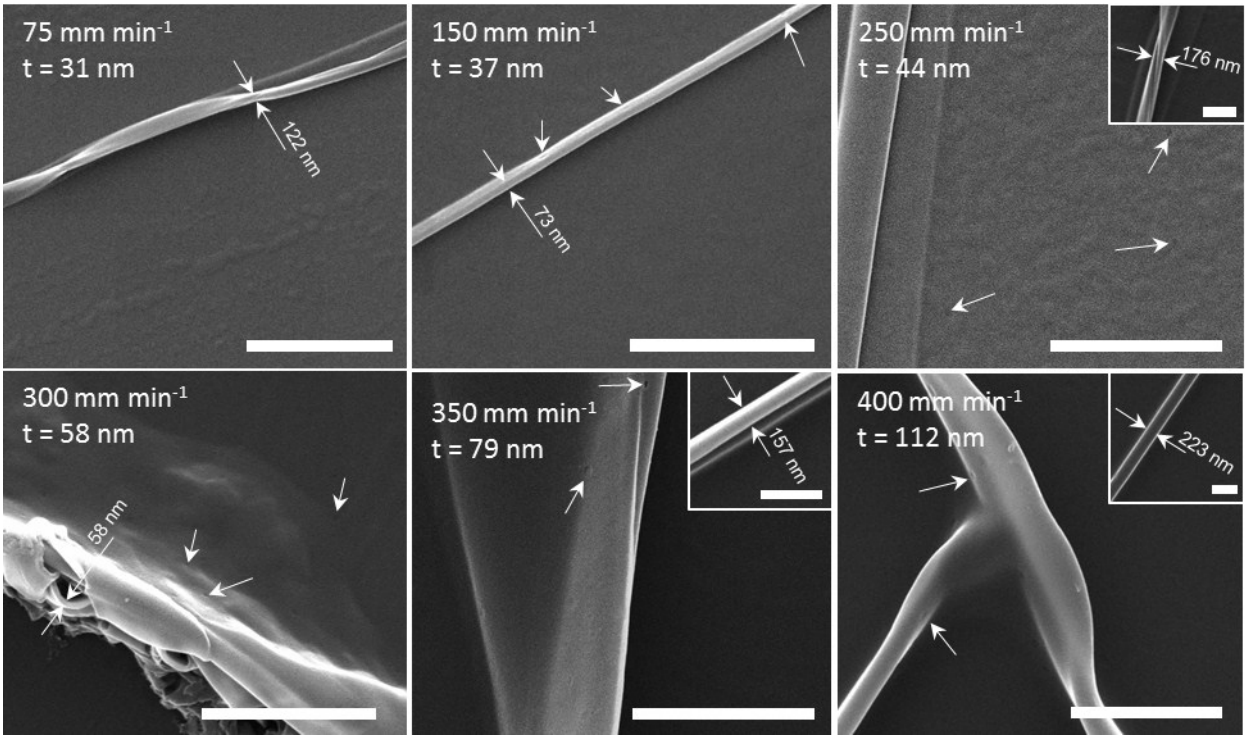

Figure S6: Membrane morphology and thickness dependence on withdraw speed during dip coating. Withdraw speeds and thickness (t) are indicated in the upper left corners. Arrows indicate where thicknesses were estimated from the membrane folds in the respective SEM image and where circular features are observable resulting from phase separation of PEI during casting. Scale bars of large images are 2 µm, scale bars of the insets are 500 nm.

The membranes in Figure S5 were cast with the dip-coating technique using non-optimized polymer concentrations. Therefore, the phase separation phenomena are not adequately adjusted and perforations that span the entire film are not formed. Interestingly and very subtly visible, starting with a withdraw speed of 150 mm min^{-1} circular features start to emerge as indicated by arrows. At increased withdraw speeds these circular features get more pronounced as the system starts with a thicker liquid film on the casting substrate and therefore has more time to undergo phase separation during drying.

Table S1: Elemental composition as deduced from XPS spectra in Figure S2.

Polymer side	Element (at.%)					
	C	F	N	O	S	Si
Top	81.81	0.53	1.83	13.90		1.93
Bottom	72.69	Traces	8.17	14.18	4.96	

The nitrogen content of the bottom side is markedly higher than at the top side (roughly 4.5 times). This indicates a higher concentration of PEI at the bottom side since PCGF does not comprise any nitrogen atoms. Interestingly, roughly 5 at.% of sulfur are present at the bottom side which could be attributable to PSS tightly adsorbing to the bottom side by interaction of the sulfate groups with the amine groups of PEI. This would also rationalize the high oxygen content at the bottom side: Since PEI does not contain any oxygen, we should observe a decreased content at the bottom side which is, however, not the case due to the presence of sulfate groups.

Table S2: Protein characteristics and average diffusion rates at different pH values.

Analyte	Size characteristics		Charge characteristics				Average transport rate ($g\ m^{-2}\ h^{-1}$)		
	MW (kDa)	R_H (nm)	IEP (pH)	charge at pH 5	7	9	pH 5	pH 7	pH 9
Cytochrome c	12.5	1.78	9.8	+	+	+/0	0.43	0.36	0.62
Myoglobin	16.7	2.12	6.85 / 7.33	+	+ / 0	-	0.08	0.47	0.41
Alcohol dehydrogenase	150	4.55	5.4-5.8	+ / 0	-	-	0.18	1.01	1.55
Aldolase	160	4.66	8.4	+	+	-	0.09	0.14	0.11
Bovine serum albumin	66	5.15[a]	4.9	0	-	-	0.04	0.09	0.09
Apoferritin	443	6.73	4	-	-	-	0.04	0.03	0.04
Thyroglobulin	670	8.58	4.5-5.0	0 /-	-	-	0.06	0	0
Blue Dextran	2000	26.89	7	+	0	-	0	0	0

[a] Hydrodynamic radius as reported for pH = 9 [2].

Table S3: Diffusion of individual proteins across different membranes. Membranes were prepared from casting solutions of different composition indicated as the reactive group ratio (reactive amines of PEI : epoxy groups of PCGF) of the precursors. Diffusion rates are given in g m^{-2} h^{-1}.

	ph 5				ph 7				ph 9			
Protein[a)]	1.2:1	1.5:1	1.5:1	1.9:1	1.2:1	1.5:1	1.5:1	1.9:1	1.2:1	1.5:1	1.5:1	1.9:1
cyt	n.d.	0.53	n.d.	0.32	0.31	0.39	0.44	0.28	0.58	0.48	0.79	0.61
myo	0.04	0.04	0.14	0.11	0.53	0.36	0.59	0.38	0.57	0.20	0.36	0.52
adh	0.19	0.21	0.12	0.21	0.77	1.09	0.94	1.23	1.82	0.73	1.78	1.85
bsa	n.d.	n.d.	n.d.	0.06	0.09	n.d.	0.20	0.04	0.14	0.11	n.d.	0.09
ald	0.07	0.10	0.08	0.02	0.20	0.02	0.09	n.d.	0.08	n.d.	0.09	n.d.
apo	0.11	0	0.03	0.03	0.03	0	0	0.09	0.15	0	0	0.02
thy	0.10	0.08	0.05	0	0	0	0	0	0	0	0	0

[a)] cyt = Cytochrome c, myo = Myoglobin, adh = yeast alcohol dehydrogenase, bsa = bovine serum albumin, ald = aldolase, apo = apoferritin, thy = thyroglobulin.

Table S4: Diffusion of individual proteins across membranes. Membranes were prepared from casting solutions of different composition indicated as the reactive group ratio (reactive amines of PEI : epoxy groups of PCGF) of the precursors. Diffusion rates are given in µmol m^{-2} h^{-1}.

	ph 5				ph 7				ph 9			
Protein[a)]	1.2:1	1.5:1	1.5:1	1.9:1	1.2:1	1.5:1	1.5:1	1.9:1	1.2:1	1.5:1	1.5:1	1.9:1
cyt	n.d.	42.41	n.d.	25.78	25.13	30.92	35.30	22.39	46.61	38.53	62.92	48.82
myo	2.33	2.31	8.46	6.42	31.55	21.54	35.60	22.98	33.92	11.83	21.28	31.03
adh	1.29	1.37	0.78	1.39	5.14	7.28	6.24	8.21	12.15	4.89	11.86	12.31
bsa	n.d.	n.d.	n.d.	0.35	0.54	n.d.	1.28	0.25	0.89	0.67	n.d.	0.58
ald	1.13	1.51	1.15	0.38	3.03	0.37	1.39	n.d.	1.22	n.d.	1.36	n.d.
apo	0.24	0	0.08	0.08	0.07	0	0	0.20	0.34	0	0	0.04
thy	0.14	0.12	0.08	0	0	0	0	0	0	0	0	0

[a)] cyt = Cytochrome c, myo = Myoglobin, adh = yeast alcohol dehydrogenase, bsa = bovine serum albumin, ald = aldolase, apo = apoferritin, thy = Thyroglobulin.

References:

[1] J. Danglad-Flores, S. Eickelmann, H. Riegler, *Chem. Eng. Sci.* **2018**, *179*, 257.
[2] J. J. Babcock, L. Brancaleon, *Int J Biol Macromol* **2013**, *53*, 42.

Publication IV

Metal-insulator transition, associated growth morphology and relations to surface free energy and reactivity of ultrathin sputtered metals on reticulated polymer thin films

Christian Schuster[1], Harald Rennhofer[2], Alois Jungbauer[1,2] and Rupert Tscheliessnig[1]*

[1]Austrian Centre of Industrial Biotechnology, Vienna, Austria,

[2]University of Natural Resources and Life Sciences, Vienna, Austria

ABSTRACT

Nanostructured metal assemblies on thin and ultrathin polymeric films enable many state of the art technologies and have further potential to revolutionize several additional fields where research is gaining momentum. Tailoring the structure-function relationship is of critical importance for the performance of these systems and finely tuned metallization of polymer surfaces based on rational design is still challenging. This is aggravated by the scarcity of systematic studies even for standard techniques such as magnetron sputter deposition. Here we studied the interplay of metal and polymer properties such as surface free energy and reactivity with emphasis on the influence of the sputtered metal on its electric conductivity and the resulting morphologies. *In situ* resistance measurements during DC magnetron sputter deposition of Ag, Au, Cu and Ni films on ultrathin covalently crosslinked polymer films collectively reveal metal-insulator transitions characteristic for Volmer-Weber growth. The substantially different nominal film thicknesses needed for the onset of percolation into a conductive network are correlated with the interfacial energy and the energy of adhesion which display a weak trend in accordance with expectations from ordinary wetting theory. A much clearer relationship of low thickness of percolation for more reactive metals falls in line with reported correlations for metals on inorganic substrates and represents an intuitive guideline. Grazing incidence small angle x-ray scattering experiments were performed at several points in the transition from isolated 3D clusters into a porous conductive network to get insight into cluster and film morphology. We use a novel approach to interpret the scattering data and extract detailed approximations of cluster geometries by transformation into real space pair distance distributions (PDD) and subsequent fitting of arbitrary shapes and arrangements by numerical PDD computation. The morphologies are discussed in view of the established parameters describing film growth behavior.

INTRODUCTION

A multitude of modern technologies rely on surfaces covered with nanometer sized metal structures or thin metal films most prominently optoelectronics, microelectronics, catalysis, energy conversion and storage, sensors and actuators and food packaging[1–4]. Also, emerging fields such as bio- and nanopore sensors[5,6], nanomedicine[7] and voltage-charging separations[8] rely on nanoscale metal structures. Many different phenomena such as surface plasmon resonance, surface enhanced Raman scattering, metal-enhanced fluorescence[9] and more are enabling these applications. A considerable portion of the above technologies is based on assemblies where the substrate in contact with the metal structure is polymer-based. Defined properties of the respective polymer-metal assembly are often crucial for functionality where the metal structure and morphology is often the dominant determining factor. However, the nature of the emergent structures varies considerably with the fabrication technique or process parameters[10,11] and the underlying processes are often not fully understood. Key properties of the final system drastically depend on the structure of the metal coating where it is either a prerequisite that the coating is electrically conductive or that the deposited metal is present in separated clusters of a certain (often nanometer) scale.

In the last decade, ultrathin polymeric materials with large lateral dimensions have attracted research attention owing to their often remarkable characteristics and potential applications in diverse fields of research and industry[12–17]. The potential applications overlap considerably with those of thin metal films in cases such as (bio-) sensors and actuators[13], microelectronics, energy conversion and storage[18], optoelectronics[19] and separations science[20,21]. Reticulated or covalently crosslinked polymer materials are particularly interesting owing to their high mechanical strength, dimensional stability and chemical and thermal resistance[22,23]. Additional functionality or robustness can be imparted by metallization of either the surface or the whole volume of the film. Again, the resulting properties depend strongly on the type as well as the morphology of the involved materials [24,25]. In any event, the presence of the covalent network is especially intriguing as it may prevent penetration of surface situated metal structures into

the polymer or migration of fillers within the polymer even above the glass transition temperature[25,26].

As a well-established process, physical vapor deposition and especially magnetron sputter deposition is used frequently[1] and in large scale[27] for the deposition of thin inorganic films. Within a low pressure atmosphere (typically Argon) a confined plasma is generated by a high potential and the ionized nuclei are accelerated towards the material source (target) to knock out atoms which then travel to the substrate and form a solid film there. Many processes, such as reemission, surface diffusion, implantation, bonding to the surface, coordination to existing clusters of sputtered material etc. are happening at the surface ultimately determining the shape and properties of the formed film. These kinetic processes and the implications for the emergent film characteristics when produced under clean ultrahigh vacuum conditions and on defined inorganic substrates are reasonably well understood[28].

For the more specific case of polymer-metal interfaces the limited amount of available literature has been extended in recent years partly due to the advent of portable microelectronics and the associated strive for lightweight and flexible electronics[1]. Describing and predicting the behavior of metal-polymer interfaces is aggravated by several circumstances such as, for instance, the intrinsically irregular shape and composition of the polymer surface. In general, however, polymeric materials possess a low surface free energy (SFE) as a result of low cohesion energy density. This can be rationalized by a low number of strong bonds as opposed to metals and metal oxides, which are more crystalline and have a high density of strong bonds. Therefore, from this surface energy mismatch and thermodynamic considerations metals are expected to and generally do poorly wet polymeric surfaces. The analogy of liquids wetting solids implies that the interfacial energy will be determining the shape of the droplets i.e. the metal clusters. Indeed, the difference in wetting behavior of gold sputter-coated on two different polymers has been inferred to correlate with the interfacial energy[29]. These results were substantiated by another study where a similar magnitude for the interfacial energy between gold and polymer was estimated based on geometries extracted from x-ray scattering

data[3]. Silver thin films have also been shown to exhibit markedly different growth morphology with respect to substrate surface energy[30].

On the other hand, metals can form transient or permanent bonds with the polymer surface upon adsorption[31,32]. Reactive metals tend to bond more readily and will thus have a reduced diffusion coefficient resulting in less tendency to accumulate in clusters and thereby, ultimately, better wetting[32]. For instance, more reactive metals evaporated onto several different polymers were shown to form interface morphologies strongly dependent on the nature of the metal[33]. Very frequently, however, metal coatings on polymers tend to evolve through different stages of non-layer-by-layer growth characterized by the presence of separated clusters that eventually undergo percolation to form a connected network where the holes are gradually filled during the transition into a continuous film.

A systematic study of different metal films growing on ultrathin covalently crosslinked polymer films by DC magnetron sputter deposition is presented in this article. In order to gauge and facilitate the predictability of the emergent structures the film growth behavior is related to readily accessible material parameters. The metal thin film formation of Silver, Gold, Copper and Nickel is studied by *in situ* resistance measurements where for all studied metals the resistance in the metal-insulator transition could be well fitted to the scaling law of an inverse swiss-cheese percolation mechanism with critical exponents in the range 1.25 - 1.36, close to theoretical predictions[34,35]. Thus, for all deposited metals a 3D island or Volmer-Weber growth mode can be presumed. Relations of the critical nominal film thickness of percolation (d_c) to the respective energy of adhesion estimated from surface free energies (SFE) of the sputter-coated metals were found to correlate very weakly. A much clearer trend with the standard heat of metal oxide formation ΔH_f^0, a textbook parameter and proxy for metal reactivity, is observed which can be rationalized intuitively so as to provide a valuable predictive guideline. Grazing incidence small angle x-ray scattering (GISAXS) experiments allowed detailed approximations of the involved cluster geometries. By applying a new method to deduce experimental pair distance distributions (PDD) to which numerically calculated PDDs of model clusters and

arrangements were fitted, we extracted geometric information. The models coincide well with the film growth behavior parameters obtained from established GISAXS analysis and might enable more profound predictions of metal nanostructures based on surface free energy and metal reactivity.

RESULTS AND DISCUSSION

Polymer surface and thin film growth:

For the investigation of metal film growth on a covalently crosslinked polymer surface an epoxy resin was used as an ultrathin film. Such 'nanomembranes' have been introduced as very robust polymer films in a free-standing fashion[22]. They were shown to retain their electrically insulating behavior for thicknesses down to 30 nm and can be fabricated to a sufficiently large scale with a facile spin-coating process. For this work, the polymer thin films were directly cast onto glass coverslips and covalent crosslinking was initiated at elevated temperature[22].

Metal thin films were deposited with a DC-magnetron sputter coater with Argon (99.999 %) as the sputtering gas at a pressure of 0.9 - 1.2 x 10^{-2} mbar. The nominal thickness (d) of the growing film was monitored with a quartz crystal microbalance. For the investigation of the resistance (R) of the thin films, *in situ* resistance measurements were conducted during sputter deposition (Figure 1a). To this end, the pristine polymer films were first sputter-coated with two 50 nm thick rectangular gold patches separated by a 4 mm gap (Figure 1b). These patches of gold served as electrodes and were contacted to an LCR-meter with copper wires. The ultrathin metal films were grown on a 4 mm wide strip between the two gold electrodes while the rest of the polymer surface was masked. This resulted in a 4 x 4 mm^2 thin film growing between the electrodes that is being measured for its resistance (Figure 1b and c). The growth rate was maintained within 0.06 – 0.08 nm sec^{-1} for all metals by adjusting the potential and the resulting plasma current.

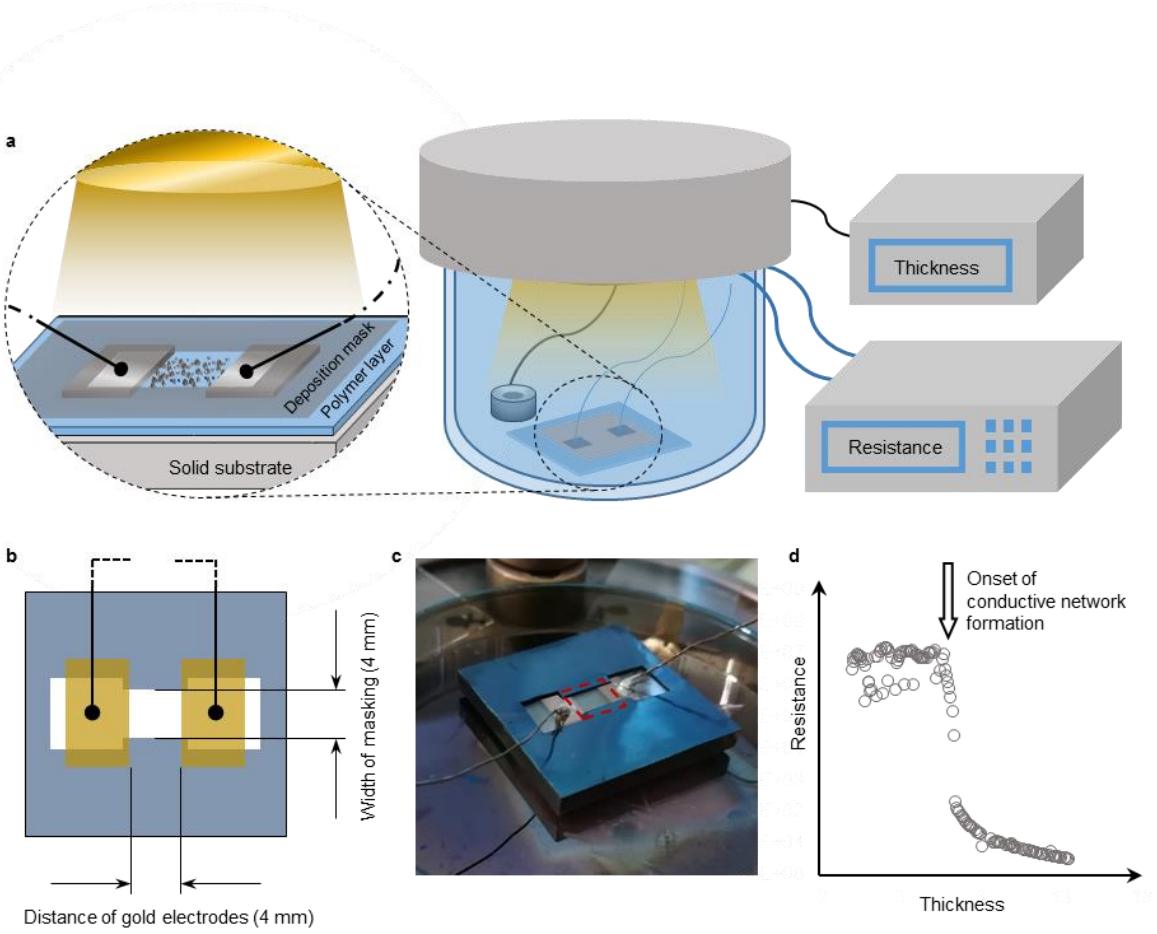

Figure 1. *In situ* resistance measurement setup. a) Schematic representation of the general setup (right side) with a detailed representation of the sampling area. b) Geometry of the growing film between the gold electrodes confined by the masking. c) Optical image of a contacted sample sitting on the sample stage. The 4 x 4 mm area of measured thin film is indicated by a red dashed rectangle. d) Typical results obtained by relating the resistance to the thickness both measured *in situ*.

The resistance was thereby obtained directly as sheet resistance ($R_{\square}$, Ohm per square) and correlated to the corresponding nominal film thickness for each experiment as in Figure 1d. For each metal, two experiments were conducted (Figure 2) and the resulting metal insulator transition in the R vs d relation was fit to the function

$$R_{\square} = A * (d - d_c)^{-t} \text{ (Equation 1)}$$

where d_c is the critical thickness, t is the universal critical exponent and A is a constant of proportionality. The resulting parameters are summarized in Table 1.

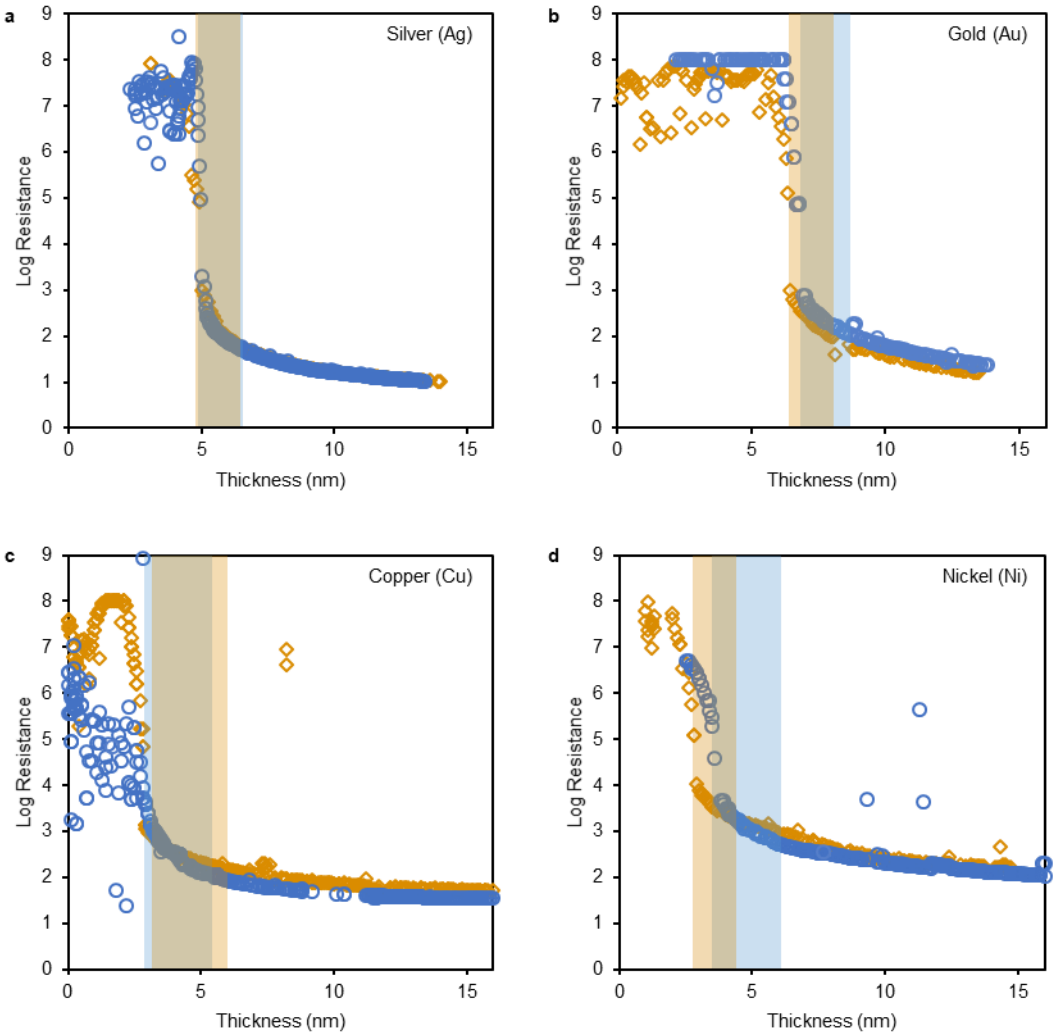

Figure 2. Results of *in situ* resistance measurements plotted as resistance versus nominal film thickness. Regions where equation 1 was fit to the data are shaded in the respective color.

All transition regions (as marked by the shaded areas in Figure 2) could be fitted reasonably well to the above relation and the critical exponents were found to range from 1.24 to 1.37, which is in close proximity to theoretical predictions (1.34)[34] and experimental values of model percolation systems (1.29 and 1.34)[36]. These systems are characterized by the growth of conducting entities (clusters) on a non-conducting plane or in a non-conducting space which undergo percolation to form a conducting network. This is equivalent to metal clusters growing on a non-conducting substrate.

Table 1. Critical thickness of percolation and critical exponents found for *in situ* resistance measurements.

Metal	d_c (nm)	t
Gold	6.16 ± 0.05	1.32 ± 0.01
Silver	4.82 ± 0.03	1.27 ± 0.03
Copper	2.47 ± 0.15	1.31 ± 0.06
Nickel	2.94 ± 0.33	1.30 ± 0.01

Thus, the acquired data indicate that in all experiments the thin film formation progressed from nucleation of clusters to a stage of coalescence and through the percolation into a conducting network to a final uniform film (Volmer-Weber growth). Note the fluctuating values of high resistance before the onset of conductivity in the low thickness regions. This conductivity can be attributed to the plasma which is present in the deposition chamber as these low resistances were only observable during the deposition and no conduction was observable when the deposition was interrupted.

Wetting, Percolation and Surface free energy:

For thin metals applied to inorganic substrates in low pressure atmosphere a thermodynamic argument can be made to estimate the degree to which the metal wets the surface[28]. The picture is equivalent to the theory describing the wetting of surfaces by liquids where the surface free energy (SFE) and the interfacial energy between the involved phases determine the extent of spreading of the liquid on the surface. These material parameters have been tabulated in great detail for most metals and their behavior on defined inorganic surfaces has been studied extensively. The surface free energy is arguably a very suitable choice as a material characteristic to correlate with the observed onsets of conduction and thin film growth in general. Indeed, a difference in surface free energy behavior of the coated surface has been linked to a change in growth behavior[29,30,37].

For the polymer surface it stands to reason that the SFE is regarded and estimated separately, due to the inherent inhomogeneity and in view of the specificity of the fabrication and testing conditions. To this end the static contact angle method has been applied here in conjunction with the by Good-van Oss-Chaudhury theory. Using the test liquids Water, Glycerol and

Formamide and solving the resulting three equations simultaneously[38] a value of γ_P = 25.4 mJ m^{-2} (γ_P^{LW} = 21.4 mJ m^{-2}, γ_P^+ = 1.3 mJ m^{-2}, γ_P^- = 3.2 mJ m^{-2}) for the SFE of the polymer was estimated (SI section 2 and Table S 1).

Furthermore, it might be similarly worthwhile to question whether the surface free energy of the bulk metal is an adequate measure to be related to the experimental polymer SFE values. On the one hand, SFE values are very prone to fluctuations (e.g. different laboratory, operator, etc.) and are therefore notoriously difficult to reproduce and compare. Therefore, values obtained in a self-consistent manner under similar conditions for all involved materials will be strongly favorable. On the other hand, it is intuitive that, compared to the bulk metal, the sputtered metal will be well relaxed due to surface diffusion and will therefore have a lower surface free energy. Indeed, by applying the same methodology as for the polymer surface, SFE values for the sputtered metals have been estimated as shown in Table 2 and are found to be substantially lower than values reported for bulk metal. Note that the contact angle values were obtained immediately after sputter deposition to keep surface contaminations minimal. We found significant drift of the contact angles when obtained after extended exposure to ambient atmosphere presumably due to airborne organic contaminants (compare Table S 1 and S 3). SFE values obtained for gold are of the same order of magnitude as those found by Ruffino et al.[29] whereas for the other elements we found no references reporting values on sputter-deposited metal surfaces. Using the relation

$$\gamma_{M/P} = \left(\sqrt{\gamma_M^{LW}} - \sqrt{\gamma_P^{LW}}\right)^2 + 2\left(\sqrt{\gamma_M^+ * \gamma_M^-} + \sqrt{\gamma_P^+ * \gamma_P^-} - \sqrt{\gamma_M^+ * \gamma_P^-} - \sqrt{\gamma_P^+ * \gamma_M^-}\right) \quad \text{(Equation 2)}$$

the interfacial free energy between the polymer surface and the sputtered metal ($\gamma_{m/p}$) was estimated from their respective SFE. Additionally, according to the following relation the corresponding adhesion energy (E_{adh}) can be estimated[28]:

$E_{adh} = \gamma_M + \gamma_P - \gamma_{M/P}$ (Equation 3).

The values estimated for the different metal-polymer pairs are listed in Table 2.

Table 2. Estimated surface free energy components, interfacial energy ($\gamma_{M/P}$) and adhesion energy (E_{adh}) for the polymer surface and the respective metal.

Surface	γ	γ^{LW}	γ^{+}	γ^{-}	$\gamma_{M/P}$	E_{adh}
	(mJ m^{-2})					
Polymer	25.4 ± 0.7	21.4 ± 0.4	1.3 ± 0.3	3.2 ± 0.2		
Ag	33.0 ± 1.3	23.1 ± 0.6	4.6 ± 0.6	5.5 ± 0.5	0.8 ± 0.7	57.6 ± 1.1
Au	31.1 ± 2.2	16.8 ± 1.3	3.4 ± 1.2	14.8 ± 1.2	0.6 ± 0.9	56.0 ± 1.0
Cu	41.3 ± 2.0	15.7 ± 0.9	6.0 ± 0.8	27.4 ± 0.8	5.7 ± 1.6	61.0 ± 0.3
Ni	46.2 ± 0.4	20.8 ± 0.2	7.2 ± 0.2	22.2 ± 0.1	6.4 ± 0.9	65.2 ± 0.1

In Figure 3a both parameters ($\gamma_{m/p}$ and E_{adh}), when plotted versus the critical percolation thickness, reveal a trend of decreasing energy with increasing thickness of percolation. Better wetting is expected for interfaces with higher energy of adhesion, since it reflects the work needed to separate the interface whereby higher values represent better adhesion. The estimated values for E_{adh} show a slight trend in accordance with this expectation. However, this correlation is very weak compared to the absolute values and might be regarded as to lie within the estimation uncertainty. According to Equation 2 the interfacial free energy $\gamma_{M/P}$ influences the work of adhesion so that this parameter is expected to correlate with the wetting behavior as well. Indeed, in terms of d_c the wetting behavior displays a pronounced trend with the interfacial free energy. However, the expected correlation would be that interfaces with higher free energy are less favorable and better wetting would be predicted for low energy interfaces which is the opposite trend as observed. Nevertheless, the values of the interfacial free energies are quite small compared to the surface free energy of the involved materials so that its influence on E_{adh} remains limited.

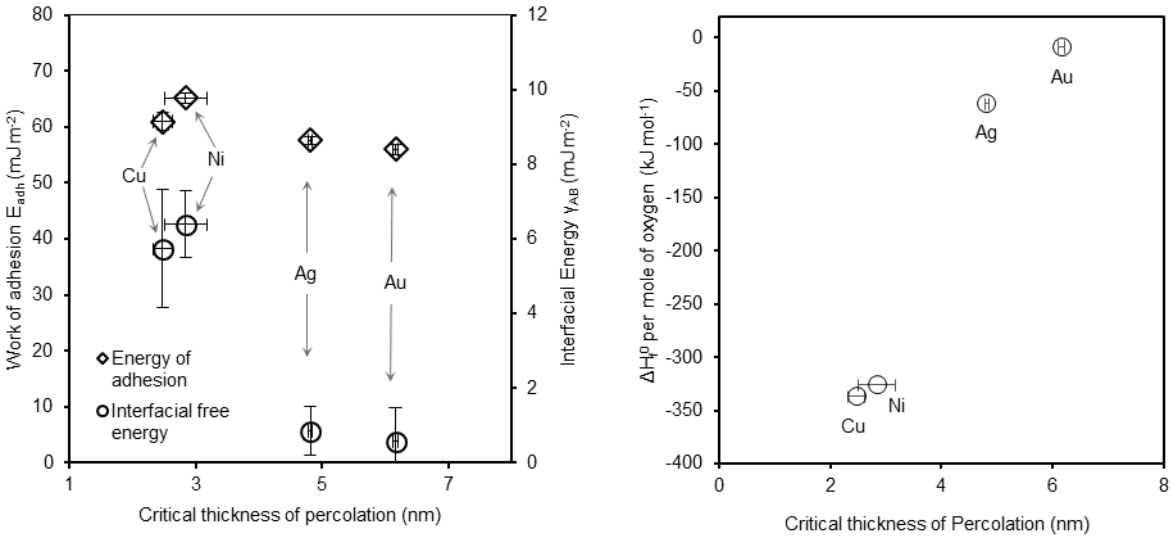

Figure 3. Plots of (a) energy of adhesion (E_{adh}), interfacial energy ($\gamma_{P/M}$) and (b) standard heat of metal-oxide formation (ΔH_f^0) per mole of oxygen versus critical thickness of percolation (d_c) for the investigated elements as indicated.

Reactivity:

Metal adatoms that impinge on the polymer surface might form bonds and thereby fix their location and prohibiting surface diffusion. Thereby cluster formation and coalescence will be diminished depending on the strength of the bond. It has been shown that metals can induce decomposition of the polymer[33] and strong bonds are formed even in non-reactive systems[39]. In consequence, it is intuitive that more reactive metals tend to form more defined interfaces and reach percolation earlier unless the growth does not proceed in a layer-by-layer fashion to begin with. As a measure of reactivity, the standard heat of formation (ΔH_f^0) of the respective most stable metal-oxide as found in textbooks[40] and plotted versus d_c in Figure 3b. A strong correlation can be observed where metals exhibit lower critical percolation thicknesses with increasing reactivity. Note that this observation is intuitive since interfacial bonding should decrease the mobility of metal adatoms and clusters which, in turn, reduces the ability to coalesce into larger particles and thereby lets the film undergo percolation at an earlier stage. The reactivity parameter used here was also reported to show correlations on selected inorganic substrates but broke down severely for others[28]. Thus, an extensive study covering more metals ideally on different polymer surfaces could help to verify the reliability and shed light onto the

dependencies of this relationship providing valuable information and guidance for the design of polymer-metal interfaces.

Cluster and Film Morphology:

The wetting behavior and onset of conduction will be tightly linked to the geometry of the metal structures present during growth. Furthermore, the number, size and geometry of the metal clusters is of vital importance for the emergent catalytic[41,42] or optical properties [43]. In order to get insight into the involved geometries grazing incidence small angle x-ray scattering (GISAXS) experiments of the metal thin films were performed at various different thicknesses.

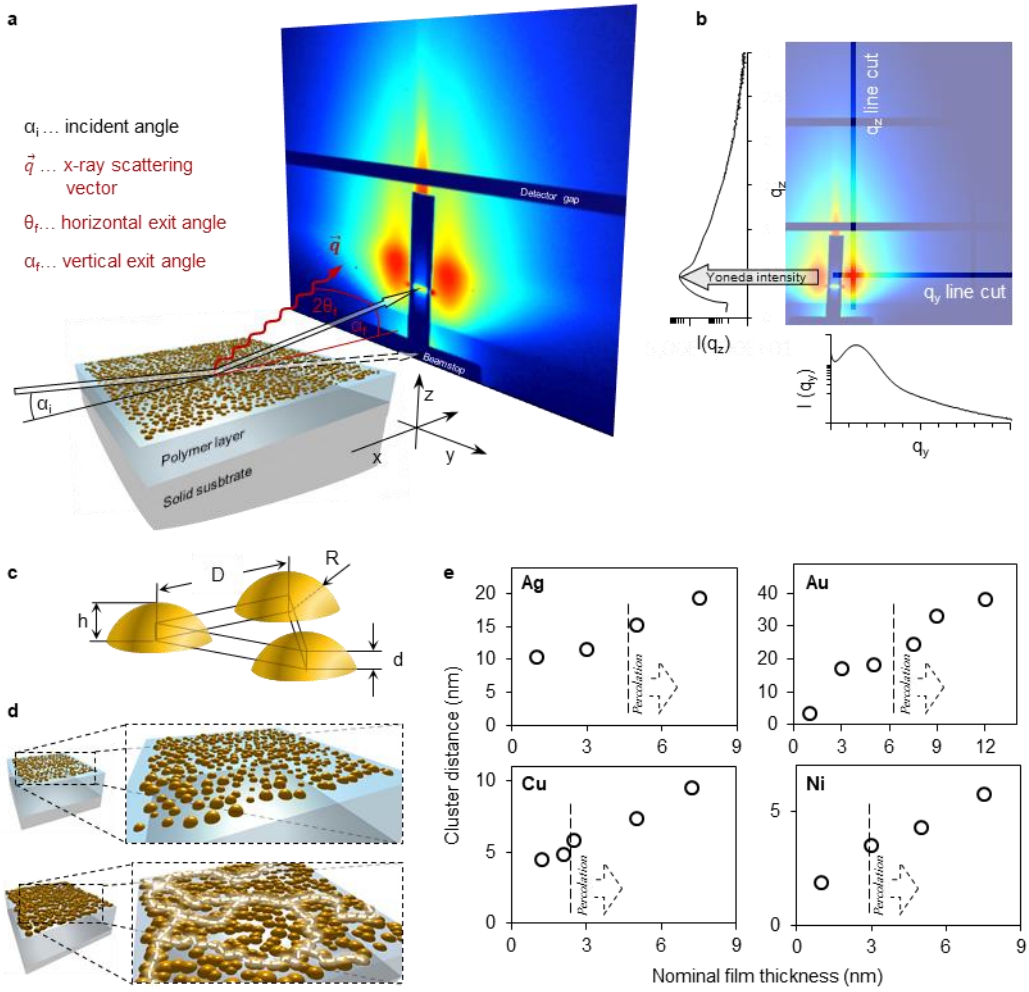

Figure 4. GISAXS experimental setup with line cuts, approximate cluster geometries and characteristic cluster distances. a) Schematic representation of the experimental setup used to obtain 2D x-ray scattering patterns at grazing incidence. b) Example of a 2D scattering pattern where the positions of cuts along the y- and the z-axis are indicated while the resulting

scattering curves are plotted below and left of the pattern, respectively. The position of the Yoneda intensity, the z position where cuts along the y-axis are made, is indicated. c) Schematic representation of an idealized equilateral triangular unit cell of spherical cap shaped clusters. d) Conceptual progression of isolated clusters of metals percolating into a conductive network. Sufficient disorder results in irregularly shaped clusters and the formation of conductive paths as indicated by white dashed lines. e) The distance estimated by Kratky analysis from the prominent scattering features caused by the interference function of the cluster arrangement plotted versus the nominal thickness for all GISAXS investigations. The respective metal is indicated in the upper left corner. The respective percolation threshold and onset of conduction is indicated.

A conventional experimental setup (Figure 4a) was used to obtain 2D scattering patterns of the metal coated polymer films. The diffuse out of plane scattering intensity as a function of the scattering vectors along the y-axis at the Yoneda intensity[44] (Figure 4b) contains information of the lateral sample morphology (q_y-cuts). As established above by the thickness-resistivity behavior the investigated metal coatings are progressing from isolated metal islands towards continuous films. The observable characteristic features of the scattering curves (maxima or shoulders, see Figure S 4) can be ascribed to the interference function of the clusters as they are arranged on the surface with a certain degree of order. To extract geometric information about the isolated clusters on the surface it is very common to approximate their assembly with a hexagonal lattice. This can be simplified to an equilateral triangular unit cell (Figure 4c). Given sufficient size and disorder of the metal clusters it is conceivable that they will eventually percolate to form a conductive network well before a close packed arrangement is established (Figure 4d). Moreover, metal clusters that are not entirely (hemi) spherical in shape but display an elongated or frayed shape an earlier onset of percolation might be expected. However, in spite of a certain disorder, for such an arrangement of clusters a characteristic average distance D to the nearest neighbor can be readily analyzed from Kratky plots of the q_y-data[45] (Figure S 2). The q_y-positions of Gaussian functions fit to the peaks give

an estimate of the average cluster distance D (Figure 4c). Furthermore, this estimated cluster distance can be utilized to discriminate between different growth regimes based on its rate of change with nominal thickness[19,37,46,47]. The evolution of this parameter for each metal (Figure 4e) can be interpreted to be subject to such a change. As indicated, the transitions to another rate of change coincides, most notably for copper and gold, with the onset of percolation at the critical thickness d_c. In fact, an additional transition should be visible for the crossover from nucleation to coalescence[46] at low nominal thicknesses which is, however, not resolved by the present investigations.

In order to estimate cluster structures and arrangements in detail without the restrictions of applying a generic geometric form factor we put forward a novel approach using the pair distance distributions (PDD), the real-space equivalents of the scattering curves[48]. PDDs which adequately represent the data were found by fitting the scattering signal reconstructed from the PDD to the experimental q_y-cuts (SI section 4, Figure S3 and S4). These experimental PDDs were then used to generate detailed approximations (Figure 5) of cluster shape, size and their arrangement on the surface by comparing and fitting (SI section 7) calculated PDDs of different geometries to the experimental data (SI section 8).

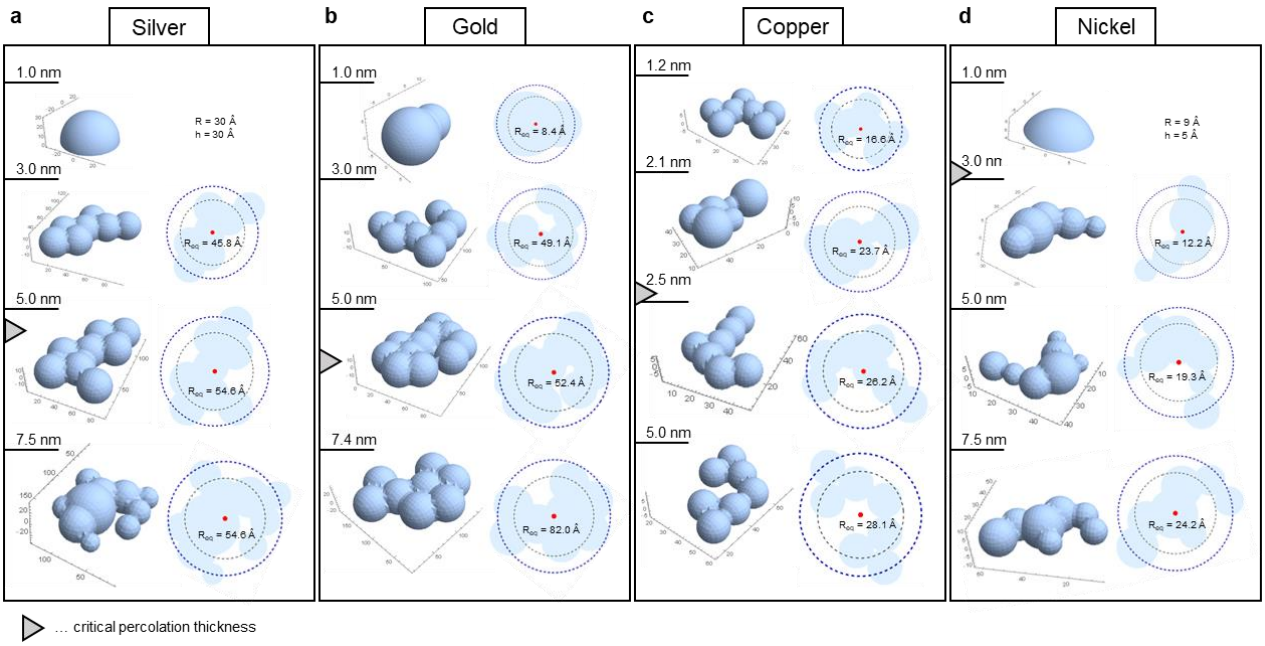

Figure 5. Approximated cluster geometries for all thin films GISAXS thin film investigations. In each panel the resulting structures are presented from top to bottom for successively thicker

films as indicated on the left-hand side. The 3D representations of the estimated cluster geometries are shown left and the top down projections with the radius of gyration (R_g, thin black dashed circles, value not shown) and the radius of a sphere with equivalent Rg (R_{eq}, thick blue dashed circles) are shown on the right side.

The resulting morphologies are discussed in more detail in the supporting information in section 8. For all four metals a consistent trend of increasing cluster size with increasing film thickness was found. However, considerable differences in cluster size with respect to the different metals can be observed with gold exhibiting the largest and nickel the smallest average cluster size. In general, however, cluster shapes evolve from displaying mostly spherical footprints to more irregular, elongated and frayed. This observation aligns well with the notion of incomplete coalescence after a certain thickness. Interestingly, gold clusters at 1.0 nm thickness (Figure 5b) were estimated to exhibit the smallest radius (R_{eq} is the radius of a sphere with equivalent radius of gyration, see SI section 7). This can be rationalized by the adhesion energy (as described above) and the low tendency for bonding such that gold clusters form the least interface area and most spherical clusters. Spheres accommodate more material than shallow clusters with identical radius and are accordingly smaller. All other geometries at the smallest investigated thickness must be chosen shallower to be appropriately close to experimental PDDs. It is also noteworthy that, the island geometries of silver and gold, which exhibit the highest onsets of percolation, display markedly more compact and circular footprints (Figure 5a and b) than those of copper and nickel (Figure 5c and d). This is in accordance with both, the notion that more spread out and wormlike structures undergo percolation at lower thicknesses and the experimentally determined rationale of adhesion energy with the associated high or low tendency to form an interface with the surface. It also falls in line with metal reactivity as the cluster mobility needed to relax into a spherical cap geometry is reduced by bonding to the surface. An interesting aspect is that nickel, despite its slightly higher critical percolation thickness than copper exhibits the smallest clusters.

Cluster arrangements were also fit to the experimental PDDs while approximating clusters as spheres (SI section 8). The characteristic distance estimated from the interference function by Kratky analysis served as a reference to validate both, the determined experimental PDDs and the applied models. Arrangements were found to exhibit the highest order at low thicknesses as order peaks gradually vanished with increasing thickness. Moreover, we found that arrangements with reasonably preserved conservative mass balance were only applicable for low equivalent thicknesses. The mass balance might be satisfied to some extent by small clusters interspersed randomly between the large one by nucleation. The remaining discrepancy may be due to (i) the loss of cluster coupling caused by increasing disorder and an associated more diffuse scattering as well as (ii) the increasing cluster distance such that information is lost due to resolution and q-range limits. Nevertheless, the fitted arrangements yielded average nearest neighbor distances which agreed well with the values obtained from the Kratky plots.

Conclusion:

The growth of thin films of Copper, Gold, Nickel and Silver forming on a covalently crosslinked polymeric substrate could be shown to weakly correlate with metal surface free energy and strongly with metal reactivity. This means that the ordinary GvOC wetting theory is applicable to these systems but must be used with caution due to the weak correlation. However, the SFE and reactivity parameters are readily available experimentally by contact angle measurements or as tabulated data, respectively, which could server in the straightforward prediction and tuning of nanostructured metal-polymer interface properties and their application performance. The combination of the observable correlations with the detailed structural information deduced from the GISAXS experiments should further aid in the rational design as well as the optimization of functional materials exploiting nanostructured polymer-metal interfaces.

EXPERIMENTAL SECTION

Materials

Chloroform ($CHCl_3$) and the polymers Poly[(o-cresyl glycidyl ether)-co-formaldehyde] (PCGF, Mn = 870) and branched Polyethylenimine (PEI, Mn = 10 000) were purchased from Sigma Aldrich and were used as received. The metal targets for sputter deposition were purchased from Gröpl (Austria) with purities no less than 99.97%. The test liquids for contact angle measurements were HQ-H_2O (0.055 μS cm^{-1}), formamide (Roth, P040.1) and glycerol (Fisher Scientific, BP229-1) and used as received.

Polymer thin film casting

Polymer thin films were fabricated on glass coverslips by spincoating with a WS650Mz-23NPP spincoater (Laurell). Glass coverslips for casting were cleaned by immersion in concentrated sulfuric acid (96%) for at least two hours before they were thoroughly rinsed with HQ-H_2O. After rinsing they were spun dry in the spincoater at 8000 rpm for 30 seconds. The polymer components PCGF and PEI were dissolved in chloroform to a concentration of 20 mg mL^{-1} and 10 mg mL^{-1}, respectively. For the casting solution 100 μL of the PCGF solution and 200 μL of PEI solution were mixed thoroughly and dropped on a freshly cleaned and dried cover slip. Covalent crosslinking of the resulting polymer film was achieved by placing the coverslip on a hot plate at 120 °C for 5 minutes.

Metal thin film deposition and monitoring

A DC-magnetron sputter coater (Leica SCD EM 005) was used with Argon (99.999 %) as the sputtering gas at a pressure of 0.9 - 1.2 x 10^{-2} mbar for metal thin film deposition. The plasma current was set by tuning the potentiostat to a value that resulted in a metal deposition rate between 0.06 and 0.08 nm sec^{-1}. The sputter current was roughly 15 mA for gold, 20 mA for Copper and Silver and 30 mA for Nickel. The nominal film thickness and the deposition rate were monitored with a quartz crystal microbalance (Leica EMQ SG100) in situ with an accuracy of 0.1 nm and 0.01 nm sec^{-1}, respectively. Samples and the microbalance were at a 10 cm distance from the sputter target in all experiments and placed at the same eccentricity

from the center (Figure S 1). For ex-situ experiments, after sputter deposition had been terminated the sample was left for another 30 seconds to let the measured thickness reach a constant value before ventilation of the vacuum chamber.

In situ resistivity measurements

The electrical resistance of the growing metal films was measured with a LCR Meter ST2817A (Sourcetronic) using a ST26011A Kelvin Clip Terminal (Sourcetronic). The instrument was used in the R-X setting at a measurement frequency of 1 kHz and a measuring voltage of 1 V with open and short correction turned off. The resistance of the setup to contact the polymer surface was determined separately and subtracted from each measurement. The polymer surface was contacted via gold electrodes which were directly sputter-coated onto the surface through an appropriate mask to a thickness of 50 nm and a size of roughly 4 x 6 mm. The gold electrodes were connected to the copper wires with silver conductive adhesive with negligible electrical resistance. The contacts of the copper wires with the Kelvin Clip terminal were checked for negligible resistance by a separate handheld LCR-meter. The samples were placed at the same perimeter as the microbalance during deposition to ensure an equal thickness of the deposited metal for at both locations (Figure S 1).

Contact angle measurements

Contact angles (θ) of the respective test liquid (Formamide, Glycero and Water, see Materials) with the surface under investigation were measured in air with a DSA30 contact angle goniometer (Krüss) and evaluated with the provided software package Advance 3.0 (Krüss). Contact angles were recorded 10 – 60 seconds after drop deposition (depending on the liquid viscosity) to allow the droplet to reach force equilibrium and a static value of θ. The average value of both observed angles in each image was recorded. Contact angles were determined as the average value of at least five individual droplets (0.5 – 3 μL) on each of two individually prepared surface samples.

GISAXS measurements

Grazing incidence small angle x-ray scattering experiments were conducted with the respective metal coated polymer film as produced by spin coating and subsequent sputter coating without further treatment. The photon energy was 8 keV (λ = 0.154 nm) in all experiments. Thin films of gold, nickel and silver were investigated at the Austrian SAXS Beamline at the Elettra Synchrotron facility. Scattering patterns were recorded at room temperature with a Pilatus 1M detector (Dectris) with an exposure time of 10 seconds. For gold samples of 1, 3, 5, and 7.5 nm nominal thickness, the sample to detector distance (D) was 1403 mm (with a resulting q-range from 0.055 to 3.02 nm^{-1}) and the incident angle was α_i = 0.24°. For gold samples with a nominal thickness of 9 and 12 nm D was 1343 mm (with a resulting q-range from 0.08 to 3.50 nm^{-1}). For silver and nickel D was set to 1395 mm (q-range from 0.06 – 3.28 nm^{-1}) and the incident angle was α_i = 0.68° and α_i = 0.625°, respectively. The copper films exhibited very high resistivity as they were checked at the synchrotron facility presumably due to oxide formation. Therefore, a separate set of copper samples were investigated shortly after deposition with a laboratory x-ray light source (Rigaku S-Max 3000 with MM002+ Cu Kα source and a Triton200 multiwire detector). The incident angle was α_i = 0.20° and D was 1500 mm (q-range 0.1 - 2.7 nm^{-1}). Horizontal line cuts of the scattering data (along the y-axis) were made at the Yoneda intensity for all samples with a pixel width of at least 5 to reduce noise for the low intensity, high q-range data.

ASSOCIATED CONTENT

Supporting Information. A listing of the contents of each file supplied as Supporting Information should be included. For instructions on what should be included in the Supporting Information as well as how to prepare this material for publications, refer to the journal's Instructions for Authors.

AUTHOR INFORMATION

Corresponding Author

*Alois Jungbauer: alois.jungbauer@boku.ac.at

Author Contributions

The manuscript was written through contributions of all authors. All authors have given approval to the final version of the manuscript.

ACKNOWLEDGMENT

This work has been supported by the Federal Ministry for Digital and Economic Affairs (bmwd), the Federal Ministry for Transport, Innovation and Technology (bmvit), the Styrian Business Promotion Agency SFG, the Standortagentur Tirol, Government of Lower Austria and ZIT - Technology Agency of the City of Vienna through the COMET-Funding Program managed by the Austrian Research Promotion Agency FFG. The funding agencies had no influence on the conduct of this research. We thank Agnes Rodler for help in measurement of gold GISAXS patterns and Dietmar Pum for sputter deposition.

ABBREVIATIONS

SFE, surface free energy; GvOC, Good – van Oss – Chaudhury; GISAXS, grazing incidence small angle x-ray scattering; PDD, pair distance distribution

REFERENCES

1. Hora, J., Hall, C., Evans, D. & Charrault, E. Inorganic Thin Film Deposition and Application on Organic Polymer Substrates. *Adv. Eng. Mater.* **20**, 1700868

2. Muslim, N., Soon, Y. W., Lim, C. M. & Voo, N. Y. Properties of nickel films growth by radio frequency magnetron sputtering at elevated substrate temperatures. *Thin Solid Films* **612**, 82–86 (2016).

3. Schwartzkopf, M. *et al.* Real-Time Monitoring of Morphology and Optical Properties during Sputter Deposition for Tailoring Metal–Polymer Interfaces. *ACS Appl. Mater. Interfaces* **7**, 13547–13556 (2015).

4. Svorcık, V., Zehentner, J., Rybka, V., Slepicka, P. & Hnatowicz, V. Characterization of thin gold layers on polyethyleneterephthalate: transition from discontinuous to continuous, homogenous layer. *Appl. Phys. A* **75**, 541–544 (2002).

5. Siwy, Z. *et al.* Protein Biosensors Based on Biofunctionalized Conical Gold Nanotubes. *J. Am. Chem. Soc.* **127**, 5000–5001 (2005).

6. Barik, A. *et al.* Dielectrophoresis-Enhanced Plasmonic Sensing with Gold Nanohole Arrays. *Nano Lett.* **14**, 2006–2012 (2014).

7. Jin, Y. Engineering Plasmonic Gold Nanostructures and Metamaterials for Biosensing and Nanomedicine. *Adv. Mater.* **24**, 5153–5165 (2012).

8. Experton, J. & Martin, C. R. The Effect of Voltage Charging on the Transport Properties of Gold Nanotube Membranes. *Small* **14**, 1703290 (2018).

9. Novotny, M., Bulir, J., Lancok, J., Pokorny, P. & Bodnar, M. In-situ monitoring of the growth of nanostructured aluminum thin film. *J. Nanophotonics* **5**, 051503 (2011).

10. Abdellaoui, N. *et al.* In situ monitoring of electrical resistance during deposition of Ag and Al thin films by pulsed laser deposition: Comparative study. *Appl. Surf. Sci.* **418**, 517–521 (2017).

11. Schwartzkopf, M. *et al.* Role of Sputter Deposition Rate in Tailoring Nanogranular Gold Structures on Polymer Surfaces. *ACS Appl. Mater. Interfaces* **9**, 5629–5637 (2017).

12. Mireles, M. & Gaborski, T. R. Fabrication techniques enabling ultrathin nanostructured membranes for separations. *ELECTROPHORESIS* n/a-n/a (2017). doi:10.1002/elps.201700114

13. Tokarev, I. & Minko, S. Stimuli-responsive hydrogel thin films. *Soft Matter* **5**, 511–524 (2009).

14. Zhao, Y. *et al.* Two-Dimensional Material Membranes: An Emerging Platform for Controllable Mass Transport Applications. *Small* **10**, 4521–4542 (2014).

15. Marchetti, P., Jimenez Solomon, M. F., Szekely, G. & Livingston, A. G. Molecular Separation with Organic Solvent Nanofiltration: A Critical Review. *Chem. Rev.* **114**, 10735–10806 (2014).

16. Kang, E. *et al.* Large-Scale, Ultrapliable, and Free-Standing Nanomembranes. *Adv. Mater.* **25**, 2167–2173 (2013).

17. Matsui, J., Mitsuishi, M., Aoki, A. & Miyashita, T. Molecular Optical Gating Devices Based on Polymer Nanosheets Assemblies. *J. Am. Chem. Soc.* **126**, 3708–3709 (2004).

18. Damasceno Borges, D., Gebel, G., Franco, A. A., Malek, K. & Mossa, S. Morphology of Supported Polymer Electrolyte Ultrathin Films: A Numerical Study. *J. Phys. Chem. C* **119**, 1201–1216 (2015).

19. Kaune, G. *et al.* In Situ GISAXS Study of Gold Film Growth on Conducting Polymer Films. *ACS Appl. Mater. Interfaces* **1**, 353–360 (2009).

20. Schuster, C., Rodler, A., Tscheliessnig, R. & Jungbauer, A. Freely suspended perforated polymer nanomembranes for protein separations. *Sci. Rep.* **8**, 4410 (2018).

21. Puiggalí-Jou, A. *et al.* Confinement of a β-barrel protein in nanoperforated free-standing nanomembranes for ion transport. *Nanoscale* (2016). doi:10.1039/C6NR04948F

22. Watanabe, H. & Kunitake, T. A Large, Freestanding, 20 nm Thick Nanomembrane Based on an Epoxy Resin. *Adv. Mater.* **19**, 909–912 (2007).

23. Watanabe, H., Muto, E., Ohzono, T., Nakao, A. & Kunitake, T. Giant nanomembrane of covalently-hybridized epoxy resin and silica. *J. Mater. Chem.* **19**, 2425–2431 (2009).

24. Takele, H. *et al.* Tuning of electrical and structural properties of metal-polymer nanocomposite films prepared by co-evaporation technique. *Appl. Phys. A* **92**, 345–350 (2008).

25. Hajati, S., Zaporojtchenko, V., Faupel, F. & Tougaard, S. Characterization of Au nano-cluster formation on and diffusion in polystyrene using XPS peak shape analysis. *Surf. Sci.* **601**, 3261–3267 (2007).

26. Siniscalco, D., Bardeau, J.-F., Edely, M., Gourbil, A. & Delorme, N. Temperature-Induced Structural Transitions on Hybrid Nanothick Metal/Polymer Assemblies. *J. Phys. Chem. C* **117**, 7391–7397 (2013).

27. Hollars, D. R. Manufacturing method for large-scale production of thin-film solar cells. (2009).

28. Campbell, C. T. Ultrathin metal films and particles on oxide surfaces: structural, electronic and chemisorptive properties. *Surf. Sci. Rep.* **27**, 1–111 (1997).

29. Ruffino, F., Torrisi, V., Marletta, G. & Grimaldi, M. G. Growth morphology of nanoscale sputter-deposited Au films on amorphous soft polymeric substrates. *Appl. Phys. A* **103**, 939 (2011).

30. Yang, X. *et al.* Optimizing ultrathin Ag films for high performance oxide-metal-oxide flexible transparent electrodes through surface energy modulation and template-stripping procedures. *Sci. Rep.* **7**, 44576 (2017).

31. Chou, N. J. & Tang, C. H. Interfacial reaction during metallization of cured polyimide: An XPS study. *J. Vac. Sci. Technol. Vac. Surf. Films* **2**, 751–755 (1984).

32. Ho, P. S. *et al.* Chemical bonding and reaction at metal/polymer interfaces. *J. Vac. Sci. Technol. Vac. Surf. Films* **3**, 739–745 (1985).

33. Bébin, P. & Prud'homme, R. E. Comparative XPS Study of Copper, Nickel, and Aluminum Coatings on Polymer Surfaces. *Chem. Mater.* **15**, 965–973 (2003).

34. Zabolitzky, J. G. Monte Carlo evidence against the Alexander-Orbach conjecture for percolation conductivity. *Phys. Rev. B* **30**, 4077–4079 (1984).

35. Halperin, B. I., Feng, S. & Sen, P. N. Differences between Lattice and Continuum Percolation Transport Exponents. *Phys. Rev. Lett.* **54**, 2391–2394 (1985).

36. Dubson, M. A. & Garland, J. C. Measurement of the conductivity exponent in two-dimensional percolating networks: square lattice versus random-void continuum. *Phys. Rev. B* **32**, 7621–7623 (1985).

37. Schwartzkopf, M. *et al.* From atoms to layers: in situ gold cluster growth kinetics during sputter deposition. *Nanoscale* **5**, 5053–5062 (2013).

38. Volpe, C. D. & Siboni, S. Acid–base surface free energies of solids and the definition of scales in the Good–van Oss–Chaudhury theory. *J. Adhes. Sci. Technol.* **14**, 235–272 (2000).

39. Chatain, D., Coudurier, L. & Eustathopoulos, N. Wetting and interfacial bonding in ionocovalent oxide-liquid metal systems. *Rev. Phys. Appliquée* **23**, 1055–1064 (1988).

40. *CRC Handbook of Chemistry and Physics, 99th Edition*. (CRC Press, 2018).

41. Valden, M., Lai, X. & Goodman, D. W. Onset of Catalytic Activity of Gold Clusters on Titania with the Appearance of Nonmetallic Properties. *Science* **281**, 1647–1650 (1998).

42. Lazzari, R., Renaud, G., Jupille, J. & Leroy, F. Self-similarity during growth of the Au/TiO2 (110) model catalyst as seen by the scattering of x-rays at grazing-angle incidence. *Phys. Rev. B* **76**, 125412 (2007).

43. Sun, H., Yu, M., Wang, G., Sun, X. & Lian, J. Temperature-Dependent Morphology Evolution and Surface Plasmon Absorption of Ultrathin Gold Island Films. *J. Phys. Chem. C* **116**, 9000–9008 (2012).

44. Yoneda, Y. Anomalous Surface Reflection of X Rays. *Phys. Rev.* **131**, 2010–2013 (1963).

45. Glatter, O. & Kratky, O. *Small angle x-ray scattering*. (Academic Press, 1983).

46. Hodas, M. *et al.* Kinetics of copper growth on graphene revealed by time-resolved small-angle x-ray scattering. *Phys. Rev. B* **95**, 035424 (2017).

47. Renaud, G., Lazzari, R. & Leroy, F. Probing surface and interface morphology with Grazing Incidence Small Angle X-Ray Scattering. *Surf. Sci. Rep.* **64**, 255–380 (2009).

48. Fritz-Popovski, G., Bergmann, A. & Glatter, O. Real space functions from experimental small angle scattering data. *Phys. Chem. Chem. Phys.* **13**, 5872–5880 (2011).

Publication IV

Supplementary Information

Metal-insulator transition, associated growth morphology and relations to surface free energy and reactivity of ultrathin sputtered metals on reticulated polymer thin films

Christian Schuster[1], Harald Rennhofer[2], Alois Jungbauer[1,2] and Rupert Tscheliessnig[1]*

1 Sputtering chamber setup

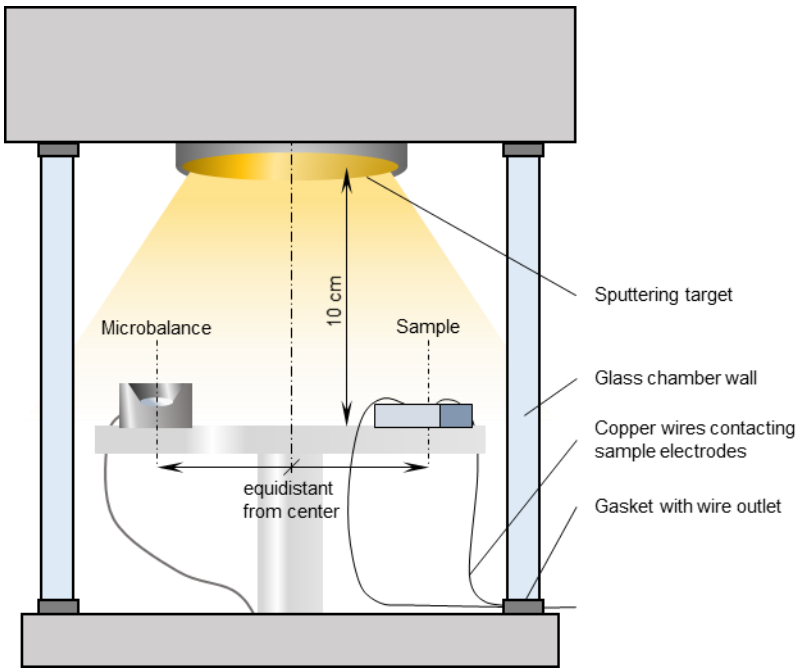

Figure S 1. Setup of the sputter deposition chamber for in-situ resistance measurements.

2 Contact angles and SFE derivation

The surface free energies of the different metals and the polymer surface was estimated by static contact angle measurements. From the contact angles of the three test liquids with the surface obtained for each material as listed in **Table S 1** the surface free energy was obtained as three components by solving for the resulting system of three equations for the unknown quantities. For the respective wetting liquid, the contact angle is related to the energy components of the tested surface as follows:

$$\sigma_L(\cos\theta + 1) = 2\left(\sqrt{\sigma_L^{LW}\sigma_S^{LW}} + \sqrt{\sigma_L^{-}\sigma_S^{+}} + \sqrt{\sigma_L^{+}\sigma_S^{-}}\right)$$

where θ is the contact angle, σ denotes the respective surface energy component for the liquid (index L) or the surface (index S), LW indicates the dispersive, Lifshitz - van der Waals component while + stands for the positive polar and - for the negative polar component. The quantity σ_L is related to the liquid surface energy components by

$$\sigma_L = \sigma_L^{LW} + 2\sqrt{\sigma_L^{+}\sigma_L^{-}}.$$

The used surface energy components of the test liquids[1] are listed in **Table S 2**.

3 Kratky analysis

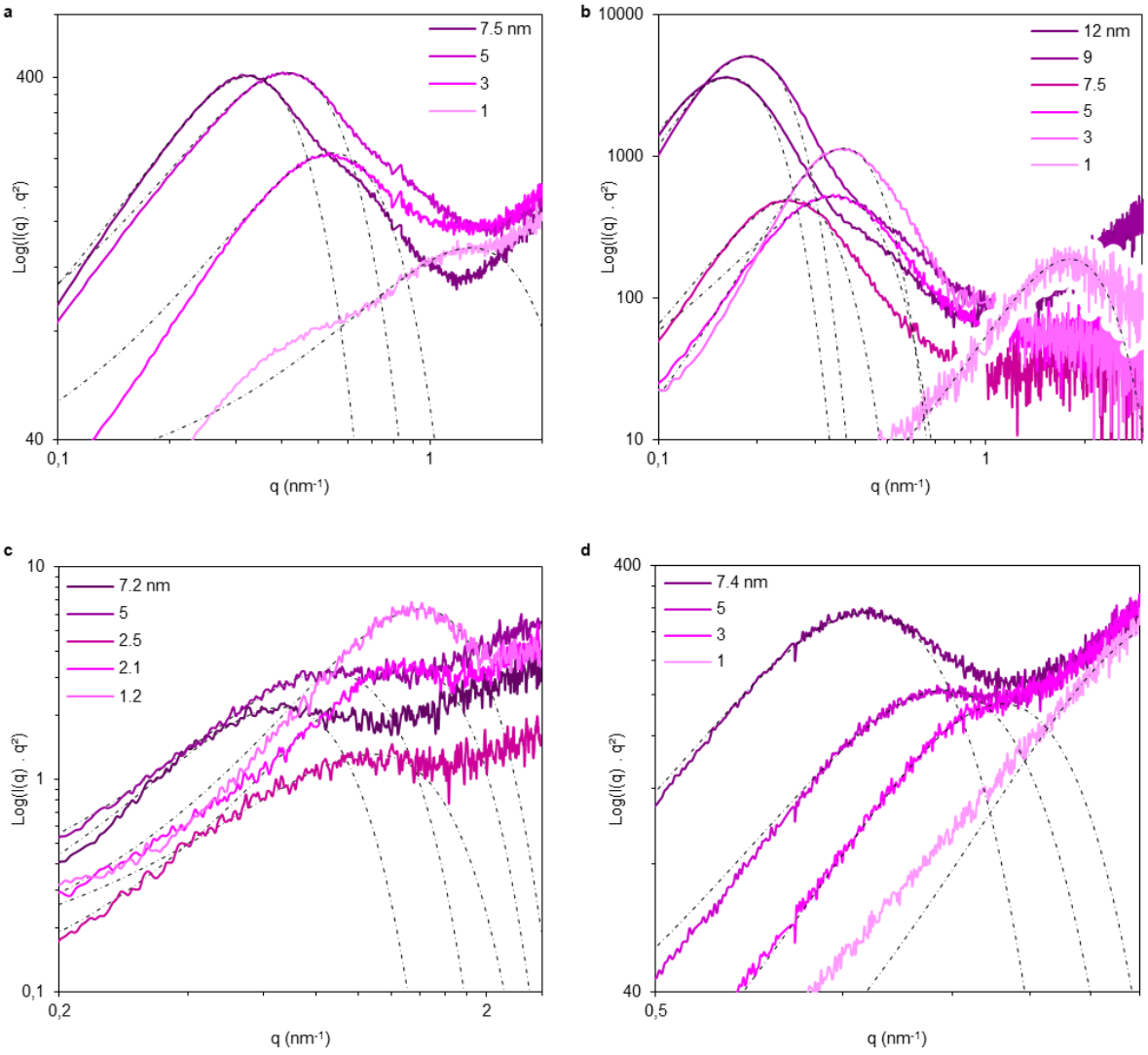

Figure S 2. Kratky plots of the scattering curves obtained from cuts along the Yoneda horizon of the scattering patterns with fitted gaussian functions indicated by dashed lines. a) Silver b) Gold c) Copper d) Nickel.

4 Pair distance distribution fitting

For the calculation of the pair distance distributions we evaluated line cuts along the y-axis (Figure 4a and b) at q_z positions of the Yoneda horizon where the intensity has its maximum. We follow the argument of Lazzari[2] and neglect changes in the gradient of the dielectric index. However, we avoid the limitations of spherical or cylindrical form factors and reformulate the working equation given by

$$I(Q) \propto |\mathcal{F}_2(\rho(r_\parallel))|^2 \times \mathcal{F}_1(p(R_\parallel))[Q]$$

to

$$I(Q) \propto \mathcal{F}_2(p_{\text{exp}}(r_\parallel))[Q].$$

The Fourier transform is the Bessel zero transform of the pair distance distribution of scattering sites in plane. It is explicitly given by

$$\mathcal{F}_2(p(r))[Q] = \int_0^\infty dr p(r) J_0(qr).$$

We minimized the L_2 norm of

$$\min \parallel I(Q) - \mathcal{F}_2(p_{\text{exp}}(r))[Q] \parallel_2$$

by computing what we term the experimental pair density. The obtained optimal fits can be regarded as the real space equivalents of the scattering intensity data. For interpretation the pair distance distributions calculated for arbitrary geometrical objects can be matched to the experimental pair distance distributions (see section 7).

5 Experimental pair distance distributions

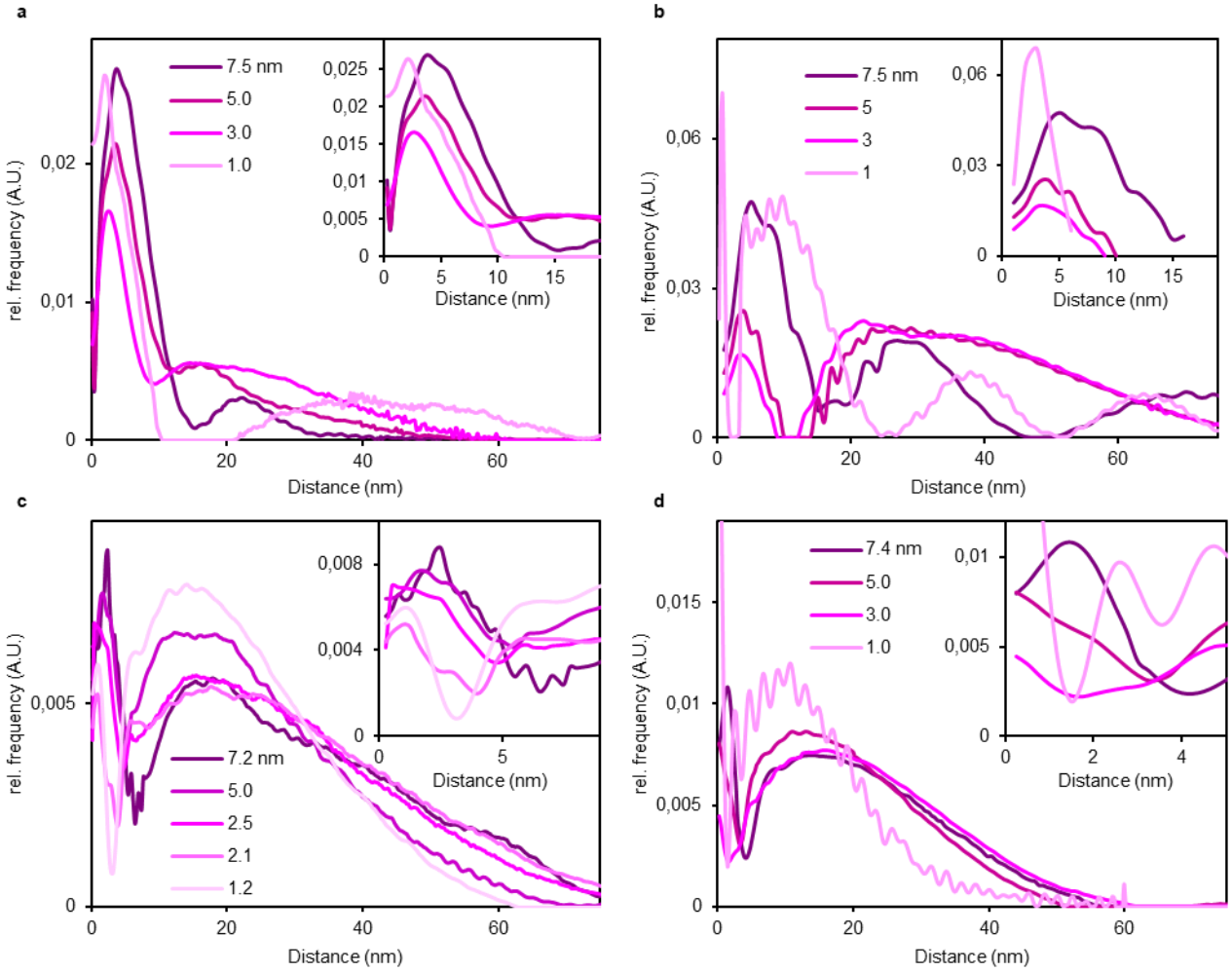

Figure S 3. Pair distance distributions as fitted to the raw qy-data of the different metal thin films. The insets are plots of the first peaks of the respective pair distance distributions for better visibiliity of the shifting maxima. a) Silver b) Gold c) Copper d) Nickel.

6 qy-cuts and scattering curves reconstructed from PDDs

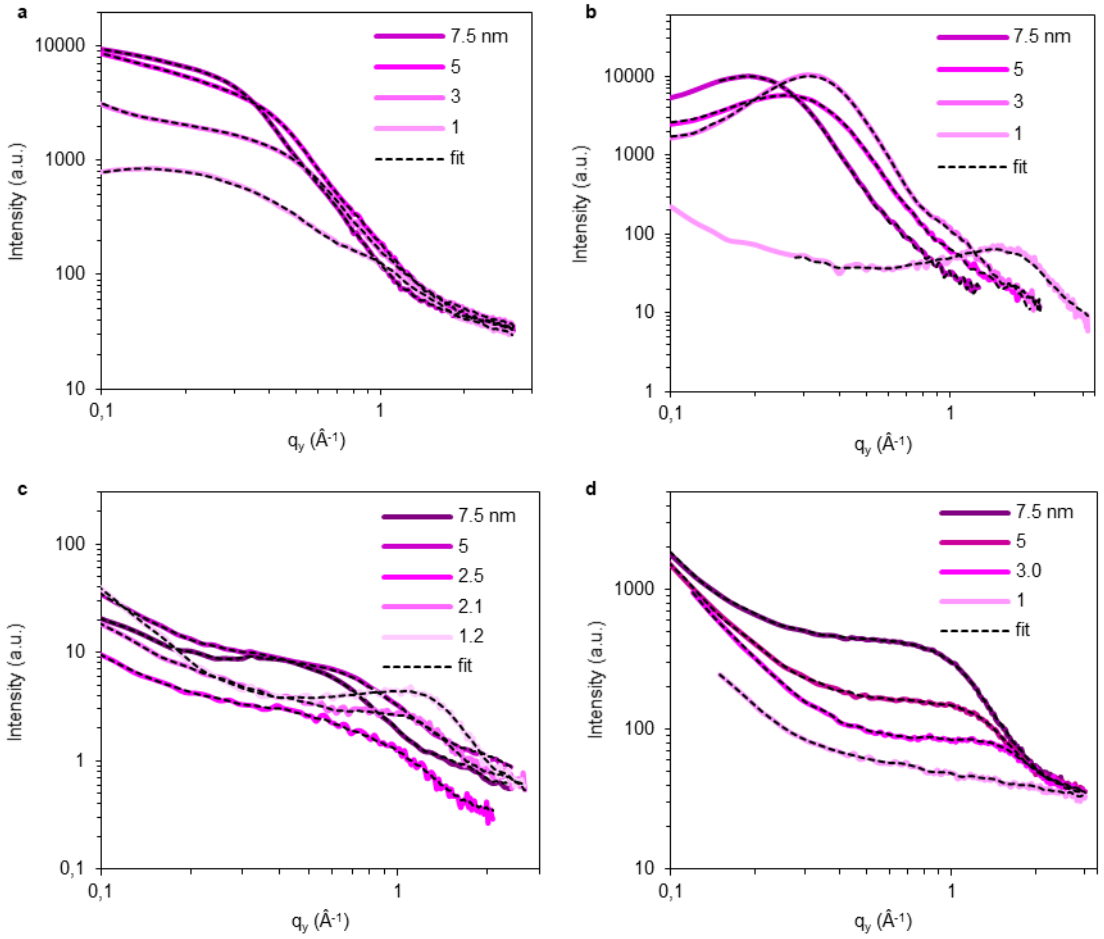

Figure S 4. Raw data of the q_y-cuts along the Yoneda horizon for the different metal films (colored lines) and the scattering patterns as reconstructed from the respective fitted pair distance distributions (dashed lines). a) Silver b) Gold c) Copper d) Nickel.

7 Pair distance distribution calculation and fitting

Pair distance distribution functions (PDDs) were calculated, fitted and visualized with the Mathematica 11.3 software package.

For the numerical calculation of PDDs the geometric region for which the distribution should be calculated is defined (e.g. a spherical cap or an ensemble of spheres on a lattice) as a first step (**Figure S 5** a). This region is then randomly filled with 5 x 10^3 to 10^4 points using the innate function "RandomPoint" as visualized in **Figure S 5** b and c for the region of interest simulating potential scattering sites. For each individual point the distances to all other points in the x-y plane were calculated and binned to the desired resolution ultimately yielding the pair distance distribution of the defined region in the q_y-direction.

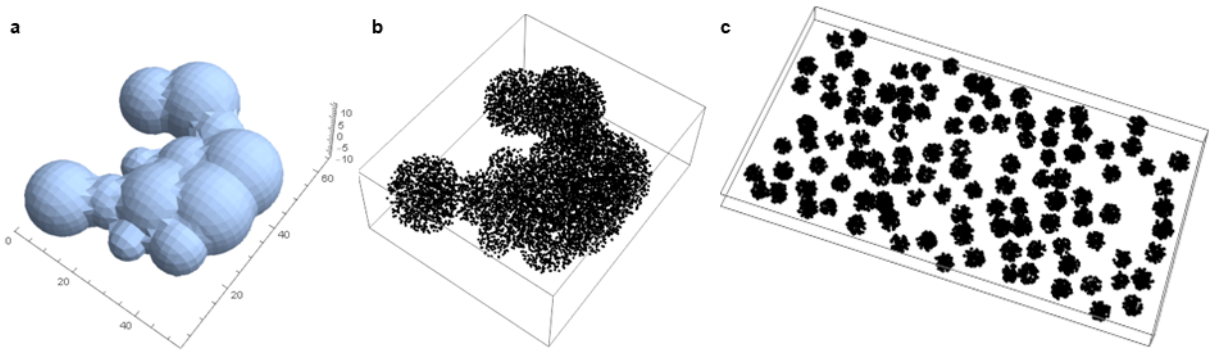

Figure S 5. Region defining and generating random points for numerical PDD calculation.

To find cluster shapes, sizes and arrangements that fit the experimental PDDs (as obtained from the fits to the raw scattering data) two approaches were chosen. Either, the shape and size of the region used for calculation was selected and adjusted manually which was mostly done with spherical cap geometries or to estimate parameters for the second approach. On the other hand, a simple approach of choosing the best fit from a randomly generated set of assemblies was implemented. The quality parameter whereby the assemblies were rated was chosen as the root mean square distance of the calculated PDD and the raw PDD in the region of interest.

Cluster shape and size was always fitted with a 4 by 4 lattice occupied to a random extent with spheres of either equal or randomly distributed size (as visualized in **Figure S 5** a). Arrangements of clusters on the surface were fit on lattices of different size (depending on the purpose) with lattice points being randomly displaced to a certain extent. The occupancy of the lattice with spheres was randomly generated within a specified range whereas the spheres were either monodisperse or their size was subject to a uniform random distribution within a specified range. For non-spherical footprint clusters (the majority) an equivalent radius (R_{eq})was calculated for comparability with spherical clusters as the radius of a sphere with identical radius of gyration R_g which is represented in a top-down projection where also both radii (R_{eq} and R_g) are indicated.

8 Pair distance distribution fits and morphology

8.1 Silver

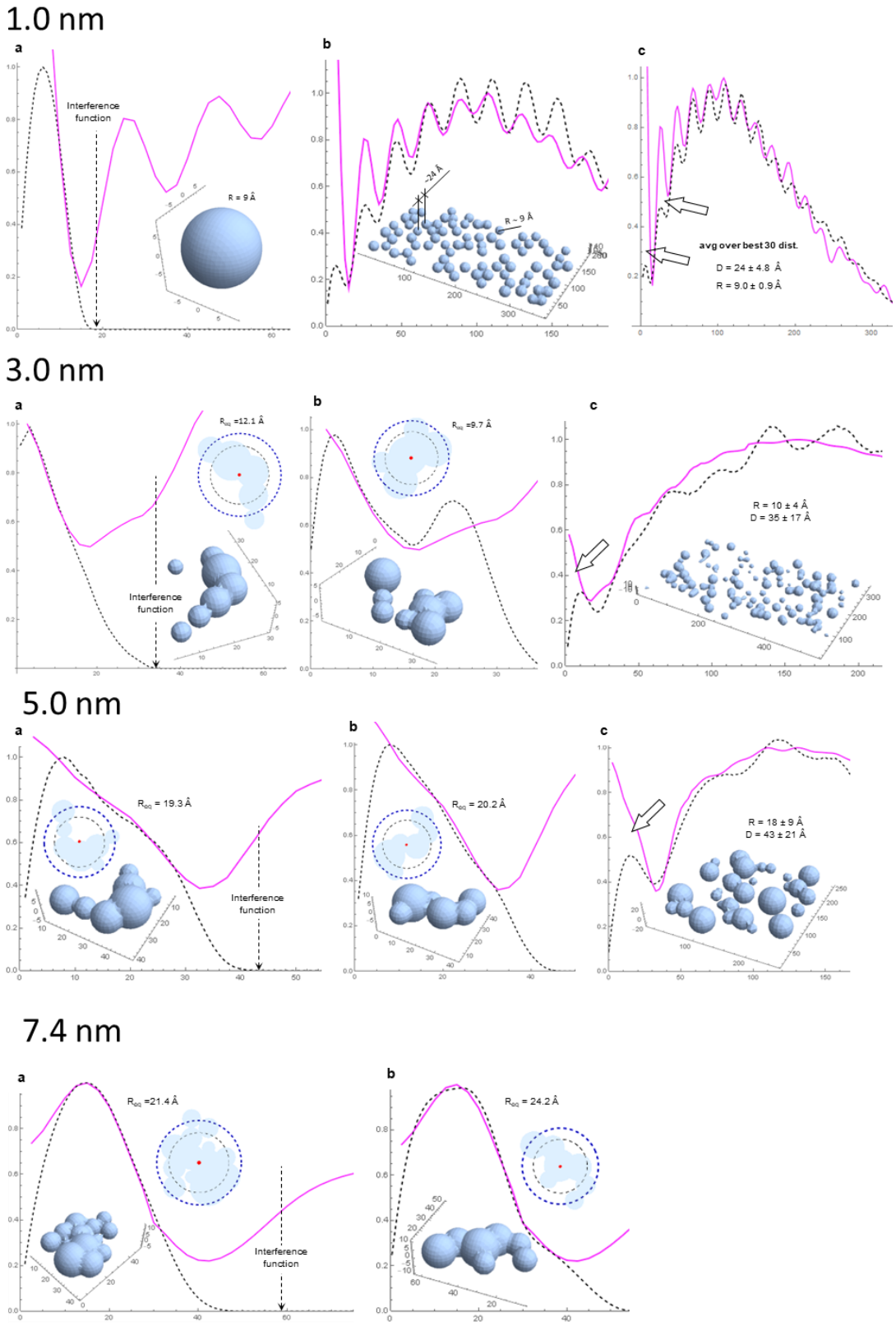

Figure S 6. Pair distance distribution function fits for silver thin films with equivalent film thicknesses of 1.0, 3.0, 5.0 and 7.5 nm.

The PDDs obtained for thin films of silver show pronounced peaks located at distances ranging from ~20 Â to 45 Â. Except for the data obtained for 1.0 nm thickness, the first peak is followed by a second peak that coincides with the distance extracted from Kratky analysis as indicated by the dashed arrow in **Figure S 6** panels a. In the data for 1.0 nm thickness a shoulder is observable at the interference function distance and no further maximum is present except for a very broad peak located at very long distance of ~400 Â starting at ~200 Â. Thus, it seems that a short-range order is not strongly established which is also hinted at by the small peak in the Kratky plot from the data of 1.0 thickness. Neglecting the contributions of nearest neighbors, the cluster shape can be approximated by a spherical cap geometry with a radius and a height of 30 Â (**Figure S 6** 1.0 nm b). However, if the unit cell approximation (Figure 4 c) and the corresponding mass balance is invoked, the spherical cap must have a height of only 17 Â which shits the PDD towards lower distances worsening the fit (as indicated by arrows in **Figure S 6** 1.0 nm b). Therefore, the cluster shape is better approximated by a somewhat elongated cluster shape (**Figure S 6** 1.0 nm c). By introducing several small neighbors, the contributions at larger distances can be accounted for. A more complete model with neighbors at further distances could eliminate the discrepancy indicated by the double arrow in **Figure S 6** 1.0 nm c. As indicated above, the remaining PDDs have the interference function peak separated from the cluster structure peak. The equivalent radii of the estimated clusters increase with increasing film thickness from ~45 to ~65 Â but cannot be approximated by a spherical shape due to considerable discrepancies at distances larger than the peak maximum (arrows in the panels b, c and c of 3.0, 5.0 and 7.5 nm, respectively). The cluster morphology transitions from quite spherical (1.0 nm) over elongated (3.0 nm) to somewhat spread out (5.0 nm) and frayed (7.5 nm). This is in accordance with the notion of small spherical clusters growing to touch and coalesce to a point where incomplete coalescence leads to the percolation into a network of irregular clusters that gets filled gradually. This filling is illustrated by the fact that

the structures obtained for 7.5 nm have a more compact and spherical footprint than the elongated ones obtained for 3.0 and 5.0 nm thickness.

In general, the PDD fits obtained for silver display quite low relative frequencies at distances beyond the minimum separating the cluster from the order peak. This can be ascribed to a weak correlation with neighboring clusters due to a relatively random arrangement on the polymer surface. This is also in line with the q_y data of silver displaying the least pronounced interference function features. Therefore, no model arrangement could be fitted to the data which covers more than a few neighbors without having substantial discrepancies. However, fitting an arrangement of several neighbors yielded distances which very well with the inter-cluster distances derived from Kratky-analysis (**Figure S 6** 1.0 nm c and 2.0 nm c).

8.2 Gold

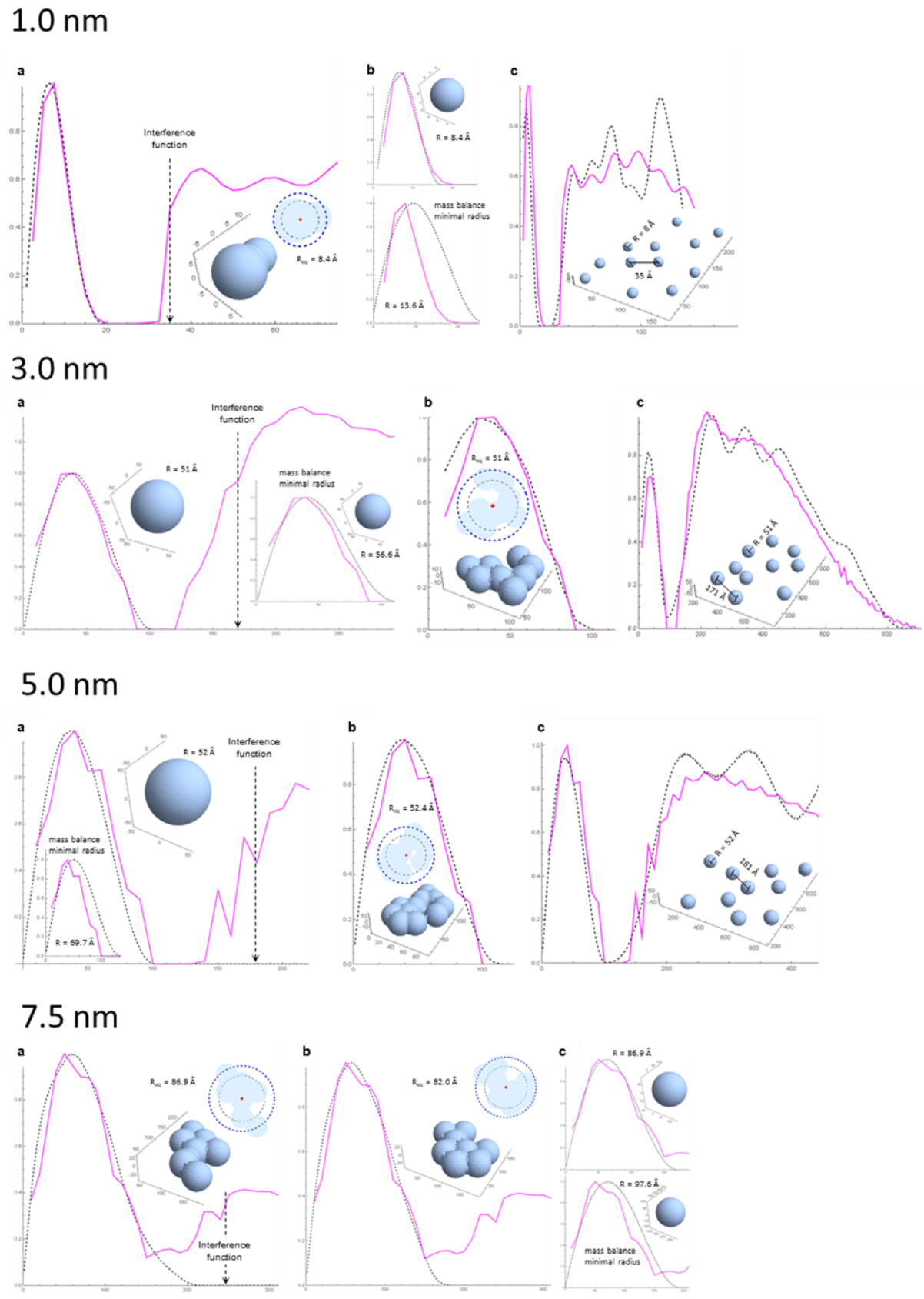

Figure S 7 Pair distance distribution function fits for gold thin films with equivalent film thicknesses of 1.0, 3.0, 5.0 and 7.5 nm.

The PDDs obtained for gold are characterized by peaks located at relatively low distances ranging from 7.5 Â to approximately 60 Â and are well separated by a substantial minimum from the spread-out peaks of the nearest neighbors (**Figure S 7** panels a). For all PDDs obtained, the location of the nearest neighbor order peak agrees well with the interference function distance. The first peaks of all distributions can be fitted reasonably well with a spherical cluster although there are some subtle discrepancies. The 1.0 nm data can be best approximated (**Figure S 7** 1.0 nm b) but a slightly elongated cluster fits better (**Figure S 7** 1.0 nm a). The peaks in the data for 3.0 nm and 5.0 nm thickness displays a sharp drop to 0 at 90 Â and 100 Â, respectively, that cannot be accounted for by the PDD of a spherical cluster. The clusters resulting from the fit procedure are somewhat elongated and exhibit a sharper decline at long distances than a spherical shape (**Figure S 7Fehler! Verweisquelle konnte nicht gefunden werden.** 3.0 and 5.0 nm b) although the fit for 3.0 nm is worse at small distances. Similarly, the first peak of the PDD corresponding to 7.5 nm film thickness is best estimated by elongated clusters (**Figure S 7** 7.5 nm a and b). However, notice that all estimated irregular cluster are still the closest to a spherical footprint of all investigated metals. Since the cluster shape for all thicknesses is very close to spherical it was interesting to apply the unit cell approximation with the associated mass balance. PDDs obtained for spherical clusters with the minimal radius implied by mass balance are indicated by “mass balance minimal radius” in **Figure S 7**. Interestingly, the cluster sizes suggested by this approach display PDDs with substantial discrepancies to the actual peaks as they are generally overestimated. This suggests that the mass balance is either closed by small clusters interspersed randomly between the larger islands or that the cluster distance is overestimated or a combination of both.

Larger arrangements of clusters were fitted to the PDDs from 1.0 nm to 5.0 nm. The PDD for 7.5 nm does not allow a meaningful fit of an arrangement since contributions of distances in the range of the nearest neighbor are quite low. This is likely the result of both, the resolution limit of the setup and an increasingly disordered arrangement of the scattering centers. The arrangement fit to the data of 1.0 nm thickness displays order peaks that coincide very well with the data corroborating the distance of 35 Â found with Kratky-analysis. The order peaks for 3.0 and 5.0 thickness vanish gradually indicating a more random arrangement due to incomplete coalescence with the consequential elongation and branching. However, the general shape is very well represented by the arrangements where the cluster distance was set to the values deduced from Kratky-analysis (171 Â and 181 Â).

8.3 Copper

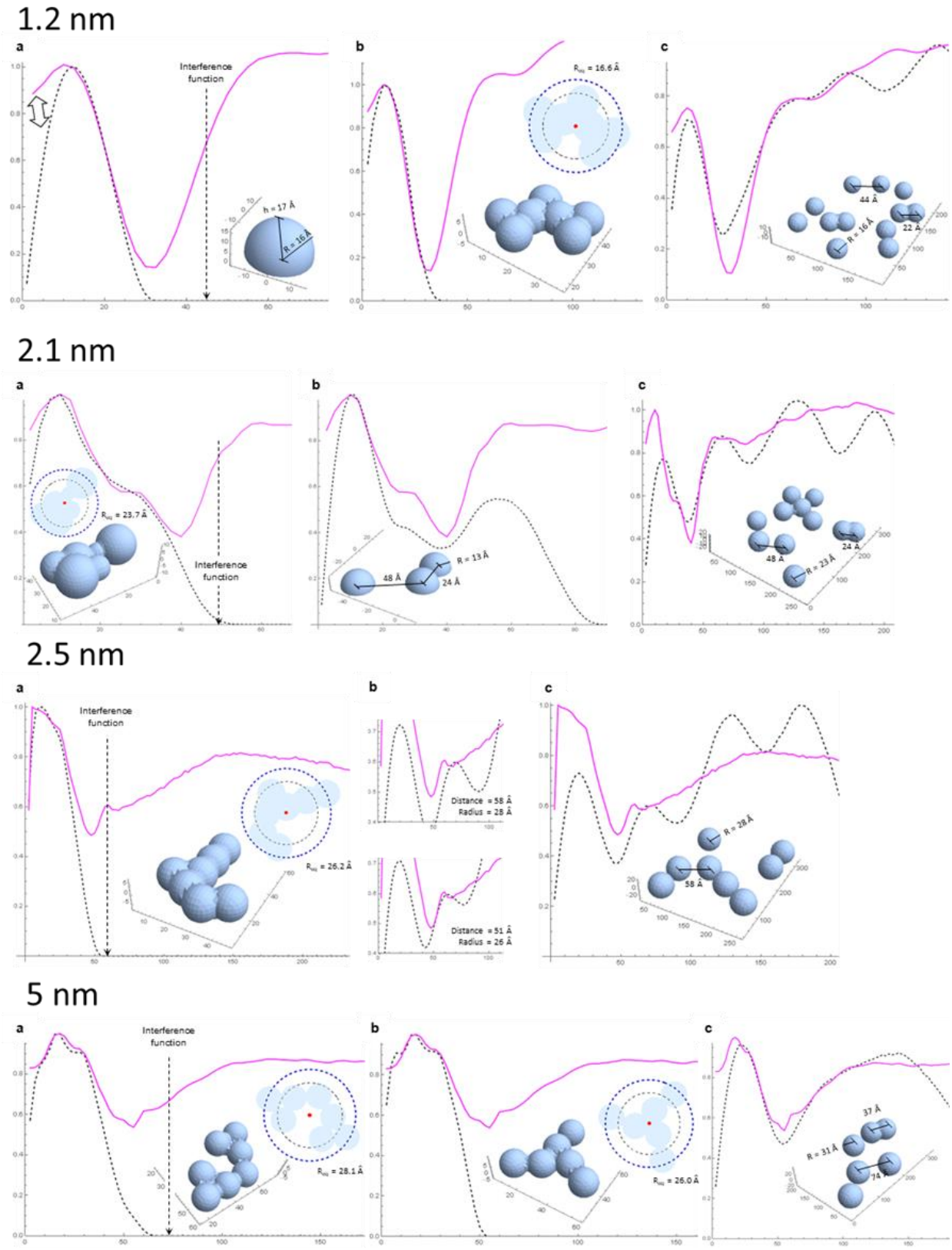

Figure S 8. Pair distance distribution function fits for nickel thin films with equivalent film thicknesses of 1.2, 2.1, 2.5 and 5.0 nm.

All PDDs fit to the q_y-data of copper exhibit a pronounced peak located at relatively low distances (roughly 15 – 20 Â) followed by a second peak that coincides, at least to some extent, with the inter-cluster distance estimated from Kratky analysis (**Figure S 8** panels a). These two maxima are separated by a minimum (roughly 30 – 60 Â). Although the first peaks can be approximated to a certain extent by spherical clusters there are already considerable deviations for the smallest clusters (**Figure S 8** 1.2 nm a indicated by the double arrow) especially at the shortest distance contributions. This shows that even at an equivalent thickness of 1.2 nm the clusters are not relaxing into spherical equilibrium shapes but are non-spherical to some extent. Accordingly, the cluster morphologies which were obtained from the fits to the first peaks are markedly non-spherical with a trend of more elongated and branched morphology with increasing film thickness. Additionally, and as expected, the cluster sizes increase with increasing deposition thickness from an equivalent sphere radius of 16.6 Â to ~27 Â. The most elongated shape was estimated for the clusters at a thickness of 2.5 nm which coincides with the onset of percolation while the cluster morphology for 5.0 nm is more compact again which fits nicely to the formation of more contact points with neighbors and the filling of holes after percolation.

The arrangement of the clusters on the surface was fit to a larger portion of the PDDs with a larger lattice. From a smallest possible inter-cluster distance half of that inferred from Kratky analysis, in the resulting fits the occupancy of lattice positions converged (with small deviations such as in (**Figure S 8** 2.5 b) to the respective interference function distance (**Figure S 8** panels c). Judging from the size of the order peaks in the PDDs compared to the fits and the absence of pronounced next peaks the arrangement of clusters on the polymer surface seems quite disordered and loses correlation relatively soon. Thus, as inferred above from the cluster shape analysis the …

8.4 Nickel

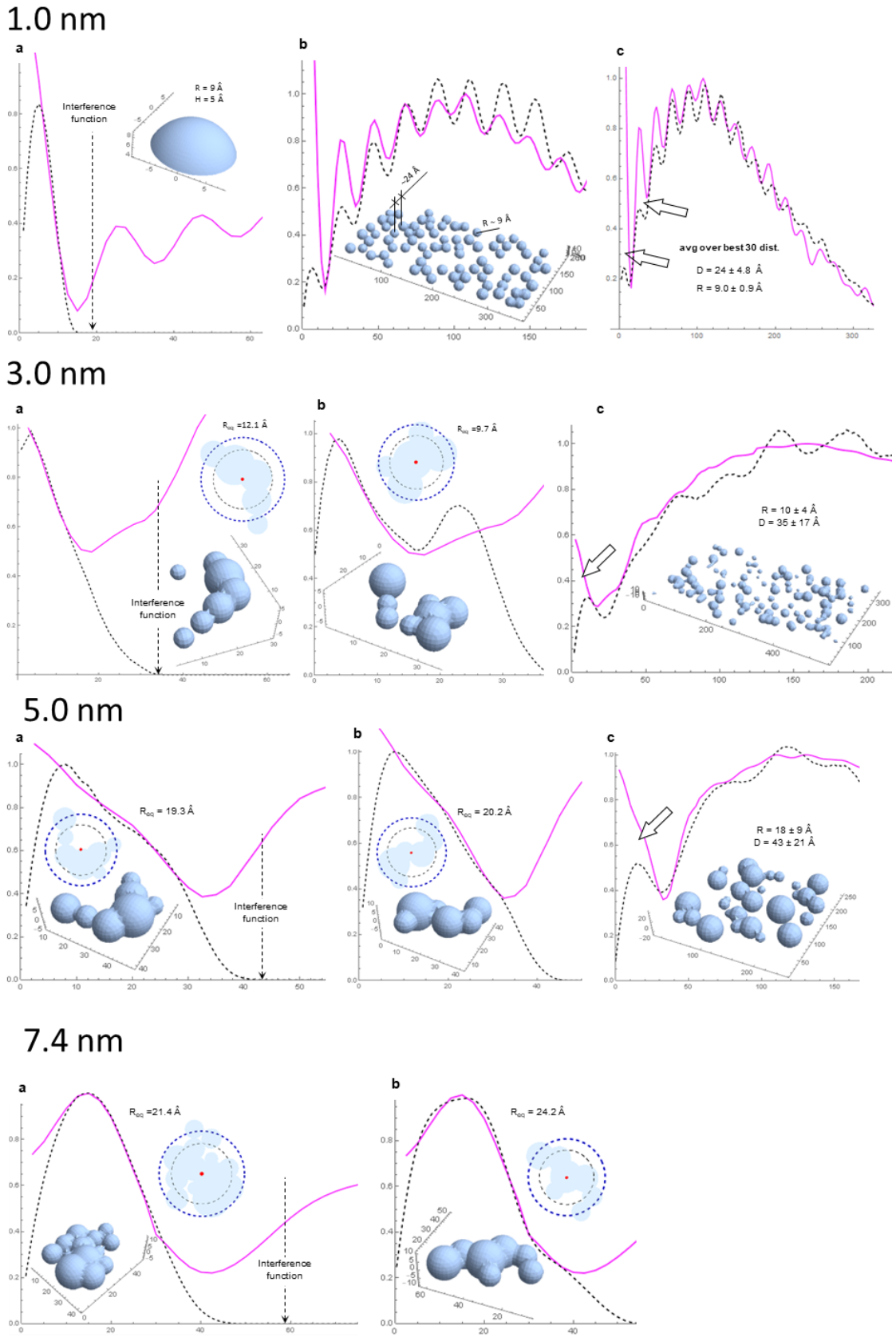

Figure S 9. Pair distance distribution function fits for nickel thin films with equivalent film thicknesses of 1.0, 3.0, 5.0 and 7.4 nm.

The PDDs obtained from the fits to the q_y-data of nickel do not exhibit peak shaped maxima for the small distance contributions apart from the one obtained for an equivalent film thickness of 7.4 nm (**Figure S 9** panels a). They rather show a maximum at the smallest distance and a following steady decrease towards a minimum located at distances between 15 and 43 Â. For the lowest thickness of 1.0 nm the PDD of a spherical cap shape with a radius of 9 Â and a height of 5 Â can mostly account for the slope of the PDD indicating compact metal island shape. However, the mass balance requires substantially larger clusters (13 Â) which could be satisfied by even smaller clusters nucleating in the regions between the larger ones. Thus, also the discrepancy at the smallest distances could be accounted for. For the thicknesses 3.0 and 5.0 nm the slope cannot be approximated with spherical clusters and elongated or somewhat branched cluster morphologies resulted from the fits. Also very small clusters which are not in contact with the large one but in close proximity can contribute to the small distances **Figure S 9** 3.0 nm a and b. This thickness of 3.0 nm is very close to the onset of percolation and therefore the shape estimations resulting from the fits are quite intuitive as neighboring clusters barely touch through contacts with small interspersed islands. Equivalent radii of the fitted structures increase from 9 to 24 Â and the shape of the clusters also increases in irregularity from a quite spherical approximation to a more frayed or branched appearance. For a thickness of 7.4 nm the inferred cluster structure can be thought of as resulting from the hole filling process happening after percolation. Thus, the structures are still somewhat branched but less elongated and more compact.

The overall shape of the PDDs was fitted only for thicknesses up to 5.0 nm. Best fits were obtained for arrangements where the average inter-cluster distance was very similar to that obtained from Kratky analysis. In general, the arrangements could be fitted reasonably well with minor discrepancies (arrows in **Figure S 9** panels c). The discrepancy at the first peak is most probably the result of approximating the clusters with a spherical rather than an elongated or branched shape so that small distance contributions from ‘offshoots’ are not represented. Furthermore, the second peak representing the nearest neighbor order in **Figure S 9** 1.0 nm c cannot be accounted for sufficiently by the fitted model. This could be caused by neglecting small clusters interspersed between the large ones. The strong oscillations of the PDD data could also be an artifact to some extent resulting from fact that only a finite window of q_y-data is available for PDD fitting. Nevertheless, the PDD shapes and the corresponding fit parameters demonstrate that the arrangement as well as the size and shape distributions get increasingly disordered and polydisperse. Especially the difference between the data of 1.0 and 3.0 nm is

striking and most likely due to transition from the nucleation to the coalescence regime (see normalized scattering data analysis).

9 Supplementary tables

Table S 1. Contact angles of the three test liquids with the respective surface given in degrees. Values are averages of at least ten independent measurements and standard deviations are indicated.

	Silver	Gold	Copper	Nickel	Polymer
Formamide	46.4 ± 1.6	57.2 ± 1.2	42.0 ± 2.5	24.6 ± 1.0	69.8 ± 2.2
Glycerol	65.1 ± 1.1	62.8 ± 1.3	47.5 ± 1.4	41.8 ± 0.5	78.2 ± 1.0
Water	71.4 ± 3.7	57.3 ± 1.2	28.3 ± 0.7	30.4 ± 1.5	84.9 ± 1.6

Table S 2. Surface energy components of test liquids according to Supporting Ref. 1.

	γ_L	γ_L^{LW}	γ_L^-	γ_L^+
	mJ m^{-2}			
Formamide	58.2	35.6	65.7	1.95
Glycerol	63.9	34.4	12.9	16.9
Water	72.8	21.8	10	65

Table S 3. Contact angles of test liquids with metals after surface exposure to ambient air for 24 hours.

	Silver	Gold	Copper	Nickel
Formamide	26.0 ± 1.6	56.7 ± 1.7	27.8 ± 4.5	20.6 ± 2.1
Glycerol	75.9 ± 0.4	72.8 ± 2.9	58.2 ± 1.4	36.6 ± 4.8
Water	79.3 ± 1.1	82.1 ± 0.4	57.9 ± 0.7	34.5 ± 1.6

10 Supporting References

(1) Volpe, C. D.; Siboni, S. Acid–Base Surface Free Energies of Solids and the Definition of Scales in the Good–van Oss–Chaudhury Theory. *J. Adhes. Sci. Technol.* **2000**, *14* (2), 235–272. https://doi.org/10.1163/156856100742546.

(2) Lazzari, R.; Renaud, G.; Revenant, C.; Jupille, J.; Borensztein, Y. Adhesion of Growing Nanoparticles at a Glance: Surface Differential Reflectivity Spectroscopy and Grazing Incidence Small Angle x-Ray Scattering. *Phys. Rev. B* **2009**, *79* (12), 125428. https://doi.org/10.1103/PhysRevB.79.125428.